Design Principles for Optimizing the Performance of Multicomponent Water Splitting Photoelectrocatalysts

by

John R. Hemmerling

A dissertation submitted in partial fulfillment
of the requirements for the degree of
Doctor of Philosophy
(Chemical Engineering)
in the University of Michigan
2021

Doctoral Committee:

Professor Suljo Linic, Chair
Assistant Professor Bryan Goldsmith
Professor Stephen Maldonado
Assistant Professor Nirala Singh

John R. Hemmerling

jhemmerl@umich.edu

ORCID iD: 0000-0002-8271-2858

Dedication

This dissertation is dedicated to my parents. And to the true joys in my life:

Sycamore Trees and Science Olympiad.

Acknowledgements

The success of my PhD and dissertation would not have been possible without the help and guidance from many people. First of all, I would like to thank Professor Suljo Linic who has been a great advisor throughout my time at the University of Michigan. I had wanted to join a high-achieving research lab that would push me to be a better scientist and researcher, and my experiences in the Linic Lab have done just that. Suljo pushed me to reach for stars and taught me the importance of thinking critically and presenting a compelling research story. I always appreciate his insightful analogies and clear explanations, and I am grateful to have developed as a versatile researcher under his guidance. I would also like to thank the members of my dissertation committee: Professor Nirala Singh, Professor Bryan Goldsmith, and Professor Stephen Maldonado. Their insightful questions and valuable feedback have been important for the quality and progression of this dissertation. My research would also have not been possible without the great staff and resources at the Lurie Nanofabrication Facility and the Materials Center for Characterization, where I have spent countless hours fabricating and characterizing my samples. I am also grateful to all of the staff, especially Jennifer, Kelly, Susan, and Nora, for being so amazing and helpful throughout my PhD. I would also like to acknowledge the National Defense Science and Engineering Graduate (NDSEG) Fellowship which I was awarded from 2017-2021. The fellowship has given me the freedom and flexibility to pursue the research that I found most compelling and impactful within the vibrant field of solar water splitting.

I also greatly appreciate all the members in the Linic Group, old and new. To the already-graduated students: Joe, Valentina, Umar, and Paul, thank you for being great role models and

setting the bar high for my PhD. In particular, Joe was instrumental for my quick progress at the beginning stages of my PhD and provided major research directions that inspired my dissertation work. He also performed much of the research in Section 5.2.1 of this dissertation. To those currently in the lab, it has been a great experience working with everyone, and thank you for the fruitful discussions and "cross-fertilization" of ideas. In particular, discussions with Steven have offered valuable insights, and he significantly contributed to Section 6.3 of this dissertation. Also, Aarti has become my wonderful protégé and contributed significantly to Chapters 6 and 7 of this dissertation. She is basically my full replacement, taking over the research project, mentorship program, and group meetings while also being a fellow NDSEG recipient. I am excited to see the new directions that she will take this research. Finally, I would like to acknowledge Sean, fellow roller coaster enthusiast, Star Wars lover, and Mars terraformer, who joined the lab at the same time as me. I could not have asked for a better friend to navigate the PhD with in the Linic Lab. I guess it was always meant to be; we basically have the same first name, and my research splits the water to produce hydrogen while his research does the opposite, using the hydrogen to make water (and electricity) in a perfect cycle.

I would also love to thank my family. My parents gave me the best love and support throughout my PhD, even if I did not share many of the details with them. Thank you for being my biggest fans and for wearing those goofy shirts. Also, a big shoutout to the Hemmerling hoard and best siblings ever: Kristina, Bobby, Michael, and AnnMarie. We make a great team surviving the zombie apocalypse in Zombicide, even if some people need to be sacrificed along the way. It is crazy how we are all going our separate ways, but continue to stay awesome and maybe we can form that band one day; after all, we already got the album cover photo. And then there is Abdulla, who has been like family during my PhD. Our friendship began forming as we

struggled in managing the glovebox and organizing the ChE Graduate Student Symposium, and we soon became inseparable. Abdulla is For Forever the Gon to my Killua and the Doctor to my Who. He is the friendliest and kindest person, and I could not have asked for a better friend.

I would also like to thank some of the important people who have helped shape my path toward getting a PhD. Professor Michael Mashtare is one of the major reasons I decided to pursue a PhD. He made research enjoyable, and I learned and developed so much, both personally and professionally, under his guidance. I cannot thank him enough you for being so kind and guiding me down this path of pursuing a PhD. Dating back to middle school, Science Olympiad has always been one of my primary passions and sparked my interest in becoming a scientist and engineer (and my fascination with sycamore trees). So many amazing memories with Chuckie, Corinne, Will, Zach, Mufaddal, Thomas, Keertan, Chelsea, Brandon, Dan, Tim Arthi, Mrs. Thompson, Mr. Farnell, and Mrs. Martin. Huge thanks to Mrs. Martin who took the helm when we were in desperate need for a new coach. Her commitment to us nerds is truly amazing. Finally, I would like to thank Mr. Smith, fellow chemical engineer and University of Michigan alum, who made chemistry fun and is one of the major reasons why I am a chemical engineer today. Interestingly, the lowest grade I ever got on a test in his AP Chemistry class was in electrochemistry with an 85% (why do I remember this?). I guess I needed revenge, pursuing a PhD heavily focused on electrochemistry.

Virtually every single day over the past 5 years was at least partially (or mostly) devoted to some progress for my research and dissertation, but there have also been so many amazing moments outside of research. In particular, intramural sports have been one of the highlights to have fun and meet new people within the ChE department. It all started during my 1st year, when my cohort was barely able to amass an ultimate frisbee team (the FrisBeasts) with about 3

minutes to spare before the deadline. Even though our team was repeatedly slaughtered that first season, we had fun making jerseys (number 11 for the win) and continued to improve throughout the years. Over 10 seasons later, we were finally crowned ultimately frisbee champions in a glorious come-back win after back-to-back games with no subs against a team that had previously beaten us by 13 to 4. The team was freshly named the "Over Reactors" with team pinnies sponsored by ChEGS, and this team also won the Intramural Sportsmanship Award for our friendly and fun demeanor. Soccer intramurals was also an amazing experience, and it was the first championship and T-shirt I had ever won from intramurals. Also, special shoutout to the volleyball squad (the legendary Volley Llamas and Serv-ivors: Alex, Cailin, Elizabeth, Emma, Ian, and sometimes Kaylee) who improved so much over the years to eventually win 2 championships before being thwarted by the pandemic. After vaccination, however, we had one last chance to compete, and we were able to win the championship on my very last intramural team—the perfect ending. Overall, I am so thankful for the many amazing people I met throughout my intramural adventures in which I played on a total of 80 teams and won 9 championships. But don't worry, all these sporting endeavors were after work hours.

I could probably blabber on forever, but instead I will just list some of the most memorable people and experiences for which I am eternally grateful.

- Being a GSI with Sean and remembering to save the Zoom recordings exactly 180 days after the fact (i.e., the day the important recordings would have been deleted forever).
- My lab mates for putting up with my excessive singing in the lab over the years
- "Golf bat." If you know, you know.
- Abdulla, Hannah, and Rachael for being an amazing team to organize "the best symposium ever!"

- Thanks to Emma, Alex, Kaylee, and Luke for being an epic squad to survive the dangers of Space Alert, despite everyone's infatuation with looking out the window.
- The wonderful board game crew that has terraformed Mars, discovered Planet Nine and Planet X, powered the grid, survived the zombie apocalypse, became mage knights, ascended, and decrypted individual words. All of this despite the deception and horrors of my arch nemesis.
- The sky diving crew: Corinne, Bobby, and Tyler; I never imagined that I would jump out of an airplane during my PhD.
- Allen for stopping me from sleep walking out of the tent while camping.
- My friends who always kept an eye on my water bottle which I constantly lost everywhere.
- Maddi for being the best cousin ever. Now with this PhD, I will finally be able to afford that beach house for you.
- Rawan and Rachel who were part of the office wild bird catching adventure.
- The Halloween door-decorating crew for earning the lab Blank Slate ice cream pints with ghastly puns: Soul-ar Water Splitting, Mem-Brain Reactors, Plas-Demonic Catalysis, and Hydrogen Ghoul Cells.
- Blank Slate for being my most-frequented business in the world with my all-time favorite ice cream: roasted butter pecan.
- Fritas for serving my all-time favorite burger, which is really saying something from a person who almost exclusively orders burgers when at any restaurant.

- Zixuan, my first roommate and fellow NDSEG recipient. Out of the 9 chemical engineers in the nation to win the 2017 award, I bet they did not expect 2 of them to be living in the same apartment.
- Kizito and everyone else who helped initiate the inaugural mentorship program with Oak Park High School to inspire the next generation of scientists and engineers.
- The volleyball squad, for tolerating my unconventional kicking attempts which mostly failed but also gloriously succeeded on rare occasions.
- The Spartan race squads for improving overall health and determination while helping distribute the punishing burpees. Best shirts and name ever: Enth-HelpMe, helping each other to overcome that energy barrier.
- The friends who finally made me into a world traveler, taking me all the way to Toronto in Canada, twice.
- To my older sibling, Kristina, for being a great role model, introducing me to Science Olympiad, and for enabling me to learn new skills at an early age.
- Corinne and Sean for being as enthusiastic as I am about roller coasters and creating new adventures on Giga and Strata coasters.
- Shoutout to my friends who married during the PhD: Josh and Christina as well as Kyle and Stephanie.
- To the legendary DnD squad, knights of the realm, protectors of Kestil, forge sworn, champions of planar teleportation, and masters of flight, stealth, and rambunctiousness.
- The pandemic which has been challenging but has helped me grow and not take things for granted. But still unfortunate that we missed conferences in San Francisco, New York, San Diego, and Hawaii.

- Chuckie for being the best tennis friend and allowing us to finally witness professional tennis. Third time's the charm for seeing Federer play, even if it was his quickest defeat in decades.
- Lauren, the best friend from Purdue for being so kind, telling the best stories, and being so relatable as we achieved advanced degrees.
- Sean, Sarah, and crew for showing me the magical places in the upper peninsula where I can summon my inner Moana (or Vaiana) on the lake.
- The lunch squad for spending many hours on our wonderful couch with epic discussions about Star Wars, franchising a Culver's, and taking over the world of science.
- **Luke,** who jokingly requested to be bolded, for providing me with unforgettable tailor-made baked goods (decorated by Sarah) and for being the best soccer partner, that is, when he was healthy enough to play.
- *Abdulla*, who in response to Luke's bolding, wanted to be italicized to be special.
- To my favorite sycamore tree at Purdue, which was germinated in space, as well as all of the wonderful sycamore trees on campus.
- Sean and Shelby for providing me dinner on the very night that I was finishing up this dissertation.

Table of Contents

List of Figures

Abstract

Affordable solar water splitting is considered the “Holy Grail” to transition our current hydrocarbon economy to a sustainable hydrogen economy. The goal is to immerse a photoelectrocatalyst in water and shine sunlight to produce hydrogen for long term energy storage and energy generation. The most common design for solar water splitting consists of light-absorbing semiconductors integrated with electrocatalysts. However, the widespread application of these multicomponent photoelectrocatalysts is limited by low efficiencies and poor stability of the materials. Throughout the past decade, research has demonstrated that insulator materials can stabilize semiconductors in metal–insulator–semiconductor (MIS) structures in which the metal layer acts as an electrocatalyst while the insulator layer protects the underlying semiconductor. Further research has demonstrated that the thickness of the insulator layer also plays a critical role in modulating the recombination rates and the performance of MIS systems. Despite significant improvements in the efficiency of MIS photoelectrocatalysts, rigorous guidelines are still needed to optimize the efficiency and approach the upper performance limits.

The overall goal of this dissertation is to shed light on the critical role of the interfaces on the performance of MIS photoelectrocatalysts and to leverage the insights to optimize their efficiency. The first scope of this dissertation focuses on the concrete example of planar n-type Si protected by a HfO_2 or Al_2O_3 insulator layer and attached to a planar Ir electrocatalyst that completes the oxygen evolution reaction, which is one of the water splitting half-reactions. This work utilizes theory and modeling to design electrochemical experiments and quantify key

parameters to evaluate the overall performance and the theoretical upper limits. The results demonstrate that the typical strategy of tuning the insulator thickness is insufficient to achieve the maximum performance. To approach the upper limits, MIS photoelectrocatalysts must overcome efficiency losses attributed to the presence of interfacial defect states, parasitic light absorption/reflection, and insufficient charge carrier selectivity of the insulator. Based on the insights from this combined experimental and modeling work, strategies such as annealing the interfaces and doping the insulator layer are implemented to optimize the performance of the MIS photoelectrocatalysts.

The second scope of this dissertation focuses on Ni nanoparticles electrodeposited on planar n-type Si which have previously demonstrated good performance and stability without an intentional insulator layer. The stability is enabled by the anodic passivation of the Si surface to form a SiO_2 layer, and the high efficiency is typically attributed to "pinched-off" nanoparticles that decrease the recombination rates. Contrary to this common perception, the results herein demonstrate that an adventitious SiO_2 insulator layer at the nanoparticle Ni/Si interface may be the primary explanation for the high efficiency of these photoelectrocatalysts. In other words, an interfacial insulator layer can significantly improve the performance for nanoparticle-based systems via a mechanism similar to traditional planar MIS systems. Overall, this collective work demonstrates the critical importance of the interfaces in optimizing the performance of solar water splitting systems and offers design principles that are broadly relevant to the field of photoelectrocatalysis.

Chapter 1

Background and Motivation

1.1 The Energy Challenge

As the countries of the world continue becoming more industrialized, the demand for energy is expected to keep increasing. Access to a supply of energy is essential for most aspects of modern life including electricity, internet, transportation, and clean food and water. The critical challenge is ensuring a sufficient and sustainable supply of energy for an increasing global population while minimizing harmful damage to humans and the environment. Considering energy on its own, however, is an incomplete piece of the overall picture. The water-food-energy nexus is a relatively new paradigm to provide a holistic view in which the supply of clean water, food, and energy are all interconnected.[1–3] For example, water is needed to produce energy from most sources, and fresh water is predicted to be scarce for up to 75% of the global population by 2050.[4] Providing access to clean water, food, and energy to improve overall health and quality of life to a growing population is considered a grand challenge which will require bold initiatives to solve.[5]

1.1.1 Current and Future Energy Consumption

In the United States in 2020, the energy consumption was about 93 quadrillion British thermal units (btu), of which about 79% was produced by fossil fuel sources (petroleum, natural gas, and coal) and only 12% was supplied from renewable sources (Figure 1-1a).[6] The largest fraction of this energy consumption is for electric power (38.5%) followed by transportation

(26%) and industrial (24%) sectors (Figure 1-1b). The overall energy consumption in the U.S. has stayed relatively constant over the past two decades.[6] But on the global scale, energy consumption is projected to increase by approximately 50% by 2050 compared to consumption in 2018.[7] Industrializing countries that are not part of the Organization for Economic Cooperation and Development are the major drivers for this increase in energy. Despite a projected increase in renewable energy, fossil fuels are still expected to be the dominant supply of energy globally in 2050.[7] Unfortunately, such increases in fossil fuel usage have their own set of challenges for global health and the environment.

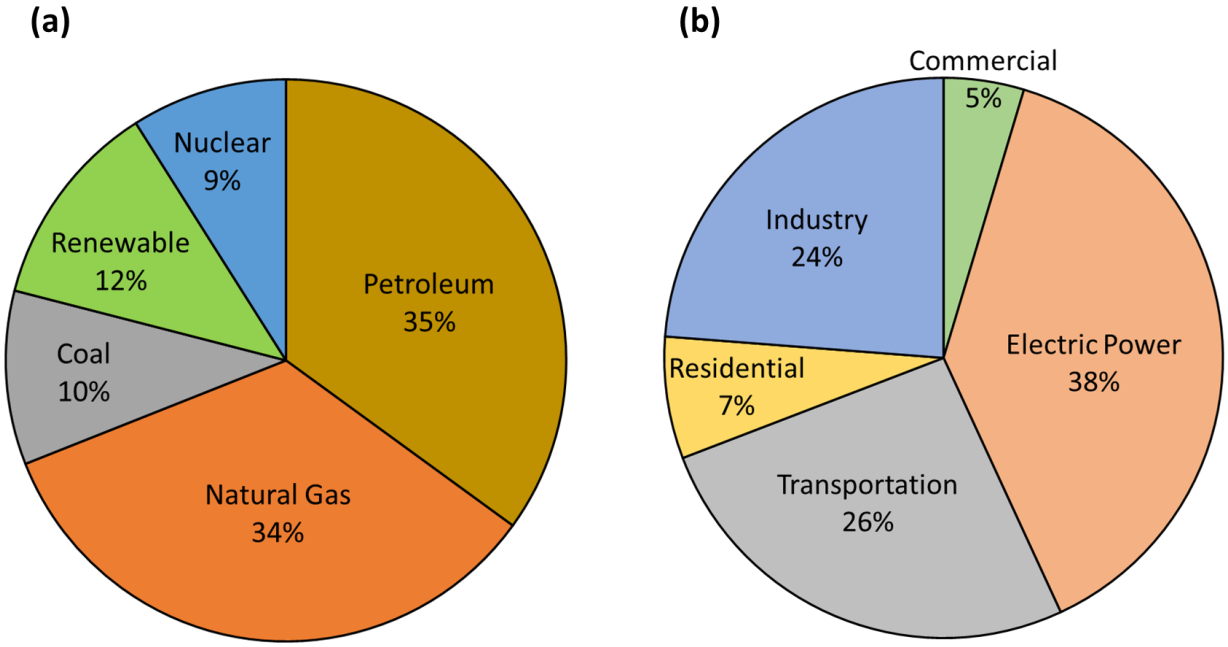

Figure 1-1: (a) Sources for energy production and (b) the energy-use sectors of the produced energy for the United States in 2020 using data from Ref. [6].

1.1.2 Issues with Fossil Fuels

The first issue with reliance on fossil fuels is that they are not a renewable source of energy and will eventually be depleted. For hundreds of millions of years, the earth has been generating large reserves of fossil fuels from decomposed plants and animals. But fossil fuels are produced on the order of millions of years, while consumption of fossil fuels is on the order of seconds.[8] A mass balance comparing the production minus the consumption of fossil fuels can show that high quality or easily-accessible fossil fuels will eventually be depleted. Specific research has provided estimates on the timeline for depleted fossil fuel reserves based on fuel consumption, fuel costs, and amount of fossil fuel reserves. One paper in 2009 projected that reserves of natural gas and oil could be depleted by 2042 while coal could remain until 2112.[9] More recent projections predict that all fossil fuels will last until at least 2075, and new reserves may still be discovered.[10] But the bottom line is that eventually fossil fuels will be depleted enough to be non-economically viable, and alternative sources will need to be implemented. Even if there were an infinite supply of fossil fuels, there are still many issues with fossil fuels and reasons for fossil fuels to be replaced by sustainable sources in the short term.

In general, fossil fuels have a significant impact on environmental and human health. These impacts are external to the fossil fuel industry and are therefore not factored into the cost of production and are called externalities. One of the most recognized externalities of fossil fuels is greenhouse gas emissions, namely CO_2 which is a product of combustion of fossil fuels. Every year since 2010, the global anthropogenic CO_2 emissions have exceeded 30 Gigatons (Gt) which unbalances the global carbon cycle between the plants and the ocean.[11] The carbon balance has also been affected by the number of trees on earth which has dropped by approximately 46% since the beginning of human civilization.[12] The result of this human behavior and consumption

of fossil fuels is that the amount of carbon dioxide that accumulates in the air has significantly increased by over 40% since the industrial revolution and even more rapidly since the 1970's.[13] As a greenhouse gas, carbon dioxide in the atmosphere results in increased temperatures, which has been demonstrated in numerous reports and climate models.[14–16] While climate models always have uncertainties, averaged outcomes over time can be more confidently predicted. In contrast to the weather, which is unpredictable and chaotic, climate is weather averaged over an extended period of time which can be predicted. This is analogous to how the result of a single coin flip cannot be predicted but the average result over hundreds of coin flips can be predicted with high accuracy. The climate models are validated by comparing the results to well-tabulated historical data. It has been shown that including anthropogenic CO_2 emissions in the modeling is essential to predict and match the historical data.[14–16] In other words, known factors such as volcanic eruptions, solar variation, and El Niño/La Niña cannot explain the historical climate data without accounting for CO_2 emissions. As the earth continues to get warmer, fresh water and food are expected to become more scarce, the intensity of natural disasters are expected to accelerate, and many millions in coastal populations will have to manage rising ocean levels.[16,17] Indeed, the 20th century saw over 6 inches in sea level rise, and the rates are accelerating and expected to continue throughout the 21st century.[16,18,19]

Ocean tide levels are not the only concern from CO_2 emissions. Most of the human emitted CO_2 emissions end up being absorbed by the ocean which can fundamentally change the pH and the chemistry of the ocean. Dissolved CO_2 in the ocean reacts with water to form hydrogen ions and bicarbonate ions. Hydrogen ions are directly related to acidity, and it has been estimated that anthropogenic CO_2 emissions has increased the acidity of the ocean by 30% and will only get worse over the coming decades.[20] The full consequences of ocean acidification are

not fully understood, but it generally has a detrimental impact on physiology of aquatic life and makes it more difficult for coral to form shells and reefs of calcium carbonate.[20,21] Furthermore, it takes decades for CO_2 to equilibrate with the ocean, so even if CO_2 emissions were stopped today, the oceans would continue becoming more acidic for decades to come; meanwhile, the long-term removal of CO_2 will take hundreds to thousands of years.[22]

The final major concern of fossil fuels is air pollution. Besides carbon, combustion of fossil fuels release toxic sulfur and nitrogen oxides as well as particulate matter which can lead to respiratory problems.[23] Research has shown that as many as 4 million excess deaths worldwide are attributed to outdoor air pollution associated with fossil fuel emissions.[24] The estimated costs from the damage and mortality from air pollution has been reported to be $184 billion in 2002 in the United States, with coal being the greatest contributor.[25] Accounting for other externalities besides air pollution, the costs of fossil fuels are even larger.[26] Even though fossil fuels are inexpensive for the consumer's direct purchase, the real cost of fossil fuels is much higher when considering these externalities.

1.1.3 The Sun as a Renewable Energy Source

There are many renewable and sustainable energy sources that have been investigated to replace the global reliance on fossil fuels. Among them, electricity from solar energy is expected to exhibit the largest increase in production in the coming decades as solar photovoltaics (solar cells) are less expensive than coal or natural gas in many countries.[27] The sun is inexhaustible and the source of most energy on earth; in a given hour, the earth collects enough power from the sun to meet the entire global energy consumption for a year.[28]

Solar cells are the most common approach to convert solar energy into electricity. While the upfront costs can be large to implement solar cells, the levelized cost of electricity averaged

over the lifetime of the solar cells is competitive with the levelized cost of electricity from coal and natural gas.[29,30] Environmental benefits of solar cells can be analyzed using a life cycle analysis to examine the overall impacts and emissions throughout the entire lifetime of solar cells vs fossil fuels. Solar cells generate orders of magnitude less CO_2 emissions and pollution compared to fossil fuels.[31,32]

One of the major challenges of utilizing solar energy is that the sun does not always shine, so there is inherent seasonal and daily intermittency in the energy generation.[33] In general, the peak power generated from solar cells matches the peak energy consumption (i.e., most energy is consumed during the day). But there is still the challenge when energy is needed at night. To solve the intermittency problem, the generated energy needs to be stored so that it can be used on demand. Batteries and fuel cells are the two major strategies (besides geography-dependent strategies like compressed air or pumped hydro) to store energy. At large scales, batteries tend to be expensive and prone to discharge over time.[34] The prospects of using hydrogen and fuels cells for energy storage are discussed below.

1.2 Harnessing Sunlight to Produce Hydrogen

1.2.1 Importance and Prospects of Hydrogen

Currently hydrogen is an important feedstock for various industrial applications such as electronics, oil refining, steel production, methanol production, and ammonia synthesis.[35] Specifically, about 37 % of hydrogen is dedicated to the petroleum industry and 50% of hydrogen is dedicated for the ammonia synthesis reaction for fertilizers.[36] It has been estimated that 1% of the entire global energy demand is used for ammonia synthesis in which hydrogen plays an important role.[37]

In addition to the already prevalent roles of hydrogen, there is also significant potential for hydrogen applications in fuel cell vehicles and energy storage. One of the advantages of hydrogen is its high specific energy (based on mass), although it suffers from relatively low energy density (based on volume).[38] Progress for implementing hydrogen for passenger vehicles has been slow. In 2018, only 11,200 hydrogen cars were globally in circulation from three brands: Toyota Mirai, Honda Clarity, and Hyundai Nexo.[39] The challenge has been high costs for the vehicles and hydrogen fueling infrastructure. However, reports have estimated that fueling costs can be lower for hydrogen vehicles compared to electric battery vehicles for high market penetration in Germany.[40] The future is also promising for fuel cell implementation for large scale transportation like trains, trucks, and boats where batteries are less practical.[39,41]

Hydrogen also has significant potential for long term energy storage applications. Long term energy storage with minimal discharge is vital to help solve the intermittency challenge with renewable energy sources. When the energy from stored hydrogen is needed, then the energy can be extracted using large-scale fuel cells. The only byproduct of these fuel cells is water, which can in turn be transformed back into hydrogen forming a closed cycle.[42]

Overall, hydrogen is an important feedstock for many industrial processes, and has the potential to have an even larger role in energy storage, transportation, and energy generation which would enable the so-called hydrogen economy. The hydrogen economy is a future route to replace the current-day hydrocarbon economy and can significantly reduce the amount of CO_2 emissions and air pollution.[43] Moving toward this goal, the path forward requires the sustainable and abundant production of green hydrogen.[22]

1.2.2 Global Hydrogen Production

Figure 1-2 shows the sources of global hydrogen production, which is dominated by fossil fuels.[44] The most common method to produce hydrogen is through natural gas steam reforming because of the cheap cost of abundant natural gas throughout the past two decades. Meanwhile, hydrogen production from water only accounts for up to 4% of hydrogen production, while the International Energy Agency recently reported that less than 0.1% of hydrogen production is derived directly from water.[39] The reason for the discrepancy is unclear as the calculation details were not provided, but the value of 4% appears to originate using 2006 data from Industrial Gases by Chemical Economics Handbook.[45–47] Other sustainable methods to produce hydrogen, such as from algae or biomass gasification are still at the lab scale rather than the industrial scale.[36] One of the major research challenges is to improve the economic viability of hydrogen production from water compared to the fossil fuels which dominate the market.

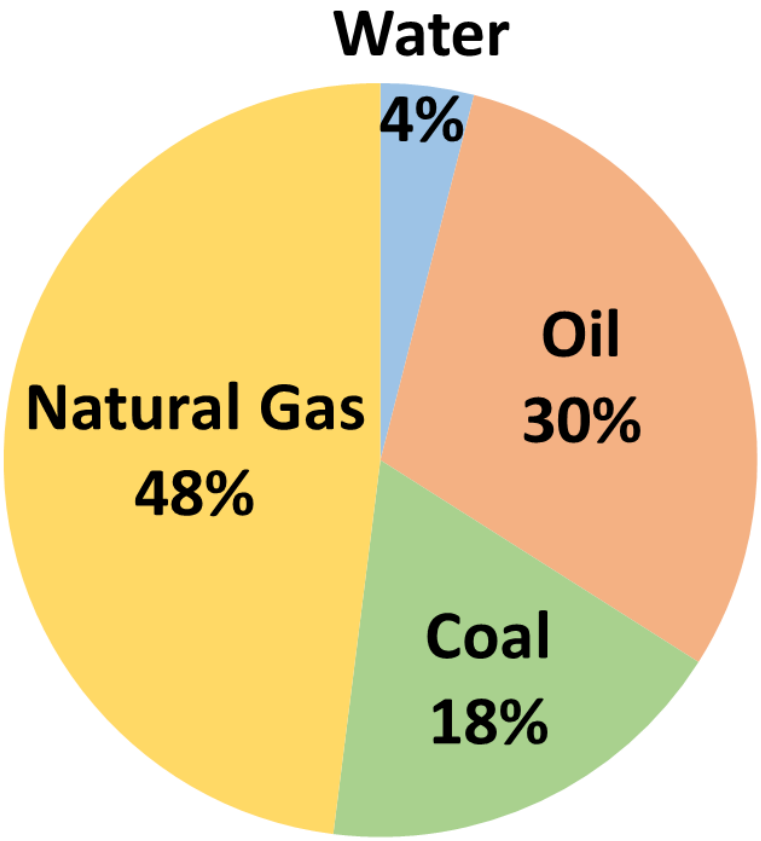

Figure 1-2: Sources for Global hydrogen production using the data from Ref. [44].

1.2.3 Water Splitting Introduction

To produce hydrogen from water, the water molecules must be split into its constituents of hydrogen and oxygen. This overall reaction process can be split up into two half-reactions: (1) the hydrogen evolution reaction (HER) which is a cathodic reduction reaction requiring electrons and (2) the oxygen evolution reaction (OER) which is an anodic oxidation reaction which produces electrons. The half-reactions depend on the pH of the water, and for alkaline conditions, the following reactions occur:

HER:	$4H_2O + 4e^- \rightarrow 2H_2 + 4OH^-$	$E_{cathode} = 0.00$ V vs SHE
OER:	$4OH^- \rightarrow O_2 + 4e^- + 2H_2O$	$E_{anode} = 1.23$ V vs SHE
Overall:	$2H_2O \rightarrow 2H_2 + O_2$	$E_{reaction} = 1.23$ V

Each half-reaction has a thermodynamic electrochemical potential associated with the reaction, and the overall water splitting reaction thermodynamically requires 1.23 Volts. This thermodynamic voltage is based on water's Gibb's free energy of reaction which is +237 kJ/mol at standard conditions of atmospheric pressure, 298 K and 1 M concentrations. The positive energy requirement means that water splitting is not a spontaneous reaction, and that energy needs to be supplied for the reaction to occur (and hence the reverse reaction to produce water in fuel cells can generate energy).

In addition to the thermodynamic voltage requirement of 1.23 V, there are also kinetic losses for the half-reactions, so voltages of greater than 1.6 V are typically needed to split water at reasonably high rates. Most of these losses are from the oxygen evolution reaction which is kinetically sluggish.[48–50] Depending on the generated currents and the design, resistance and mass transport losses can also become significant.[51]

Essentially all of the water-based hydrogen production in Figure 1-2 is from electrolyzers which use electricity to apply a voltage and split water. Several types of electrolyzers include polymer electrolyte membrane which operate in acid, alkaline electrolyzer which operate in base, and solid oxide membranes which operate at higher temperatures and pressures.[51–53] The challenge with electrolyzers is economically competing with hydrogen production from fossil fuel sources.

A quick calculation can demonstrate the economic challenge for water splitting using electricity. The Department of Energy techno-economic target for water electrolysis is $2.3 per

kilogram of H_2.[54] The typical cost of electricity for industry is about 7 cents per kWh.[55] For an electrolyzer that is 80% efficiency (i.e., operating at a voltage of 1.23/0.8 = 1.54 V), then the minimum cost to produce hydrogen would be $3 per kilogram which exceeds the DOE target. And this is only accounting for the cost of electricity, not including the cost of materials or balance of plant. Based on only the cost of electricity, the breakeven cost for electricity would have to be less than 5.4 cents per kWh to match the DOE target $2.3 per kilogram of H_2. Specifically, the DOE target for electricity price is 3.7 cents per kWh which accounts for about 68% of the total cost to produce hydrogen.[54]

Another challenge with using electricity to split water is that a large fraction of the electricity may be produced from fossil fuels. Solar cells have continued to produce electricity at record low costs and have also been integrated with electrolyzers to sustainably produce hydrogen from water. Despite the relatively low costs of electricity from solar cells, the techno-economic analyses of photovoltage plus electrolyzer designs suggest that the cost of hydrogen from this technology still exceeds $6 per kg of hydrogen.[56,57] Due to these economic challenges, alternative methods to produce hydrogen from water, such as photoelectrochemical water splitting, is an active area of research.

1.3 Photoelectrochemical Water Splitting: Introduction, Efficiency and Techno-economics

1.3.1 Introduction to Photoelectrochemical Water Splitting

As discussed in the previous section, solar energy can be used to split water using semiconductor-based solar cell technology that is externally coupled to an electrolyzer. But a simpler, possibly more economical design is photoelectrochemical water splitting which involves a fully integrated system that is entirely immersed in water to split the water molecules directly. In other words, the electricity generation (using a semiconductor light absorber similar to a solar

cell) and the chemical reactions all take place in the water.[58,59] The first demonstration of photoelectrochemical water splitting was by Honda and Fujishima in 1972 using the semiconductor TiO_2.[60] In the 50 years since the seminal work, the materials that have received the most attention in photoelectrochemical water splitting are electrocatalyst nanoparticles that are attached to the surface of the semiconductor light absorber.[61–63] In these multicomponent systems, the semiconductor absorbs photons from the sun if the photons have energy greater than the band gap of the semiconductor. The light absorption forms electron-hole pairs in which the electrons move to the hydrogen evolving electrocatalyst and holes move to the oxygen evolving electrocatalyst, as shown in Figure 1-3.

Photoelectrochemical cells have some similar principles related to absorption of the photons from the sun, but they have fundamentally different constraints. For solar cells, the band gap of the semiconductor is optimized to maximize the fraction of sunlight that can be absorbed which is based on the Shockley-Queisser limit.[64] For photoelectrochemical cells, the semiconductor also needs to generate sufficient voltage (>1.6 V) and have sufficient catalytic activity to split water.[42] Stability of the semiconductor is another key concern because there is a thermodynamic driving force to change their chemical and therefore optical (light absorption) properties under the conditions of photoelectrochemical water splitting.[65–68]

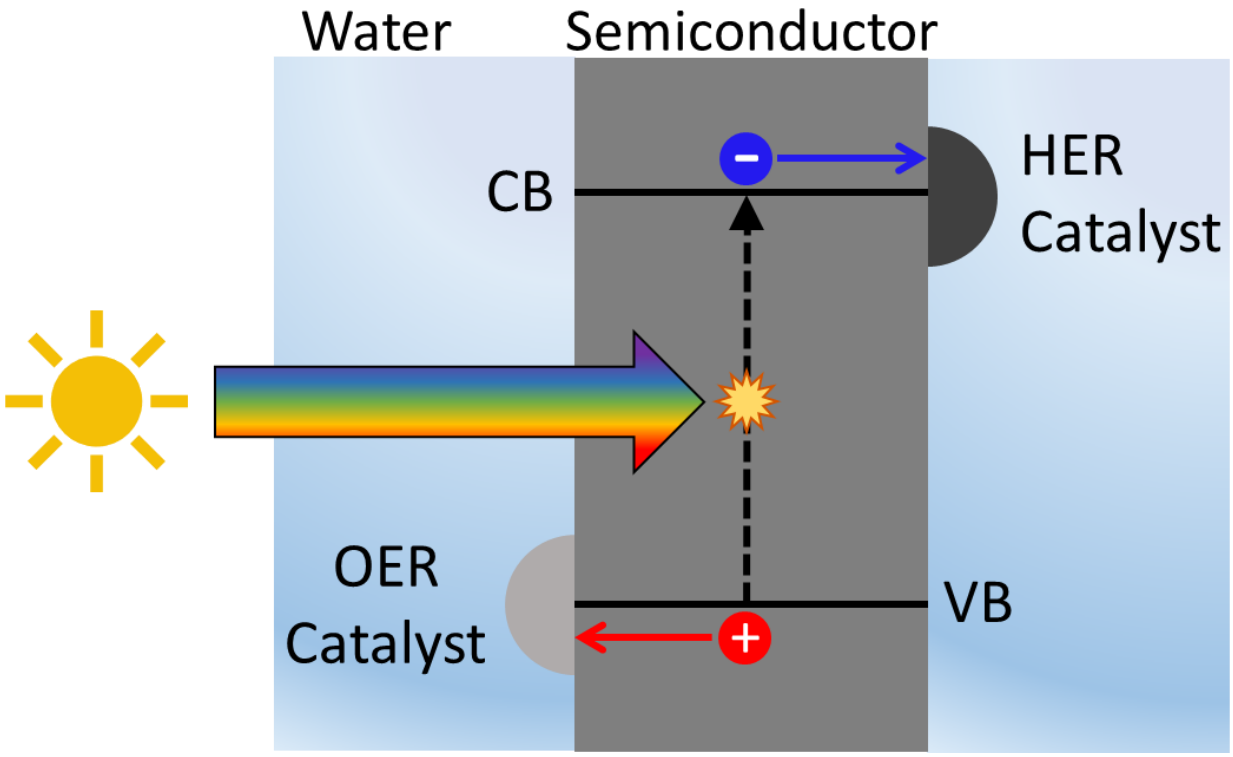

Figure 1-3: Components of a photoelectrochemical water splitting cell include the semiconductor with a characteristic band gap. The semiconductor is coupled to electrocatalysts, immersed in water electrolyte, and illuminated with sunlight to split water.

1.3.2 Photoelectrochemical Reactor Designs and Techno-economics

The widespread use of photoelectrochemical water splitting for hydrogen production ultimately depends on its economic viability. Techno-economic analyses have been performed to study the economic viability of various systems taking into account the reactor design, the stability/lifetime of the systems, the costs of materials, and the solar-to-hydrogen efficiency (i.e., the fraction of solar energy turned into the chemical energy of the hydrogen products).[69–71] In a techno-economic analysis by Pinaud et al.,[69] the two broad types of photoelectrochemical reactor designs considered were particulate systems and planar systems.

Particulate systems involve nanoscale or microscale particles that are immersed in a giant bath to form a slurry of particles. One design that has been analyzed for techno-economics is the single baggie design which inflates as the hydrogen and oxygen are coevolved together (Figure 1-4a).[69] A single semiconductor nanoparticle or microparticle is integrated with an OER and HER electrocatalyst to coevolve hydrogen and oxygen. The base case metrics used to model these systems assume 10% STH efficiency, a lifetime of 5 years, and particle costs based on nanoparticle coating processes which have been utilized in the pharmaceutical industry.[69]

Planar systems resemble solar cells in that bulk systems are fabricated in a planar architecture and pointed toward the sun (Figure 1-4b).[69] A planar semiconductor or photovoltaic is integrated with an OER catalyst on one side and an HER catalyst on the other side. When immersed in water and after shining light on the system, and one side of the system produce hydrogen and the other side produces oxygen. The products are physically separated from each other because they are produced on opposite side, and a membrane can prevent cross-over of the products. The base case metrics used to model these systems assume 10% STH efficiency, a lifetime of 10 years, and costs based on photovoltaic cost projections.[69]

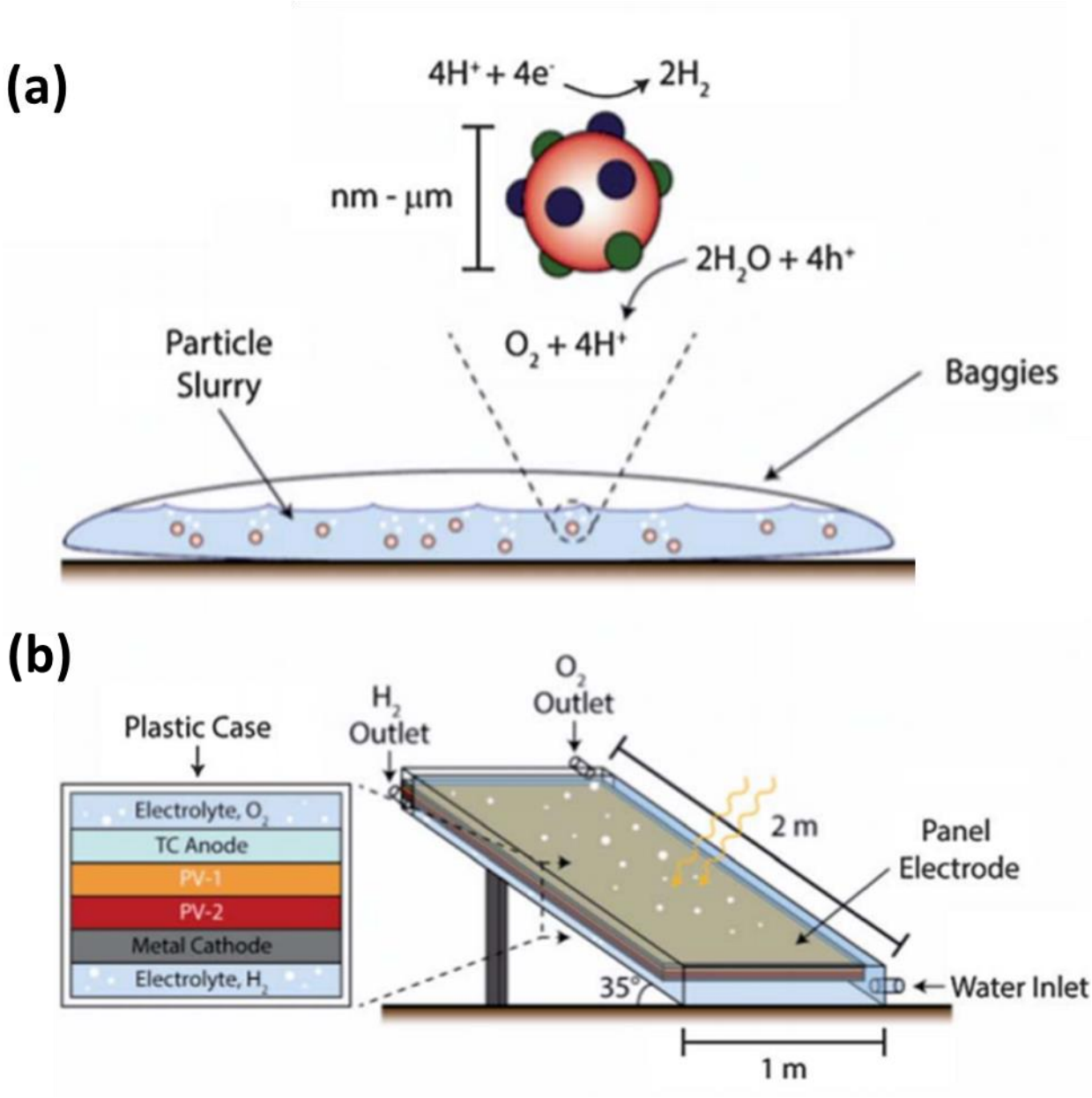

Figure 1-4: Illustrations of (a) particulate and (b) planar reactor designs for photoelectrochemical water splitting. Adapted from Ref. [69] with permission from the Royal Society of Chemistry.

To perform the techno-economic analysis, the production rate was 10 tons of hydrogen per day.[69] Each type of system was evaluated based on realistic baseline values for solar-to-hydrogen efficiency, overall costs, and lifetime. The baseline values are reported in Figure 1-5 and the predicted cost of hydrogen is 1.6 $/kg for the particulate system and 10.4 $/kg for the

planar system. Each of the parameters are also varied to analyze how they impact the overall cost to produce hydrogen. As shown in Figure 1-5, the efficiency of the system is the most important factor in driving the costs. A higher efficiency means that fewer materials are needed to produce a given amount of hydrogen which can also result in significant savings on the costs for pumping, compressing, land area, etc.[69]

Overall, the techno-economic analysis demonstrates the potential for particulate systems to reach the 2020 DOE target of 2 $/kg. However, this is a less developed technology, and achieving even 1% efficiency has remained a challenge in the literature.[63,72] The planar design in Figure 1-4b is prohibitively expensive for producing hydrogen. However, the costs can be significantly reduced down to 4 $/kg (or 2.9 $/kg with increased efficiency) by using concentrated sunlight.[69] Thus, planar designs also have potential for economic viability, but achieving high efficiencies is essential.

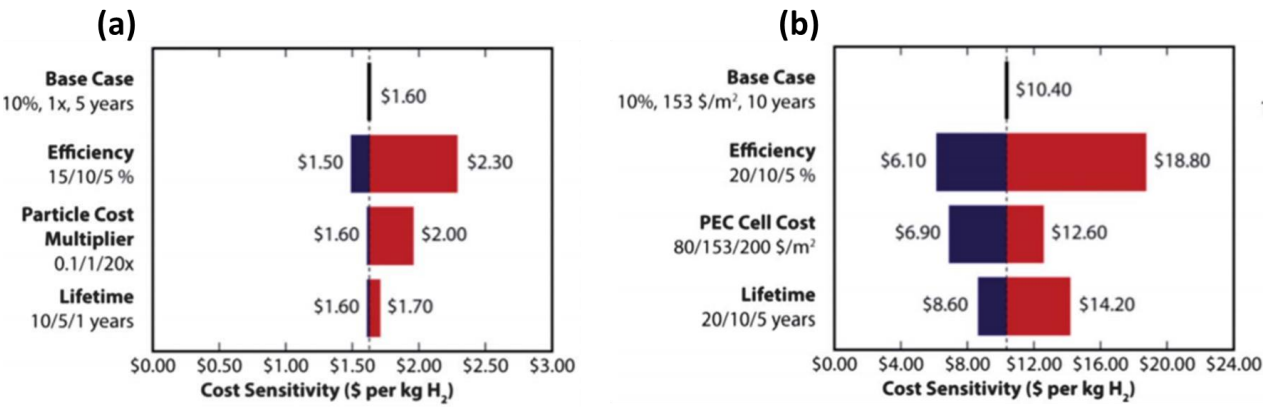

Figure 1-5: Cost sensitivity analysis as a function of efficiency, material cost, and lifetime for particulate (a) and planar (b) reactor designs for photoelectrochemical water splitting. Adapted from Ref. [69] with permission from the Royal Society of Chemistry.

1.3.3 Efficiency of Photoelectrochemical Water Splitting

Given the importance of the solar-to-hydrogen (STH) efficiency, substantial research has focused on identifying the achievable performance limits in photoelectrochemical water splitting systems.[69–71,73–75] These analyses are based on efficiency losses in these photocatalytic systems which include: (1) free energy losses associated with radiative recombination and Shockley-Queisser losses, which are theoretically between 0.4 and 0.6 V for most semiconductors[64,76–78] and (2) catalytic losses associated with slow kinetics for performing the OER and HER half-reactions.[48,49,79–83]

Figure 1-6 summarizes realistically achievable STH efficiencies that can be obtained by photoelectrochemical water splitting systems as a function of the semiconductor band gap.[73] For a system with a single semiconductor photo-absorber, Figure 1-6a shows that the optimal STH efficiency is around 12% for a band gap of ~2.2 eV.[73] Semiconductors with lower band gaps generate insufficient voltage to thermodynamically split water while semiconductors with higher band gaps do not adsorb enough photons from the sun. For example, many oxide semiconductors such as TiO_2 and $SrTiO_3$ have a band gap of above 3 eV, meaning that they can only absorb wavelengths in the UV region, which is only ~ 3 percent of the solar spectrum.[84–96]

The data in Figure 1-6b using a similar technical analysis shows that tandem semiconductor architectures (i.e., two semiconductors on top of each other) can yield STH efficiencies between 20-23% which can reach the DOE targets.[54] This is achieved for band gap combinations in the range of 1.0 to 1.4 eV for the bottom semiconductor and 1.7 to 2.1 eV for the top semiconductor (Figure 1-6b).[69,73,74,97,98] Such high efficiencies are possible because multiple semiconductors can absorb a larger fraction of the solar spectrum to generate higher currents while also generating sufficient voltage to split water.

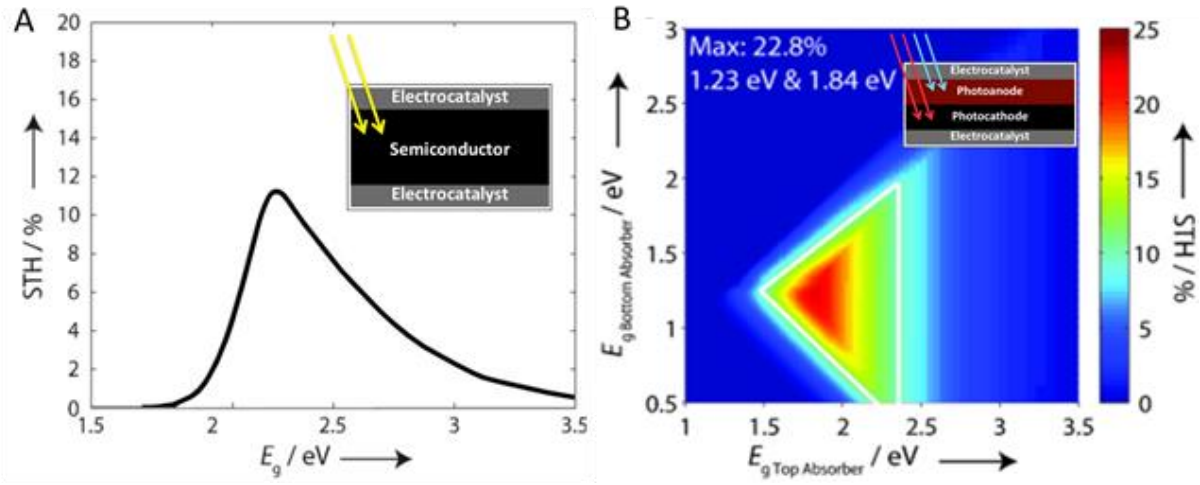

Figure 1-6: (a) STH efficiency as a function of semiconductor band gap for a single semiconductor system. (b) Optimal band gap combinations for a tandem semiconductor photoelectrochemical water splitting system. Adapted with permission from from Ref. [73]. Copyright 2014 John Wiley and Sons.

1.4 Materials and Interfaces for Efficient and Stable Photoelectrochemical Water Splitting

In many cases, research has focused on one half-reaction and a single semiconductor at a time. Once each of these half-cells have been optimized, then they can be combined together to perform overall water splitting in a tandem system.[99–103] Many semiconductor materials have been studied, and as described in the previous section, the highest efficiencies can be obtained if the band gap is between about 1 to 2 eV. As shown in Figure 1-7, there are many semiconductors that meet the band gap requirements for high efficiency tandem systems.[104] Among investigated systems, silicon (Si) with band gap of 1.1 eV is the prominent choice for the lower band gap semiconductor because of its earth abundance, low cost, and extensive commercial use.[102,105] A critical challenge in the application of Si and almost all semiconductors with desirable band gaps is their corrosion under water splitting conditions. Figure 1-7 shows the oxidation and reduction potentials for various semiconductors, suggesting that most semiconductors are not stable under the conditions of water splitting, i.e., there is a thermodynamic driving force to change their

chemical and therefore optical (light absorption) properties.[68,104] Overcoming the instability of the semiconductors while maintaining high efficiency is a major challenge hindering economic viability.

Stability has been an intense focus in the literature,[106–109] and many reviews have been published on the topic.[65,66,97,104,110–112] In many cases, the strategy to enhance stability is by physically separating the unstable semiconductor from the electrolyte by depositing an overlayer (typically a metal or a metal oxide). The overall goals are to (1) stabilize the system on the order of years, (2) minimize parasitic recombination as the overlayer may interfere with the incident illumination, and (3) maximize the charge transfer of the desired energetic carriers so that they can split water with high efficiency. However, improving in one area can have negative consequences in another area. For example, the stability of a system may be enhanced by using a thicker protective coating, but a thicker protective coating may decrease the charge transfer thereby lowering the efficiency.

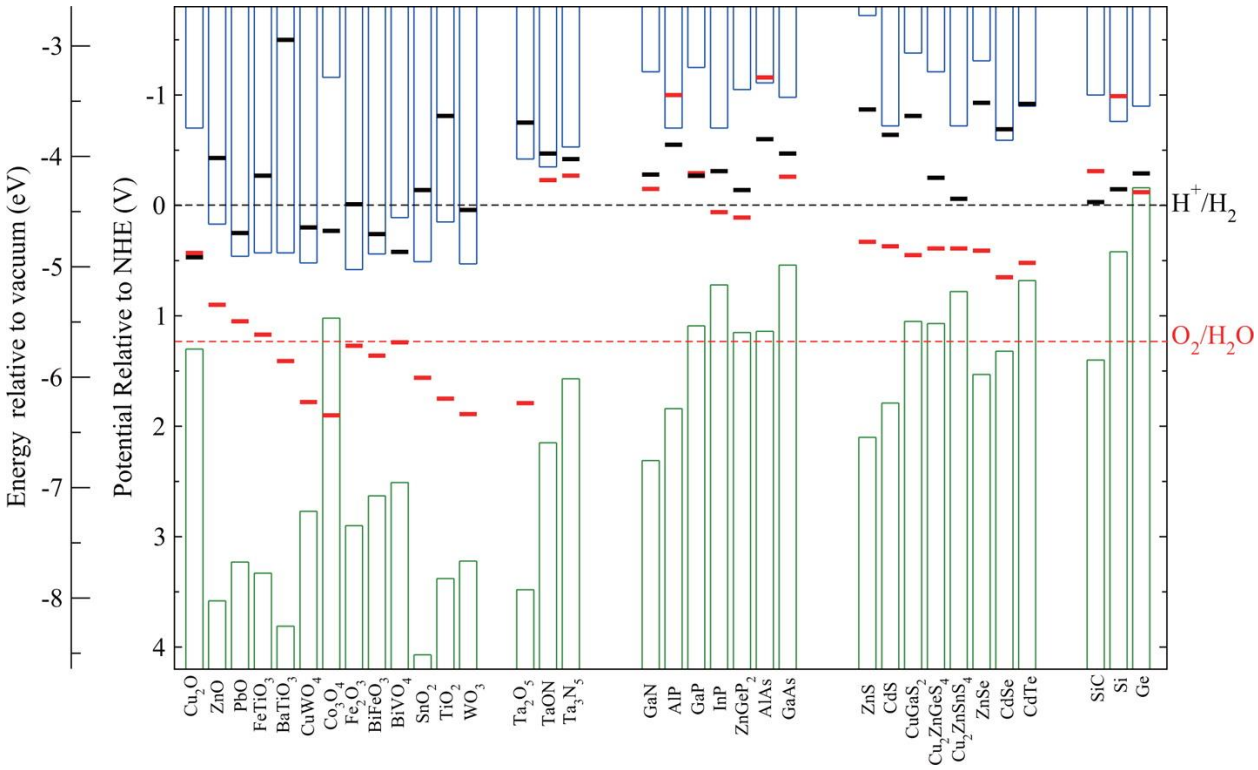

Figure 1-7: Properties of various semiconductors used for photocatalytic water splitting. The green and blue columns are the valence and conduction band edge positions, respectively. The red and black bars are the oxidation and reduction potentials of each semiconductor. Values are relative to the normal hydrogen electrode and the vacuum level for pH = 0, temperature of 298.15 K, and pressure of 1 bar. Under the water splitting conditions, the semiconductor will self-oxidize if the oxidation potential is above the OER redox potential, and the semiconductor will self-reduce if the reduction potential is below the HER redox potential. Reproduced with permission from Ref. [104]. Copyright 2012 American Chemical Society.

1.4.1 Scope of Dissertation: Metal-Insulator-Semiconductor Systems for Efficient and Stable Solar Water Splitting

Over the past decade, it has been shown that oxide insulators can be introduced to protect some semiconductors against corrosion. In these systems, a stabilizing insulator layer is placed between a semiconductor and a metal-based electrocatalyst forming so-called metal-insulator-semiconductor (MIS) device architectures.[66,113] One of the first MIS water splitting systems used a TiO_2 insulator layer to stabilize Si.[114] Since this work, many protective insulators have been utilized in Si-based MIS photocatalysts, including Al_2O_3,[115–121] HfO_2,[122–125] SiO_2,[126–140]

$SrTiO_3$,[141] TiO_2,[114,142–161] and ZrO_2.[162] The widespread deployment of these insulators was enabled by atomic layer deposition (ALD), which is a layer-by-layer growth technique to deposit conformal and pinhole-free layers of materials with sub-nanometer precision.[66,68,104,110,162,163] The uniform insulator layer physically prevents the semiconductor from being exposed to the corrosive electrolyte, thereby enhancing the stability. With this strategy, only a few nanometers are necessary to obtain stability, and such a thin insulator can enable efficient charge transfer as well.

Another major advantage of MIS systems is the adaptability to be applied to a variety of semiconductors, unlike p-n junctions which are often limited to specific semiconductors which can be easily doped.[122] Indeed, p-n homojunctions is one of the main competitors for using Si in tandem photoelectrochemical systems in part because of its widespread success in solar cells.[164] Si p-n homojunctions for water splitting still typically utilize an insulator protective coating and a metal catalyst similar to MIS systems.[66,102,105,106,165–169] The key is how the systems separate and drive the charge transfer of photo-excited charge carriers: p-n junctions using doping in the semiconductor to form a built-in junction that selectively drives the transfer of a specific charge carrier, while for MIS systems, the metal layer forms the built-in junction (see Chapter 4 for the full explanation).[66]

MIS systems also offer a simpler design (i.e., no additional doping step) and the fabrication strategy for MIS systems does not require high temperatures compared to the high temperature diffusion step in pn junction fabrication. Other benefits of MIS systems include high collection efficiency since the catalyst is located immediately at the surface of the junction and the removal of high doping which eliminates problems with Auger recombination and low diffusion lengths in highly doped regions.[170]

It is also worth noting that back in the 1970s through 1990s, MIS solar cells have been extensively studied,[171–177] and this architecture is still being explored in recent times.[178–182] This previous work in solar cells typically used SiO_2 as the insulator layer, but ALD has enabled the use of a variety of insulators which may enhance the stability and the efficiency. MIS systems for application in solar cells vs water splitting are subjected to a few fundamentally different constraints. These include different stability requirements and the integration with electrocatalysts to perform the chemical reactions.

Substantial research endeavors are still needed to understand and optimize optical absorption, overall performance, and stability of MIS systems for photoelectrochemical water splitting. Chapter 2 of this thesis provides the critical methods to fabricate, characterize, and experimentally evaluate MIS systems for water splitting application. Chapter 3 is a case study of an Ir/HfO_2/n-Si MIS photoelectrocatalyst in which the thickness of the insulator layer is controlled. The HfO_2 insulator was selected for these systems because it is expected to be thermodynamically stable under water oxidation conditions in alkaline electrolyte based on the Pourbaix diagrams.[183] The Ir/HfO_2/n-Si MIS system is thoroughly characterized and experimentally tested to quantify the key parameters that impact the performance and to evaluate the performance limits. Chapter 4 focuses on analytical modeling of MIS systems to quantify the performance losses and identify key strategies to optimize the performance and improve the performance limits. Chapter 5 builds off from the theoretical insights from Chapter 4 to implement strategies that can significantly enhance the performance and the performance limits. This combined work ultimately provides design principles to develop MIS photoelectrocatalysts with optimized performance.

1.4.2 Scope of Dissertation: Insights from Modeling and Interfacial Analysis of Nanoparticle Electrocatalysts/Si Photoelectrocatalysts

In most cases, protective strategies have involved uniform coatings to prevent exposure of the semiconductor to the electrolyte. Recently, unexpected stability has been demonstrated for photoelectrochemical systems consisting of electrodeposited Ni nanoparticles on Si. Despite direct exposure of Si to corrosive alkaline electrolyte, hours of stability have been achieved because of anodic passivation of the Si, forming stable SiO_x.[184] In addition to providing stability, nanoparticle catalysts can be tuned to minimize parasitic light absorption.[185–187] Furthermore, nanoparticle catalyst/semiconductor systems may exhibit enhanced performance if operating in the "pinch-off" regime, where sufficiently small nanoparticles with a low potential barrier to recombination are surrounded by a region with a high potential barrier to recombination.[188] The effective barrier height of the nanocontact is significantly larger than otherwise predicted for the nanoparticle itself, or when compared to systems with bulk films.[188–191]

A decade after being predicted, the pinch-off effect has been experimentally demonstrated for Ni nanoparticles on a Si substrate.[192,193] These works suggest that the pinch-off effect may be an important feature of sufficiently small nanoparticle catalysts deposited on semiconductors, and this phenomenon has been of recent interest in the field of water splitting. Electrodepositing Ni nanoparticles on Si has been the most-reported strategy. For example, high photovoltages and good onset potentials have been obtained using activated Ni nanoparticles,[184,194,195] Fe-modified Ni nanoparticles,[196] Ir-modified Ni nanoparticles,[197] and thermally oxidized Ni nanoparticles.[198] Co and Fe nanoparticles have also been electrodeposited on Si to achieve good performance and stability.[147,151,152]

Despite all of these studies, there is still debate as to whether the pinch-off effect occurs due to high barriers from a metal oxide shell surrounding the nanoparticles or from the electrolyte.[192,193,199] Furthermore, there has been minimal theoretical guidance on the key parameters necessary to optimize the performance of these nanoparticle-based systems. In Chapter 6, a physically tractable model is established to obtain a better understanding of the factors that influence the performance of pinched-off photoelectrocatalysts. It is found that the pinch-off effect cannot fully explain the high performance of experimental nanoparticle-based photoelectrocatalysts. Chapter 7 uses a combined experimental and modeling approach to investigate the atomistic characteristics of the interfaces and the geometry of systems with Ni planar catalysts and Ni nanoparticles deposited on Si. It is found that an adventitious interfacial insulator layer significantly improves the performance similar to the enhancements observed in traditional MIS systems. This work highlights the critical importance of the interfaces in driving the performance of nanoparticle-based systems which are ubiquitous in photoelectrocatalysis.

1.5 References

(1) Ghodsvali, M.; Krishnamurthy, S.; de Vries, B. Review of Transdisciplinary Approaches to Food-Water-Energy Nexus: A Guide towards Sustainable Development. *Environ. Sci. Policy* **2019**, *101*, 266–278. https://doi.org/10.1016/j.envsci.2019.09.003.

(2) Smajgl, A.; Ward, J.; Pluschke, L. The Water–Food–Energy Nexus – Realising a New Paradigm. *J. Hydrol.* **2016**, *533*, 533–540. https://doi.org/10.1016/j.jhydrol.2015.12.033.

(3) Shannak, S.; Mabrey, D.; Vittorio, M. Moving from Theory to Practice in the Water–Energy–Food Nexus: An Evaluation of Existing Models and Frameworks. *Water-Energy Nexus* **2018**, *1* (1), 17–25. https://doi.org/10.1016/j.wen.2018.04.001.

(4) Hightower, M.; Pierce, S. A. The Energy Challenge. *Nature* **2008**, *452* (7185), 285–286. https://doi.org/10.1038/452285a.

(5) Ferraro, F.; Etzion, D.; Gehman, J. Tackling Grand Challenges Pragmatically: Robust Action Revisited. *Organ. Stud.* **2015**, *36* (3), 363–390. https://doi.org/10.1177/0170840614563742.

(6) U.S. energy facts explained - consumption and production - U.S. Energy Information Administration (EIA) https://www.eia.gov/energyexplained/us-energy-facts/ (accessed 2021 -07 -05).

(7) EIA projects nearly 50% increase in world energy usage by 2050, led by growth in Asia - Today in Energy - U.S. Energy Information Administration (EIA) https://www.eia.gov/todayinenergy/detail.php?id=41433 (accessed 2021 -07 -05).

(8) Mulvaney, D.; Robbins, P. *Green Energy: An A-to-Z Guide*; Thousand Oaks, California, 2011. https://doi.org/10.4135/9781412971850.

(9) Shafiee, S.; Topal, E. When Will Fossil Fuel Reserves Be Diminished? *Energy Policy* **2009**, *37* (1), 181–189. https://doi.org/10.1016/j.enpol.2008.08.016.

(10) Bp Statistical Review of World Energy 2020. **2020**, 68.

(11) Global Energy Review: CO2 Emissions in 2020 – Analysis https://www.iea.org/articles/global-energy-review-co2-emissions-in-2020 (accessed 2021 -07 -05).

(12) Crowther, T. W.; Glick, H. B.; Covey, K. R.; Bettigole, C.; Maynard, D. S.; Thomas, S. M.; Smith, J. R.; Hintler, G.; Duguid, M. C.; Amatulli, G.; Tuanmu, M.-N.; Jetz, W.; Salas, C.; Stam, C.; Piotto, D.; Tavani, R.; Green, S.; Bruce, G.; Williams, S. J.; Wiser, S. K.; Huber, M. O.; Hengeveld, G. M.; Nabuurs, G.-J.; Tikhonova, E.; Borchardt, P.; Li, C.-F.; Powrie, L. W.; Fischer, M.; Hemp, A.; Homeier, J.; Cho, P.; Vibrans, A. C.; Umunay, P. M.; Piao, S. L.; Rowe, C. W.; Ashton, M. S.; Crane, P. R.; Bradford, M. A. Mapping Tree Density at a Global Scale. *Nature* **2015**, *525* (7568), 201–205. https://doi.org/10.1038/nature14967.

(13) Monroe, R. The Keeling Curve https://keelingcurve.ucsd.edu (accessed 2021 -07 -05).

(14) Risbey, J. S.; Lewandowsky, S.; Langlais, C.; Monselesan, D. P.; O'Kane, T. J.; Oreskes, N. Well-Estimated Global Surface Warming in Climate Projections Selected for ENSO Phase. *Nat. Clim. Change* **2014**, *4* (9), 835–840. https://doi.org/10.1038/nclimate2310.

(15) Hausfather, Z.; Drake, H. F.; Abbott, T.; Schmidt, G. A. Evaluating the Performance of Past Climate Model Projections. *Geophys. Res. Lett.* **2020**, *47* (1), e2019GL085378. https://doi.org/10.1029/2019GL085378.

(16) AR5 Synthesis Report: Climate Change 2014 — IPCC.

(17) National Climate Assessment https://nca2014.globalchange.gov/report (accessed 2021 -07 -05).

(18) Church, J. A.; White, N. J.; Aarup, T.; Wilson, W. S.; Woodworth, P. L.; Domingues, C. M.; Hunter, J. R.; Lambeck, K. Understanding Global Sea Levels: Past, Present and Future. *Sustain. Sci.* **2008**, *3* (1), 9–22. https://doi.org/10.1007/s11625-008-0042-4.

(19) Church, J. A.; White, N. J.; Konikow, L. F.; Domingues, C. M.; Cogley, J. G.; Rignot, E.; Gregory, J. M.; Broeke, M. R. van den; Monaghan, A. J.; Velicogna, I. Revisiting the Earth's Sea-Level and Energy Budgets from 1961 to 2008. *Geophys. Res. Lett.* **2011**, *38* (18). https://doi.org/10.1029/2011GL048794.

(20) Allemand, D.; Osborn, D. Ocean Acidification Impacts on Coral Reefs: From Sciences to Solutions. *Reg. Stud. Mar. Sci.* **2019**, *28*, 100558. https://doi.org/10.1016/j.rsma.2019.100558.

(21) Cornwall, C. E.; Hurd, C. L. Experimental Design in Ocean Acidification Research: Problems and Solutions. *ICES J. Mar. Sci.* **2016**, *73* (3), 572–581. https://doi.org/10.1093/icesjms/fsv118.

(22) Lewis, N. S.; Nocera, D. G. Powering the Planet: Chemical Challenges in Solar Energy Utilization. *Proc. Natl. Acad. Sci.* **2006**, *103* (43), 15729–15735. https://doi.org/10.1073/pnas.0603395103.

(23) Epstein, P. R.; Buonocore, J. J.; Eckerle, K.; Hendryx, M.; Stout Iii, B. M.; Heinberg, R.; Clapp, R. W.; May, B.; Reinhart, N. L.; Ahern, M. M.; Doshi, S. K.; Glustrom, L. Full Cost Accounting for the Life Cycle of Coal. *Ann. N. Y. Acad. Sci.* **2011**, *1219*, 73–98. https://doi.org/10.1111/j.1749-6632.2010.05890.x.

(24) Lelieveld, J.; Klingmüller, K.; Pozzer, A.; Burnett, R. T.; Haines, A.; Ramanathan, V. Effects of Fossil Fuel and Total Anthropogenic Emission Removal on Public Health and Climate. *Proc. Natl. Acad. Sci.* **2019**, *116* (15), 7192–7197.

(25) Muller, N. Z.; Mendelsohn, R.; Nordhaus, W. Environmental Accounting for Pollution in the United States Economy. *Am. Econ. Rev.* **2011**, *101* (5), 1649–1675. https://doi.org/10.1257/aer.101.5.1649.

(26) Johnson, L. T.; Hope, C. The Social Cost of Carbon in U.S. Regulatory Impact Analyses: An Introduction and Critique. *J. Environ. Stud. Sci.* **2012**, *2* (3), 205–221. https://doi.org/10.1007/s13412-012-0087-7.

(27) World Energy Outlook 2020 – Analysis https://www.iea.org/reports/world-energy-outlook-2020 (accessed 2021 -07 -06).

(28) Solar FAQs.Pdf.

(29) Ray, D. Lazard's Levelized Cost of Energy Analysis—Version 12.0. **2018**, 20.

(30) Levelized Costs of New Generation Resources in the Annual Energy Outlook 2021. **2021**, 25.

(31) Kreith, F.; Norton, P.; Brown, D. A Comparison of CO2 Emissions from Fossil and Solar Power Plants in the United States. *Energy* **1990**, *15* (12), 1181–1198. https://doi.org/10.1016/0360-5442(90)90110-N.

(32) Sherwani, A. F.; Usmani, J. A.; Varun. Life Cycle Assessment of Solar PV Based Electricity Generation Systems: A Review. *Renew. Sustain. Energy Rev.* **2010**, *14* (1), 540–544. https://doi.org/10.1016/j.rser.2009.08.003.

(33) Kannan, N.; Vakeesan, D. Solar Energy for Future World: - A Review. *Renew. Sustain. Energy Rev.* **2016**, *62*, 1092–1105. https://doi.org/10.1016/j.rser.2016.05.022.

(34) Castillo, A.; Gayme, D. F. Grid-Scale Energy Storage Applications in Renewable Energy Integration: A Survey. *Energy Convers. Manag.* **2014**, *87*, 885–894. https://doi.org/10.1016/j.enconman.2014.07.063.

(35) Ramachandran, R.; Menon, R. K. An Overview of Industrial Uses of Hydrogen. *Int. J. Hydrog. Energy* **1998**, *23* (7), 593–598. https://doi.org/10.1016/S0360-3199(97)00112-2.

(36) Sharma, A.; Arya, S. K. Hydrogen from Algal Biomass: A Review of Production Process. *Biotechnol. Rep.* **2017**, *15*, 63–69. https://doi.org/10.1016/j.btre.2017.06.001.

(37) Capdevila-Cortada, M. Electrifying the Haber–Bosch. *Nat. Catal.* **2019**, *2* (12), 1055–1055. https://doi.org/10.1038/s41929-019-0414-4.

(38) Züttel, A.; Remhof, A.; Borgschulte, A.; Friedrichs, O. Hydrogen: The Future Energy Carrier. *Philos. Trans. R. Soc. Math. Phys. Eng. Sci.* **2010**, *368* (1923), 3329–3342. https://doi.org/10.1098/rsta.2010.0113.

(39) The Future of Hydrogen – Analysis https://www.iea.org/reports/the-future-of-hydrogen (accessed 2021 -07 -03).

(40) Moriarty, P.; Honnery, D. Prospects for Hydrogen as a Transport Fuel. *Int. J. Hydrog. Energy* **2019**, *44* (31), 16029–16037. https://doi.org/10.1016/j.ijhydene.2019.04.278.

(41) Pivovar, B. Catalysts for Fuel Cell Transportation and Hydrogen Related Uses. *Nat. Catal.* **2019**, *2* (7), 562–565. https://doi.org/10.1038/s41929-019-0320-9.

(42) Walter, M. G.; Warren, E. L.; McKone, J. R.; Boettcher, S. W.; Mi, Q.; Santori, E. A.; Lewis, N. S. Solar Water Splitting Cells. *Chem. Rev.* **2010**, *110* (11), 6446–6473. https://doi.org/10.1021/cr1002326.

(43) Crabtree, G. W.; Dresselhaus, M. S.; Buchanan, M. V. The Hydrogen Economy. 7.

(44) Voldsund, M.; Jordal, K.; Anantharaman, R. Hydrogen Production with CO2 Capture. *Int. J. Hydrog. Energy* **2016**, *41* (9), 4969–4992. https://doi.org/10.1016/j.ijhydene.2016.01.009.

(45) Zakkour, P.; Cook, G. *CCS Roadmap for Industry: High-Purity CO2 Sources Sectoral Assessment – Final Report*; 2010. https://doi.org/10.13140/RG.2.1.3717.8722.

(46) Arno A. Evers FAIR-PR http://www.hydrogenambassadors.com/background/worldwide-hydrogen-production-analysis.php (accessed 2021 -08 -05).

(47) To make better decisions, you need to see the big picture. https://ihsmarkit.com/products/hydrogen-chemical-economics-handbook.html (accessed 2021 -08 -05).

(48) Jung, S.; L. McCrory, C. C.; M. Ferrer, I.; C. Peters, J.; F. Jaramillo, T. Benchmarking Nanoparticulate Metal Oxide Electrocatalysts for the Alkaline Water Oxidation Reaction. *J. Mater. Chem. A* **2016**, *4* (8), 3068–3076. https://doi.org/10.1039/C5TA07586F.

(49) McCrory, C. C. L.; Jung, S.; Peters, J. C.; Jaramillo, T. F. Benchmarking Heterogeneous Electrocatalysts for the Oxygen Evolution Reaction. *J. Am. Chem. Soc.* **2013**, *135* (45), 16977–16987. https://doi.org/10.1021/ja407115p.

(50) Man Isabela C.; Su Hai-Yan; Calle-Vallejo Federico; Hansen Heine A.; Martínez José I.; Inoglu Nilay G.; Kitchin John; Jaramillo Thomas F.; Nørskov Jens K.; Rossmeisl Jan. Universality in Oxygen Evolution Electrocatalysis on Oxide Surfaces. *ChemCatChem* **2011**, *3* (7), 1159–1165. https://doi.org/10.1002/cctc.201000397.

(51) Abdol Rahim, A. H.; Tijani, A. S.; Kamarudin, S. K.; Hanapi, S. An Overview of Polymer Electrolyte Membrane Electrolyzer for Hydrogen Production: Modeling and Mass Transport. *J. Power Sources* **2016**, *309*, 56–65. https://doi.org/10.1016/j.jpowsour.2016.01.012.

(52) David, M.; Ocampo-Martínez, C.; Sánchez-Peña, R. Advances in Alkaline Water Electrolyzers: A Review. *J. Energy Storage* **2019**, *23*, 392–403. https://doi.org/10.1016/j.est.2019.03.001.

(53) Mohammadi, A.; Mehrpooya, M. A Comprehensive Review on Coupling Different Types of Electrolyzer to Renewable Energy Sources. *Energy* **2018**, *158*, 632–655. https://doi.org/10.1016/j.energy.2018.06.073.

(54) DOE Technical Targets for Hydrogen Production from Electrolysis https://www.energy.gov/eere/fuelcells/doe-technical-targets-hydrogen-production-electrolysis (accessed 2021 -07 -03).

(55) Electric Power Monthly - U.S. Energy Information Administration (EIA) https://www.eia.gov/electricity/monthly/epm_table_grapher.php (accessed 2021 -07 -03).

(56) Grimm, A.; de Jong, W. A.; Kramer, G. J. Renewable Hydrogen Production: A Techno-Economic Comparison of Photoelectrochemical Cells and Photovoltaic-Electrolysis. *Int. J. Hydrog. Energy* **2020**, *45* (43), 22545–22555. https://doi.org/10.1016/j.ijhydene.2020.06.092.

(57) R. Shaner, M.; A. Atwater, H.; S. Lewis, N.; W. McFarland, E. A Comparative Technoeconomic Analysis of Renewable Hydrogen Production Using Solar Energy. *Energy Environ. Sci.* **2016**, *9* (7), 2354–2371. https://doi.org/10.1039/C5EE02573G.

(58) Grätzel, M. Photoelectrochemical Cells. *Nature* **2001**, *414* (6861), 338–344. https://doi.org/10.1038/35104607.

(59) Chen, Z.; Dinh, H. N.; Miller, E. *Photoelectrochemical Water Splitting*; SpringerBriefs in Energy; Springer New York: New York, NY, 2013. https://doi.org/10.1007/978-1-4614-8298-7.

(60) Fujishima, A.; Honda, K. Electrochemical Photolysis of Water at a Semiconductor Electrode. *Nature* **1972**, *238* (5358), 37–38. https://doi.org/10.1038/238037a0.

(61) Zhong, S.; Xi, Y.; Chen, Q.; Chen, J.; Bai, S. Bridge Engineering in Photocatalysis and Photoelectrocatalysis. *Nanoscale* **2020**, *12* (10), 5764–5791. https://doi.org/10.1039/C9NR10511E.

(62) Lee, S. A.; Choi, S.; Kim, C.; Yang, J. W.; Kim, S. Y.; Jang, H. W. Si-Based Water Oxidation Photoanodes Conjugated with Earth-Abundant Transition Metal-Based Catalysts. *ACS Mater. Lett.* **2020**, *2* (1), 107–126. https://doi.org/10.1021/acsmaterialslett.9b00422.

(63) Wang, Z.; Li, C.; Domen, K. Recent Developments in Heterogeneous Photocatalysts for Solar-Driven Overall Water Splitting. *Chem. Soc. Rev.* **2019**, *48* (7), 2109–2125. https://doi.org/10.1039/C8CS00542G.

(64) Shockley, W.; Queisser, H. J. Detailed Balance Limit of Efficiency of P-n Junction Solar Cells. *J. Appl. Phys.* **1961**, *32* (3), 510–519. https://doi.org/10.1063/1.1736034.

(65) Hu, S.; Lewis, N. S.; Ager, J. W.; Yang, J.; McKone, J. R.; Strandwitz, N. C. Thin-Film Materials for the Protection of Semiconducting Photoelectrodes in Solar-Fuel Generators. *J. Phys. Chem. C* **2015**, *119* (43), 24201–24228. https://doi.org/10.1021/acs.jpcc.5b05976.

(66) Scheuermann, A. G.; McIntyre, P. C. Atomic Layer Deposited Corrosion Protection: A Path to Stable and Efficient Photoelectrochemical Cells. *J. Phys. Chem. Lett.* **2016**, *7* (14), 2867–2878. https://doi.org/10.1021/acs.jpclett.6b00631.

(67) Lichterman, M. F.; Sun, K.; Hu, S.; Zhou, X.; McDowell, M. T.; Shaner, M. R.; Richter, M. H.; Crumlin, E. J.; Carim, A. I.; Saadi, F. H.; Brunschwig, B. S.; Lewis, N. S. Protection of Inorganic Semiconductors for Sustained, Efficient Photoelectrochemical Water Oxidation. *Catal. Today* **2016**, *262*, 11–23. https://doi.org/10.1016/j.cattod.2015.08.017.

(68) Bae, D.; Seger, B.; Vesborg, P. C. K.; Hansen, O.; Chorkendorff, I. Strategies for Stable Water Splitting via Protected Photoelectrodes. *Chem. Soc. Rev.* **2017**, *46* (7), 1933–1954. https://doi.org/10.1039/C6CS00918B.

(69) A. Pinaud, B.; D. Benck, J.; C. Seitz, L.; J. Forman, A.; Chen, Z.; G. Deutsch, T.; D. James, B.; N. Baum, K.; N. Baum, G.; Ardo, S.; Wang, H.; Miller, E.; F. Jaramillo, T. Technical and Economic Feasibility of Centralized Facilities for Solar Hydrogen Production via Photocatalysis and Photoelectrochemistry. *Energy Environ. Sci.* **2013**, *6* (7), 1983–2002. https://doi.org/10.1039/C3EE40831K.

(70) R. Shaner, M.; A. Atwater, H.; S. Lewis, N.; W. McFarland, E. A Comparative Technoeconomic Analysis of Renewable Hydrogen Production Using Solar Energy. *Energy Environ. Sci.* **2016**, *9* (7), 2354–2371. https://doi.org/10.1039/C5EE02573G.

(71) Chen, Y.; Hu, S.; Xiang, C.; Lewis, N. S. A Sensitivity Analysis to Assess the Relative Importance of Improvements in Electrocatalysts, Light Absorbers, and System Geometry on the Efficiency of Solar-Fuels Generators. *Energy Environ. Sci.* **2015**, *8* (3), 876–886.

(72) Lin, L.; Hisatomi, T.; Chen, S.; Takata, T.; Domen, K. Visible-Light-Driven Photocatalytic Water Splitting: Recent Progress and Challenges. *Trends Chem.* **2020**, *2* (9), 813–824. https://doi.org/10.1016/j.trechm.2020.06.006.

(73) Seitz, L. C.; Chen, Z.; Forman, A. J.; Pinaud, B. A.; Benck, J. D.; Jaramillo, T. F. Modeling Practical Performance Limits of Photoelectrochemical Water Splitting Based on the Current State of Materials Research. *ChemSusChem* **2014**, *7* (5), 1372–1385. https://doi.org/10.1002/cssc.201301030.

(74) Hu, S.; Xiang, C.; Haussener, S.; D. Berger, A.; S. Lewis, N. An Analysis of the Optimal Band Gaps of Light Absorbers in Integrated Tandem Photoelectrochemical Water-Splitting Systems. *Energy Env. Sci* **2013**, *6*. https://doi.org/10.1039/C3EE40453F.

(75) Li, J.; Wu, N. Semiconductor-Based Photocatalysts and Photoelectrochemical Cells for Solar Fuel Generation: A Review. *Catal. Sci. Technol.* **2015**, *5* (3), 1360–1384. https://doi.org/10.1039/C4CY00974F.

(76) Wiley: Physics of Semiconductor Devices, 3rd Edition - Simon M. Sze, Kwok K. Ng http://www.wiley.com/WileyCDA/WileyTitle/productCd-0471143235.html (accessed 2017 -10 -11).

(77) Sah, C. t; Noyce, R. N.; Shockley, W. Carrier Generation and Recombination in P-N Junctions and P-N Junction Characteristics. *Proc. IRE* **1957**, *45* (9), 1228–1243. https://doi.org/10.1109/JRPROC.1957.278528.

(78) Loferski, J. J. Theoretical Considerations Governing the Choice of the Optimum Semiconductor for Photovoltaic Solar Energy Conversion. *J. Appl. Phys.* **1956**, *27* (7), 777–784. https://doi.org/10.1063/1.1722483.

(79) Zou, X.; Zhang, Y. Noble Metal-Free Hydrogen Evolution Catalysts for Water Splitting. *Chem. Soc. Rev.* **2015**, *44* (15), 5148–5180. https://doi.org/10.1039/C4CS00448E.

(80) McCrory, C. C. L.; Jung, S.; Ferrer, I. M.; Chatman, S. M.; Peters, J. C.; Jaramillo, T. F. Benchmarking Hydrogen Evolving Reaction and Oxygen Evolving Reaction Electrocatalysts for Solar Water Splitting Devices. *J. Am. Chem. Soc.* **2015**, *137* (13), 4347–4357. https://doi.org/10.1021/ja510442p.

(81) Blakemore, J. D.; Crabtree, R. H.; Brudvig, G. W. Molecular Catalysts for Water Oxidation. *Chem. Rev.* **2015**, *115* (23), 12974–13005. https://doi.org/10.1021/acs.chemrev.5b00122.

(82) Zhao, T.; Wang, Y.; Karuturi, S.; Catchpole, K.; Zhang, Q.; Zhao, C. Design and Operando/in Situ Characterization of Precious-Metal-Free Electrocatalysts for Alkaline Water Splitting. *Carbon Energy* **2020**, *2* (4), 582–613. https://doi.org/10.1002/cey2.79.

(83) Masa, J.; Andronescu, C.; Schuhmann, W. Electrocatalysis as the Nexus for Sustainable Renewable Energy: The Gordian Knot of Activity, Stability, and Selectivity. *Angew. Chem. Int. Ed.* **2020**, *59* (36), 15298–15312. https://doi.org/10.1002/anie.202007672.

(84) Fujishima, A.; Zhang, X.; Tryk, D. A. TiO2 Photocatalysis and Related Surface Phenomena. *Surf. Sci. Rep.* **2008**, *63* (12), 515–582. https://doi.org/10.1016/j.surfrep.2008.10.001.

(85) Kudo, A.; Miseki, Y. Heterogeneous Photocatalyst Materials for Water Splitting. *Chem. Soc. Rev.* **2008**, *38* (1), 253–278. https://doi.org/10.1039/B800489G.

(86) Asahi, R.; Morikawa, T.; Ohwaki, T.; Aoki, K.; Taga, Y. Visible-Light Photocatalysis in Nitrogen-Doped Titanium Oxides. *Science* **2001**, *293* (5528), 269–271. https://doi.org/10.1126/science.1061051.

(87) Tang, J.; Durrant, J. R.; Klug, D. R. Mechanism of Photocatalytic Water Splitting in TiO2. Reaction of Water with Photoholes, Importance of Charge Carrier Dynamics, and Evidence for Four-Hole Chemistry. *J. Am. Chem. Soc.* **2008**, *130* (42), 13885–13891. https://doi.org/10.1021/ja8034637.

(88) Takata, T.; Jiang, J.; Sakata, Y.; Nakabayashi, M.; Shibata, N.; Nandal, V.; Seki, K.; Hisatomi, T.; Domen, K. Photocatalytic Water Splitting with a Quantum Efficiency of Almost Unity. *Nature* **2020**, *581* (7809), 411–414. https://doi.org/10.1038/s41586-020-2278-9.

(89) Ingram, D. B.; Linic, S. Water Splitting on Composite Plasmonic-Metal/Semiconductor Photoelectrodes: Evidence for Selective Plasmon-Induced Formation of Charge Carriers near the Semiconductor Surface. *J. Am. Chem. Soc.* **2011**, *133* (14), 5202–5205. https://doi.org/10.1021/ja200086g.

(90) Pai, Y.-Y.; Tylan-Tyler, A.; Irvin, P.; Levy, J. Physics of SrTiO3-Based Heterostructures and Nanostructures: A Review. *Rep. Prog. Phys.* **2018**, *81* (3), 036503. https://doi.org/10.1088/1361-6633/aa892d.

(91) Ni, M.; Leung, M. K. H.; Leung, D. Y. C.; Sumathy, K. A Review and Recent Developments in Photocatalytic Water-Splitting Using TiO2 for Hydrogen Production. *Renew. Sustain. Energy Rev.* **2007**, *11* (3), 401–425. https://doi.org/10.1016/j.rser.2005.01.009.

(92) Eidsvåg, H.; Bentouba, S.; Vajeeston, P.; Yohi, S.; Velauthapillai, D. TiO2 as a Photocatalyst for Water Splitting—An Experimental and Theoretical Review. *Molecules* **2021**, *26* (6), 1687. https://doi.org/10.3390/molecules26061687.

(93) Singh, R.; Dutta, S. A Review on H2 Production through Photocatalytic Reactions Using TiO2/TiO2-Assisted Catalysts. *Fuel* **2018**, *220*, 607–620. https://doi.org/10.1016/j.fuel.2018.02.068.

(94) Humayun, M.; Raziq, F.; Khan, A.; Luo, W. Modification Strategies of TiO2 for Potential Applications in Photocatalysis: A Critical Review. *Green Chem. Lett. Rev.* **2018**, *11* (2), 86–102. https://doi.org/10.1080/17518253.2018.1440324.

(95) Patial, S.; Hasija, V.; Raizada, P.; Singh, P.; Khan Singh, A. A. P.; Asiri, A. M. Tunable Photocatalytic Activity of SrTiO3 for Water Splitting: Strategies and Future Scenario. *J. Environ. Chem. Eng.* **2020**, *8* (3), 103791. https://doi.org/10.1016/j.jece.2020.103791.

(96) Chen, S.; Takata, T.; Domen, K. Particulate Photocatalysts for Overall Water Splitting. *Nat. Rev. Mater.* **2017**, *2* (10), 1–17. https://doi.org/10.1038/natrevmats.2017.50.

(97) Bae, D.; Seger, B.; K. Vesborg, P. C.; Hansen, O.; Chorkendorff, I. Strategies for Stable Water Splitting via Protected Photoelectrodes. *Chem. Soc. Rev.* **2017**, *46* (7), 1933–1954. https://doi.org/10.1039/C6CS00918B.

(98) Fountaine, K. T.; Lewerenz, H. J.; Atwater, H. A. Interplay of Light Transmission and Catalytic Exchange Current in Photoelectrochemical Systems. *Appl. Phys. Lett.* **2014**, *105* (17), 173901. https://doi.org/10.1063/1.4900612.

(99) Verlage, E.; Hu, S.; Liu, R.; R. Jones, R. J.; Sun, K.; Xiang, C.; S. Lewis, N.; A. Atwater, H. A Monolithically Integrated, Intrinsically Safe, 10% Efficient, Solar-Driven Water-Splitting System Based on Active, Stable Earth-Abundant Electrocatalysts in Conjunction with Tandem III–V Light Absorbers Protected by Amorphous TiO 2 Films. *Energy Environ. Sci.* **2015**, *8* (11), 3166–3172. https://doi.org/10.1039/C5EE01786F.

(100) Oh, S.; Song, H.; Oh, J. An Optically and Electrochemically Decoupled Monolithic Photoelectrochemical Cell for High-Performance Solar-Driven Water Splitting. *Nano Lett.* **2017**, *17* (9), 5416–5422. https://doi.org/10.1021/acs.nanolett.7b02023.

(101) Cheng, W.-H.; Richter, M. H.; May, M. M.; Ohlmann, J.; Lackner, D.; Dimroth, F.; Hannappel, T.; Atwater, H. A.; Lewerenz, H.-J. Monolithic Photoelectrochemical Device for Direct Water Splitting with 19% Efficiency. *ACS Energy Lett.* **2018**, *3* (8), 1795–1800. https://doi.org/10.1021/acsenergylett.8b00920.

(102) Luo, Z.; Wang, T.; Gong, J. Single-Crystal Silicon-Based Electrodes for Unbiased Solar Water Splitting: Current Status and Prospects. *Chem. Soc. Rev.* **2019**, *48* (7), 2158–2181. https://doi.org/10.1039/C8CS00638E.

(103) Vanka, S.; Zhou, B.; Awni, R. A.; Song, Z.; Chowdhury, F. A.; Liu, X.; Hajibabaei, H.; Shi, W.; Xiao, Y.; Navid, I. A.; Pandey, A.; Chen, R.; Botton, G. A.; Hamann, T. W.; Wang, D.; Yan, Y.; Mi, Z. InGaN/Si Double-Junction Photocathode for Unassisted Solar Water Splitting. *ACS Energy Lett.* **2020**, *5* (12), 3741–3751. https://doi.org/10.1021/acsenergylett.0c01583.

(104) Chen, S.; Wang, L.-W. Thermodynamic Oxidation and Reduction Potentials of Photocatalytic Semiconductors in Aqueous Solution. *Chem. Mater.* **2012**, *24* (18), 3659–3666. https://doi.org/10.1021/cm302533s.

(105) Fan, R.; Mi, Z.; Shen, M. Silicon Based Photoelectrodes for Photoelectrochemical Water Splitting. *Opt. Express* **2019**, *27* (4), A51–A80. https://doi.org/10.1364/OE.27.000A51.

(106) Seger, B.; Pedersen, T.; Laursen, A. B.; Vesborg, P. C. K.; Hansen, O.; Chorkendorff, I. Using TiO2 as a Conductive Protective Layer for Photocathodic H2 Evolution. *J. Am. Chem. Soc.* **2013**, *135* (3), 1057–1064. https://doi.org/10.1021/ja309523t.

(107) Han, T.; Shi, Y.; Song, X.; Mio, A.; Valenti, L.; Hui, F.; Privitera, S.; Lombardo, S.; Lanza, M. Ageing Mechanisms of Highly Active and Stable Nickel-Coated Silicon Photoanodes for Water Splitting. *J. Mater. Chem. A* **2016**, *4* (21), 8053–8060. https://doi.org/10.1039/C5TA09990K.

(108) Nandjou, F.; Haussener, S. Degradation in Photoelectrochemical Devices: Review with an Illustrative Case Study. *J. Phys. Appl. Phys.* **2017**, *50* (12), 124002. https://doi.org/10.1088/1361-6463/aa5b11.

(109) Nandjou, F.; Haussener, S. Kinetic Competition between Water-Splitting and Photocorrosion Reactions in Photoelectrochemical Devices. *ChemSusChem* **2019**, *12* (9), 1984–1994. https://doi.org/10.1002/cssc.201802558.

(110) Yang, W.; Ramanujam Prabhakar, R.; Tan, J.; David Tilley, S.; Moon, J. Strategies for Enhancing the Photocurrent, Photovoltage, and Stability of Photoelectrodes for Photoelectrochemical Water Splitting. *Chem. Soc. Rev.* **2019**, *48* (19), 4979–5015. https://doi.org/10.1039/C8CS00997J.

(111) Chen, S.; Huang, D.; Xu, P.; Xue, W.; Lei, L.; Cheng, M.; Wang, R.; Liu, X.; Deng, R. Semiconductor-Based Photocatalysts for Photocatalytic and Photoelectrochemical Water Splitting: Will We Stop with Photocorrosion? *J. Mater. Chem. A* **2020**, *8* (5), 2286–2322. https://doi.org/10.1039/C9TA12799B.

(112) Zheng, J.; Lyu, Y.; Wu, B.; Wang, S. Defect Engineering of the Protection Layer for Photoelectrochemical Devices. *EnergyChem* **2020**, *2* (4), 100039. https://doi.org/10.1016/j.enchem.2020.100039.

(113) Thalluri, S. M.; Bai, L.; Lv, C.; Huang, Z.; Hu, X.; Liu, L. Strategies for Semiconductor/Electrocatalyst Coupling toward Solar-Driven Water Splitting. *Adv. Sci.* **2020**, *7* (6), 1902102. https://doi.org/10.1002/advs.201902102.

(114) Chen, Y. W.; Prange, J. D.; Dühnen, S.; Park, Y.; Gunji, M.; Chidsey, C. E. D.; McIntyre, P. C. Atomic Layer-Deposited Tunnel Oxide Stabilizes Silicon Photoanodes for Water Oxidation. *Nat. Mater.* **2011**, *10* (7), 539–544. https://doi.org/10.1038/nmat3047.

(115) Digdaya, I. A.; Trześniewski, B. J.; Adhyaksa, G. W. P.; Garnett, E. C.; Smith, W. A. General Considerations for Improving Photovoltage in Metal–Insulator–Semiconductor

Photoanodes. *J. Phys. Chem. C* **2018**, *122* (10), 5462–5471. https://doi.org/10.1021/acs.jpcc.7b11747.

(116) Park, M.-J.; Jung, J.-Y.; Shin, S.-M.; Song, J.-W.; Nam, Y.-H.; Kim, D.-H.; Lee, J.-H. Photoelectrochemical Oxygen Evolution Improved by a Thin Al2O3 Interlayer in a NiOx/n-Si Photoanode. *Thin Solid Films* **2016**, *599*, 54–58. https://doi.org/10.1016/j.tsf.2015.12.062.

(117) Luo, Z.; Liu, B.; Li, H.; Chang, X.; Zhu, W.; Wang, T.; Gong, J. Multifunctional Nickel Film Protected N-Type Silicon Photoanode with High Photovoltage for Efficient and Stable Oxygen Evolution Reaction. *Small Methods 0* (0), 1900212. https://doi.org/10.1002/smtd.201900212.

(118) G. Scheuermann, A.; W. Kemp, K.; Tang, K.; Q. Lu, D.; F. Satterthwaite, P.; Ito, T.; D. Chidsey, C. E.; C. McIntyre, P. Conductance and Capacitance of Bilayer Protective Oxides for Silicon Water Splitting Anodes. *Energy Environ. Sci.* **2016**, *9* (2), 504–516. https://doi.org/10.1039/C5EE02484F.

(119) Digdaya, I. A.; Adhyaksa, G. W. P.; Trześniewski, B. J.; Garnett, E. C.; Smith, W. A. Interfacial Engineering of Metal-Insulator-Semiconductor Junctions for Efficient and Stable Photoelectrochemical Water Oxidation. *Nat. Commun.* **2017**, *8*, ncomms15968. https://doi.org/10.1038/ncomms15968.

(120) Zhao, C.; Guo, B.; Xie, G.; Li, C.; Xie, W.; Dai, Y.; Gong, J.; Gong, J. R. Metal Sputtering Buffer Layer for High Performance Si-Based Water Oxidation Photoanode. *ACS Appl. Energy Mater.* **2020**, *3* (9), 8216–8223. https://doi.org/10.1021/acsaem.0c00609.

(121) Wang, S.; Wang, T.; Liu, B.; Li, H.; Feng, S.; Gong, J. Spatial Decoupling of Light Absorption and Reaction Sites in N-Si Photocathodes for Solar Water Splitting. *Natl. Sci. Rev.* **2020**, No. nwaa293. https://doi.org/10.1093/nsr/nwaa293.

(122) Quinn, J.; Hemmerling, J.; Linic, S. Maximizing Solar Water Splitting Performance by Nanoscopic Control of the Charge Carrier Fluxes across Semiconductor–Electrocatalyst Junctions. *ACS Catal.* **2018**, *8* (9), 8545–8552. https://doi.org/10.1021/acscatal.8b01929.

(123) Quinn, J.; Hemmerling, J.; Linic, S. Guidelines for Optimizing the Performance of Metal–Insulator–Semiconductor (MIS) Photoelectrocatalytic Systems by Tuning the Insulator Thickness. *ACS Energy Lett.* **2019**, *4* (11), 2632–2638. https://doi.org/10.1021/acsenergylett.9b01609.

(124) Hemmerling, J.; Quinn, J.; Linic, S. Quantifying Losses and Assessing the Photovoltage Limits in Metal–Insulator–Semiconductor Water Splitting Systems. *Adv. Energy Mater.* **2020**, *10* (12), 1903354. https://doi.org/10.1002/aenm.201903354.

(125) Hemmerling, J. R.; Mathur, A.; Linic, S. Design Principles for Efficient and Stable Water Splitting Photoelectrocatalysts. *Acc. Chem. Res.* **2021**, *54* (8), 1992–2002. https://doi.org/10.1021/acs.accounts.1c00072.

(126) Mikolasek, M.; Frohlich, K.; Husekova, K.; Racko, J.; Rehacek, V.; Chymo, F.; Tapajna, M.; Harmatha, L. Silicon Based MIS Photoanode for Water Oxidation: A Comparison of RuO2 and Ni Schottky Contacts. *Appl. Surf. Sci.* **2018**, *461*, 48–53. https://doi.org/10.1016/j.apsusc.2018.04.234.

(127) Hill, J. C.; Landers, A. T.; Switzer, J. A. An Electrodeposited Inhomogeneous Metal–Insulator–Semiconductor Junction for Efficient Photoelectrochemical Water Oxidation. *Nat. Mater.* **2015**, *14* (11), 1150–1155. https://doi.org/10.1038/nmat4408.

(128) Oh, S.; Jung, S.; Lee, Y. H.; Song, J. T.; Kim, T. H.; Nandi, D. K.; Kim, S.-H.; Oh, J. Hole-Selective CoOx/SiOx/Si Heterojunctions for Photoelectrochemical Water Splitting. *ACS Catal.* **2018**, *8* (10), 9755–9764. https://doi.org/10.1021/acscatal.8b03520.

(129) Esposito, D. V.; Levin, I.; Moffat, T. P.; Talin, A. A. H_2 Evolution at Si-Based Metal–Insulator–Semiconductor Photoelectrodes Enhanced by Inversion Channel Charge Collection and H Spillover. *Nat. Mater.* **2013**, *12* (6), 562–568. https://doi.org/10.1038/nmat3626.

(130) Ji, L.; Hsu, H.-Y.; Li, X.; Huang, K.; Zhang, Y.; Lee, J. C.; Bard, A. J.; Yu, E. T. Localized Dielectric Breakdown and Antireflection Coating in Metal–Oxide–Semiconductor Photoelectrodes. *Nat. Mater.* **2017**, *16* (1), 127–131. https://doi.org/10.1038/nmat4801.

(131) Loget, G.; Mériadec, C.; Dorcet, V.; Fabre, B.; Vacher, A.; Fryars, S.; Ababou-Girard, S. Tailoring the Photoelectrochemistry of Catalytic Metal-Insulator-Semiconductor (MIS) Photoanodes by a Dissolution Method. *Nat. Commun.* **2019**, *10* (1), 1–11. https://doi.org/10.1038/s41467-019-11432-1.

(132) V. Esposito, D.; Lee, Y.; Yoon, H.; M. Haney, P.; Y. Labrador, N.; P. Moffat, T.; Alec Talin, A.; A. Szalai, V. Deconvoluting the Influences of 3D Structure on the Performance of Photoelectrodes for Solar-Driven Water Splitting. *Sustain. Energy Fuels* **2017**, *1* (1), 154–173. https://doi.org/10.1039/C6SE00073H.

(133) Yul Lim, S.; Ha, K.; Ha, H.; Youn Lee, S.; Seok Jang, M.; Choi, M.; Dong Chung, T. Three-Dimensionally Patterned Ag–Pt Alloy Catalyst on Planar Si Photocathodes for Photoelectrochemical H 2 Evolution. *Phys. Chem. Chem. Phys.* **2019**, *21* (8), 4184–4192. https://doi.org/10.1039/C8CP07304J.

(134) Hendricks, O. L.; Tang-Kong, R.; Babadi, A. S.; McIntyre, P. C.; Chidsey, C. E. D. Atomic Layer Deposited TiO2–IrOx Alloys Enable Corrosion Resistant Water Oxidation on Silicon at High Photovoltage. *Chem. Mater.* **2019**, *31* (1), 90–100. https://doi.org/10.1021/acs.chemmater.8b03092.

(135) Yul Lim, S.; Ha, K.; Ha, H.; Youn Lee, S.; Seok Jang, M.; Choi, M.; Dong Chung, T. Three-Dimensionally Patterned Ag–Pt Alloy Catalyst on Planar Si Photocathodes for Photoelectrochemical H 2 Evolution. *Phys. Chem. Chem. Phys.* **2019**, *21* (8), 4184–4192. https://doi.org/10.1039/C8CP07304J.

(136) Li, S.; She, G.; Chen, C.; Zhang, S.; Mu, L.; Guo, X.; Shi, W. Enhancing the Photovoltage of Ni/n-Si Photoanode for Water Oxidation through a Rapid Thermal Process. *ACS Appl. Mater. Interfaces* **2018**, *10* (10), 8594–8598. https://doi.org/10.1021/acsami.7b16986.

(137) Jung, J.-Y.; Yu, J.-Y.; Lee, J.-H. Dynamic Photoelectrochemical Device Using an Electrolyte-Permeable NiOx/SiO2/Si Photocathode with an Open-Circuit Potential of 0.75 V. *ACS Appl. Mater. Interfaces* **2018**, *10* (9), 7955–7962. https://doi.org/10.1021/acsami.7b16918.

(138) Jung, J.-Y.; Yu, J.-Y.; Shinde, S. S.; Kim, S.-H.; Kim, D.-H.; Lin, C.; Wehrspohn, R. B.; Lee, J.-H. Remarkable Improvements in the Performance and Stability of Si Photoanodes Adopting Nanocrystalline NiOx Electrocatalyst and Stoichiometric SiO2 Protection. *Appl. Surf. Sci.* **2019**, *493*, 1150–1158. https://doi.org/10.1016/j.apsusc.2019.07.128.

(139) Li, Y.; Xu, G.; Zhu, X.; Man, Z.; Fu, X.; Hao, Z.; Cui, Y.; Yuan, C.; Zhang, W.; Yan, S.; Ge, H.; Chen, Y.; Zou, Z. A Hierarchical Dual-Phase Photoetching Template Route to Assembling Functional Layers on Si Photoanode with Tunable Nanostructures for Efficient Water Splitting. *Appl. Catal. B Environ.* **2019**, *259*, 118115. https://doi.org/10.1016/j.apcatb.2019.118115.

(140) Li, C.; Huang, M.; Zhong, Y.; Zhang, L.; Xiao, Y.; Zhu, H. Highly Efficient NiFe Nanoparticle Decorated Si Photoanode for Photoelectrochemical Water Oxidation. *Chem. Mater.* **2019**, *31* (1), 171–178. https://doi.org/10.1021/acs.chemmater.8b03775.

(141) Ji, L.; McDaniel, M. D.; Wang, S.; Posadas, A. B.; Li, X.; Huang, H.; Lee, J. C.; Demkov, A. A.; Bard, A. J.; Ekerdt, J. G.; Yu, E. T. A Silicon-Based Photocathode for Water Reduction with an Epitaxial $SrTiO_3$ Protection Layer and a Nanostructured Catalyst. *Nat. Nanotechnol.* **2015**, *10* (1), 84–90. https://doi.org/10.1038/nnano.2014.277.

(142) Scheuermann, A. G.; Lawrence, J. P.; Meng, A. C.; Tang, K.; Hendricks, O. L.; Chidsey, C. E. D.; McIntyre, P. C. Titanium Oxide Crystallization and Interface Defect Passivation for High Performance Insulator-Protected Schottky Junction MIS Photoanodes. *ACS Appl. Mater. Interfaces* **2016**, *8* (23), 14596–14603. https://doi.org/10.1021/acsami.6b03688.

(143) Scheuermann, A. G.; Lawrence, J. P.; Kemp, K. W.; Ito, T.; Walsh, A.; Chidsey, C. E. D.; Hurley, P. K.; McIntyre, P. C. Design Principles for Maximizing Photovoltage in Metal-Oxide-Protected Water-Splitting Photoanodes. *Nat. Mater.* **2016**, *15* (1), 99–105. https://doi.org/10.1038/nmat4451.

(144) Jung, J.-Y.; Kim, D. W.; Park, T. J.; Lee, J.-H. Design Guidelines of Insulator for Improving Stability and Performance of Nanoelectrocatalyst/Insulator/Semiconductor Photoelectrochemical Cells. *ACS Appl. Energy Mater.* **2020**, *3* (1), 1046–1053. https://doi.org/10.1021/acsaem.9b02070.

(145) Siddiqi, G.; Luo, Z.; Xie, Y.; Pan, Z.; Zhu, Q.; Röhr, J. A.; Cha, J. J.; Hu, S. Stable Water Oxidation in Acid Using Manganese-Modified TiO2 Protective Coatings. *ACS Appl. Mater. Interfaces* **2018**, *10* (22), 18805–18815. https://doi.org/10.1021/acsami.8b05323.

(146) Chen, C.-J.; Veeramani, V.; Wu, Y.-H.; Jena, A.; Yin, L.-C.; Chang, H.; Hu, S.-F.; Liu, R.-S. Phosphorous-Doped Molybdenum Disulfide Anchored on Silicon as an Efficient Catalyst for Photoelectrochemical Hydrogen Generation. *Appl. Catal. B Environ.* **2020**, *263*, 118259. https://doi.org/10.1016/j.apcatb.2019.118259.

(147) Zheng, J.; Lyu, Y.; Wang, R.; Xie, C.; Zhou, H.; Jiang, S. P.; Wang, S. Crystalline TiO 2 Protective Layer with Graded Oxygen Defects for Efficient and Stable Silicon-Based Photocathode. *Nat. Commun.* **2018**, *9* (1), 1–10. https://doi.org/10.1038/s41467-018-05580-z.

(148) Chuang, C.-H.; Lai, Y.-Y.; Hou, C.-H.; Cheng, Y.-J. Annealed Polycrystalline TiO2 Interlayer of the N-Si/TiO2/Ni Photoanode for Efficient Photoelectrochemical Water Splitting. *ACS Appl. Energy Mater.* **2020**, *3* (4), 3902–3908. https://doi.org/10.1021/acsaem.0c00319.

(149) Choi, S.; Lee, S. A.; Yang, H.; Lee, T. H.; Kim, C.; Lee, C. W.; Shin, H.; Jang, H. W. Stabilization of NiFe Layered Double Hydroxides on N-Si by an Activated TiO2 Interlayer for Efficient Solar Water Oxidation. *ACS Appl. Energy Mater.* **2020**, *3* (12), 12298–12307. https://doi.org/10.1021/acsaem.0c02355.

(150) Yang, W.; Moehl, T.; Service, E.; Tilley, S. D. Operando Analysis of Semiconductor Junctions in Multi-Layered Photocathodes for Solar Water Splitting by Impedance Spectroscopy. *Adv. Energy Mater.* **2021**, *11* (9), 2003569. https://doi.org/10.1002/aenm.202003569.

(151) G. Scheuermann, A.; D. Prange, J.; Gunji, M.; D. Chidsey, C. E.; C. McIntyre, P. Effects of Catalyst Material and Atomic Layer Deposited TiO 2 Oxide Thickness on the Water Oxidation Performance of Metal–Insulator–Silicon Anodes. *Energy Environ. Sci.* **2013**, *6* (8), 2487–2496. https://doi.org/10.1039/C3EE41178H.

(152) Scheuermann, A. G.; Lawrence, J. P.; Meng, A. C.; Tang, K.; Hendricks, O. L.; Chidsey, C. E. D.; McIntyre, P. C. Titanium Oxide Crystallization and Interface Defect Passivation for High Performance Insulator-Protected Schottky Junction MIS Photoanodes. *ACS Appl. Mater. Interfaces* **2016**, *8* (23), 14596–14603. https://doi.org/10.1021/acsami.6b03688.

(153) Cai, Q.; Hong, W.; Jian, C.; Li, J.; Liu, W. Impact of Silicon Resistivity on the Performance of Silicon Photoanode for Efficient Water Oxidation Reaction. *ACS Catal.* **2017**, *7* (5), 3277–3283. https://doi.org/10.1021/acscatal.7b00507.

(154) Chandrasekaran, S.; Kaeffer, N.; Cagnon, L.; Aldakov, D.; Fize, J.; Nonglaton, G.; Baleras, F.; Mailley, P.; Artero, V. A Robust ALD-Protected Silicon-Based Hybrid Photoelectrode for Hydrogen Evolution under Aqueous Conditions. *Chem. Sci.* **2019**, *10* (16), 4469–4475. https://doi.org/10.1039/C8SC05006F.

(155) Gao, L.; Li, Q.; Chen, H.; Hayase, S.; Ma, T. In Situ Fabrication of Nanoepitaxial TiO2 Protection Layer on Si Substrate: Hole Chemical Conduction Instead of Tunneling Effect. *Sol. RRL* **2017**, *1* (8), 1700064. https://doi.org/10.1002/solr.201700064.

(156) Nunez, P.; Richter, M. H.; Piercy, B. D.; Roske, C. W.; Cabán-Acevedo, M.; Losego, M. D.; Konezny, S. J.; Fermin, D. J.; Hu, S.; Brunschwig, B. S.; Lewis, N. S. Characterization of Electronic Transport through Amorphous TiO2 Produced by Atomic Layer Deposition. *J. Phys. Chem. C* **2019**, *123* (33), 20116–20129. https://doi.org/10.1021/acs.jpcc.9b04434.

(157) Chen, C.-J.; Liu, C.-W.; Yang, K.-C.; Yin, L.-C.; Wei, D.-H.; Hu, S.-F.; Liu, R.-S. Amorphous Phosphorus-Doped Cobalt Sulfide Modified on Silicon Pyramids for Efficient Solar Water Reduction. *ACS Appl. Mater. Interfaces* **2018**, *10* (43), 37142–37149. https://doi.org/10.1021/acsami.8b14571.

(158) Andoshe, D. M.; Jin, G.; Lee, C.-S.; Kim, C.; Kwon, K. C.; Choi, S.; Sohn, W.; Moon, C. W.; Lee, S. H.; Suh, J. M.; Kang, S.; Park, J.; Heo, H.; Kim, J. K.; Han, S.; Jo, M.-H.; Jang, H. W. Directly Assembled 3D Molybdenum Disulfide on Silicon Wafer for Efficient Photoelectrochemical Water Reduction. *Adv. Sustain. Syst.* **2018**, *2* (3), 1700142. https://doi.org/10.1002/adsu.201700142.

(159) Tang-Kong, R.; Winter, R.; Brock, R.; Tracy, J.; Eizenberg, M.; Dauskardt, R. H.; McIntyre, P. C. The Role of Catalyst Adhesion in ALD-TiO2 Protection of Water Splitting Silicon Anodes. *ACS Appl. Mater. Interfaces* **2018**, *10* (43), 37103–37109. https://doi.org/10.1021/acsami.8b13576.

(160) Cui, W.; Moehl, T.; Siol, S.; David Tilley, S. Operando Electrochemical Study of Charge Carrier Processes in Water Splitting Photoanodes Protected by Atomic Layer Deposited TiO 2. *Sustain. Energy Fuels* **2019**, *3* (11), 3085–3092. https://doi.org/10.1039/C9SE00399A.

(161) Hu, S.; Richter, M. H.; Lichterman, M. F.; Beardslee, J.; Mayer, T.; Brunschwig, B. S.; Lewis, N. S. Electrical, Photoelectrochemical, and Photoelectron Spectroscopic Investigation of the Interfacial Transport and Energetics of Amorphous TiO2/Si Heterojunctions. *J. Phys. Chem. C* **2016**, *120* (6), 3117–3129. https://doi.org/10.1021/acs.jpcc.5b09121.

(162) Cai, Q.; Hong, W.; Jian, C.; Li, J.; Liu, W. Insulator Layer Engineering toward Stable Si Photoanode for Efficient Water Oxidation. *ACS Catal.* **2018**, *8* (10), 9238–9244. https://doi.org/10.1021/acscatal.8b01398.

(163) Cao, S.; Zhang, Z.; Liao, Q.; Kang, Z.; Zhang, Y. Interface Engineering for High-Performance Photoelectrochemical Cells via Atomic Layer Deposition Technique. *Energy Technol.* **2021**, *9* (2), 2000819. https://doi.org/10.1002/ente.202000819.

(164) Green, M. A. *Solar Cells: Operating Principles, Technology, and System Applications*; 1982.

(165) Fan, R.; Dong, W.; Fang, L.; Zheng, F.; Shen, M. More than 10% Efficiency and One-Week Stability of Si Photocathodes for Water Splitting by Manipulating the Loading of the Pt Catalyst and TiO 2 Protective Layer. *J. Mater. Chem. A* **2017**, *5* (35), 18744–18751. https://doi.org/10.1039/C7TA04986B.

(166) Wang, T.; Liu, S.; Li, H.; Li, C.; Luo, Z.; Gong, J. Transparent Ta2O5 Protective Layer for Stable Silicon Photocathode under Full Solar Spectrum. *Ind. Eng. Chem. Res.* **2019**, *58* (14), 5510–5515. https://doi.org/10.1021/acs.iecr.9b00147.

(167) Cui, W.; Niu, W.; Wick-Joliat, R.; Moehl, T.; David Tilley, S. Operando Deconvolution of Photovoltaic and Electrocatalytic Performance in ALD TiO 2 Protected Water Splitting Photocathodes. *Chem. Sci.* **2018**, *9* (28), 6062–6067. https://doi.org/10.1039/C8SC01453A.

(168) Fan, R.; Dong, W.; Fang, L.; Zheng, F.; Su, X.; Zou, S.; Huang, J.; Wang, X.; Shen, M. Stable and Efficient Multi-Crystalline N+p Silicon Photocathode for H2 Production with Pyramid-like Surface Nanostructure and Thin Al2O3 Protective Layer. *Appl. Phys. Lett.* **2015**, *106* (1), 013902. https://doi.org/10.1063/1.4905511.

(169) Ros, C.; Carretero, N. M.; David, J.; Arbiol, J.; Andreu, T.; Morante, J. R. Insight into the Degradation Mechanisms of Atomic Layer Deposited TiO2 as Photoanode Protective Layer. *ACS Appl. Mater. Interfaces* **2019**, *11* (33), 29725–29735. https://doi.org/10.1021/acsami.9b05724.

(170) Godfrey, R. B.; Green, M. A. 655 MV Open-circuit Voltage, 17.6% Efficient Silicon MIS Solar Cells. *Appl. Phys. Lett.* **1979**, *34* (11), 790–793. https://doi.org/10.1063/1.90646.

(171) Pulfrey, D. L. MIS Solar Cells: A Review. *IEEE Trans. Electron Devices* **1978**, *25* (11), 1308–1317. https://doi.org/10.1109/T-ED.1978.19271.

(172) Olsen, L. C. Model Calculations for Metal-Insulator-Semiconductor Solar Cells. *Solid-State Electron.* **1977**, *20* (9), 741–751. https://doi.org/10.1016/0038-1101(77)90002-8.

(173) Shewchun, J.; Burk, D.; Spitzer, M. B. MIS and SIS Solar Cells. *IEEE Trans. Electron Devices* **1980**, *27* (4), 705–716. https://doi.org/10.1109/T-ED.1980.19926.

(174) Aberle, A. G.; Kuhlmann, B.; Meyer, R.; Hübner, A.; Hampe, C.; Hezel, R. Comparison of P-n Junction and Inversion-Layer Silicon Solar Cells by Means of Experiment and Simulation. *Prog. Photovolt. Res. Appl.* **1996**, *4* (3), 193–204. https://doi.org/10.1002/(SICI)1099-159X(199605/06)4:3<193::AID-PIP118>3.0.CO;2-S.

(175) Hezel, R. Recent Progress in MIS Solar Cells. *Prog. Photovolt. Res. Appl.* **1997**, *5* (2), 109–120. https://doi.org/10.1002/(SICI)1099-159X(199703/04)5:2<109::AID-PIP160>3.0.CO;2-8.

(176) Card, H. C.; Rhoderick, E. H. Studies of Tunnel MOS Diodes I. Interface Effects in Silicon Schottky Diodes. *J. Phys. Appl. Phys.* **1971**, *4* (10), 1589–1601. https://doi.org/10.1088/0022-3727/4/10/319.

(177) Doghish, M. Y.; Ho, F. D. A Comprehensive Analytical Model for Metal-Insulator-Semiconductor (MIS) Devices: A Solar Cell Application. *IEEE Trans. Electron Devices* **1993**, *40* (8), 1446–1454. https://doi.org/10.1109/16.223704.

(178) Har-Lavan, R.; Cahen, D. 40 Years of Inversion Layer Solar Cells: From MOS to Conducting Polymer/Inorganic Hybrids. *IEEE J. Photovolt.* **2013**, *3* (4), 1443–1459. https://doi.org/10.1109/JPHOTOV.2013.2270347.

(179) Chang, T.-Y.; Chang, C.-L.; Lee, H.-Y.; Lee, P.-T. Characteristics of MIS Solar Cells Using Sputtering SiO2 Insulating Layers. In *2010 35th IEEE Photovoltaic Specialists Conference*; 2010; pp 001318–001321. https://doi.org/10.1109/PVSC.2010.5614304.

(180) Oener, S. Z.; van de Groep, J.; Macco, B.; Bronsveld, P. C. P.; Kessels, W. M. M.; Polman, A.; Garnett, E. C. Metal–Insulator–Semiconductor Nanowire Network Solar Cells. *Nano Lett.* **2016**, *16* (6), 3689–3695. https://doi.org/10.1021/acs.nanolett.6b00949.

(181) Watanabe, M. N.; Junior, W. C.; Christiano, V.; Izumi, F.; Filho, S. G. dos S. Fabrication and Electrical Characterization of MOS Solar Cells for Energy Harvesting. In *2018 33rd Symposium on Microelectronics Technology and Devices (SBMicro)*; 2018; pp 1–4. https://doi.org/10.1109/SBMicro.2018.8511579.

(182) Machiche, S. B.; Dehimi, L.; Bencherif, H.; Pezzimenti, F. An Enhanced Conversion Efficiency of Metal Insulator Semiconductor Solar Cells by Using Different High-K Dielectrics. *Silicon* **2021**. https://doi.org/10.1007/s12633-021-01025-3.

(183) Pourbaix, M. *Atlas of Electrochemical Equilibria in Aqueous Solutions*; National Association of Corrosion Engineers, 1974.

(184) Oh, K.; Mériadec, C.; Lassalle-Kaiser, B.; Dorcet, V.; Fabre, B.; Ababou-Girard, S.; Joanny, L.; Gouttefangeas, F.; Loget, G. Elucidating the Performance and Unexpected Stability of Partially Coated Water-Splitting Silicon Photoanodes. *Energy Environ. Sci.* **2018**, *11* (9), 2590–2599. https://doi.org/10.1039/C8EE00980E.

(185) Hernley, P. A.; Chavez, S. A.; Quinn, J. P.; Linic, S. Engineering the Optical and Catalytic Properties of Co-Catalyst/Semiconductor Photocatalysts. *ACS Photonics* **2017**, *4* (4), 979–985. https://doi.org/10.1021/acsphotonics.7b00047.

(186) Hong, W.; Cai, Q.; Ban, R.; He, X.; Jian, C.; Li, J.; Li, J.; Liu, W. High-Performance Silicon Photoanode Enhanced by Gold Nanoparticles for Efficient Water Oxidation. *ACS Appl. Mater. Interfaces* **2018**, *10* (7), 6262–6268. https://doi.org/10.1021/acsami.7b16749.

(187) Hernley, P. A.; Linic, S. Modeling the Impact of Metallic Plasmonic Resonators on the Solar Conversion Efficiencies of Semiconductor Photoelectrodes: When Does Introducing Buried Plasmonic Nanostructures Make Sense? *J. Phys. Chem. C* **2018**, *122* (42), 24279–24286. https://doi.org/10.1021/acs.jpcc.8b07214.

(188) Sullivan, J. P.; Tung, R. T.; Pinto, M. R.; Graham, W. R. Electron Transport of Inhomogeneous Schottky Barriers: A Numerical Study. *J. Appl. Phys.* **1991**, *70* (12), 7403–7424. https://doi.org/10.1063/1.349737.

(189) Tung, R. T. Electron Transport of Inhomogeneous Schottky Barriers. *Appl. Phys. Lett.* **1991**, *58* (24), 2821–2823. https://doi.org/10.1063/1.104747.

(190) Tung, R. T. Electron Transport at Metal-Semiconductor Interfaces: General Theory. *Phys. Rev. B* **1992**, *45* (23), 13509–13523. https://doi.org/10.1103/PhysRevB.45.13509.

(191) Loget, G. Water Oxidation with Inhomogeneous Metal-Silicon Interfaces. *Curr. Opin. Colloid Interface Sci.* **2019**, *39*, 40–50. https://doi.org/10.1016/j.cocis.2019.01.001.

(192) Rossi, R. C.; Lewis, N. S. Investigation of the Size-Scaling Behavior of Spatially Nonuniform Barrier Height Contacts to Semiconductor Surfaces Using Ordered Nanometer-Scale Nickel Arrays on Silicon Electrodes. *J. Phys. Chem. B* **2001**, *105* (49), 12303–12318. https://doi.org/10.1021/jp011861c.

(193) Laskowski, F. A. L.; Oener, S. Z.; Nellist, M. R.; Gordon, A. M.; Bain, D. C.; Fehrs, J. L.; Boettcher, S. W. Nanoscale Semiconductor/Catalyst Interfaces in Photoelectrochemistry. *Nat. Mater.* **2020**, *19* (1), 69–76. https://doi.org/10.1038/s41563-019-0488-z.

(194) Tilley, S. D.; Cornuz, M.; Sivula, K.; Grätzel, M. Light-Induced Water Splitting with Hematite: Improved Nanostructure and Iridium Oxide Catalysis. *Angew. Chem. Int. Ed.* **2010**, *49* (36), 6405–6408. https://doi.org/10.1002/anie.201003110.

(195) Oh, K.; Dorcet, V.; Fabre, B.; Loget, G. Dissociating Water at N-Si Photoanodes Partially Covered with Fe Catalysts. *Adv. Energy Mater.* **2020**, *10* (3), 1902963. https://doi.org/10.1002/aenm.201902963.

(196) Cai, Q.; Hong, W.; Jian, C.; Liu, W. Ultrafast Hot Ion-Exchange Triggered Electrocatalyst Modification and Interface Engineering on Silicon Photoanodes. *Nano Energy* **2020**, *70*, 104485. https://doi.org/10.1016/j.nanoen.2020.104485.

(197) Zhang, P.; Wang, W.; Wang, H.; Li, Y.; Cui, C. Tuning Hole Accumulation of Metal Oxides Promotes the Oxygen Evolution Rate. *ACS Catal.* **2020**, *10* (18), 10427–10435. https://doi.org/10.1021/acscatal.0c02882.

(198) Lee, S. A.; Lee, T. H.; Kim, C.; Lee, M. G.; Choi, M.-J.; Park, H.; Choi, S.; Oh, J.; Jang, H. W. Tailored NiOx/Ni Cocatalysts on Silicon for Highly Efficient Water Splitting Photoanodes via Pulsed Electrodeposition. *ACS Catal.* **2018**, *8* (8), 7261–7269. https://doi.org/10.1021/acscatal.8b01999.

(199) Hill, J. C.; Landers, A. T.; Switzer, J. A. An Electrodeposited Inhomogeneous Metal-Insulator-Semiconductor Junction for Efficient Photoelectrochemical Water Oxidation. *Nat. Mater.* **2015**, *14* (11), 1150–1155. https://doi.org/10.1038/nmat4408.

(200) Lee, S. A.; Lee, T. H.; Kim, C.; Choi, M.-J.; Park, H.; Choi, S.; Lee, J.; Oh, J.; Kim, S. Y.; Jang, H. W. Amorphous Cobalt Oxide Nanowalls as Catalyst and Protection Layers on N-Type Silicon for Efficient Photoelectrochemical Water Oxidation. *ACS Catal.* **2020**, *10* (1), 420–429. https://doi.org/10.1021/acscatal.9b03899.

Chapter 2

Fabrication, Characterization, and Experimental Methods

2.1 Introduction

The purpose of this chapter is to provide a general overview of the fabrication, characterization, and experimental methods used through this dissertation. This includes a general description of the techniques as well as important details for performing the techniques successfully and with rigor. Each of these techniques are applied to specific applications throughout this dissertation in the respective chapters. In addition to the fabrication, characterization, and experiments, many chapters throughout this dissertation also include analytic modeling and finite element modeling. However, the full details of the computational modeling techniques are not provided in this chapter, but rather those details are fully discussed in the specific chapters in which they are the most relevant.

2.2 Fabrication Techniques for Photoelectrocatalysts

2.2.1 Silicon Preparation

The three types of silicon 4-inch wafers that are used throughout the work include: (1) phosphorus doped (n-type, resistivity 1–10 Ω-cm, <100>-oriented, 525 μm thick) wafers purchased from Silicon Valley Microelectronics, (2) phosphorus doped (n-type, resistivity 0.1–1 Ω-cm, <100>-oriented, 525 μm thick) wafers purchased from Addison Engineering, and (3) boron doped (p-type, resistivity 0.001–0.005, <100>-oriented, 525 μm) wafers purchased from Addison Engineering.

In general, samples are fabricated at the wafer scale, and then diced into smaller pieces for further characterization and testing. First, the wafers are cleaned with NanoStrip (a commercial piranha solution) for 10 min at 60 °C and rinsed in distilled water. Then the wafers are dipped in buffered hydrofluoric acid for 1 min to remove the native oxide layer. Finally, the wafers are rinsed by flushing water for about 5 minutes, and dried by either spin drying or with a stream of nitrogen and then immediately transferred to the next step in the process, typically atomic layer deposition.

2.2.2 Atomic Layer Deposition (ALD)

ALD, which is a subset of chemical vapor deposition, has been a key technology for water splitting applications. The primary benefit of ALD is the conformal and uniform deposition of materials with sub-nanometer precision. The applications of ALD and the general ALD process has been thoroughly described elsewhere.[1–6] In short, the ALD process involves repeating cycles of four steps. (1) A precursor is pulsed for a long enough time to uniformly coat the entire exposed surface of the substrate via chemical adsorption. The process is self-limiting such that only a monolayer of the precursor is deposited. (2) The excess precursor is purged away with an inert gas. (3) An oxidizing agent (typically water vapor or ozone or oxygen plasma) which makes the layer hydrophilic and suitable for the next monolayer of precursor. (4) The excess oxidizing agent is purged away with an inert gas. Each cycle deposits a single monolayer of the material, so the thickness can be precisely controlled at the atomic scale by setting the number of cycles.

One of the main drawbacks is that the ALD is a slow deposition process, but the process has been applied at the industrial scale for applications in the electronics industry.[7] To speed up

the process, industry uses spatial ALD to spatially separate the precursor and oxidizing steps which eliminates the need for purging excess reactants.[8]

After cleaning and etching the Si wafers, the samples are transferred to the vacuum chamber in a Veeco Fiji ALD System within about 5-10 minutes to minimize air exposure. The ALD pumps down to 2.5 mT and preheated to 200 C for all depositions. The precursor used for depositing HfO_2 is tetrakis(dimethylamino)hafnium (TDMAH). An ALD cycle consists of a 250 ms H_2O pulse followed by a 12 second purge and a 60 ms TDMAH pulse and a 12 second purge. Generally, 10-25 cycles were used to deposit 1-3 nm of HfO_2.

The precursor used for depositing Al_2O_3 is trimethylaluminum (TMA). An ALD cycle consists of a 60 ms TMA pulse followed by a 10 s purge and then a H_2O pulse for 65 ms and a 10 s purge. Generally, 20 cycles were used to deposit ~2 nm of Al_2O_3.

The above processes are typically for depositing individual materials, but multilayer systems as well as doped or alloyed materials can also be deposited by alternating the types of precursors. This strategy is used in Chapter 5 to create mixtures or alloys of Al_2O_3 and HfO_2.

2.2.3 Metal Evaporation

The metals in this work were deposited by physical vapor deposition (PVD) techniques, specifically either electron-beam (e-beam) evaporation or magnetron sputter deposition. These techniques allow for uniform coatings of pure or oxidized metals down to a few nm. In general, a metal source is bombarded or heated and transformed in a vapor that condenses on the substrate. For sputter deposition, a metal source or target is bombarded with an argon plasma while for e-beam evaporation, the metal source is bombarded by electrons which are directed from a tungsten filament. In both cases, high vacuum is necessary to prevent collisions and reactions with molecules as the metal vapor travels to the substrate.[9]

Within a few minutes of completing the ALD process, the wafers are transferred to the vacuum chamber of the PVD tool. Ir was deposited using a Lab 18-02 magnetron sputtering system with a base pressure of less than 3×10^{-6} Torr. The sputtering time 33 seconds with a DC power of 100 W and a pressure of about 5×10^{-3} Torr. The deposition rate depends on the age of the Ir target, and the rate averaged at a rate of 1.1 Å s^{-1}.

Ni was deposited using an SJ-20 electron-beam evaporator system with a base pressure of 2×10^{-6} Torr. The deposition time was 50 seconds at a rate of 1.0 Å s^{-1} which is monitored in real-time with a quartz microcrystal. Typical pressure during the deposition is 4×10^{-6} Torr.

After the fabrication, the final step is to dice the samples for eventual testing and characterization. The samples were either mechanically diced with an ADT 7100 Dicing Saw to 13x13 mm square pieces, or manually diced into 12 x 12 mm pieces using a diamond scribe and cleaving pliers from LatticeGear.

2.3 Materials Characterization Techniques

2.3.1 Scanning Electron Microcopy

Samples are prepared for SEM processing and imaging by scratching the back surface with a diamond scribe, adding conductive InGa eutectic. Then the sample is attached to a SEM stub using double-sided copper tape. Top-down SEM images are typically obtained using a Thermo Fisher Nova 200 Nanolab SEM. An Everhart-Thornley Detector (ETD) 5 kV operating voltage and 0.4 nA current was used for lower resolution, while immersion mode, higher operating voltages, and a Through the Lens Detector (TLD) was used to obtain high resolution images (>20,000x magnification).[10]

The Nova was also used to prepare samples for high-resolution images via Scanning Transmission Electron Microcopy (STEM). For this process, a small (10-15 micron wide, and

~10 um deep) region is cut out from the sample using a focused ion beam (FIB).[11] The FIB can damage the surface of the sample, so a layer of C or Pt is first deposited on the surface of the sample to protect it. After cutting out the piece, an omniprobe is used to lift-out the sample and the sample is ultimately attached to a TEM copper grid using Pt glue. Then the sample is slowly thinned down until its thickness is less than ~100 nm such that electrons can transmit through the sample. This process allows us to take cross-sectional images of the interface to observe the layers using STEM.

2.3.2 Scanning Transmission Electron Microcopy (STEM)

The samples for STEM analysis were prepared using the procedure described above in section 2.3.1 . The goal is to obtain high resolution cross-sectional images of the layers and interfaces of fabricated systems. STEM was performed using either a JEOL 2100F probe-corrected electron microscope or a JEOL 3100R05 double-corrected STEM. The accelerating voltage for imaging is 200 kV. Typically, a double-tilt holder is used to perpendicularly align the sample and align the sample to see the <100> crystal plane of the Si substrate. Combined with >1,000,000x magnification enables clear visualization of the Si atomic lattice. Both bright field and dark field images are used to capture cross-sectional images. The contrast seen in both types of images is primarily related to the atomic number of the atoms and the density of electrons striking the detector. These images reveal each of the distinct layers and interfaces in various systems. The thicknesses of these layers were measured by analyzing cross-sectional images with IMAGEJ software at various points throughout the sample.

2.3.3 Energy-Dispersive X-Ray Spectroscopy (EDS)

For EDS analysis, the electron beam with high kinetic energy strikes the atoms and electrons in the sample. The incident beam can excite the inner shell electrons of the atoms, but

eventually the outer electrons will relax and fill the hole in the inner shell, which releases an X-ray that can be collected by a detector from the energy-dispersive spectrometer. The specific energy of these X-rays from electron relaxation is a characteristic of the properties of the individual atom.[10]

To confirm the presence of specific atoms and their concentrations in the cross-sectional STEM images, an EDS detector was used with the 2100 and 3100 STEM. To maximize counts, EDS with Thermo Fisher Talos F200X G2 STEM was also used in Chapter 7. Only specific elements expected to be present in the sample were explicitly searched. These include Si, O, C (used as protective layer), Pt (used as protective layer and as an adhesive during sample preparation), and the Ni and Ir metals used as electrocatalysts. Elemental mapping was used to count the atoms throughout the entire STEM image. An elemental line scan was also used to probe the atomic composition across the interface.

2.3.4 Light Absorption and Ultraviolet-Visible Spectroscopy (UV-vis)

Light absorption is an important consideration for solar energy conversion. In any system, incident light will either be absorbed by the materials, reflected by the surfaces/interfaces, or transmitted through the entire sample. UV-vis spectroscopy is a common technique to measure the optical properties of systems by measuring the absorbance, reflectance, and transmittance throughout the ultraviolet and visible wavelength range, which is the most relevant range for most solar water splitting systems.[12] A Thermo Scientific Evolution 300 UV-Vis Spectrometer was used for the measurements, in which a Xe lamp and a monochromator generates a narrow band of light from wavelengths of 200 to 1100 nm that strikes the sample. The light is either absorbed by the materials, reflected off the materials, or transmitted through the materials, which is measured by a detector. Data in Figure 2-1 shows example plots of the

light transmission through catalyst layers as obtained with UV-vis. For the Ni and Ir films in this study, the average light transmission is between 50-60%, which means that 40-50% of the light is reflected or parasitically absorbed by the metal overlayers. These losses are significant, although it is noted that even without any metal overlay, greater than 30% of incident radiation is reflected from planar Si.[13] Finally, it is also noted that the expected light absorption properties can also be evaluated using theory and modeling.[15] In general, the photocurrents obtained experimentally should match the expected results based on the parasitic reflection and absorption losses.

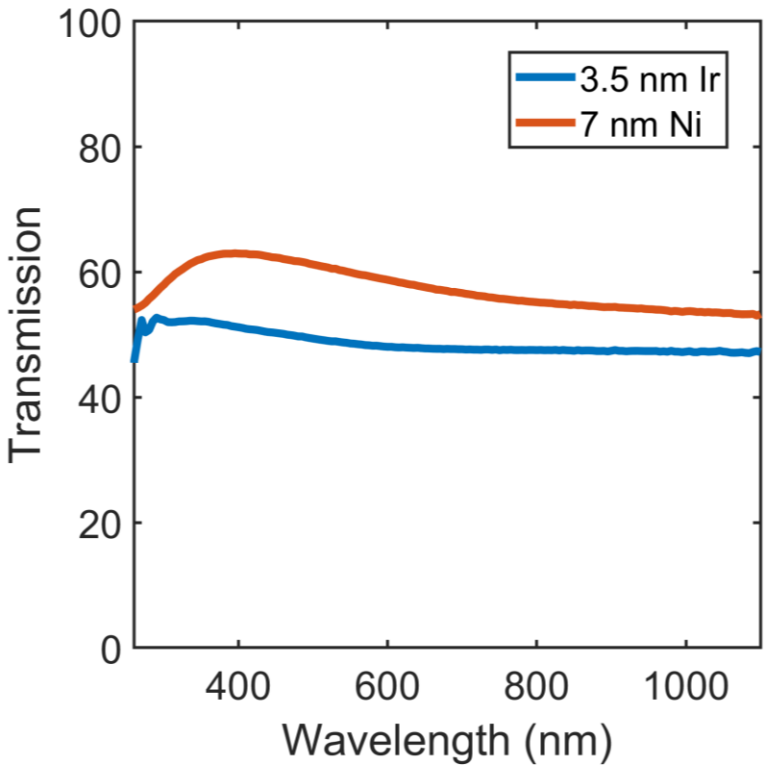

Figure 2-1: Light transmission obtained using UV-vis spectroscopy for a 7 nm Ni film and a 3.5 nm Ir film.

2.4 Photoelectrochemical Experiments

2.4.1 Three-Electrode Setup

A three-electrode setup is a versatile strategy to perform a variety of electrochemical experiments. In short, the typical three-electrode setup consists of (1) a potentiostat (Reference Gamry 3000 Potentiostat in this work) which controls and measures the input and output currents and voltages, (2) three electrodes which are electrically connected to the potentiostat via cables and alligator clips, (3) an electrolyte solution which depends on the specific experiment but should be conductive to minimize resistance, and (4) a light source if performing photoelectrochemical water splitting. A schematic of the three-electrode setup is illustrated in Figure 2-2a.

The three electrodes in the setup include the working electrode, the counter electrode and the reference electrode. The working electrode is the specific system that is meant to be tested and analyzed which in this work is primarily multicomponent water oxidation photoelectrocatalysts. The counter electrode balances the charge in the system and performs the opposite half-reaction compared to the working electrode (i.e., the counter electrode will do a reduction reaction if the working electrode is performing an oxidation reaction). The counter electrode should have a relatively large surface area for the reaction to take place with minimal polarization losses. The counter electrode should also be placed somewhat isolated from the other electrodes and should remain stable in the solution, which is a possible concern when using Pt or graphite for certain sensitive reactions.[16–20] The reference electrode is used for measuring the potential of the working electrode relative to the redox potential of the equilibrium within the reference electrode. The choice of reference electrode depends on its stability in the specific electrolyte. In basic environment, the preferred reference electrode is Hg/HgO which has a

standard redox potential of 0.098 V relative to the standard hydrogen electrode (SHE).[21,22] In many cases it is useful to convert the potential relative to the reversible hydrogen electrode (RHE) in which the scale changes as a function of the pH of the electrolyte. The conversion can be made to the RHE using the following equation:

$$E_{ref,RHE} = E_{ref,SHE} + 0.591 * pH \quad \text{2-1}$$

Where $E_{ref,RHE}$ is potential of the reference electrode relative to RHE, $E_{ref,SHE}$ is potential of the reference electrode relative to SHE, and pH is the pH of the electrolyte. In general, it is not good practice to assume $E_{ref,SHE}$ for a given reference electrode because the standard potential can fluctuate over time, or because the reference electrode may not be at standard conditions or could become contaminated. Therefore, it is better to calibrate the reference electrode directly in case the potential has drifted over time. One way to complete this calibration is by comparing the open-circuit potential to a pristine master reference electrode.[21] But the method to calibrate the reference electrode in this work is by creating a reversible hydrogen electrode. Hydrogen is bubbled for 30 minutes to saturate the electrolyte which contains the reference electrode to be calibrated and Pt wires as the counter and working electrodes. The potential of the reference electrode relative to the RHE ($E_{ref,RHE}$) can then be directly measured using the open-circuit potential function with the potentiostat.

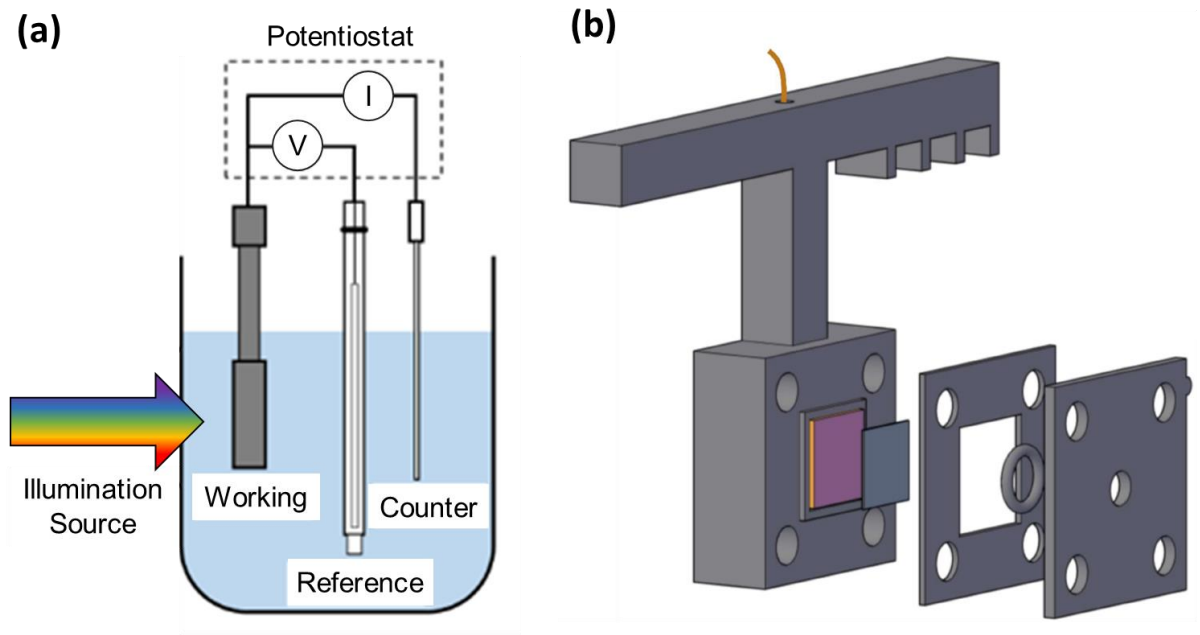

Figure 2-2: (a) Schematic of a typical three-electrode setup used for electrochemical experiments. (b) Schematic of 3D printed working electrode holder which enables precise control of the illuminated area and electrolyte-exposed area of the tested sample. From left to right: main housing with notches to precisely position the setup within the beaker. A Cu plate and Cu wire are contacted with a metal spring to ensure electrical contact between the potentiostat and the tested sample. A rubber gasket and a rubber O-ring are used to prevent the electrolyte from leaking into the system and to define the area of the sample that is exposed to the electrolyte. The front face plate (with an aperture to allow the passage of light) is secured to the main housing using four screws and bolts that are fastened in the corners of the main housing. The front face plate is spray painted black to ensure that no light can pass through the plate except for through the aperture.

2.4.2 Working Electrode Construction

For all electrochemical experiments with the three-electrode setup, diced samples were housed in a 3D-printed electrode (Figure 2-2b). The back contacts of the samples were scratched with a diamond scribe to remove part of the native oxide, and a gallium–indium eutectic was applied to ensure ohmic contact. The back contacts were then pressed against a copper plate. The working electrode's exposure to electrolyte was defined by an O-ring which also prevented the electrolyte from leaking to the back contact. The samples were exposed to a light source via an aperture with an area of either 0.46 cm^2 or 0.26 cm^2.

2.4.3 Illumination Source and Calibration

The samples in the working electrode were illuminated using a 300 W UV 16S-Series Solar Simulator (Solar Light Company) with an AM 1.5G filter. The broadband spectrum emitted from the solar simulator using a new lamp bulb is shown in Figure 2-3. The power that is irradiated on the sample is measured and calibrated using a Newport 919P-020-12 thermopile detector which covers wavelengths ranging from 190 nm to 11 μm with power ranging from 10 mW to 20 W. The thermopile was housed in a modified 3D printed electrode with a cover plate with the 0.46 cm^2 aperture. The distance between the thermopile and the light source is adjusted until the power reads 46 mW. This corresponds to approximately 1-sun illumination (100 mW/cm^2) after normalizing the power to the exposed surface area. One of the primary benefits of using the 3D printed setup is precise placement of the samples and the thermopile and the consistent 0.46 cm^2 aperture ensures accurate calibration and results.

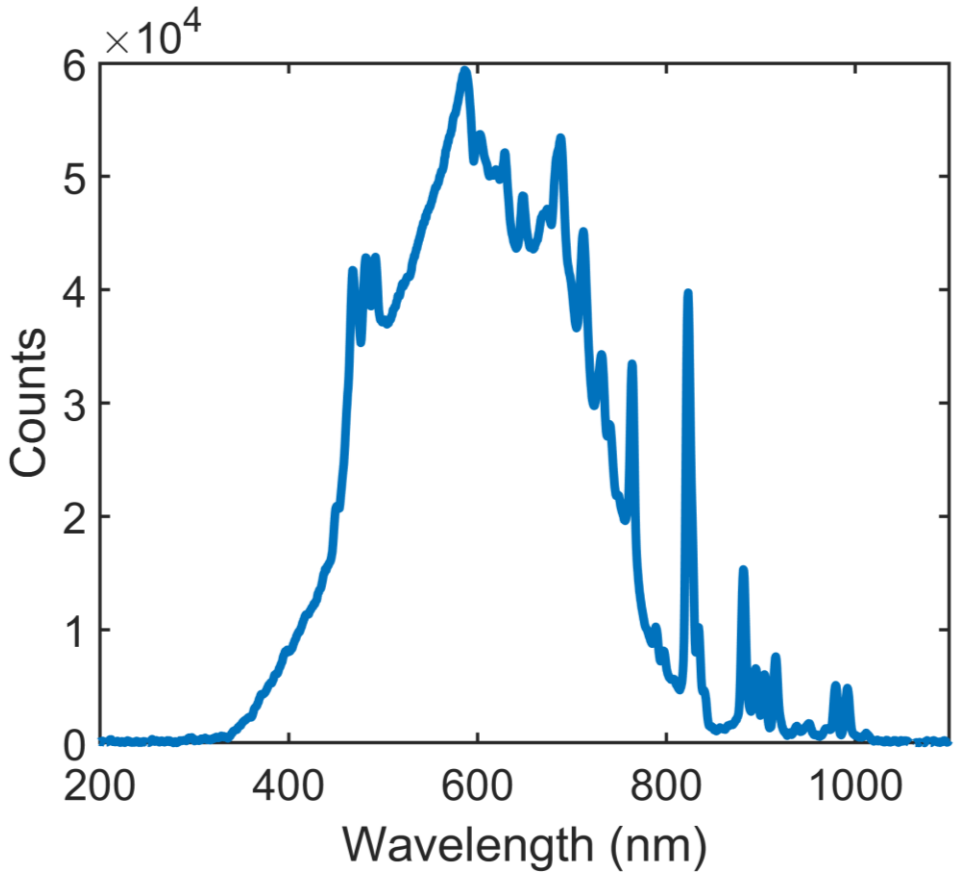

Figure 2-3: Broadband spectrum emitted from a 300 W UV 16S-Series Solar Simulator (Solar Light Company) with AM 1.5 filter.

The most common set of experiments with a three-electrode setup is cyclic voltammetry, in which the potentiostat sweeps the potential (typically at a scan rate of 100 mV s^{-1}) back-and-forth over a specified range, and the potentiostat measures the current that is generated by the chemical reactions on the working electrode surface. Linear sweep voltammetry (LSV) is a similar technique but only sweeps the potential in a single direction rather than back-and-forth. In analogy to thermochemical reactions, the applied voltage analogous to the energy or temperature that is input into the system, and the current is directly analogous to the reaction rate.

In general, there are multiple possible reactions that can take place at the catalyst on the working electrocatalyst, including degradation reactions. The percentage of the electrons (i.e., the current) that goes toward the desired reaction (for this dissertation, water oxidation reaction), compared to the undesired reactions is known as the Faradaic efficiency.[23,24] By directly measuring the amount of oxygen evolved during the reaction relative to the generated currents, a Faradaic efficiency of essentially 100% has been well documented for many solar water oxidation systems as long as they are relatively stable.[21] This is because there are no other species in the water to oxidize and the formation of peroxides are unfavorable. Therefore, it can be assumed that the entirety of the current generated by an illuminated sample is from the water oxidation reaction.

The cyclic voltammetry experiments are performed either in light (1-Sun illumination) or in dark. For water oxidation experiments, a 1 M KOH (Fischer Scientific) electrolyte was used and magnetically stirred. A graphite rod counter electrode and an Hg/HgO reference electrode were used in the three-electrode setup. In some cases, oxygen was bubbled into the electrolyte, although this is generally not necessary.[22] The potentiostat controls the voltage relative to the Hg/HgO reference electrode ($V_{Hg/HgO}$), and this voltage is converted to the RHE (V_{RHE}) at pH 14 using the following equation:

$$V_{RHE} = V_{Hg/HgO} + E_{Hg/HgO,SHE} + 0.591 * pH \qquad 2\text{-}2$$

Here, $E_{Hg/HgO,SHE}$ is the redox potential of the Hg/HgO reference electrode which was determined from the calibration process previously described using equation 2-1.

A representative example and shape of a typical CV plot is shown in Figure 2-4a for an illuminated sample (light n-Si) and a dark electrocatalytic control (dark p^+-Si). Degenerately doped p^+-Silicon is used because it behaves essentially like a metal such that it is conductive and

does not absorb light to create photons like it would if it were moderately doped. Therefore, the p^+-Si control sample has no contributions from illumination, and the only current generated will be directly related to the electrochemical kinetic reaction of interest. The dark p^+-Si electrocatalytic control sample generates almost no current until the applied potential exceeds the redox potential of the desired electrochemical reaction, in this case water oxidation with a redox potential of 1.23 V vs RHE (vertical dashed line in Figure 2-4a). Thermodynamically, the applied potential must exceed 1.23 V vs RHE before the oxidation can occur. But significant current is not observed until >1.5 V vs RHE because the kinetics of this 4-electron reaction are slow.[25–28] The kinetic overpotential (η_{op}) is the amount of voltage beyond the thermodynamic redox potential that is needed to generate a specified current (typically 1 mA/cm^2). As higher voltages are applied, the current exponentially increases according to the Butler-Volmer equation.[23] The current will continue to exponentially increase until resistance losses or mass transport losses become dominant, although mass transport losses are typically negligible for the relative low currents generated in photoelectrochemical hydrogen and oxygen evolution reactions.[23]

For the illuminated sample (n-Si), now the system not only has an electrochemical kinetic contribution, but it also has an illumination component as the moderately doped n-Si can absorb photons from the light. As shown in the CV of Figure 2-4a, the reaction current can be generated even before the OER redox potential. This is not a violation of thermodynamics because the system internally generates a photovoltage upon illumination, which is discussed more in the next section. At low applied potential and low currents (< 5 mA/cm^2, the CV response is dominated by kinetics and is similarly shaped to the dark electrocatalytic control. At higher applied potentials, however, the current begins to plateau, which is known as the photo-limited

current density (J_{ph}). The photo-limited current density is governed by the total number of photons that can be absorbed by the semiconductor substrate. For Si with a band gap of 1.1 eV, the theoretical limit to the photo-limited current is about 44 mA/cm^2,[29] but the current will be much lower due to parasitic absorption, reflection, and transmission discussed in section 2.3.4 In Figure 2-4a, the photo-limited current is about 35 mA/cm^2. If the light is turned off on the sample, then the photo-limited current would drop to zero as there are no photo-generated electrons/holes. Therefore, the currents are very low in the dark for n-Si systems, but can include some current due to capacitive charging, recombination currents, or shunt resistance.

2.4.4 Photovoltage and Open-Circuit Potential

The photovoltage is the voltage that a system generates upon illumination due to the buildup and separation of the photo-exited charge carriers. The photovoltage is a key performance metric for water splitting systems, and an overall solar water splitting system would need to generate a photovoltage of at least 1.6 V to split water efficiently (~500 to 700 mV from the low band gap semiconductor and ~900 to 1100 mV from the high band gap semiconductor).[30,31] One of the ways to measure the photovoltage (V_{ph}) is by measuring the voltage shift between the illuminated sample and the dark electrocatalytic control, as shown in Figure 2-4a**.** The photovoltage can be evaluated at any specified current, and the value will ultimately depend on the specified current. In Figure 2-4a, the photovoltage is evaluated at a current of 1 mA/cm^2 ($V_{ph,1}$) and 20 mA/cm^2 ($V_{ph,20}$), and these photovoltages differ by about 4%. The photovoltage is typically evaluated at a low current density of 1 mA/cm^2 because there will a negligible impact from the resistance which scales linearly with current. There is also merit to evaluating the photovoltage at a current of 10 mA/cm^2 which is a desired operating potential for achieving >10 % STH efficiency systems.[21,31]

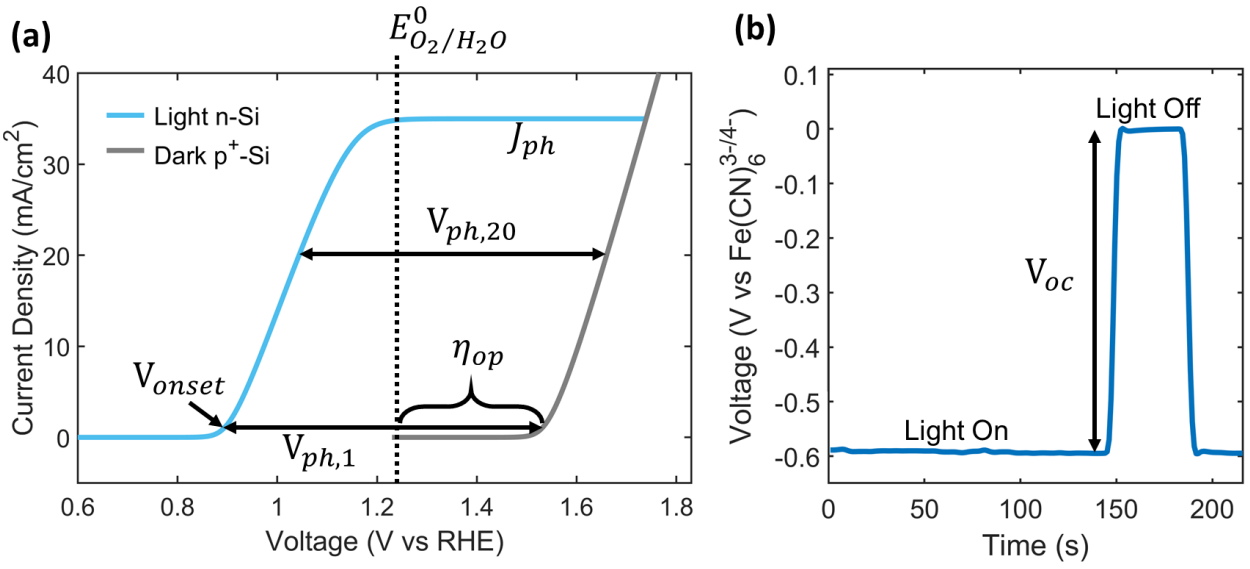

Figure 2-4: (a) Representative CV for an illuminated sample (light n-Si) and a dark electrocatalytic control (dark p^+-Si). $V_{ph,1}$ and $V_{ph,20}$ are the generated photovoltages evaluated at a current density of 1 mA/cm^2 and 20 mA/cm^2, respectively. V_{onset} is the onset potential for the illuminated sample, which is another commonly reported performance metric for solar water splitting.[21] η_{op} is the kinetic overpotential associated with kinetic losses at the catalyst performing OER. J_{ph} is the photo-limited current. (b) Open-circuit voltage plot obtained in a ferri/ferrocyanide electrolyte by switching on and off the light. The open-circuit photovoltage (V_{oc}) can be obtained by observing the shift in the potential from light on to light off.

It is important to note that the above-described method to measure the photovoltage is only strictly accurate if the illuminated sample and the dark electrocatalytic control have similar electrocatalyst surface area and if the data is properly corrected for solution resistance (although measuring photovoltage at the low current of 1 mA/cm^2 makes the contribution from the series resistance negligible). This requirement is typically met for systems with planar electrocatalysts because the electrocatalyst surface area is similar for all samples and proportional to the 0.46 cm^2 aperture which defines how much of surface is performing the electrochemical reactions. For the case of systems with Ni electrocatalyst, the electrochemically active surface area (ECSA) can be approximated by integrating the Ni redox peaks in the CVs.[21,32,33] This is particularly important when evaluating the validity of the photovoltage and the electrocatalyst surface area for systems with nanoparticle electrocatalysts (Chapter 7). As described in the next paragraph, the

requirement for similar electrocatalyst active area can be relaxed when evaluating the open-circuit photovoltage.

The photovoltage can also be evaluated at open-circuit (0 mA/cm^2) using a well-defined redox couple with facile kinetics (as long as the materials in the system are stable in the electrolyte and therefore don't have a corrosion potential). The facile kinetics means that the photovoltage can be more easily decoupled from the electrocatalyst kinetics. The open-circuit photovoltage (V_{oc}) is essentially identical to the photovoltage at 1 mA/cm^2, and this is another way to validate the performance. A ferri-/ferrocyanide (FFC) solution consisting of 10×10^{-3} m potassium hexacyanoferrate(II) trihydrate, 10×10^{-3} M potassium hexacyanoferrate(III) (EMD Millipore), and 1 M KCl (Fischer Scientific) was used for measuring the open-circuit photovoltage. The electrolyte was stagnant for the CV experiments (100 mV s^{-1}) but was stirred for measuring the open-circuit photovoltage. A graphite reference electrode and Pt wire counter electrode were used such that the applied voltage is relative to the FFC redox potential (because the graphite reference electrode is in equilibrium with the electrolyte).

The open-circuit photovoltage (V_{oc}) can be evaluated using one of two methods: (1) directly measuring the open-circuit voltage difference under illumination and in the dark, and (2) performing CVs on an illuminated sample and an electrocatalytic control sample. Both approaches will yield the same results, but the first of these two strategies is convenient because an electrocatalyst control sample is not required at all. Figure 2-4b illustrates a typical open-circuit voltage response for the experiments under light on and light off conditions. The experiment is conducted on an n-Si based sample and no electrocatalytic control sample is

necessary for this approach. The shift in the open-circuit voltage is the measured open-circuit photovoltage (arrow in Figure 2-4b).

2.4.5 Chronoamperometry

Chronoamperometry is a simple electrochemical experiment in which the voltage is held at a specific potential (rather than being swept), and the generated current is measured. This type of experiment is common for analyzing the long-term stability of a water splitting system. Sometimes the stability test is performed while alternating between the dark and light to simulate the night and day of a practical system operating from sunlight. The sample can be considered stable if the current is constant (not decreasing) throughout the duration of the experiments. Although the current could drop over time due to the formation of bubbles, which can be regularly removed during the experiments. During the stability test, it is also important to intermittently perform a CV experiment to determine if the resistance or performance has changed in any way.

2.4.6 Electrochemical Impedance Spectroscopy and Mott-Schottky Analysis

EIS is a frequency-based method in which different physical phenomena can be probed using distinct frequencies. The finer details and applications of EIS have been well documented.[34–36] In short, the key word "impedance" is analogous to resistance, but it is generalized to apply for alternating currents (AC). The real component of impedance is the resistance while the imaginary component is the reactance which both depend on the frequency of the AC. During EIS experiments, a sinusoidal AC potential perturbation is applied to the working electrode, producing an AC current whose phase shift and amplitude are measured. The key as well as the challenge to analyzing EIS data is to fit the experimental system to a physically meaningful equivalent circuit consisting of resistors, capacitors, and/or inductors.

One of the key circuit features in any electrochemical cell is resistance from the working electrode, wires, and the electrolyte. This combined resistance is in series with the working electrode, which is typically MIS systems in this dissertation. There is also a parallel resistance associated with the charge transfer through these systems. Furthermore, systems with electrocatalyst also have a charge transfer resistance that can be related to the kinetic rates.[37] For the EIS experiments in this dissertation, the selected electrolyte solution consists of ferri/ferrocyanide and KCl to lower the resistance. The oxidation and reduction reactions to transition to and from ferri/ferrocyanide ions is very fast, so the charge transfer resistance is neglected in these systems.

Any semiconductor in equilibrium with an electrolyte or metal will have a characteristic capacitance due to the charge build-up in the space charge region (also known as the band bending or depletion region).[38] The analytical expression for the space charge capacitance (C_{sc}) in a semiconductor is given by the Mott-Schottky equation:

$$\left(\frac{1}{C_{sc}}\right)^2 = \frac{2}{\varepsilon_0 \varepsilon_s A^2 q N_D}\left(V_a - V_{fb} - \frac{kT}{q}\right) \qquad 2\text{-}3$$

Here, A is the surface area of the junction, ε_0 is the vacuum permittivity, ε_s is the semiconductor relative permittivity, N_D is the doping density of the semiconductor, V_a is the applied voltage relative to the redox potential of the electrolyte, and V_{fb} is the flat-band potential.

In addition to the semiconductor, the insulator also has a capacitance which can be described like a traditional capacitor.

$$C_{ox} = \frac{\varepsilon_{ox} A}{d} \qquad 2\text{-}4$$

Here, C_{ox} is the capacitance of the oxide insulator, ε_{ox} is the permittivity of the HfO_2 which is assumed to be equivalent to the bulk permittivity of $25\varepsilon_0$ (ε_0=8.85×10^{-12} C V^{-1} m^{-1}), A is the area

covered by the insulator, and d is the thickness of the insulator. There is also a capacitance in the Helmholtz double layer of the electrolyte, which may need to be considered.[39,40] But for the systems in this dissertation, this capacitance contribution has a negligible influence on the system's total series capacitance, so it is not included in the equivalent circuit.[41] All of these circuit components can be combined into a physically meaningful equivalent circuit that is illustrated in Figure 2-5.

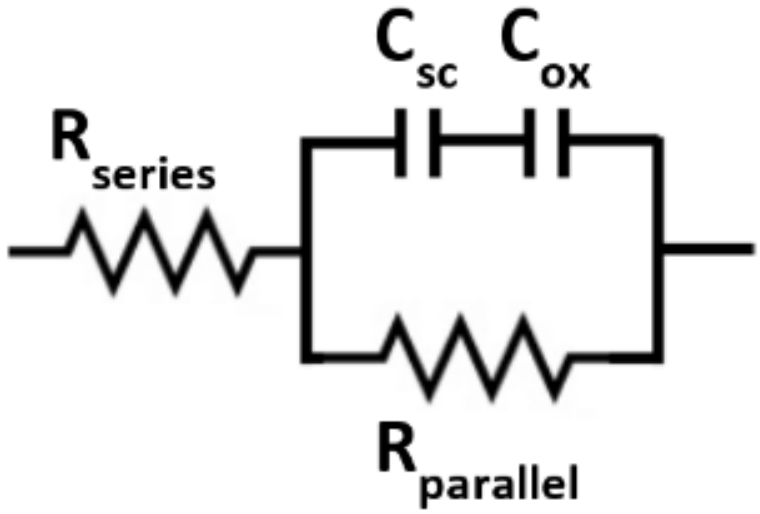

Figure 2-5: Equivalent circuit used to fit the impedance data.

EIS experiments run throughout a range of voltages and frequencies, and the data is fit to this equivalent circuit to extract each of the individual electrical components in these systems. This fitting procedure was conducted using Gamry Echem Analyst Software.[42] The flat-band potential is commonly extracted from EIS measurements using the Mott-Schottky equation 2-3.[40] Specifically, the space charge capacitance (C_{sc}) is measured as a function of voltage and over a range of frequencies by fitting the data to the equivalent circuit model. A so-called Mott-Schottky plot is obtained by plotting $1/C_{sc}^2$ against V_a as shown in Figure 2-6. By examining equation 2-3, it is clear that the slope of the line gives the n-Si doping density and the x-intercept

gives the flat-band potential (all other parameters are in the equation are constants or otherwise known values). The black data points in Figure 2-6 are obtained by fitting the data over a wide range of frequencies to the full equivalent circuit in Figure 2-5. However, alternative approaches are also available in most softwares as described in the next paragraph. These alternatives, however, may not be as accurate and should be used with caution or at least be coupled with a more rigorous approach.

Most potentiostat softwares have an automatic single-frequency Mott-Schottky analysis experiment, but in many cases this approach will result in signficant errors in the measured flat-band potentials.[40] This single-frequency approach utilizes a simplified equivalent circuit consisting of either (a) a single resistor and capacitor in series, hence ignoring the parallel resistor in Figure 2-5 or (b) a single resistor and capacitor in parallel hence ignoring the series resistor in Figure 2-5. In many cases with these simplified circuits, the space charge capacitance may not be accurately measured, espcially if other capacitances are present in the system. To achieve accurate results with this single frequency approach, it is essential to carefully choose the single frequency in which the space charge capacitrance dominants the EIS response.[40,43] Using different frequencies without any physical basis will result in significant errors in the measured flat-band potential. Even if the proper frequency is selected, the results can still be inaccurate if other capacitances or resistances also contribute to the EIS response at that frequency. Therefore, it is best practice to perform potentiostatic EIS measurements over a range of frequencies and voltages, and fitting the data to the more rigorous equivalent circuit.[40]

The accuracy of the flat-band potential can be evaluated by comparing the results using the full equivalent circuit and the two simplified circuits. The simplified series circuit provides an upper bound on the measured capacitance, while the simplified parallel circuit provides a

lower bound on the measured capacitance.[44] Therefore, the capacitance (as well as the inverse capacitance squared $1/C_{sc}^2$) that is measured using the full equivalent circuit should be intermediate between these two bounds. In Figure 2-6, the blue and red data points are obtained by fitting to the simplified parallel circuit and the simplified series circuit, respectively. Indeed, the black data points from the full equivalent circuit are with the two bounds. The insert shows a closeup near the x-axis of the Mott-Schottky Plot which demonstrates that all of the methods result in similar flat-band potentials within 20 meV from each other. It is always good practice to verify the accuracy of the Mott-Schottky approach as some systems could result in large inaccuracies.

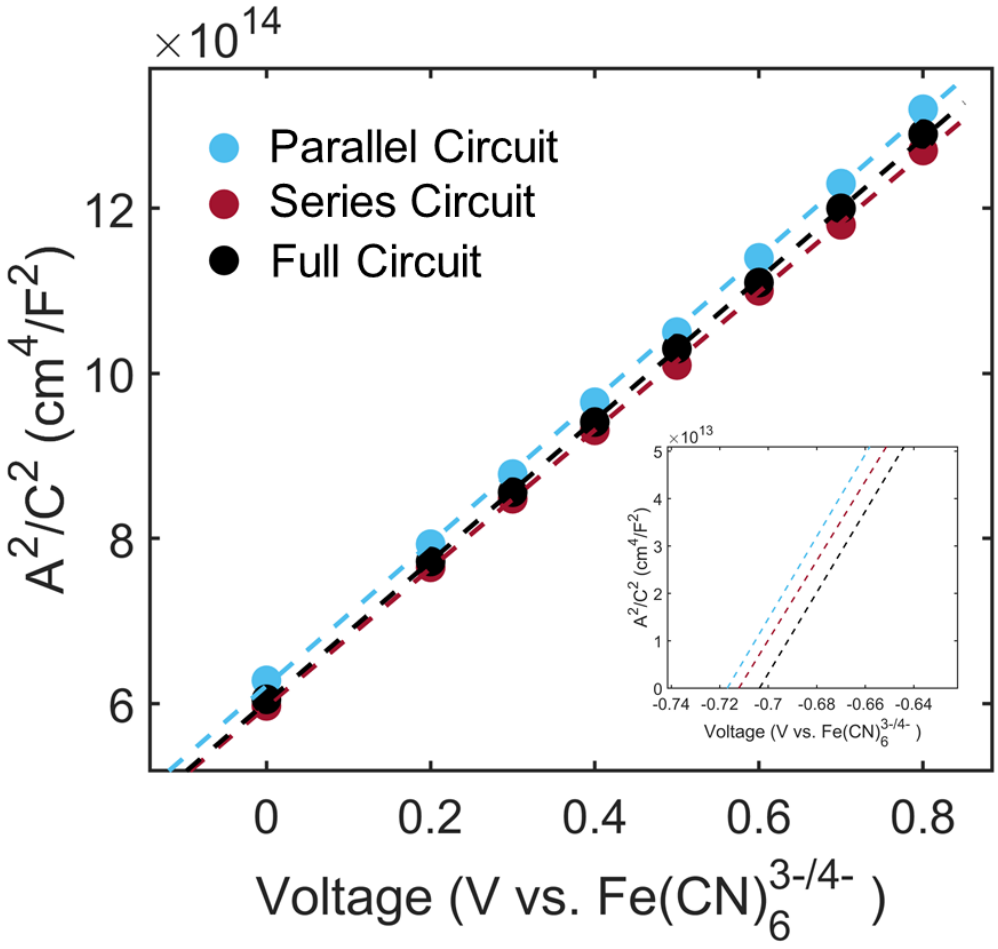

Figure 2-6: Mott-Schottky plots created by fitting the data with different equivalent circuits and frequency ranges for a representative Ir/Al_2O_3/n-Si MIS system. All of the potentiostatic EIS measurements were performed in the dark in

a 10mM/10mM ferri/ferrocyanide electrolyte at 0.1 V intervals between 0–0.8 V versus $Fe(CN)_6^{3-/4-}$. The black data points were obtained by fitting the data to the full equivalent circuit over a frequency range of 50 to 100,000 Hz and an AC voltage of 10 rms mV. The blue and red data points are obtained by fitting to the simplified parallel circuit and the simplified series circuit, respectively. In both cases, the data was fit using a single frequency of 16,000 Hz which corresponds to frequency in which the space charge capacitrance dominants the EIS response.

2.4.7 Varying Light Intensity

Key physical parameters can be extracted by varying the light intensity and observing the resulting photo-limited current and the open-circuit photovoltage. To understand why, a closer look at the physics and equations is necessary. The details are described in more thoroughly in Chapter 4, but in short, it is well known that Si-based photovoltaic and photoelectrochemical devices exhibit current-voltage relationships that follow the diode equation:

$$J_{net} = J_{ph} - J_s \left[exp\left(-\frac{qV_a}{nkT} \right) - 1 \right] \quad 2\text{-}5$$

Here, J_{net} is the net current traveling through the system, J_{ph} is the photocurrent density which is the total hole current generated from solar absorption in the semiconductor (these holes ultimately drive the OER at the electrocatalyst), J_s is the dark reverse saturation current (also called the recombination parameter[45]), q is the elementary charge of an electron (1.6×10^{-19} Coulombs), V_a is the applied voltage defined as the difference between the semiconductor majority-carrier Fermi level and the solution Fermi level (this voltage can be applied using a potentiostat, and it can be replaced by or added to the photovoltage generated upon illuminating the semiconductor), n is the ideality factor (n=1 is ideal, n>1 is non-ideal), k is the Boltzmann constant, and T is the operating temperature.

An analytical expression for the photovoltage (V_{ph}) generated by a semiconductor-based system as a function of the net current (J_{net}) can be easily obtained by rearranging the diode equation:[43,46–48]

$$-V_{ph} \approx \frac{nkT}{q}\left[ln\frac{J_{ph}-J_{net}}{J_s}\right] = \frac{nkT}{q}ln\left(J_{ph}-J_{net}\right) - \frac{nkT}{q}ln(J_s) \quad \text{2-6}$$

Here, the "-1" term is removed from the diode equation because $\frac{J_{ph}-J_{net}}{J_s} \gg 1$ under most relevant conditions for the forward bias of these systems. This is the analytic equation to describe the photovoltage, and it is clear that the photovoltage is dependent on the net current through the system and the maximum photovoltage is obtained when the net current is zero (i.e., at open-circuit). As previously discussion in Section 2.4.4 it is often convenient to evaluate the open-circuit photovoltage (V_{oc}) in which the net current is zero, resulting in the following analytical expression:

$$-V_{oc} = -V_{ph}(J_{net} = 0) \approx \frac{nkT}{q}\left[ln\frac{J_{ph}}{J_s}\right] = \frac{nkT}{q}ln\left(J_{ph}\right) - \frac{nkT}{q}ln(J_s) \quad \text{2-7}$$

From this expression, a plot of V_{oc} vs $ln(J_{ph})$ should yield a line with a slope that is related to the ideality factor and an intercept that is related to the saturation recombination current (J_s).[43,49–55] Varying the light intensity (which in turn varies J_{ph}) and measuring the open-circuit photovoltage at each light intensity therefore allows us to extract the ideality factor and the recombination current from any system. After experimentally measuring J_{ph}, J_s, and n, every parameter in the diode equation is known, and the current-voltage relationship can be modeled, making this a powerful technique.

An FFC solution consisting of 350×10^{-3} M potassium hexacyanoferrate(II) trihydrate, 50×10^{-3} M potassium hexacyanoferrate(III), and 1 M KCl was used for the light intensity experiments. The solution was magnetically stirred to prevent mass transport limitations which could otherwise impact the measured photo-limited current). A graphite reference electrode and Pt wire counter electrode was used. The light intensity was varied using neutral density filters which uniformly attenuate the incident light source over a broad range of wavelengths.[52] Three

neutral density filters were purchased from Newport with optical densities of 0.1, 0.2 and 0.4, and up to two of these filters were placed in series between the sample and the light source to attenuate the intensity of incident light. The light transmission through the neutral density filters is calculated using the following equation:

$$T = 10^{-OD} \quad \text{2-8}$$

Where OD is the optical density of the filter. When two filters are in series, the optical densities are added together. Therefore, the neutral density filters can modulate the light intensity by up to a factor of 4 (i.e., $1/10^{-0.6}$). In typical experiments, the light intensity is modulated between 0.6 Suns (60 mW/cm^2) and 1.5 Suns (150 mW/cm^2). At each light intensity, linear sweep voltammetry was performed with a scan rate of 100 mV s^{-1}. The open-circuit photovoltage was measured before and after each linear sweep for about 60 seconds until stable values were reached.

2.5 Conclusion

This chapter has described fabrication, characterization, and experimental methods that have been prevalently used throughout this dissertation. The goal was to provide a general overview of each of the procedures and techniques and enable a better understanding of how to perform these methods with rigor and accuracy. The following chapters will highlight many of these techniques as they are used for specific applications.

2.6 References

(1) Scheuermann, A. G.; McIntyre, P. C. Atomic Layer Deposited Corrosion Protection: A Path to Stable and Efficient Photoelectrochemical Cells. *J. Phys. Chem. Lett.* **2016**, *7* (14), 2867–2878. https://doi.org/10.1021/acs.jpclett.6b00631.

(2) Ritala, M.; Leskelä, M. Atomic Layer Epitaxy - a Valuable Tool for Nanotechnology? *Nanotechnology* **1999**, *10* (1), 19–24. https://doi.org/10.1088/0957-4484/10/1/005.

(3) Cao, S.; Zhang, Z.; Liao, Q.; Kang, Z.; Zhang, Y. Interface Engineering for High-Performance Photoelectrochemical Cells via Atomic Layer Deposition Technique. *Energy Technol.* **2021**, *9* (2), 2000819. https://doi.org/10.1002/ente.202000819.

(4) Elam, J. W.; Dasgupta, N. P.; Prinz, F. B. ALD for Clean Energy Conversion, Utilization, and Storage. *MRS Bull.* **2011**, *36* (11), 899–906. https://doi.org/10.1557/mrs.2011.265.

(5) Johnson, R. W.; Hultqvist, A.; Bent, S. F. A Brief Review of Atomic Layer Deposition: From Fundamentals to Applications. *Mater. Today* **2014**, *17* (5), 236–246. https://doi.org/10.1016/j.mattod.2014.04.026.

(6) Leskelä, M.; Mattinen, M.; Ritala, M. Review Article: Atomic Layer Deposition of Optoelectronic Materials. *J. Vac. Sci. Technol. B* **2019**, *PAULH2019* (1), 030801. https://doi.org/10.1116/1.5083692@jvb.2019.PAULH2019.issue-1.

(7) Zhao, C.; Xiang, J. Atomic Layer Deposition (ALD) of Metal Gates for CMOS. *Appl. Sci.* **2019**, *9* (11), 2388. https://doi.org/10.3390/app9112388.

(8) Poodt, P.; Cameron, D. C.; Dickey, E.; George, S. M.; Kuznetsov, V.; Parsons, G. N.; Roozeboom, F.; Sundaram, G.; Vermeer, A. Spatial Atomic Layer Deposition: A Route towards Further Industrialization of Atomic Layer Deposition. *J. Vac. Sci. Technol. A* **2012**, *30* (1), 010802. https://doi.org/10.1116/1.3670745.

(9) Handbook of Evaporation Technology - 1st Edition https://www.elsevier.com/books/handbook-of-evaporation-technology/minton/978-0-8155-1097-0 (accessed 2021 -07 -18).

(10) Reimer, L. *Scanning Electron Microscopy*; Hawkes, P. W., Lotsch, H. K. V., Series Eds.; Springer Series in Optical Sciences; Springer Berlin Heidelberg: Berlin, Heidelberg, 1998; Vol. 45. https://doi.org/10.1007/978-3-540-38967-5.

(11) Li, J.; Malis, T.; Dionne, S. Recent Advances in FIB–TEM Specimen Preparation Techniques. *Mater. Charact.* **2006**, *57* (1), 64–70. https://doi.org/10.1016/j.matchar.2005.12.007.

(12) Perkampus, H.-H. *UV-VIS Spectroscopy and Its Applications*; Springer Science & Business Media, 2013.

(13) Nguyen, K. N.; Abi-Saab, D.; Basset, P.; Richalot, E.; Marty, F.; Angelescu, D.; Leprince-Wang, Y.; Bourouina, T. Black Silicon with Sub-Percent Reflectivity: Influence of the 3D Texturization Geometry. In *2011 16th International Solid-State Sensors, Actuators and Microsystems Conference*; 2011; pp 354–357. https://doi.org/10.1109/TRANSDUCERS.2011.5969470.

(14) OPAL 2 https://www2.pvlighthouse.com.au/calculators/opal%202/opal%202.aspx (accessed 2021 -08 -12).

(15) McIntosh, K. R.; Baker-Finch, S. C. OPAL 2: Rapid Optical Simulation of Silicon Solar Cells. In *2012 38th IEEE Photovoltaic Specialists Conference*; 2012; pp 000265–000271. https://doi.org/10.1109/PVSC.2012.6317616.

(16) Ji, S. G.; Kim, H.; Choi, H.; Lee, S.; Choi, C. H. Overestimation of Photoelectrochemical Hydrogen Evolution Reactivity Induced by Noble Metal Impurities Dissolved from Counter/Reference Electrodes. *ACS Catal.* **2020**, *10* (5), 3381–3389. https://doi.org/10.1021/acscatal.9b04229.

(17) Chen, J. G.; Jones, C. W.; Linic, S.; Stamenkovic, V. R. Best Practices in Pursuit of Topics in Heterogeneous Electrocatalysis. *ACS Catal.* **2017**, *7* (9), 6392–6393. https://doi.org/10.1021/acscatal.7b02839.

(18) Wei, R.; Fang, M.; Dong, G.; Ho, J. C. Is Platinum a Suitable Counter Electrode Material for Electrochemical Hydrogen Evolution Reaction? *Sci. Bull.* **2017**, *62* (14), 971–973. https://doi.org/10.1016/j.scib.2017.06.006.

(19) Chen, R.; Yang, C.; Cai, W.; Wang, H.-Y.; Miao, J.; Zhang, L.; Chen, S.; Liu, B. Use of Platinum as the Counter Electrode to Study the Activity of Nonprecious Metal Catalysts for the Hydrogen Evolution Reaction. *ACS Energy Lett.* **2017**, *2* (5), 1070–1075. https://doi.org/10.1021/acsenergylett.7b00219.

(20) Ji, S. G.; Kim, H.; Park, C.; Kim, W.; Choi, C. H. Underestimation of Platinum Electrocatalysis Induced by Carbon Monoxide Evolved from Graphite Counter Electrodes. *ACS Catal.* **2020**, *10* (18), 10773–10783. https://doi.org/10.1021/acscatal.0c01783.

(21) Stevens, M. B.; Enman, L. J.; Batchellor, A. S.; Cosby, M. R.; Vise, A. E.; Trang, C. D. M.; Boettcher, S. W. Measurement Techniques for the Study of Thin Film Heterogeneous Water Oxidation Electrocatalysts. *Chem. Mater.* **2017**, *29* (1), 120–140. https://doi.org/10.1021/acs.chemmater.6b02796.

(22) Garcia, A. C.; Koper, M. T. M. Effect of Saturating the Electrolyte with Oxygen on the Activity for the Oxygen Evolution Reaction. *ACS Catal.* **2018**, *8* (10), 9359–9363. https://doi.org/10.1021/acscatal.8b01447.

(23) Chen, Z.; Dinh, H. N.; Miller, E. *Photoelectrochemical Water Splitting*; SpringerBriefs in Energy; Springer New York: New York, NY, 2013. https://doi.org/10.1007/978-1-4614-8298-7.

(24) Chen, Z.; Jaramillo, T. F.; Deutsch, T. G.; Kleiman-Shwarsctein, A.; Forman, A. J.; Gaillard, N.; Garland, R.; Takanabe, K.; Heske, C.; Sunkara, M.; McFarland, E. W.; Domen, K.; Miller, E. L.; Turner, J. A.; Dinh, H. N. Accelerating Materials Development for Photoelectrochemical Hydrogen Production: Standards for Methods, Definitions, and Reporting Protocols. *J. Mater. Res.* **2010**, *25* (1), 3–16. https://doi.org/10.1557/JMR.2010.0020.

(25) Gao, R.; Yan, D. Recent Development of Ni/Fe-Based Micro/Nanostructures toward Photo/Electrochemical Water Oxidation. *Adv. Energy Mater. 0* (0), 1900954. https://doi.org/10.1002/aenm.201900954.

(26) McCrory, C. C. L.; Jung, S.; Peters, J. C.; Jaramillo, T. F. Benchmarking Heterogeneous Electrocatalysts for the Oxygen Evolution Reaction. *J. Am. Chem. Soc.* **2013**, *135* (45), 16977–16987. https://doi.org/10.1021/ja407115p.

(27) Jung, S.; L. McCrory, C. C.; M. Ferrer, I.; C. Peters, J.; F. Jaramillo, T. Benchmarking Nanoparticulate Metal Oxide Electrocatalysts for the Alkaline Water Oxidation Reaction. *J. Mater. Chem. A* **2016**, *4* (8), 3068–3076. https://doi.org/10.1039/C5TA07586F.

(28) Wei, C.; Rao, R. R.; Peng, J.; Huang, B.; Stephens, I. E. L.; Risch, M.; Xu, Z. J.; Shao-Horn, Y. Recommended Practices and Benchmark Activity for Hydrogen and Oxygen Electrocatalysis in Water Splitting and Fuel Cells. *Adv. Mater.* **2019**, *31* (31), 1806296. https://doi.org/10.1002/adma.201806296.

(29) Fan, R.; Mi, Z.; Shen, M. Silicon Based Photoelectrodes for Photoelectrochemical Water Splitting. *Opt. Express* **2019**, *27* (4), A51–A80. https://doi.org/10.1364/OE.27.000A51.

(30) Walter, M. G.; Warren, E. L.; McKone, J. R.; Boettcher, S. W.; Mi, Q.; Santori, E. A.; Lewis, N. S. Solar Water Splitting Cells. *Chem. Rev.* **2010**, *110* (11), 6446–6473. https://doi.org/10.1021/cr1002326.

(31) Scheuermann, A. G.; Chidsey, C. E. D.; McIntyre, P. C. Understanding Photovoltage in Insulator-Protected Water Oxidation Half-Cells. *J. Electrochem. Soc.* **2016**, *163* (3), H192–H200. https://doi.org/10.1149/2.0601603jes.

(32) Görlin, M.; Chernev, P.; Ferreira de Araújo, J.; Reier, T.; Dresp, S.; Paul, B.; Krähnert, R.; Dau, H.; Strasser, P. Oxygen Evolution Reaction Dynamics, Faradaic Charge Efficiency, and the Active Metal Redox States of Ni–Fe Oxide Water Splitting Electrocatalysts. *J. Am. Chem. Soc.* **2016**, *138* (17), 5603–5614. https://doi.org/10.1021/jacs.6b00332.

(33) Anantharaj, S.; Kundu, S. Do the Evaluation Parameters Reflect Intrinsic Activity of Electrocatalysts in Electrochemical Water Splitting? *ACS Energy Lett.* **2019**, *4* (6), 1260–1264. https://doi.org/10.1021/acsenergylett.9b00686.

(34) Bredar, A. R. C.; Chown, A. L.; Burton, A. R.; Farnum, B. H. Electrochemical Impedance Spectroscopy of Metal Oxide Electrodes for Energy Applications. *ACS Appl. Energy Mater.* **2020**, *3* (1), 66–98. https://doi.org/10.1021/acsaem.9b01965.

(35) *Electrochemical Impedance Spectroscopy*, 1st ed.; John Wiley & Sons, Ltd, 2017. https://doi.org/10.1002/9781119363682.

(36) Lopes, T.; Andrade, L.; Ribeiro, H. A.; Mendes, A. Characterization of Photoelectrochemical Cells for Water Splitting by Electrochemical Impedance Spectroscopy. *Int. J. Hydrog. Energy* **2010**, *35* (20), 11601–11608. https://doi.org/10.1016/j.ijhydene.2010.04.001.

(37) Lopes, T.; Andrade, L.; Formal, F. L.; Gratzel, M.; Sivula, K.; Mendes, A. Hematite Photoelectrodes for Water Splitting: Evaluation of the Role of Film Thickness by Impedance Spectroscopy. *Phys. Chem. Chem. Phys.* **2014**, *16* (31), 16515–16523. https://doi.org/10.1039/C3CP55473B.

(38) *Physics of Semiconductor Devices*, 1st ed.; John Wiley & Sons, Ltd, 2006. https://doi.org/10.1002/0470068329.

(39) Moniri, S.; Van Cleve, T.; Linic, S. Pitfalls and Best Practices in Measurements of the Electrochemical Surface Area of Platinum-Based Nanostructured Electro-Catalysts. *J. Catal.* **2017**, *345*, 1–10. https://doi.org/10.1016/j.jcat.2016.11.018.

(40) Hankin, A.; E. Bedoya-Lora, F.; C. Alexander, J.; Regoutz, A.; H. Kelsall, G. Flat Band Potential Determination: Avoiding the Pitfalls. *J. Mater. Chem. A* **2019**, *7* (45), 26162–26176. https://doi.org/10.1039/C9TA09569A.

(41) Natu, G.; Hasin, P.; Huang, Z.; Ji, Z.; He, M.; Wu, Y. Valence Band-Edge Engineering of Nickel Oxide Nanoparticles via Cobalt Doping for Application in p-Type Dye-Sensitized Solar Cells. *ACS Appl. Mater. Interfaces* **2012**, *4* (11), 5922–5929. https://doi.org/10.1021/am301565j.

(42) Potentiostat/Electrochemical Instrument Software for Gamry Instruments https://www.gamry.com/support/software/ (accessed 2021 -07 -18).

(43) Hemmerling, J.; Quinn, J.; Linic, S. Quantifying Losses and Assessing the Photovoltage Limits in Metal–Insulator–Semiconductor Water Splitting Systems. *Adv. Energy Mater.* **2020**, *10* (12), 1903354. https://doi.org/10.1002/aenm.201903354.

(44) Newman, N.; van Schilfgaarde, M.; Kendelwicz, T.; Williams, M. D.; Spicer, W. E. Electrical Study of Schottky Barriers on Atomically Clean GaAs(110) Surfaces. *Phys. Rev. B* **1986**, *33* (2), 1146–1159. https://doi.org/10.1103/PhysRevB.33.1146.

(45) Cuevas, A. The Recombination Parameter J0. *Energy Procedia* **2014**, *55*, 53–62. https://doi.org/10.1016/j.egypro.2014.08.073.

(46) Quinn, J.; Hemmerling, J.; Linic, S. Maximizing Solar Water Splitting Performance by Nanoscopic Control of the Charge Carrier Fluxes across Semiconductor–Electrocatalyst Junctions. *ACS Catal.* **2018**, *8* (9), 8545–8552. https://doi.org/10.1021/acscatal.8b01929.

(47) Digdaya, I. A.; Trześniewski, B. J.; Adhyaksa, G. W. P.; Garnett, E. C.; Smith, W. A. General Considerations for Improving Photovoltage in Metal–Insulator–Semiconductor Photoanodes. *J. Phys. Chem. C* **2018**, *122* (10), 5462–5471. https://doi.org/10.1021/acs.jpcc.7b11747.

(48) Card, H. C.; Rhoderick, E. H. Studies of Tunnel MOS Diodes I. Interface Effects in Silicon Schottky Diodes. *J. Phys. Appl. Phys.* **1971**, *4* (10), 1589. https://doi.org/10.1088/0022-3727/4/10/319.

(49) Hill, J. C.; Landers, A. T.; Switzer, J. A. An Electrodeposited Inhomogeneous Metal–Insulator–Semiconductor Junction for Efficient Photoelectrochemical Water Oxidation. *Nat. Mater.* **2015**, *14* (11), 1150–1155. https://doi.org/10.1038/nmat4408.

(50) V. Esposito, D.; Lee, Y.; Yoon, H.; M. Haney, P.; Y. Labrador, N.; P. Moffat, T.; Alec Talin, A.; A. Szalai, V. Deconvoluting the Influences of 3D Structure on the Performance of Photoelectrodes for Solar-Driven Water Splitting. *Sustain. Energy Fuels* **2017**, *1* (1), 154–173. https://doi.org/10.1039/C6SE00073H.

(51) Yul Lim, S.; Ha, K.; Ha, H.; Youn Lee, S.; Seok Jang, M.; Choi, M.; Dong Chung, T. Three-Dimensionally Patterned Ag–Pt Alloy Catalyst on Planar Si Photocathodes for Photoelectrochemical H 2 Evolution. *Phys. Chem. Chem. Phys.* **2019**, *21* (8), 4184–4192. https://doi.org/10.1039/C8CP07304J.

(52) Moreno-Hernandez, I. A.; Brunschwig, B. S.; Lewis, N. S. Tin Oxide as a Protective Heterojunction with Silicon for Efficient Photoelectrochemical Water Oxidation in Strongly Acidic or Alkaline Electrolytes. *Adv. Energy Mater.* **2018**, *8* (24), 1801155. https://doi.org/10.1002/aenm.201801155.

(53) Khan, F.; Singh, S. N.; Husain, M. Effect of Illumination Intensity on Cell Parameters of a Silicon Solar Cell. *Sol. Energy Mater. Sol. Cells* **2010**, *94* (9), 1473–1476. https://doi.org/10.1016/j.solmat.2010.03.018.

(54) Tress, W.; Yavari, M.; Domanski, K.; Yadav, P.; Niesen, B.; Baena, J. P. C.; Hagfeldt, A.; Graetzel, M. Interpretation and Evolution of Open-Circuit Voltage, Recombination, Ideality Factor and Subgap Defect States during Reversible Light-Soaking and Irreversible Degradation of Perovskite Solar Cells. *Energy Environ. Sci.* **2018**, *11* (1), 151–165. https://doi.org/10.1039/C7EE02415K.

(55) Meyer, E. L. Extraction of Saturation Current and Ideality Factor from Measuring Voc and Isc of Photovoltaic Modules https://www.hindawi.com/journals/ijp/2017/8479487/ (accessed 2019 -11 -15). https://doi.org/10.1155/2017/8479487.

Chapter 3

Quantifying Performance and Assessing the Photovoltage Limits of MIS Water Splitting Photoelectrocatalysts

3.1 Introduction

As previously discussed in Chapter 1, MIS water splitting photoelectrocatalysts are promising multicomponent systems to achieve efficient and stable solar water splitting. Initially, the performance of insulators was mainly evaluated in the context of their ability to improve the chemical stability of semiconductors by physically separating it from the corrosive electrolyte.[1] Previous work in the group has demonstrated that the thickness of the insulator is a critical design parameter which can be tuned to maximize the photovoltage.[2,3] For example, we have shown that the thickness of the HfO_2 tunnel insulator significantly impacts the photovoltage generated by Ni/HfO_2/n-Si MIS system in photoelectrocatalytic water oxidation.[2] We demonstrated that by tuning the thickness of the HfO_2 insulator, we can tune the flux of minority and majority charge carriers from the semiconductor to the electrocatalyst and therefore minimize the rate of charge recombination and maximize the photovoltage.

This chapter focuses on analyzing and quantifying the underlying mechanisms by which the thickness of an insulator impacts the performance of the MIS photoelectrocatalysts. We performed our studies by focusing on a concrete example of an Ir/HfO_2/n-Si MIS system for the oxygen evolution reaction (OER). The HfO_2 insulator is thermodynamically stable under water oxidation conditions in alkaline electrolyte based on the Pourbaix diagrams,[4] and the HfO_2 insulator layer thickness is precisely controlled using atomic layer deposition. Each of the key

characterization and experimental processes are outlined to fully understand and quantify the critical parameters and properties of the metal, insulator, and semiconductor as well as their interfaces. These include the photovoltage, metal work function, insulator thickness, semiconductor doping density, ideality factor, flat-band potential, and overall stability. We find that while the insulator thickness controls the flux of charge carriers from the semiconductor to the electrocatalysts (and therefore controls the charge recombination), which can be very beneficial to improve photovoltage, the introduction of additional interfaces in the system can simultaneously result in nonidealities which can increase parasitic electron/hole recombination and decrease photovoltage in the system. Despite experimentally optimizing the thickness of the HfO_2 insulator, the photovoltage generated by the photoelectrocatalysts is far below the upper performance limit, meaning there are paths for further optimization. The experimental protocols, when combined with the theory and modeling in Chapter 4, enables a complete understanding of MIS systems and design guidelines to optimize the performance. The strategy is general to other water splitting systems and provides insights to further optimize the photovoltage for water splitting applications.

3.2 MIS System Fabrication and Characterization

The MIS systems consisted of n-type silicon (n-Si) or degenerately doped p^+-Si covered by HfO_2 that was deposited using atomic layer deposition (ALD). The thickness of the insulator HfO_2 layer was controlled by varying the number of ALD cycles from 0 to 25 resulting in 0-3 nm thick HfO_2. ALD is a widely used method to deposit pinhole-free, uniform layers with sub-nanometer precision.[5,6] After the HfO_2 deposition, a 3.5 nm Ir layer was deposited by direct current magnetron sputtering. Further details of the fabrication are provided in the Experimental Section.

To characterize the MIS samples, we performed scanning transmission electron microscopy (STEM) on cross sections of the Ir/HfO_2/n-Si samples as shown in Figure 3-1. The cross-sectional images show clearly identifiable components of the layered nanostructures and defined boundaries between the different components. Data in Figure 3-1e shows the HfO_2 thickness as a function of the ALD cycles used in the fabrication process. On average one ALD cycle results in ~0.1 nm of deposited HfO_2. While the native SiO_2 layer on Si was etched away prior to HfO_2 deposition, an adventitious SiO_2 layer may form during ~5-minute exposure to atmosphere prior to ALD. The SiO_2 layer is evident from the ~0.5 nm white layer between the Si and HfO_2. This layer was similar for all samples so its effect should be uniform among samples.

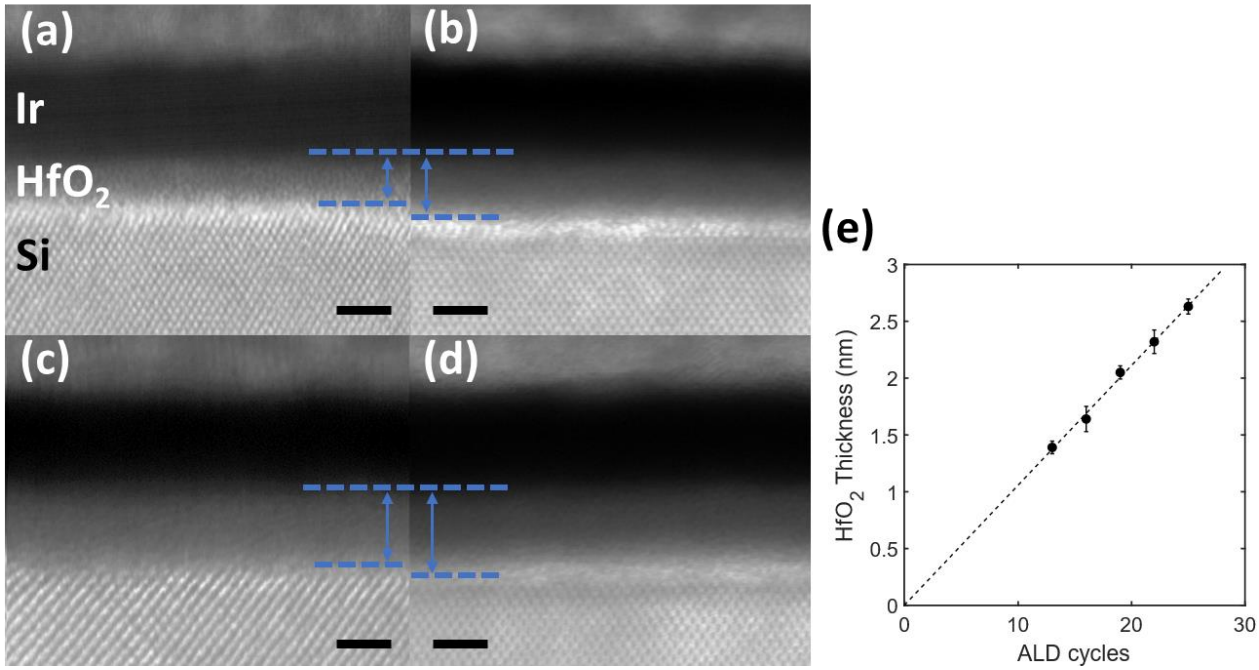

Figure 3-1. Characterization of 3.5 nm-Ir/x- HfO_2/n-Si. Cross-sectional STEM images for (a) 16 cycles (1.6 nm) HfO_2, (b) 19 cycles (2.0 nm) HfO_2, (c) 22 cycles (2.3 nm) HfO_2, and (d) 25 cycles (2.6 nm) HfO_2. The blue dashed lines mark the boundaries between the HfO_2 and the metal and semiconductor. The blue arrows represent the thickness of the HfO_2 layer. The black scale bars are 2 nm. (e) HfO_2 thicknesses as a function of the number of HfO_2 ALD cycles.

3.2.1 Insulator Uniformity

The lower magnification STEM image in Figure 3-2a shows that the insulator thickness is uniform over a wide region and that there are no obvious pinholes of gaps in the insulator, which is important for the performance and stability. However, even the low magnification image represents a very small fraction of the sample, and so further investigations were performed to analyze the insulator uniformity. In general, ALD is a widely-recognized method to deposit pinhole-free, conformal layers with sub-nanometer precision.[5,6] Many papers in the water splitting literature have reported ALD of insulator layers in the 1-3 nm range, and no evidence of pinholes has been found for TiO_2,[5,7] Al_2O_3,[3,8,9] and HfO_2[2,10]. To further support this point, we performed cyclic voltammetry on unmodified n-Si, and on a sample with 19 cycles of HfO_2 deposited on n-Si without a metal layer (Figure 3-2). The current density of the unmodified n-Si was ~1000 times higher than the HfO_2 sample indicating that the HfO_2 sufficiently protects the underlying Si. If pinholes were present, the electrolyte would quickly travel through the pinholes causing an increased and unstable current. Upon cycling the HfO_2 sample, the current remained low and stable, so the presence of pinholes is negligible.

Despite the fact that STEM cross-sections cover a small portion of a given sample, we expect the insulator layer to be quite uniform throughout and therefore even small samples can be a good representative for the entire wafer.[5,10] This is because for a given HfO_2 thickness deposited on a wafer, the photovoltage was evaluated from multiple pieces throughout the wafer, and only a few mV photovoltage variation is obtained. Even small variations in HfO_2 thickness would significantly change the photovoltage (as discussed in the next section). Therefore, we conclude the HfO_2 thickness obtained from STEM cross-sections is representative throughout the wafer and that the HfO_2 thickness is uniform throughout the wafer.

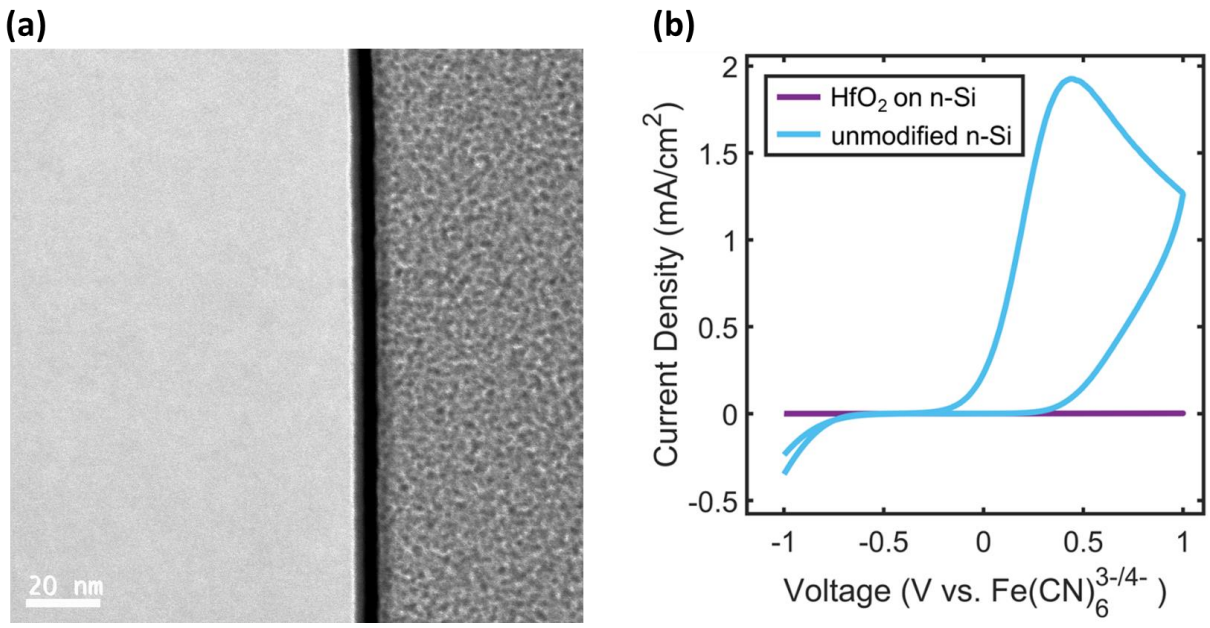

Figure 3-2: (a) Lower magnification image of the 3.5 nm-Ir/2.3 nm- HfO_2/n-Si sample showing the clear, uniform layers over a wide area. From left to right, the layers are the thick Silicon substrate, thin 0.5nm SiO_2, 2.3 nm HfO_2, 3.5 nm Ir, thick Pt glue/protection. CVs performed in 10/10 mM FFC under 1 sun illumination for an unmodified n-Si sample, and on a sample with 2 nm HfO_2 deposited on n-Si without a metal layer.

3.3 Cyclic Voltammetry to Evaluate Photovoltage and Stability

To evaluate the performance of these MIS materials in photocatalytic OER, we performed cyclic voltammetry (CV) measurements in a three-electrode setup under 1 sun illumination in an oxygen-saturated 1 M KOH electrolyte (Figure 3-3a). Additional CV measurements were performed in 1 M KCl and 10/10 mM Ferri/Ferrocyanide (FFC), measuring the reduction and oxidation of the FFC redox couple (Figure 3-3b).

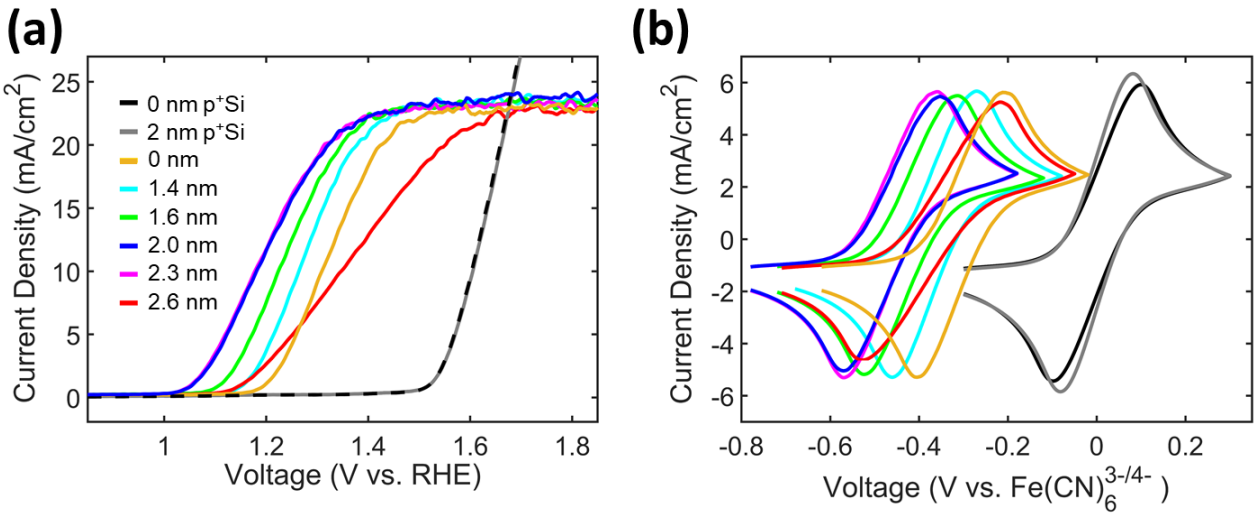

Figure 3-3. Electrochemical testing of the 3.5 nm-Ir /x-HfO_2/n-Si and 3.5 nm-Ir /x-HfO_2/ p^+-Si samples. (a) CV curves upon 1 sun illumination in 1 M KOH. (b) CVs upon 1 sun illumination in 10/10 mM FFC and 1 M KCl. The legend in (a) also corresponds to the CVs in (b).

For OER experiments in KOH experiments, the photovoltage is defined as the difference between the voltage at a current of 1 mA cm^{-2} for the illuminated n-Si samples and the voltage at a current of 1 mA cm^{-2} for the dark p^+-Si control system. For FFC experiments, the photovoltage is defined as the difference between the open-circuit voltage (the voltage when the net current is 0 mA cm^{-2}) of the n-Si and p^+-Si samples. As shown in Figure 3-4, the photovoltages measured from both methods in KOH and FFC are similar for a given HfO_2 thickness. The data show that the photovoltage improves considerably as the HfO_2 thickness increases from 0-19 HfO_2 ALD cycles (0-2.0 nm), plateaus between 19-22 cycles (2.0-2.3 nm), and decreases for greater thickness. Specifically, the photovoltage increases by 160 mV, from 330 mV for 0 nm HfO_2 to 490 mV for 2.0 nm HfO_2.

The photovoltage loss for the thickest 2.6 nm HfO_2 sample is due to an additional resistance to charge transfer attributed to the thicker insulator layer, i.e., the resistance to tunneling through the insulator becomes large enough to limit the charge transfer rate. The

resistance is evident by the lower slope and fill factor in Figure 3-3a and the wider peak to peak splitting in Figure 3-3b. For 0-22 cycle HfO_2 samples, the slopes and peak to peak splitting are similar, which indicates that these samples are in a thickness regime where the tunneling resistance is not the dominant loss in these systems. We also note that the performance of p^+-Si with 0 and 19 cycles of HfO_2 are nearly identical, which further suggests that a thin HfO_2 layer does not significantly affect the series resistance. In the next chapter, we provide the theoretical explanation for this HfO_2 thickness-dependent photovoltage and volcano relationship, which has also been reported in our group's previous work.[2,10]

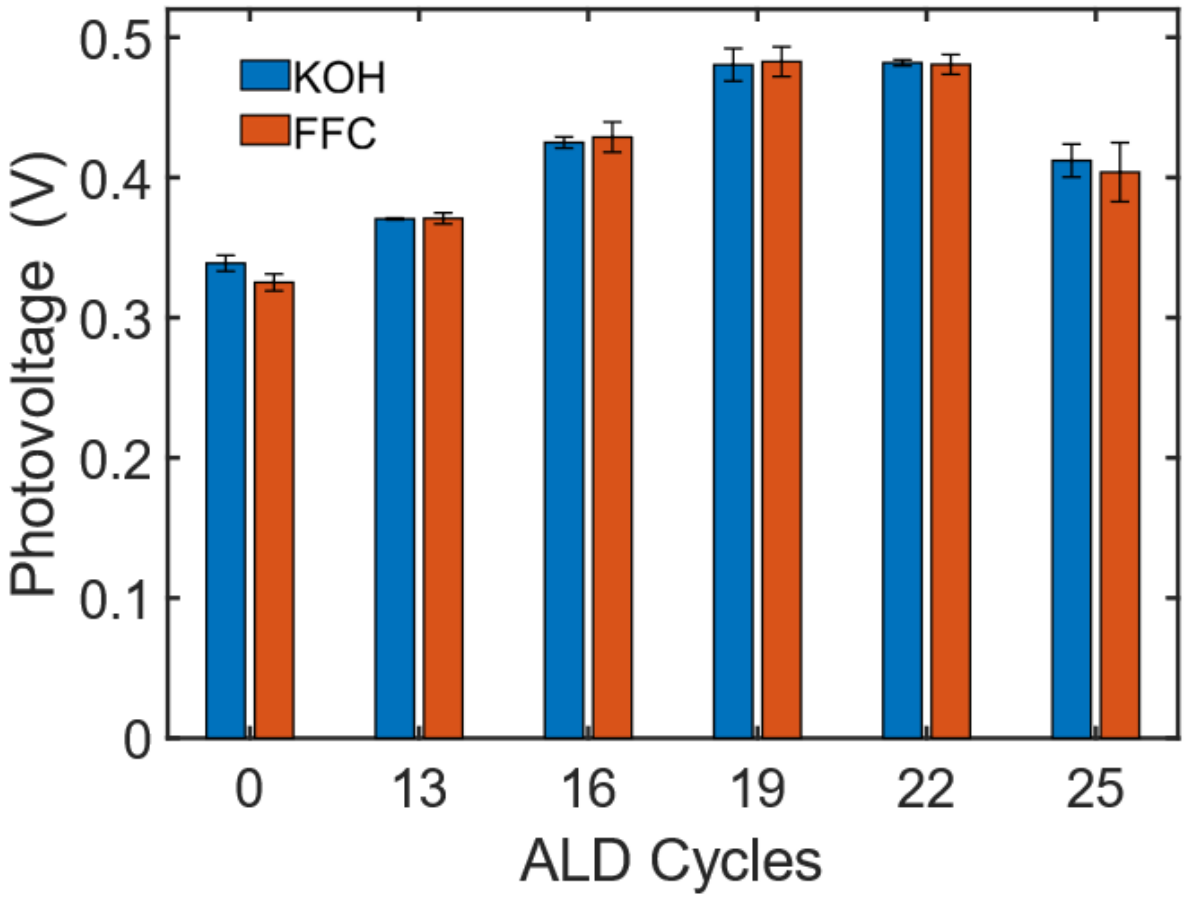

Figure 3-4: Photovoltage measured at 1 mA cm^{-2} in KOH and measured at open-circuit potential in FFC for 3.5 nm-Ir /x-HfO_2/n-Si MIS systems.

3.4 Electrochemical Impedance Spectroscopy to Evaluate Flat-band Potential

The above results have demonstrated significant photovoltage improvements by tuning the thickness of the HfO_2 insulator layer. The question is what are the upper photovoltage limits of these MIS systems and how do the measured photovoltages compare to the fundamental performance limits of these MIS systems? To answer this question, we use EIS to evaluate the flat-band potential, which is the upper photovoltage limit for these systems (as described in more detail in Chapter 4).

More details were provided in Chapter 2, but in short, the impedance measurements were performed in 10/10 mM FFC and 1 M KCl at different applied potentials. A representative example of an EIS Bode plot and Nyquist plot for the 19 cycle sample at 0.3 V vs $Fe(CN)_6^{3-/4-}$ is shown in Figure 3-5. The fitting occurs in a frequency range of 3000-200,000 Hz which is the region dominated by the capacitive response (phase angle close to -90 degrees).[3,11] Frequencies lower than 3000 Hz resulted in deviations from the characteristic semicircle shape in the Nyquist plot, indicating surface states may be influencing the capacitance for these lower frequencies. By performing EIS at higher frequencies, the surface states cannot generate significant capacitance or influence the calculated barrier height, i.e., at these frequencies the surface states are not charged or discharged.[12] Therefore, the capacitance associated with surface states can be ignored while the capacitance of the space-charge region in the semiconductor can be quantified.

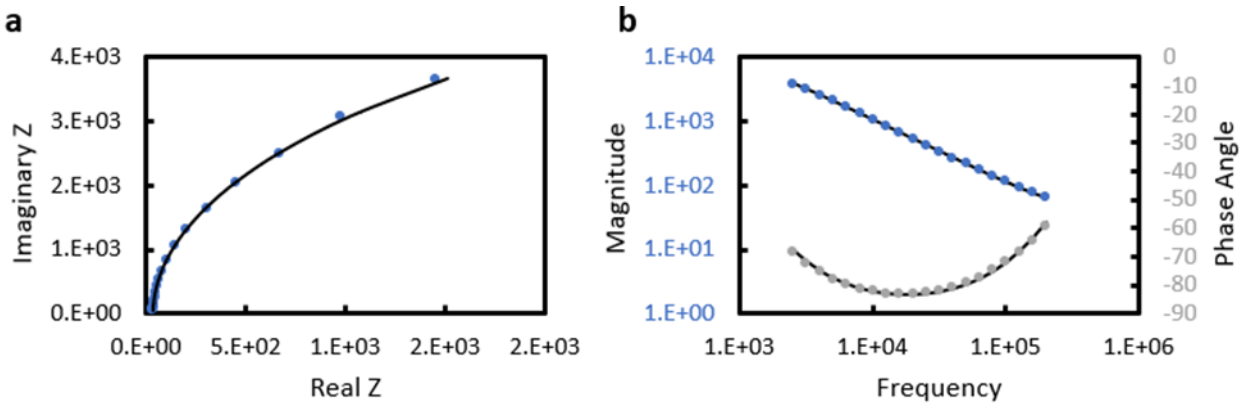

Figure 3-5: Representative Nyquist plot (a) and Bode plot (b) for the 3.5 nm-Ir/2.0 nm-HfO_2/n-Si sample at 0.3 V vs $Fe(CN)_6^{3-/4-}$ measured in the frequency range of 3000-200,000 Hz in 10/10 mM FFC. The data points are the experimental values, and the black lines are the corresponding fits using the equivalent circuit.

The capacitance of the space charge (band bending) region (C_{sc}) in the semiconductor is given by the Mott-Schottky equation:

$$\left(\frac{1}{C_{sc}}\right)^2 = \frac{2}{\varepsilon_0 \varepsilon_s A^2 q N_D}\left(V_a - V_{fb} - \frac{kT}{q}\right) \qquad 3\text{-}1$$

Here, A is the surface area of the junction, ε_0 is the vacuum permittivity, ε_s is the semiconductor relative permittivity, N_D is the doping density of the semiconductor, V_a is the applied voltage, and V_{fb} is the flat-band potential. V_{fb}, also known as the built-in potential is ideally defined by the difference between the Fermi levels of the semiconductor and the metal before contact or equilibration. As further discussed in the next chapter, V_{fb} is the upper limit to the photovoltage that a system can generate in the limit of zero recombination.

A Mott-Schottky plot for systems with varied HfO_2 thickness is obtained by plotting $1/C_{sc}^2$ against V_a as shown in Figure 3-6a. The slope of the line gives the n-Si doping density and the x-intercept gives the flat-band potential. The extracted values for V_{fb} and N_d as a function of HfO_2 thickness are shown in Figure 3-6b. Both variables are essentially independent of HfO_2

thickness which is expected given that these parameters are governed by the semiconductor and metal properties, not the insulator properties.

The observed range of the doping density determined from the slope of the Mott-Schottky plots is consistent with the manufacturer's specifications. The small variation in N_D results in a Si Fermi level change of less than 10 mV, so it affects the calculated values of the photovoltages by less than 1.5%. The accuracy of the technique was also evaluated by comparing the doping density extracted from Mott-Schottky plots with the doping density extracted from four-point probe measurements. The comparison was performed for a sample without HfO_2 (0 cycles) and with HfO_2 (19 cycles). Before any fabrication steps, the resistivity of the pristine Si wafer substrates was measured using a four-point probe, and the resistivity was converted to doping density. After measuring resistivity, the wafers were processed and fabricated like normal. The resulting doping density from the EIS experiments differed from 4-point probe measurements by less than 0.6%. This analysis confirms the experimental accuracy of the Mott-Schottky plots.

The data in Figure 3-6b show that V_{fb} for all Ir/HfO_2/n-Si MIS samples averaged around 630 mV with minimal variation. This means that the maximum theoretical voltage that these MIS systems could achieve is ~630 mV. The photovoltage for the optimal HfO_2 thickness, however, is only about 480 mV (Figure 3-4). These results demonstrate that there are still a total of ~150 mV in losses in the system that could not be addressed by optimizing the insulator thickness.

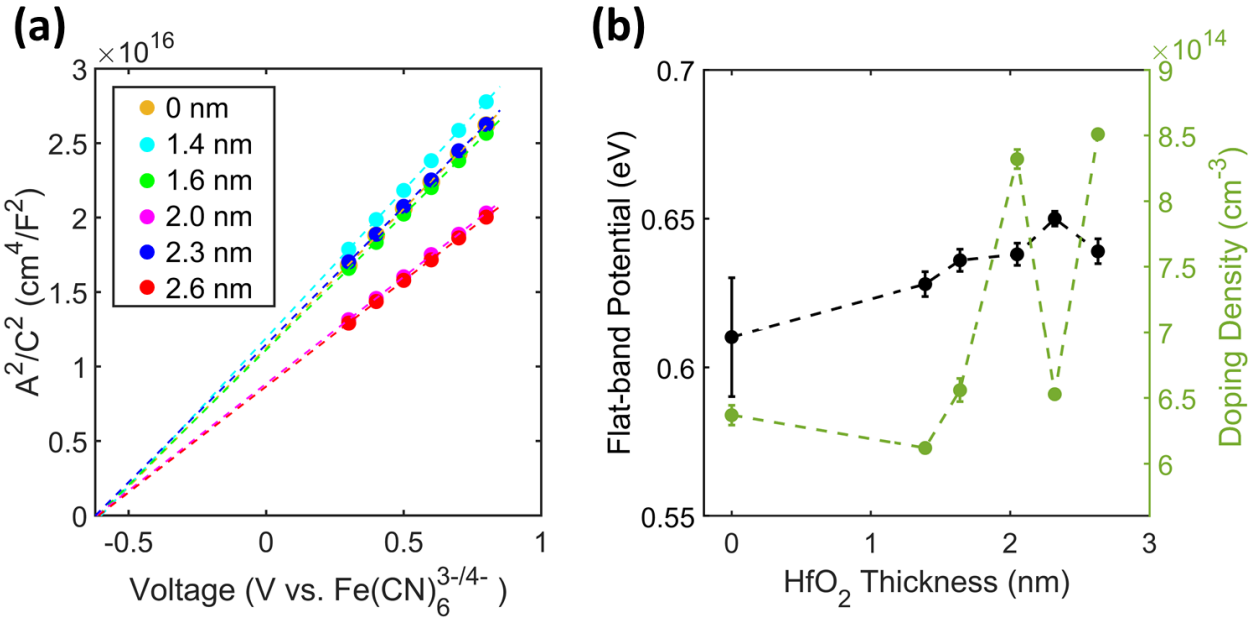

Figure 3-6: EIS and Mott-Schottky results for the 3.5 nm-Ir/x-HfO_2/n-Si samples in 10/10 mM FFC and 1 M KCl. (a) Mott-Schottky plots showing the linear relationship and the extrapolated intercepts converged to a similar flat-band potential. (b) Values extracted from the Mott-Schottky plot for the flat-band potential and the semiconductor doping density.

3.5 Vary Light Intensity to Evaluate Ideality Factor and Recombination Current

To understand why these systems fail to reach the upper performance limits, we analyzed the impact of the insulator on the ideality factor and recombination current, which can both significantly impact a system's generated photovoltage. As discussed in the next chapter, the ideality factor is a measure of how closely the current-voltage relationship matches the ideal diode equation. This is important because any source of nonidealities could lower the performance of the system and therefore should be identified. To calculate the ideality factor for each HfO_2 thickness, the open-circuit voltage was measured at different light intensities in a ferri/ferrocyanide redox couple (see Chapter 2 for more details about the experiments).[13–16] Figure 3-7a shows the experimental CVs obtained after varying the light intensity, and Figure

3-7b plots the calculated open circuit photovoltage vs the natural log of the photo-limited current density which yields a straight line.

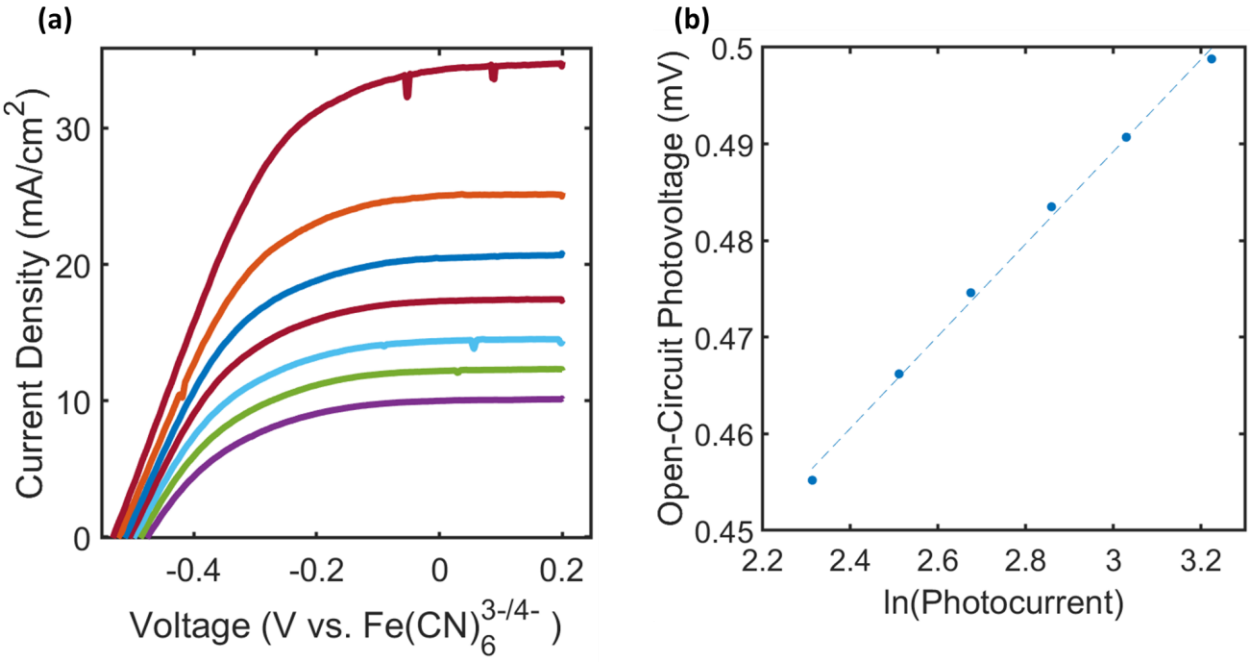

Figure 3-7: a) Cyclic Voltammetry of a Ir/19-HfO_2/n-Si measured in 350/50 mM FFC and 1 M KCl at different light intensities. (b) A plot of the resulting open-circuit photovoltages versus the natural log of the photocurrent density for different light intensities for the same sample.

As discussed in Chapter 2, the slope of this line in Figure 3-7b gives the ideality factor (*n*), and the values for each HfO_2 thickness are plotted in Figure 3-8. If the systems were behaving ideally, then the ideality factor would be equal to 1. However, the ideality factor for all systems is greater than 1, which indicates that there are significant sources of nonidealities in each of the system. Interestingly, the ideality factor increases as the insulator thickness increases, suggesting that the nonidealities are associated with the insulator layer. The theory behind the nonidealities as well as the possible causes of the nonidealities is discussed in Chapter 4.

The reverse saturation recombination current is another important parameter that can be evaluated from the varied light intensity experiments. Also called the recombination parameter, it

is directly related to the recombination rates and therefore governs the generated photovoltage.[17] The theoretical framework for this recombination current is provided Chapter 4, and it can be quantified from the and the x-intercept of the line in Figure 3-7b. The measured values for each HfO_2 thickness are reported in Figure 3-8. It is observed that the recombination current significantly decreases upon introducing the HfO_2 layer which is in line with the increased photovoltage. However, the recombination current is roughly unaffected when the HfO_2 thickness increases from 1.5 to 2.0 nm. Meanwhile, the photovoltage increases by about 110 mV when the HfO_2 thickness increases from 1.5 to 2.0 nm (Figure 3-4). The fact that the photovoltage increases while the reverse saturation recombination current remains roughly the same suggests that the nonidealities (which get increasingly worse for the 2.0 nm HfO_2) are playing a significant role. A deeper understanding of the theory and coupling the theory to these experimental results is critical to acquire a full understanding of these MIS systems, and this is explored in full detail in Chapter 4. Finally, it is noted that the 2.3 nm and 2.6 nm HfO_2 samples are not included in Figure 3-8 because the theoretical equations used in the analysis are not accurate for thicker insulators.[16]

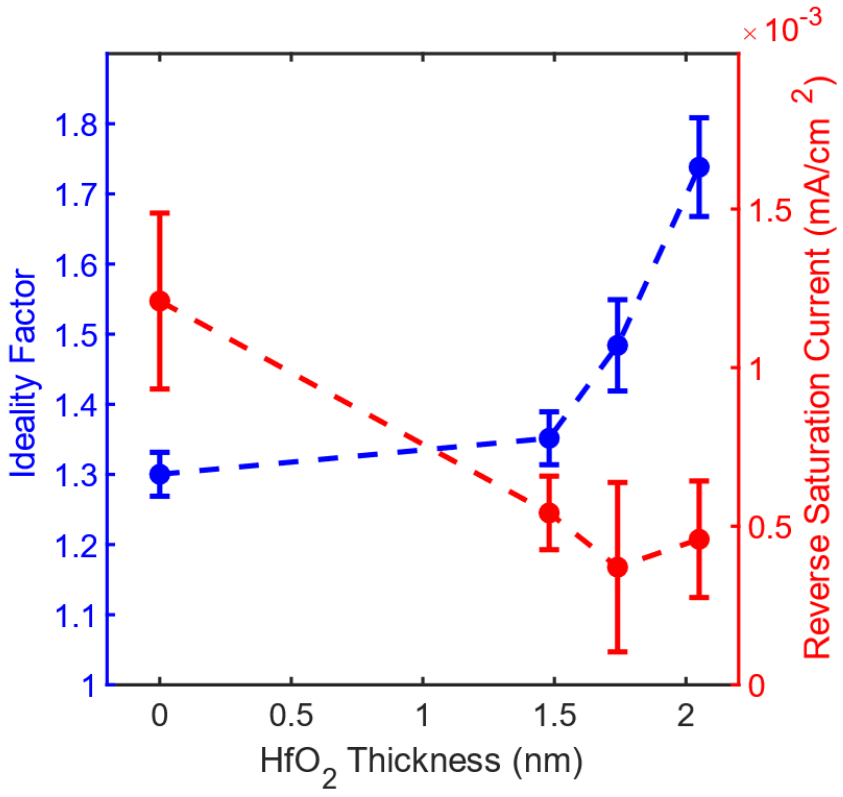

Figure 3-8: Ideality factor and reverse saturation current determined from varying the light intensity for 3.5 nm-Ir/x-HfO_2/n-Si samples.

3.6 Evaluating Stability

Chronoamperometry was used to assess the stability of a 3.5nm-Ir/2.3nm-HfO_2/n-Si sample. The stability test was performed in 1 M KOH under 1 sun illumination and the sample was held at 1.8 V vs RHE. As shown in Figure 3-9, the photocurrent was stable (and slightly increased) over the course of 6 hours with no signs of permanent degradation. Transient drops in the current during the chronoamperometry test are due to the formation and removal of bubbles. LSVs taken every two hours are shown in Figure 3-9. The photovoltage and fill factor remained the same throughout the stability test. The photolimited current slightly increased over time as the Ir layer oxidized to IrO_x which allows more light transmission. The increased oxidation of Ir

over time is evident from the increase in the oxidation peaks just before the onset of oxygen evolution at about 1 V vs RHE. Overall the MIS system shows no signs of performance losses throughoutthe 6 hour stability test, and it even shows some performance enhancements. Long-term (on the order of days to weeks) was outside of the scope of this work, but continued performance without degradation is expected unless the Ir layer completely oxidizes. After this, the HfO_2 is still expected to protect the underlying Si, but the system would be very resistive as IrO_x is less conductive than pure Ir.

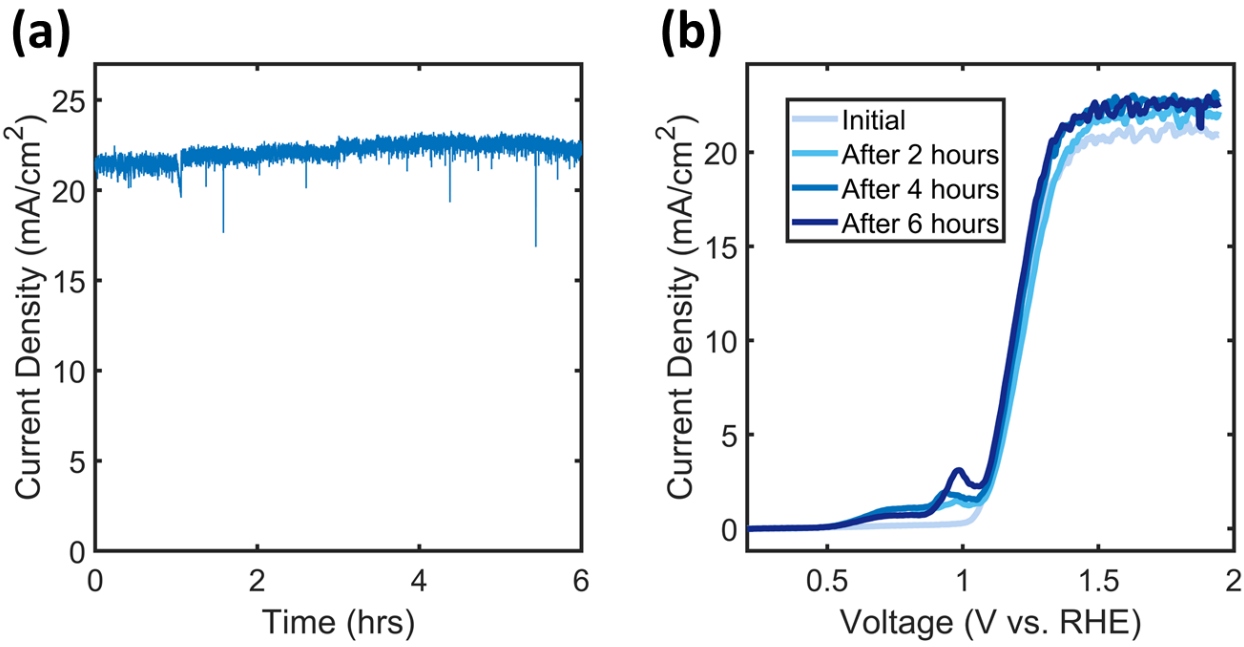

Figure 3-9: Stability tests on the 3.5nm Ir/2.3nm HfO_2/n-Si sample performed in 1 M KOH under 1 sun illumination (a) Chronoamperometry stability test at an applied potential of 1.8 V vs RHE. (b) LSVs at 2-hour intervals showing stable photovoltage and fill factor.

3.7 Conclusions

In summary, this chapter has focused on the accurate and rigorous characterization and electrochemical experimentation of photoelectrocatalysts. The key parameters that were experimentally quantified included the generated photovoltage, metal work function, insulator

thickness, semiconductor doping density, ideality factor, flat-band potential, and overall stability. The experimental analysis demonstrates that tuning the HfO_2 thickness has a net-beneficial effect to enhance the generated photovoltage, but that the introduction of the insulator layer can also result in nonidealities (i.e., ideality factor > 1) which may ultimately lower the performance relative to the upper limit of the flat-band potential. To quantify the voltage losses associated with these nonidealities and other factors, theory and analytical modeling are explored in the next chapter. A deeper understanding of the theory and coupling the theory to these experimental results is critical to acquire a complete picture and develop design principles for MIS photoelectrocatalysts for water splitting.

3.8 References

(1) Hu, S.; Lewis, N. S.; Ager, J. W.; Yang, J.; McKone, J. R.; Strandwitz, N. C. Thin-Film Materials for the Protection of Semiconducting Photoelectrodes in Solar-Fuel Generators. *J. Phys. Chem. C* **2015**, *119* (43), 24201–24228. https://doi.org/10.1021/acs.jpcc.5b05976.

(2) Quinn, J.; Hemmerling, J.; Linic, S. Maximizing Solar Water Splitting Performance by Nanoscopic Control of the Charge Carrier Fluxes across Semiconductor–Electrocatalyst Junctions. *ACS Catal.* **2018**, *8* (9), 8545–8552. https://doi.org/10.1021/acscatal.8b01929.

(3) Digdaya, I. A.; Trześniewski, B. J.; Adhyaksa, G. W. P.; Garnett, E. C.; Smith, W. A. General Considerations for Improving Photovoltage in Metal–Insulator–Semiconductor Photoanodes. *J. Phys. Chem. C* **2018**, *122* (10), 5462–5471. https://doi.org/10.1021/acs.jpcc.7b11747.

(4) Pourbaix, M. *Atlas of Electrochemical Equilibria in Aqueous Solutions*; National Association of Corrosion Engineers, 1974.

(5) G. Scheuermann, A.; D. Prange, J.; Gunji, M.; D. Chidsey, C. E.; C. McIntyre, P. Effects of Catalyst Material and Atomic Layer Deposited TiO 2 Oxide Thickness on the Water Oxidation Performance of Metal–Insulator–Silicon Anodes. *Energy Environ. Sci.* **2013**, *6* (8), 2487–2496. https://doi.org/10.1039/C3EE41178H.

(6) Ritala, M.; Leskelä, M. Atomic Layer Epitaxy - a Valuable Tool for Nanotechnology? *Nanotechnology* **1999**, *10* (1), 19–24. https://doi.org/10.1088/0957-4484/10/1/005.

(7) Scheuermann, A. G.; McIntyre, P. C. Atomic Layer Deposited Corrosion Protection: A Path to Stable and Efficient Photoelectrochemical Cells. *J. Phys. Chem. Lett.* **2016**, *7* (14), 2867–2878. https://doi.org/10.1021/acs.jpclett.6b00631.

(8) Luo, Z.; Liu, B.; Li, H.; Chang, X.; Zhu, W.; Wang, T.; Gong, J. Multifunctional Nickel Film Protected N-Type Silicon Photoanode with High Photovoltage for Efficient and Stable Oxygen Evolution Reaction. *Small Methods 0* (0), 1900212. https://doi.org/10.1002/smtd.201900212.

(9) Digdaya, I. A.; Adhyaksa, G. W. P.; Trześniewski, B. J.; Garnett, E. C.; Smith, W. A. Interfacial Engineering of Metal-Insulator-Semiconductor Junctions for Efficient and Stable Photoelectrochemical Water Oxidation. *Nat. Commun.* **2017**, *8*, 15968. https://doi.org/10.1038/ncomms15968.

(10) Quinn, J.; Hemmerling, J.; Linic, S. Guidelines for Optimizing the Performance of Metal–Insulator–Semiconductor (MIS) Photoelectrocatalytic Systems by Tuning the Insulator Thickness. *ACS Energy Lett.* **2019**, *4* (11), 2632–2638. https://doi.org/10.1021/acsenergylett.9b01609.

(11) Lin, F.; Bachman, B. F.; Boettcher, S. W. Impact of Electrocatalyst Activity and Ion Permeability on Water-Splitting Photoanodes. *J. Phys. Chem. Lett.* **2015**, *6* (13), 2427–2433. https://doi.org/10.1021/acs.jpclett.5b00904.

(12) Altındal, Ş.; Karadeniz, S.; Tuğluoğlu, N.; Tataroğlu, A. The Role of Interface States and Series Resistance on the I–V and C–V Characteristics in Al/SnO2/p-Si Schottky Diodes. *Solid-State Electron.* **2003**, *47* (10), 1847–1854. https://doi.org/10.1016/S0038-1101(03)00182-5.

(13) Hill, J. C.; Landers, A. T.; Switzer, J. A. An Electrodeposited Inhomogeneous Metal–Insulator–Semiconductor Junction for Efficient Photoelectrochemical Water Oxidation. *Nat. Mater.* **2015**, *14* (11), 1150–1155. https://doi.org/10.1038/nmat4408.

(14) V. Esposito, D.; Lee, Y.; Yoon, H.; M. Haney, P.; Y. Labrador, N.; P. Moffat, T.; Alec Talin, A.; A. Szalai, V. Deconvoluting the Influences of 3D Structure on the Performance of Photoelectrodes for Solar-Driven Water Splitting. *Sustain. Energy Fuels* **2017**, *1* (1), 154–173. https://doi.org/10.1039/C6SE00073H.

(15) Yul Lim, S.; Ha, K.; Ha, H.; Youn Lee, S.; Seok Jang, M.; Choi, M.; Dong Chung, T. Three-Dimensionally Patterned Ag–Pt Alloy Catalyst on Planar Si Photocathodes for Photoelectrochemical H 2 Evolution. *Phys. Chem. Chem. Phys.* **2019**, *21* (8), 4184–4192. https://doi.org/10.1039/C8CP07304J.

(16) Hemmerling, J.; Quinn, J.; Linic, S. Quantifying Losses and Assessing the Photovoltage Limits in Metal–Insulator–Semiconductor Water Splitting Systems. *Adv. Energy Mater.* **2020**, *10* (12), 1903354. https://doi.org/10.1002/aenm.201903354.

(17) Cuevas, A. The Recombination Parameter J0. *Energy Procedia* **2014**, *55*, 53–62. https://doi.org/10.1016/j.egypro.2014.08.073.

Chapter 4

Insights from Theory and Modeling of MIS Photoelectrocatalysts

4.1 Introduction

In the previous chapter, Ir/HfO_2/n-Si MIS photoelectrocatalysts were experimentally characterized, and it was demonstrated that the generated photovoltage could be significantly increased by tuning the thickness of the HfO_2 insulator layer. Based on experiments with varying the light intensity, these systems also exhibit a large degree of nonidealities (high ideality factor) which may result in suboptimal performance. Furthermore, the photovoltage generated by the optimal HfO_2 thickness (2.0 nm) is still significantly lower than the upper photovoltage limit as governed by flat-band potential. To quantify the source of the losses in these systems, it is important to obtain a fundamental understanding of the theory and physics to rigorously model these systems. This chapter provides explanations and modeling of the solid-state physics and the catalysis of MIS systems to better understand (1) the specific underlying mechanisms for how tuning the insulator layer thickness improves the photovoltage, (2) how the presence of nonidealities significantly impact the generated photovoltage, and (3) how to design systems that can approach the upper photovoltage limit governed by the flat-band potential.

4.2 Energy Band Diagrams and the Diode Equation

Energy band diagrams are a useful tool to visualize the physics and energy levels of electronic structures, and it is simplest to start with a direct metal/semiconductor (MS) system immersed in electrolyte and then later generalize this system to include an insulator layer. The

metal, semiconductor and electrolyte solution each have a characteristic Fermi level (E_m, E_s, E_{sol}), which is a thermodynamic quantity related to the electrochemical potential of the electrons in these materials. Before coming into electrical contact, each of these materials have a distinct Fermi level associated with their intrinsic properties (based on the solution redox potentials for the electrolyte, the doping density of the semiconductor, and the work function of the metal).

Figure 4-1 illustrates the equilibrium energy band diagram of a MS system with a planar metal electrocatalyst in direct contact with a planar n-type semiconductor and immersed in electrolyte. When each of the materials come into electrical contact in the dark, the system will shift toward thermal equilibrium by exchanging electrons between the metal, semiconductor, and electrolyte until their Fermi levels ($E_m, E_s,$ and E_{sol}) are equilibrated.[1] For the equilibration of the electrons between electrolyte with the metal, the charge transfer results in an electric field and corresponding potential drop in the electrolyte. This results in the buildup of charged ions nears the metal surface, forming an electrolyte double layer also known as the Helmholtz layer.[2,3] Meanwhile, the metal experiences no voltage drop because of its effectively infinite permittivity and ability to screen charge (negate the electric field).[4]

For the equilibration of an n-type semiconductor/metal interface, higher-energy free electrons from the semiconductor will transfer from the semiconductor to the metal, leaving behind a positively charged depletion region (also called a space-charge region).[5] This charge redistribution results in an electric field and band bending (i.e., a potential voltage drop) in the semiconductor as well as an electric potential barrier (V_{bb} and ϕ_b in Figure 4-1a). This electric potential barrier (or more fundamentally, the resulting changes in the charge carrier conductivities[6]) is essential to create a photovoltage because it promotes the transport of holes to

the metal electrocatalyst where they can ultimately perform the desired water oxidation reaction, and it promotes the transport of electrons away from the metal so that they will not recombine. In other words, the energetics of metal/semiconductor contacts results in the separation of charge carriers as well as the selective transport of these charge carriers to decrease their recombination. The higher the barrier, the better the charges are separated from each other and the higher the photovoltage that can be generated, which is discussed in more detail below.

Upon illumination, the MS system generates a photovoltage (V_{ph}), which is defined by the free energy difference between the electrons/holes which is also known as the splitting of the electron/hole quasi-Fermi levels (E_{fn}, E_{fp} in Figure 4-1b).[7] The generated photovoltage is influenced by the quasi-equilibrium concentrations and flux of electrons (J_e) and holes (J_h) across the MS junction. In general, the relationship between the (photo)voltage and the flux of charge carriers can be captured using the illuminated diode equation, which describes the net current (J_{net}) between the semiconductor and electrocatalyst as a function of voltage.

$$J_{net} = J_h + J_e = J_{ph} - J_s\left[exp\left(-\frac{qV_a}{nkT}\right) - 1\right] \quad (1) \qquad \text{4-1}$$

Here, J_{ph} is the photocurrent density which is the total hole current (J_h) generated from solar absorption in the semiconductor. These holes ultimately drive the OER at the electrocatalyst. J_e is the electron current from the semiconductor that reaches the metal by crossing the electric potential barrier (blue arrow in Figure 4-1b). Since e^-/h^+ recombination in metals is very fast, this is essentially a recombination current. J_s is the dark saturation current, q is the elementary charge of an electron, V_a is the applied voltage defined as the difference between the semiconductor majority-carrier Fermi level and the solution Fermi level (this voltage can be applied using a potentiostat, and it is affected by the photovoltage generated upon

illuminating the semiconductor), n is the ideality factor (n=1 is ideal, n>1 is nonideal), k is the Boltzmann constant, and T is temperature.

J_s is a key parameter governing the electron current and therefore governs the e^-/h^+ recombination rates as well as the generated photovoltage. The expression for J_s depends on the system architecture. For MS systems with a Si semiconductor, the dominant recombination mechanism is due to the thermionic emission of electrons from the semiconductor into the metal, and J_s can be analytically expressed by the following equation:[5]

$$J_s = A^* T^2 exp\left(-\frac{q\phi_b}{kT}\right) \quad 4\text{-}2$$

Here, A^* is Richardson's constant. The electric potential barrier height (ϕ_b) is defined as the difference between the metal work function (which is directly related to the Fermi level, E_m) and the semiconductor conduction band edge (E_{cb}) (see Figure 4-1).

A large barrier height is desired to improve the charge carrier separation, thereby minimizing the charge carrier recombination. For water oxidation with an n-type semiconductor, a metal with a high work function is necessary to achieve a large barrier height (and conversely a low work function metal is needed for water reduction with p-type semiconductors[8–10]). This is why Ir with a high work function of 5-5.67 eV[11] and Ni with a high work function of 5.04-5.35 eV[11] have been commonly used for water oxidation systems (in addition to the fact that these metals are also quite stable and kinetically active for water oxidation[12,13]). The theoretical barrier height expected based on the conduction band edge of Si (4.05 eV) and the work function of Ni and Ir (>5.0 eV) exceeds 0.95 eV (i.e., 5.0 eV – 4.05 eV = 0.95 eV).

In real metal/semiconductor contacts, however, the experimental barrier heights are typically much lower than the theoretical value (e.g., the barrier height for Ni/n-Si contacts are typically only about 0.6 or 0.7 eV[14–16]). There have been many discussions in the literature to

explain this behavior related to Fermi level pinning, metal-induced gap states, lateral inhomogeneities, and formation of metal silicide layers at the interface.[5,17–19] For these reasons, direct metal/semiconductor contacts generally do not perform well for water splitting applications, but adding an insulator layer between the metal and semiconductor can address these challenges.

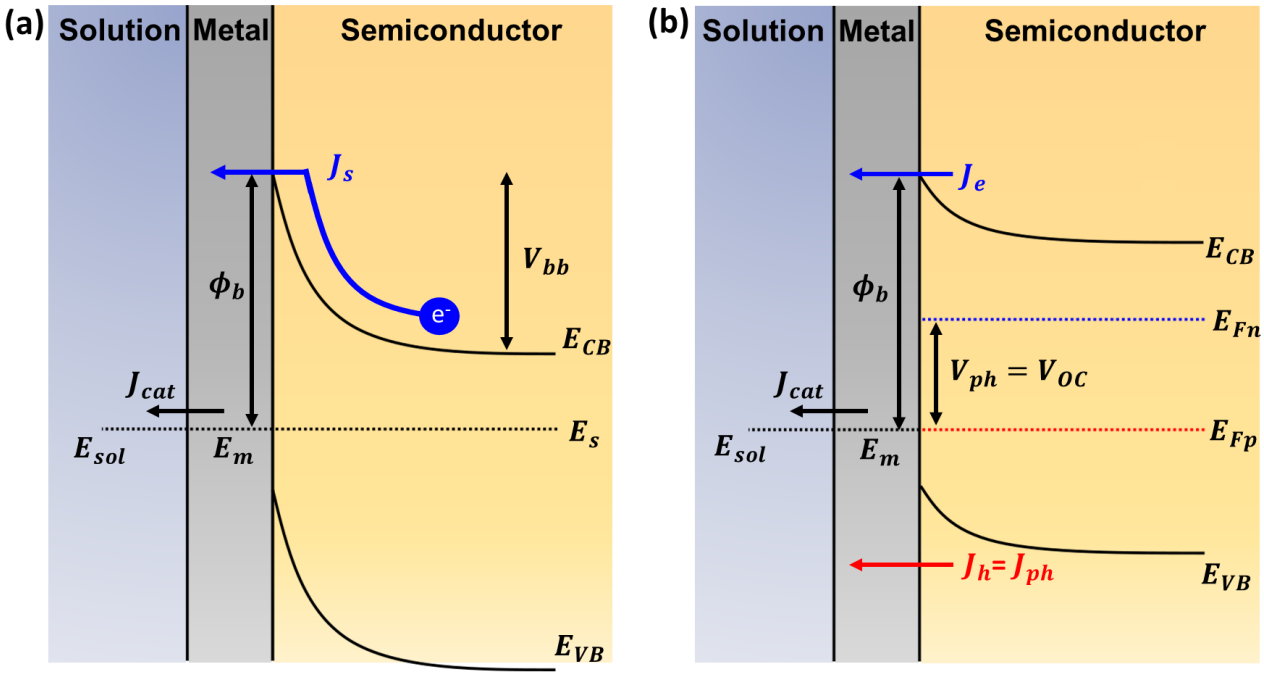

Figure 4-1. Energy band diagrams of an MS system with an n-type semiconductor and high work function metal immersed in an electrolyte. (a) System in the dark at equilibrium ($V_a = 0$, $J_{net} = 0$, and $E_{sol} = E_m = E_s$). The reverse saturation current (J_s) is governed by the barrier height (ϕ_b). (b) Illuminated system in quasi-equilibrium at the open-circuit potential (V_{oc}) such that there is no catalytic current ($J_{net} = J_{cat} = 0$). The photovoltage at open-circuit ($V_{ph} = V_{oc}$) is defined by the splitting of the electrons/holes quasi-Fermi levels (E_{fn}, E_{fp}). It is noted that the vacuum level is not shown in these energy band diagrams.

4.3 Impact of the Insulator Layer

It has been widely demonstrated that equations 4-1 and 4-2 capture the relationships between photogenerated current and voltage in MS systems. We wanted to understand how the introduction of a thin insulator between the metal and semiconductor impacts the performance

and generalize the model to include MIS systems. In the limit of low insulator thickness (up to ~2 nm of thickness), the MIS system behavior can also be described by augmenting the diode equations (4-1 and 4-2) by recognizing that the insulator layer effectively serves as an additional barrier that decreases the electron dark saturation current (J_s). In order to reach the metal and recombine, the electrons in MIS systems must not only overcome the potential barrier height but must also have sufficient energy to traverse the insulator layer. The expression for J_s in MIS systems is:[20]

$$J_s = A^* T^2 exp\left(-\frac{q\phi_b}{kT}\right) exp\left(-\propto d\phi_e^{1/2}\right) \quad 4\text{-}3$$

The second exponential term is the probability that an electron will tunnel through the insulator in which $\propto$ is a constant related to the effective mass of the electrons in the insulator, d is the insulator thickness, and ϕ_e is the offset between the insulator conduction band and semiconductor conduction band. See Figure 4-2 for illustrations of these variables.

An analytical expression for the photovoltage (V_{ph}) generated by an MIS system (in the limit of low insulator thickness) as a function of the net current (J_{net}) can be easily obtained by substituting equation 4-3 into equation 4-1:[20–23]

$$\left|V_{ph}\right| \approx \frac{nkT}{q}\left[ln\frac{J_{ph}-J_{net}}{J_s}\right] = \frac{nkT}{q}\left[ln\frac{J_{ph}-J_{net}}{A^*T^2} + \frac{q}{kT}\phi_b + \propto d\phi_e^{1/2}\right] \quad 4\text{-}4$$

This expression is valid when $\frac{J_{ph}-J_{net}}{J_s} \gg 1$, which is met for essentially all relevant operating conditions. The maximum photovoltage is obtained when the net current is 0. This voltage is labeled as the open-circuit photovoltage ($V_{oc} = V_{ph}(J_{net} = 0)$). Equation 4-4 suggests that in addition to the properties of the insulator layer that affect the tunneling probability (d, ϕ_e), the photovoltage is also impacted by the ideality factor (n), the barrier height (ϕ_b), and the photocurrent (J_{ph}).

Based on equation 4-4, a plot of V_{oc} vs $ln(J_{ph})$ should yield a line with a slope that is related to the ideality factor and an intercept that is related to the saturation recombination current (J_s).[22,23] In the previous chapter, both the ideality factor and recombination current were experimentally quantified using this approach by varying the light intensity (hence changing J_{ph}) and observing the shift in photovoltage.

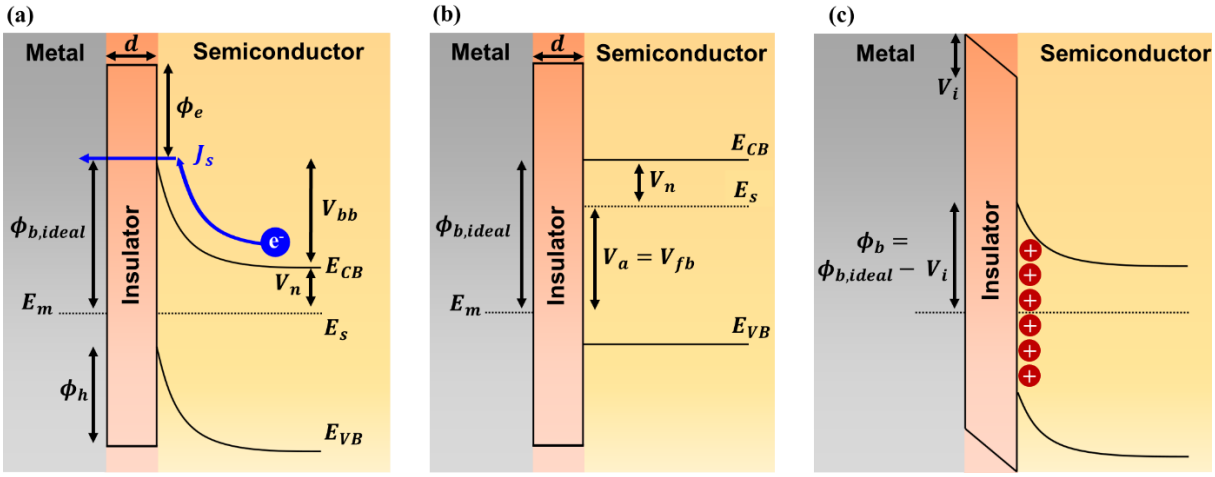

Figure 4-2: Energy band diagrams of an MIS system with an n-type semiconductor and high work function metal. (a) Ideal system (n=1) in the dark at equilibrium ($V_a = 0,\ J_{net} = 0$). ϕ_e is defined as the difference between the insulator and semiconductor conduction band edges while d is the thickness of the insulator layer. (b) Ideal system (n=1) in the dark at the flat-band potential ($V_a = V_{fb}$). (c) Nonideal system (n>1) with positively charged defects at the insulator/semiconductor interface. These defects cause an insulator voltage drop (V_i) which ultimately lowers the barrier height and photovoltage. It is noted that the vacuum level is not shown in these energy band diagrams.

4.3.1 Thick Insulator Regime

Equation 4-4 indicates that increasing the insulator thickness would indefinitely continue increasing the open-circuit photovoltage. However, this trend is not observed experimentally as thicknesses exceeding 2.3 nm of HfO_2 result in photovoltage losses. The above expression can only describe MIS systems in the thin insulator regime in which the recombination is dominated by the electron current while the hole current (J_{ph} in equation 4-1) is not affected significantly by the insulator.[24] In the thick insulator regime (>2.3 nm HfO_2), the hole current tunneling through

the insulator is impeded and the recombination is dominated by the hole current. The hole tunneling current is given by:[25]

$$J_{h,t} = \frac{4qm_{h,eff}(kT)^2}{h^3 N_V} p_s exp\left(-\propto_t d\sqrt{\phi_p}\right) exp\left(1 - \frac{-\Delta}{kT}\right) \quad 4\text{-}5$$

Here, $m_{h,eff}$ is the effective mass for holes, h is Planck's constant, N_V is the effective density of states in the silicon valence band, p_s is the concentration of holes at the Si-insulator interface, ϕ_p is the mean barrier for holes provided by the insulator, and Δ is the energy difference between the metal Fermi level and the hole quasi-Fermi level (see Figure 4-3c). For thin insulators, effectively all the photogenerated holes will tunnel through the insulator layer to the metal where it can catalyze the reaction. For thick insulators, p_s and Δ must increase to enable the same tunneling current through the insulator. Essentially voltage must be sacrificed in order to maintain the flow of holes through the insulator. The photovoltage loss is manifested in the Δ term, which is described as a charge extraction loss.[22,26–28]

Figure 4-3 illustrates the thickness dependent tradeoff for the different insulator thickness regimes. For the thin insulator in Figure 4-3a, $J_{h,t}$ is not significantly impeded so there are no losses associated with holes tunneling through the thin insulator. However, J_s is also relatively large resulting in significant electron recombination and a lower photovoltage (i.e., the photovoltage losses are dominated by electron tunneling through the insulator and recombining). For the intermediate insulator thickness in Figure 4-3b, electron recombination is reduced while not significantly impeding $J_{h,t}$. This is the sweet spot where the photovoltage is optimized. For the thick insulator in Figure 4-3c, $J_{h,t}$ is significantly impeded, resulting in a charge extraction loss (Δ) which limits the photovoltage (i.e., the photovoltage losses are dominated by holes that cannot tunnel through the insulator and thus recombine). In summary, there is a fundamental tradeoff associated with balancing the losses from the electron recombination current (J_s) and the

losses from the hole tunneling current ($J_{h,t}$). The optimal thickness of a given insulator layer is therefore ultimately governed by the relative tunneling probabilities of the electrons and holes, which is further discussed in section 4.10

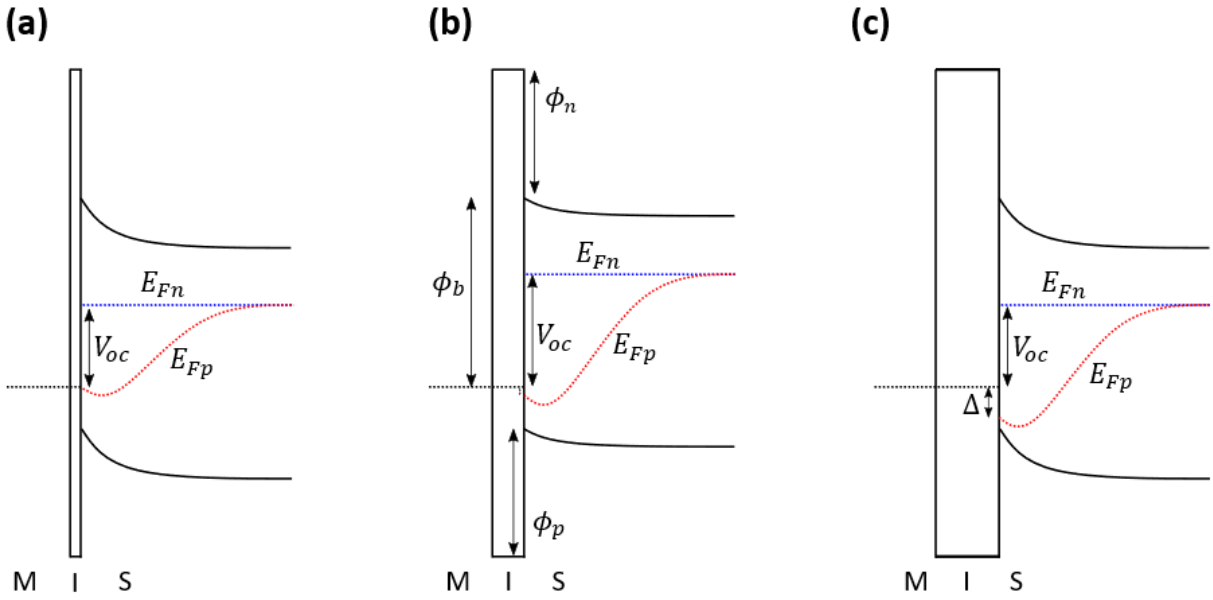

Figure 4-3: Energy band diagram in quasi-equilibrium (no applied voltage) for illuminated MIS systems with different insulator thicknesses. (a) Thin insulator with a low photovoltage due to significant electron recombination current. (b) Intermediate insulator thickness with optimal photovoltage due to balanced electron recombination current and hole tunneling current. (c) Thick insulator with a lower photovoltage due to impeded hole tunneling current resulting in a charge extraction barrier (Δ). These systems are ideal (n=1) meaning there is negligible voltage drop in the insulator. V_{ph} is the photovoltage which corresponds to 400 mV in (a, c) and 550 mV in (b). Panel (b) illustrates the barrier height (ϕ_b), and insulator barrier for holes (ϕ_p) and electrons (ϕ_n), which are all identical for each of the systems. E_{fn} and E_{fp} are the quasi-Fermi levels for electrons and holes, respectively.

4.4 Performance Limits

Following this initial work, we wanted to understand how the measured photovoltage compared to the fundamental performance limits of these MIS systems. The detailed balance photovoltage limit for Si, which assumes that the only recombination mechanism is via radiative recombination, is about 840 mV depending on the Si thickness.[29–31] However, practical systems generate much less photovoltage due to additional recombination pathways. In MIS systems, the

recombination is dominated by thermionic emission as previously discussed. The upper photovoltage limit for an MIS system is the flat-band potential (V_{fb}) which is also known as the built-in potential. This is the applied voltage or generated photovoltage required to reach the state where the semiconductor bands no longer bend (i.e., become flat, see Figure 4-2b). In other words, there is no electric field in the semiconductor and so the system no longer can effectively separate the charge. Therefore, essentially all of the photogenerated charge carriers will recombine with each other when the photovoltage is large enough to achieve the flat-band condition, so the photovoltage cannot exceed this limit.

The flat-band potential is defined by the Fermi levels of the metal (E_m) and the semiconductor (E_s) as well as by the presence of bulk and fixed charge in the insulator layer:[26]

$$V_{fb} = E_m - E_s - \frac{Q_f}{C_{ox}} - \frac{Q_{bulk}d}{2C_{ox}} \qquad 4\text{-}6$$

Here, Q_f is the fixed charge per unit area located at the semiconductor/insulator interface and Q_{bulk} is the bulk charge per unit volume in the insulator layer, and C_{ox} is the capacitance of the oxide insulator layer. If significant bulk charge or fixed charge are also present in the system, the flat-band potential would be a linear or parabolic function of the insulator thickness based on the above equation. Experimentally, however, the flat-band potentials were independent of insulator thickness which indicates the samples have a negligible amount of fixed or bulk charges. It is also noted that all of the Mott-Schottky plots are linear, which indicates that surface states are not affecting the measured capacitance for the selected frequency range.[32,33]

Because the insulator does not significantly impact the flat-band potential for the Ir/HfO_2/n-Si systems, the expression for the flat-band potential can be simplified, only being defined by the Fermi levels of the metal (E_m) and the semiconductor (E_s) (see Figure 4-2b):

$$V_{fb} = E_m - E_s \quad (4\text{-}7)$$

As discussed in the Chapters 2 and 3, a common method to experimentally quantify the flat-band potential is based on the Mott-Schottky equation, which for an n-type semiconductor takes the following form:[22,34]

$$\left(\frac{1}{C_{sc}}\right)^2 = \frac{2}{\varepsilon_0 \varepsilon_s A^2 q N_D}\left(V_a - V_{fb} - \frac{kT}{q}\right) \quad (4\text{-}8)$$

Here, A, ε_0, and ε_s and are the surface area of the junction, vacuum permittivity, and semiconductor relative permittivity, respectively. The flat-band potential and the doping density were experimentally extracted using this method for the Ir/HfO_2/n-Si MIS photoelectrocatalysts. From this analysis, the upper photovoltage limit for these systems is 630 mV. This is far greater than 480 mV photovoltage obtained from optimizing the HfO_2 thickness. Specifically, there are ~150 mV of losses in the system that could not be addressed by tuning the insulator thickness.[22]

4.5 Barrier Height and Nonidealities

To understand why these MIS systems fail to reach the upper performance limits, we analyzed the impact of the insulator on the barrier height and ideality factor which also affect the photovoltage (equation 4-4). For an ideal system ($n = 1$), the ideal barrier height ($\phi_{b,ideal}$) can be determined from the flat-band potential (see Figure 4-2b):[19]

$$\phi_{b,ideal} = V_{fb} + V_n = V_{fb} + \frac{kT}{q} ln \frac{N_C}{N_D} \quad (4\text{-}9)$$

Here, V_n is the offset between the semiconductor Fermi level and conduction band edge (see Figure 4-2a). It is a function of the doping density (N_D) and the effective density of states in the semiconductor conduction band (N_C). The values for $\phi_{b,ideal}$ and V_n can be computed via equation 4-9 by using the measured V_{fb} and N_D from the previous Mott-Schottky analysis. The measured values for $\phi_{b,ideal}$ (~0.9 eV for all HfO_2 thicknesses) and V_n (~0.27 eV for all HfO_2

thicknesses) as well as the previously measured flat-band potential and open-circuit photovoltage are plotted in Figure 4-4a. Using the calculated V_n and given the well-known electron affinity for Si (i.e., energy of the conduction band) of 4.05 eV, then the Si Fermi level is about 4.32 eV. Given the average V_{fb} of ~0.63 eV, this puts the effective Ir work function at a value of 4.95 eV, which is at the lower end of the work function range of 5-5.67 eV for Iridium.[35]

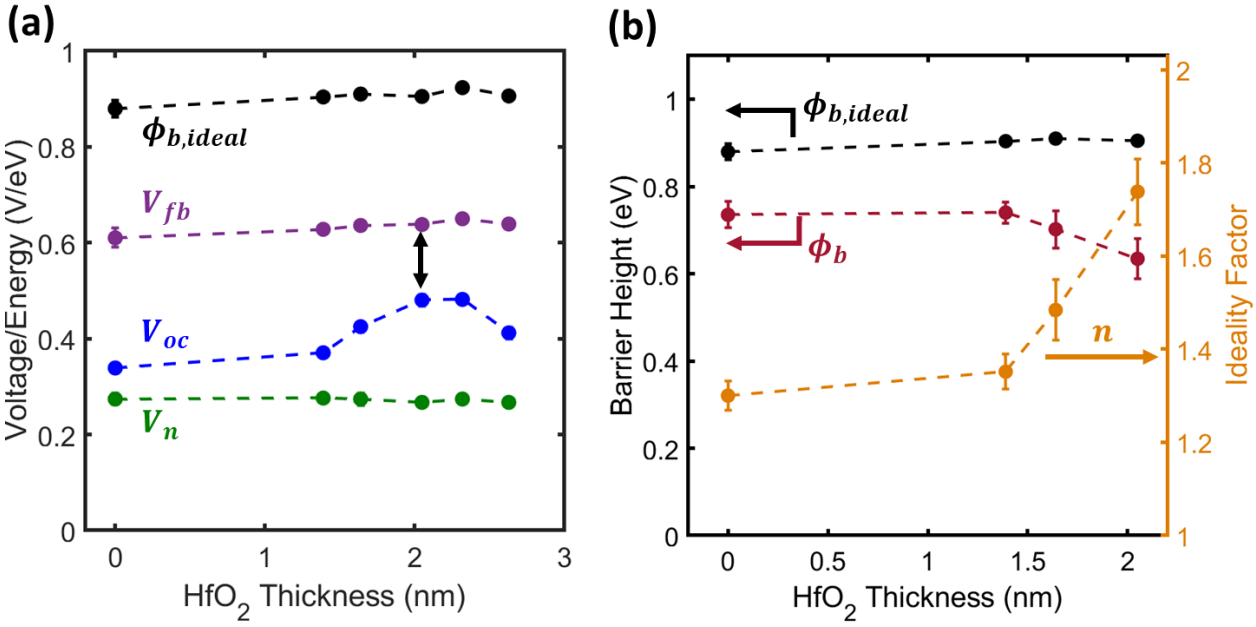

Figure 4-4. Compiled experimental and measured results for Ir/HfO_2/n-Si photoelectrocatalysts with varied HfO_2thickness. (a) Values for V_n, V_{fb}, and $\phi_{b,ideal}$ are using results obtained from Mott-Schottky plots and V_{oc} was determined by comparing to an Ir/p^+-Si electrocatalyst control. (b) n was obtained by measuring the performance as a function of light intensity, while ϕ_b was calculated from equation 4-10.

Compared to ideal systems, the presence of nonidealities (n>1) causes the barrier height in MIS systems to be lower than the ideal barrier height according to the following expression:[19,22]

$$\phi_b = \frac{\phi_{b,ideal}}{n} + \left(\frac{n-1}{n}\right) V_n \qquad 4\text{-}10$$

As discussed above and compiled in Figure 4-4, $\phi_{b,ideal}$, n, and V_n have already been experimentally determined for Ir/HfO_2/n-Si systems, and therefore the actual barrier height (ϕ_b)

can be evaluated using this equation. The relationship between $\phi_{b,ideal}$, n, and ϕ_b are provided in Figure 4-4b. The results demonstrate that the nonidealities (n>1) in these Ir/HfO_2/n-Si systems significantly lower the barrier height (ϕ_b) compared to the ideal value ($\phi_{b,ideal}$). For example, the sample with optimal photovoltage (2.0 nm HfO_2) exhibits an ideality factor of 1.74, yielding a barrier height of 0.63 eV, which is 0.27 eV lower than the ideal barrier height of 0.9 eV. This lowering of the barrier height will ultimately lower the generated photovoltage of the nonideal system relative to the system if it behaved ideally. This statement is proven in the next section.

4.5.1 Proving that Nonidealities Fundamentally Lower the Photovoltage

By plugging equation 4-10 into equation 4-4 and setting the net current to zero (i.e., open-circuit), an expression for V_{oc} is obtained:

$$-V_{oc} = \frac{nkT}{q} ln\left(\frac{J_{ph}}{A^*T^2}\right) + \phi_{b,ideal} + (n-1)V_n + \frac{nkT}{q} \propto d\sqrt{\phi_e} \quad 4\text{-}11$$

The ideal form of equation 4-4 in which n =1 and $\phi_b = \phi_{b,ideal}$ can be written as:

$$\left|V_{oc,ideal}\right| = \frac{kT}{q}\left[ln\frac{J_{ph}-J_{net}}{A^*T^2} + \frac{q}{kT}\phi_{b,ideal} + \propto d\phi_e^{1/2}\right] \quad 4\text{-}12$$

Then $|V_{oc}| - |V_{oc,ideal}|$ can be evaluated:

$$|V_{oc}| - \left|V_{oc,ideal}\right| = (n-1)\frac{kT}{q}\ ln\left(\frac{J_{ph}}{A^*T^2}\right) + \ (n-1)V_n + \ (n-1)\frac{kT}{q} \propto d\sqrt{\phi_e} \quad 4\text{-}13$$

Which simplifies to:

$$\left|V_{oc,non-ideal}\right| - \left|V_{oc,ideal}\right| = (n-1)\left[\frac{kT}{q}\ ln\left(\frac{J_{ph}}{A^*T^2}\right) + V_n + \ \frac{kT}{q} \propto d\sqrt{\phi_e}\right] \quad 4\text{-}14$$

The term $(n-1)$ is always a positive number so it can be shown that $|V_{oc,non-ideal}| > |V_{oc,ideal}|$ only if:

$$J_{ph} > \ A^*T^2 exp\left(-\frac{q}{kT}V_n - \propto d\sqrt{\phi_e}\ \ \right) \quad 4\text{-}15$$

Using the experimental values measured in the paper, the value of J_{ph} necessary for this condition to be true is ~290 mA/cm^2 for the 2.0 nm HfO_2 system and even larger for lower HfO_2 thicknesses. This is significantly larger than the experimental J_{ph} of ~25 mA/cm^2 (Figure 2a). Therefore, the constraint in equation 4-15 does not hold and this shows that a high ideality factor will result in a lower open-circuit photovoltage for all practical conditions and confirms $|V_{oc}| < |V_{oc,ideal}|$. The loss in open-circuit voltage as a function of ideality factor is plotted in Figure 4-5.

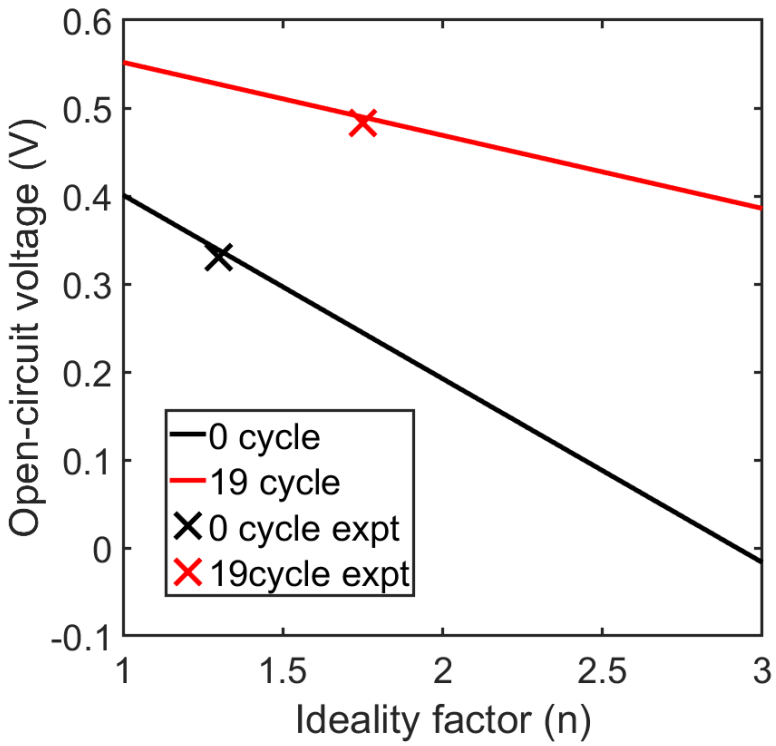

Figure 4-5: Plot of open-circuit voltage decreasing as a function of ideality factor for the 0 cycle and 19 cycle samples. The "x" indicates the experimental values.

4.5.2 Ideality factor, Sources of Nonidealities, and Barrier Height Lowering

Now that the presence of nonidealities has been confirmed to be detrimental to the system performance, the next question is related to the physical meaning of the ideality factor and the

origin of these nonidealities. The ideality factor is simply a measure of how much a system deviates from the ideal diode equation. Under forward bias, a common representation of the ideality factor is based on the ratio of the derivative of the natural log of the current ($dln(J)$) and the derivative of the applied voltage ($d(V_a)$):[36]

$$\frac{1}{n} = \frac{kT}{q}\frac{dln(J)}{d(V_a)} \qquad 4\text{-}16$$

Based on this equation, the ideality factor can be measured by finding of the slope of the plot of $ln(J)$ vs V_a of a solid-state photovoltage junction as long as resistance losses are minimal. For water splitting systems, however, the slope of current-voltage plot contains contributions from both the solid-state photovoltaic junction and from the catalysis. To analyze the current-voltage relationship of the catalysts, Tafel slopes are commonly measured and can be linked to coverages of reaction intermediates.[37] If the catalysis can be deconvoluted from the solid-state junction and resistance losses, then the ideality factor could possibly be measured from equation 4-16, but measuring the ideality factor from the light intensity experiments described in Chapter 2 remains a more reliable method.

When thermionic emission is the dominant recombination pathway, it can be shown that the ideality factor is related to a barrier height that linearly changes as a function of the applied voltage ($\phi_b(V_a)$):[19]

$$\phi_b(V_a) = \phi_b + \frac{n-1}{n}V_a \qquad 4\text{-}17$$

Here, ϕ_b is the barrier height evaluated at zero bias ($V_a = 0$), which is also the barrier height that is typically included in the diode equation. It can be shown with simple algebra that plugging in $\phi_b(V_a)$ from 4-17 into the *ideal* diode equation (without any n) yields the diode equation (equation 4-1). An ideal system ($n = 1$) has a voltage-independent barrier height, while a

nonideal system results in a voltage dependent barrier height which can be caused by a variety of physical phenomena.

Although there are several possible sources of nonidealities, they are typically attributed to defects at the semiconductor/insulator interface in MIS systems which ultimately result in an insulator voltage drop (see section 4.5.3 for the full details).[22] Besides the insulator voltage drop, several other nonidealities will also have a small effect on the ideality factor. These include image force lowering, barrier height inhomogeneity, field emission, recombination in the semiconductor space charge (band bending) region and the dielectric properties of the interfacial region.

Image force lowering results from image charges building up in the metal as charge carriers approach the metal/semiconductor interface. The potential associated with these image charges lowers the barrier height, and the ideality factor resulting from image forces (n_{imf}) is given by:[5]

$$\frac{1}{n_{imf}} = 1 - \frac{1}{4}\left(\frac{q^3 N_d}{8\pi^2 \varepsilon_s^3}\right)^{\frac{1}{4}} \left(\phi_b - V_a - V_n - \frac{kT}{q}\right)^{-\frac{3}{4}} \qquad 4\text{-}18$$

The resulting ideality factors for all systems is less than 1.005 for V_a = 0V and less than 1.03 for V_a =0.5V. The resulting reduction in the barrier height is less than 13 meV for all samples. Thus, the image force lowering has a low impact on the ideality factor and system performance.

Field emission occurs when electrons travel to the metal by tunneling through the space charge region rather than by thermionically emitting over the barrier. This occurs in highly doped semiconductors where the space charge region is very narrow which enables facile electron tunneling. The result is a reduction in the effective barrier height and an increase in ideality factor. The ideality factor from field emission (n_{fe}) is given by:[38]

$$n_{fe} = \frac{qE_{00}}{kT}\coth\left(\frac{qE_{00}}{kT}\right) \quad ; \quad E_{00} = \frac{h}{4\pi}\left(\frac{N_d}{m_e^*\varepsilon_s}\right)^{1/2} \qquad 4\text{-}19$$

Here, m_e^* is the effective mass of the electron. For the systems studied, the n_{fe} is effectively equal to 1 and the maximum lowering of the barrier height is less than 4 meV. Thus field emission cannot account for the high ideality found in each sample.

The diode equation is derived assuming that the recombination occurs radiatively in the semiconductor bulk. However, real systems may have some degree of recombination in the space charge region. The theoretical ideality factor for such a system is about 2.[39,40] Silicon based diodes have large charge carrier mobilities and thus the space charge recombination is usually not significant at room temperature.[5] Previous studies have found that recombination in the space charge region have a negligible effect on the performance in MIS systems at room temperature.[38,41] Using a typical carrier lifetime of 2×10^{-5} seconds for silicon,[38,41,42] the calculated reverse saturation current from space charge recombination is 3.5×10^{-6} mA/cm^2, which is 2 orders of magnitude lower than the values calculated in Figure 3a of main text. Thus, the contributions from space charge recombination are expected to be small.

Another situation that may result in high ideality factor is inhomogeneous barrier heights throughout the system. It is generally assumed that the thickness of the insulator is not constant throughout the system, but exhibits a Gaussian distribution.[38,41,43,44] As voltage is applied, the charge carriers can overcome higher barriers which changes the overall effective barrier height of the system. From the variation in the HfO_2 thickness measurements, we don't expect significant differences between samples with different HfO_2 thicknesses. To help confirm this, we have synthesized a 19 cycle sample on a higher doped wafers (0.1-1 ohm-cm resistivity) as opposed to the other samples which were on lower doped wafers (5-8 ohm-cm resistivity). Both the higher doped and lower doped wafers were processed in parallel under identical conditions,

so each 19 cycle sample should have similar thickness and inhomogeneity of the HfO_2 layer. Therefore, if inhomogeneous barrier heights were dominating the ideality factor, then both 19 cycle samples would be expected to have the same ideality factor. The resulting ideality factor for the higher doped sample was about 2.7 compared to 1.7 for the lower doped sample.[22] Thus inhomogeneous barrier heights are not expected to be a dominant factor contributing to nonidealities.

4.5.3 Insulator Voltage Drop and Density of Surface States

None of the other factors in the previous section can explain the high ideality factors observed in the MIS systems, which leaves the voltage drop resulting from surface states as the most likely source of nonidealities. These defects can result in significant charge build-up at the interface which causes a voltage drop in the insulator (V_i in Figure 4-2c).[20] As illustrated in Figure 4-2c, the charge build-up lowers the barrier height relative to the ideal value as some of the voltage is lost as a voltage drop in the insulator (i.e., $\phi_b = \phi_{b,ideal} - V_i$). We note that the 0 nm HfO_2 sample exhibited a relatively high ideality factor of 1.3 even without the presence of an HfO_2 layer. Here, the nonidealities may be attributed to an interfacial SiO_2 layer which has been widely discussed in the metal-semiconductor Schottky diode literature.[5]

The origin of the voltage drop in the insulator layer is the buildup of charge in the system as governed by Gauss's Law:[32]

$$\Delta V_i = -d\frac{Q_m}{\varepsilon_i} \qquad 4\text{-}20$$

Where d is the insulator thickness, Q_m is the charge in the metal and ε_i is the insulator permittivity. From conservation of charge, the charge in the metal is balanced by the charge on the other side of the insulator which includes contributions from the space charge region (Q_{sc}), the charge in the surface states (Q_{ss}) and the fixed charge (Q_f):

$$-Q_m = Q_{sc} + Q_{ss} + Q_f \quad (4\text{-}21)$$

Making the substitution:

$$\Delta V_i = \frac{d}{\varepsilon_i}\left(Q_{sc} + Q_{ss} + Q_f\right) \quad (4\text{-}22)$$

It is shown in below discussion fixed charge in the system is negligible. Furthermore, the CV's in Figure 4-6 show that there is no photoinduced charging of the insulator upon illuminating a 19 cycle p^+-Si sample.

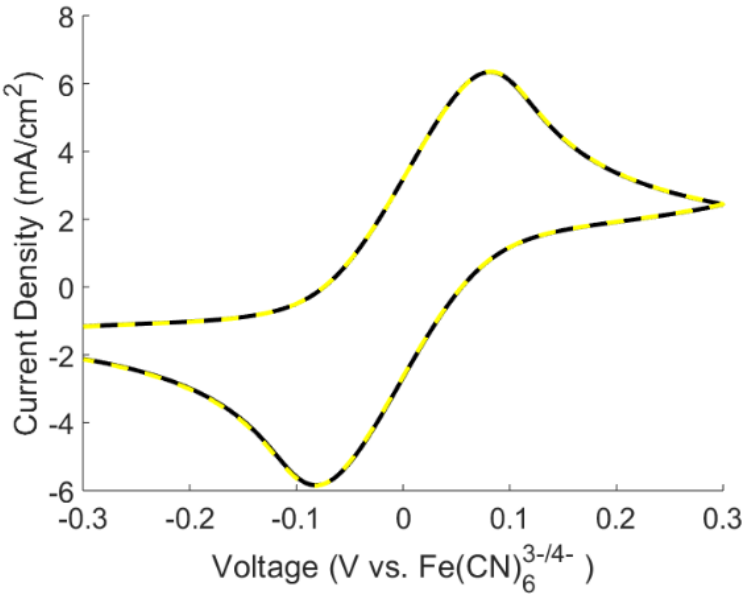

Figure 4-6: CV of a 3.5 nm-Ir/19 cycle HfO_2/p^+-Si sample in dark (black) and under illumination (yellow) in 10/10 mM FFC solution. The curves are identical which indicates that there is no photoinduced charging of the insulator.

Therefore, the fixed charge term can be removed and the following expression relating the ideality factor to the density of surface states and charge in the space charge region has been previously derived:[32]

$$n = 1 + \frac{\frac{d}{\varepsilon_i}\left(\frac{\varepsilon_s}{W} + qD_s\right)}{1 + \frac{d}{\varepsilon_i}qD_m} \quad (4\text{-}23)$$

Where, W is the width of the space charge region, ε_s and ε_i are the semiconductor and insulator permittivity. D_s and D_m are the density of surface states in equilibrium with the semiconductor and the metal, respectively. Using the common assumption that the surface states are only in equilibrium with the semiconductor (i.e., that $D_m = 0$), then the following expression is obtained.

$$n = 1 + \frac{d}{\varepsilon_i}\left(\frac{\varepsilon_s}{W} + qD_s\right) \quad \text{4-24}$$

From this equation, it is evident that an MIS system will become less ideal as the insulator thickness increase, if all other parameters are constant. Based on the experimentally obtained ideality factor of 1.7 for the Ir/2.0 nm HfO_2/n-Si sample, the expected voltage drop in the insulator layer is 270 mV which results in significant lowering of the barrier height. Assuming that $D_m = 0$ and that the ideality factor is entirely described by equation 4-24 and, then the density of surface states in equilibrium with the semiconductor can be calculated. These values are shown in Figure 4-7. The 0 cycle sample, which is assumed to have an interfacial SiO_2 layer of 0.5 nm, has the highest density of surface states. This is the expected result because metal/semiconductor contacts are known to have a significant density of defects from metal-induced gap states (MIGS).[5,17] The number of defects decreases significantly when an HfO_2 layer is introduced. HfO_2 and other high-k dielectrics are known to passivate defects present at metal/semiconductor contacts and reduce the influence of MIGS. However, thicker HfO_2 results in a higher density of defects in Figure 4-7 while MIGS theory predicts the opposite behavior. It is not clear exactly why the surface state density would increase with increasing HfO_2 thickness, but these types of trends have also been previously observed with SiO_2.[32] We note that the data in Figure 4-7 is the upper limit of the density of surface states because here it is assumed that all

of the nonidealities are from insulator voltage drop. Other nonidealities may be present to a small degree, as discussed in the previous section.

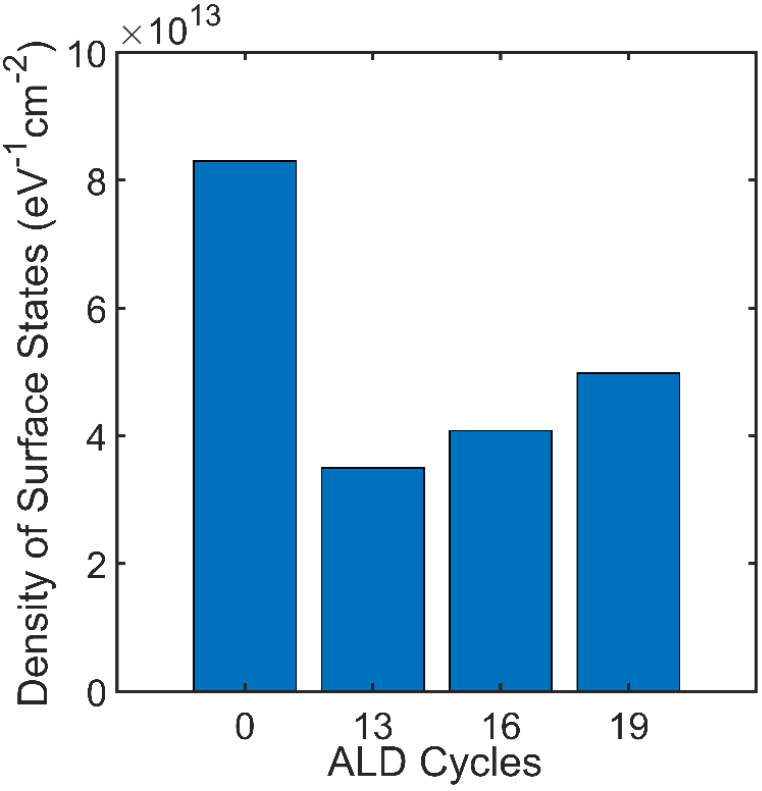

Figure 4-7: Estimated density of interface states as a function of insulator thickness (HfO_2 ALD cycles).

Finally, it is noted than even an ideal system without surface states ($D_m = D_s = 0$), will fundamentally exhibit a voltage drop due to the buildup of charge in the semiconductor space charge region when the system is in equilibrium. In this ideal case, the expression for the ideality factor simplifies to:

$$n = 1 + \frac{d\varepsilon_s}{W\varepsilon_i} \qquad 4\text{-}25$$

The ideality factor measured from this equation is the lowest theoretical value that the system can obtain because the charge in the space charge region is unavoidable. This equation also highlights the important role of the insulator permittivity/dielectric constant on the ideality

factor. Indeed, organic molecules with low permittivity result in significant deviations from ideal behavior.[45] Because the ε_i for HfO_2 is relatively large,[46] the lower limit to the ideality factor obtained from equation 4-25 is less than 1.001, even for the thickest samples of 2.6 nm. This results in only a 1 mV expected drop in the insulator layer. Therefore, the system can achieve essentially ideal performance if there are no contributions from surface states. This decreased voltage drop and better theoretical ideality factors are some of the additional advantages of using a high-dielectric insulator layer as opposed to SiO_2 which has a lower dielectric constant. If all else were identical, replacing the HfO_2 with SiO_2 would result in a larger voltage drop (albeit still relatively small), and hence a less ideal system with lower photovoltage. Upon analysis of the STEM cross-sections, the Ir/HfO_2/n-Si systems may exhibit an SiO_2 layer with thickness of a few Angstroms, but its contribution is expected to be negligible compared to the much thicker HfO_2 layer.

4.6 Tunneling Probability

As previously discussed, the probability that the electrons will tunnel through the insulator layer critically determines the recombination rates. The tunneling probability can be estimated by combining the experimental results with the above-described theory. From the varied light intensity experiments, the overall value of the reverse saturation recombination current (equation 4-3) is determined. This recombination current contains contributions from both the barrier height (ϕ_b) and the tunneling probability $exp\left(-\propto d\sqrt{\phi_e}\right)$ which need to be deconvoluted from each other. To deconvolute these parameters, the barrier height can be calculated using equation 4-10 and using the experimental parameters calculated in the previous chapter: ideality factor, ideal barrier height, and doping density. This has already been done, and

the barrier heights reported in Figure 4-4b. Using the calculated values for ϕ_b, then the tunneling probability term can calculated from the values of J_s

By following this procedure, the tunneling probability is calculated for each thickness of HfO_2 and the values are reported in Figure 4-8. As expected, increasing insulator thickness exponentially decreases the tunnel probability term as the electron charge transfer is impeded. We note that the 0 nm HfO_2 sample has a tunnel probability below 1 because of the likely formation of an adventitious SiO_2 layer present at the interface (otherwise, a pure metal/semiconductor interface should have a tunnel probability of 1 because there is no insulator to tunnel through). The lowest tunnel probability term for the 2.0 nm HfO_2 results in a ~500-fold reduction of electron recombination, which yields a 160 mV photovoltage improvement relative to the 0 nm HfO_2 sample.

It is also critical to understand the individual parameters in the tunneling probability term. The thickness of the insulator layer has already been readily determined for each system using the cross-section STEM imaging. However, the other two terms, $\propto$ and ϕ_n, are not readily known for nanoscale HfO_2 Because of the inherent differences between bulk HfO_2 and HfO_2 at the nanoscale.

The constant $\propto$ is given by the following equation:[32]

$$\propto = \frac{4\pi}{h}\sqrt{2m_e^*} \qquad 4\text{-}26$$

In literature, the effective mass of the electron (m_e^*) through the insulator is generally assumed to equal the mass of an electron, which results in the constant being approximately equal to 1 and thus $\propto$ is often assumed to be insignificant.[23,32] However, the effective mass of an electron in nanoscale HfO_2 (with small contributions from the thin interfacial SiO_2 layer) is unknown and may deviate significantly from the bulk value. The same applies for ϕ_e, so we combine $\propto$ with

ϕ_e into one term as it is not possible to confidently deconvolute these parameters. The combined term $\propto \sqrt{\phi_e}$ was calculated using the average HfO_2 thickness from STEM cross-sections, and the values are reported in Figure 4-8. The term increases with increasing HfO_2 thickness, which is desirable for minimizing the electron recombination tunnel current. This indicates that the tunnel properties of HfO_2 may change as a function of thickness as they approach the properties of bulk HfO_2. Depending on the actual value of $\propto$, the estimated range of ϕ_e is between ~0.1-1 eV, which is significantly lower than what might be achievable for HfO_2 on Si (~2 eV).[46] If the insulator can be engineering to increase ϕ_e up to the HfO_2 bulk value of 2 eV, then the photovoltage of the systems could be significantly improve. The extent to which the photovoltage could be improved and the necessary tunneling probability required to achieve the upper photovoltage limit is discussed in section 4.8

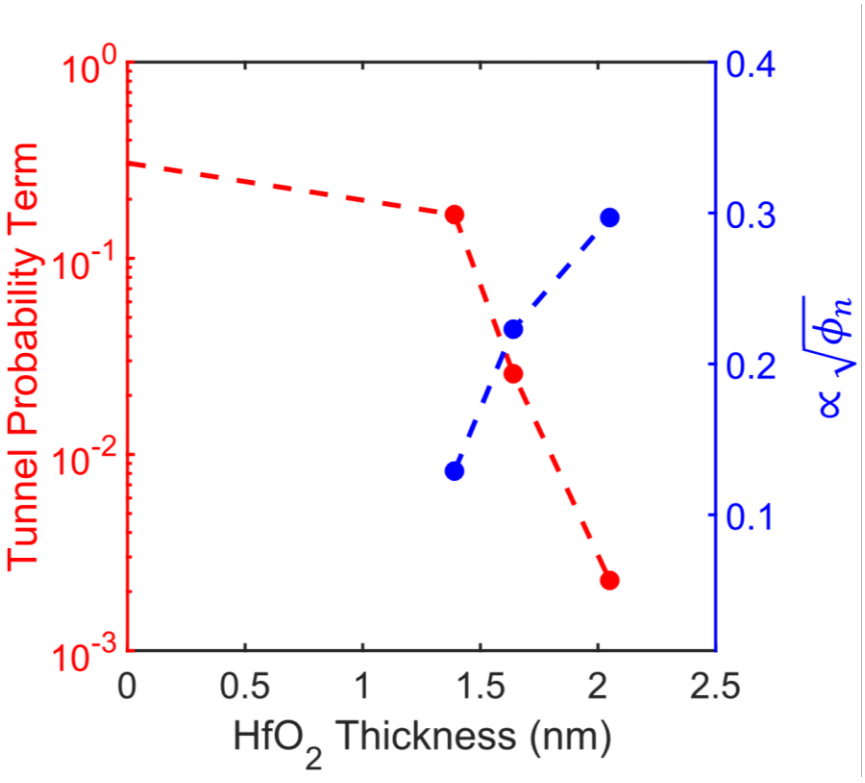

Figure 4-8: Tunnel probability term $\exp(-\propto d\sqrt{\phi_n})$ and combined term $\propto \sqrt{\phi_n}$ as a function of HfO_2 thickness.

4.7 Modeling Current-Voltage Plots

Now that all the key parameters have been quantified for the Ir/HfO_2/n-Si systems using the combined experimental and theoretical approach, the current-voltage relationship can be modeled. The theoretical equations and analyses so far have strictly focused on the solid-state physics of the MIS junction (basically applies for a system acting as a solar cell). The other critical component for application in solar water splitting is the kinetics of the electrocatalytic reaction. Here, we employed the Butler-Volmer equation to approximate the dark electrocatalytic reaction of the Ir/p^+Si sample:

$$J_{cat} = J_{ocat}\left[exp\left(\frac{z\beta F(V_{cat} - J_{cat}R_s)}{RT}\right) - exp\left(\frac{-z\beta F(V_{cat} - J_{cat}R_s)}{RT}\right)\right] \quad 4\text{-}27$$

Where J_{cat} is the current through the metal electrocatalyst, J_{ocat} is the electrocatalyst exchange current density, V_{cat} is the overpotential applied to the catalyst, z is the number of electrons in the electron transfer, β is the symmetry factor, F is Faraday's constant, and R_s is the series resistance. The current through the MIS junction and the catalyst are in series, so the overall current-voltage relationship of the system is calculated by:

$$J_{total} = J_{cat} = J_{MIS} \quad ; \quad V_{total} = V_{cat} + V_{MIS} \quad 4\text{-}28$$

where the total current, J_{total}, is equal to the current passing through the system as measured by the potentiostat. The total voltage, (V_{total}) is the summation of the voltage required by the electrocatalyst (V_{cat}) and generated by the MIS junction (V_{MIS}).

To model the CVs, first the p^+-Si control sample are fit to the Butler-Volmer Equation using J_{ocat}, z, and R_s as fitting parameters. Since the p^+-Si and n-Si samples have identical thicknesses of Ir catalyst, all samples are assumed to have the same catalytic activities. For the n-Si samples, the Butler-Volmer equation is then coupled to the MIS diode equations using the experimentally obtained values for J_{ph}, n, J_s, $\phi_{b,ideal}$, and V_n. By varying the input current and

measuring the corresponding voltages in series, the current-voltage characteristics can be modeled and compared to experiment. The data in Figure 4-9 show that the model closely matches the experimental data for samples with and without HfO_2. This analysis validates the modeling, and so the model can be used to leverage new insights and design principles to optimize the generated photovoltage of MIS systems.

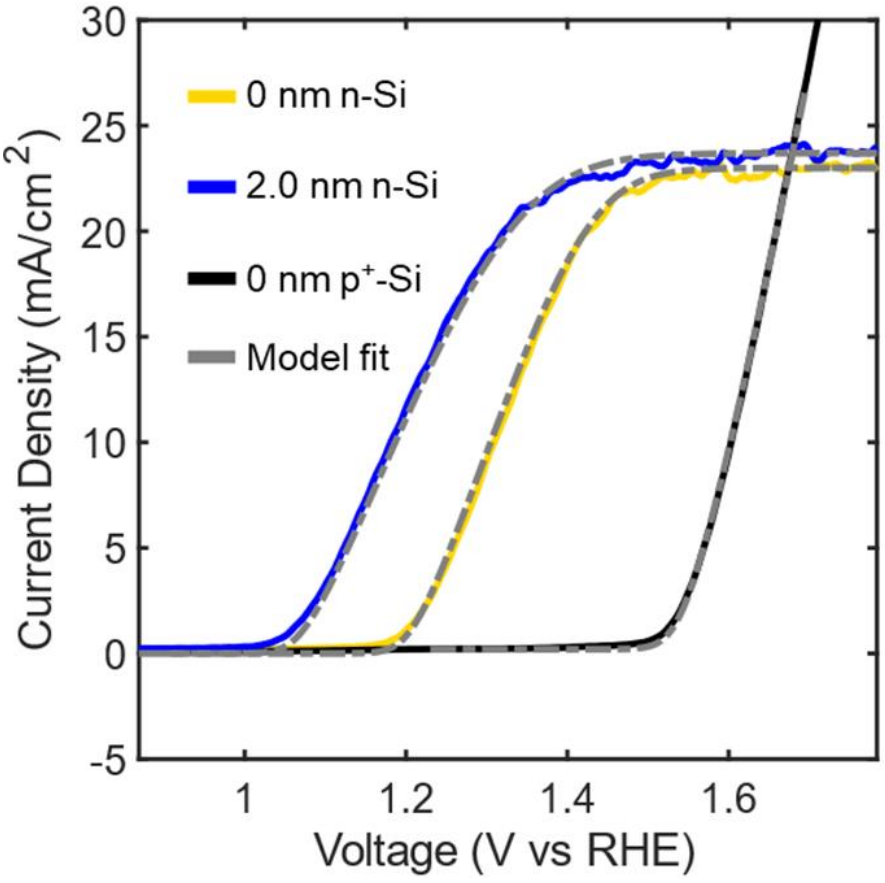

Figure 4-9. Experimental and modeled current-voltage plots demonstrate excellent agreement between experiment and modeling for Ir/2.0nm-HfO_2/n-Si, Ir/n-Si, and Ir/p+-Si electrocatalytic control.

4.8 Quantifying Losses with Modeling

As previously discussed, the photovoltage experimentally obtained for the optimal 2.0 nm HfO_2 sample (480 mV) is 150 mV below the upper photovoltage limit of the flat-band

potential. It is therefore important to identify the specific loss mechanisms in these systems using the insights from the models. To quantify the losses, we introduce a new metric, V_{losses} which is the difference between a system's flat-band potential (i.e., the upper photovoltage limit) and its generated open-circuit photovoltage. This difference will be zero for a system without losses (i.e., negligible recombination). The analytical expression for V_{losses} in MIS systems can be obtained by algebraic manipulation of equations 4-9, 4-10, and 4-11:

$$V_{losses} = V_{fb} - |V_{oc}| \approx \frac{nkT}{q}\left[ln\left(\frac{A^*T^2}{J_{ph}}\right) - \frac{q}{kt}V_n - \propto d\phi_e^{1/2}\right] \quad 4\text{-}29$$

The main parameters that impact the performance of these systems are the photocurrent (J_{ph}), the properties of the insulator (d and ϕ_e), the presence of nonidealities (n), and the semiconductor doping density (related to V_n). We note that the Richardson constant (A^*) is not a tunable parameter but is rather an inherent property for a given semiconductor.

Using equation 4-29, we can quantify the losses in MIS systems and suggest ways to achieve a photovoltage that approaches the upper limits. The data in Figure 4-10a show the photovoltage as a function of the insulator tunneling probability and the ideality factor for our Ir/HfO_2/n-Si systems as calculated using equation 4-29. The other parameters were measured as described above. The stars in the plot refer to the measured experimental data. The ideality factors of 1, 1.3, and 1.74 correspond to an ideal system, the experimental Ir/n-Si system (i.e., 0 nm HfO_2), and the experimental 2 nm HfO_2 system, respectively. For both, Ir/n-Si and Ir/2nm-HfO_2/n-Si, the photovoltage losses associated with nonidealities (i.e., the difference between the performance of an ideal and a nonideal system) are ~70 mV, as indicated by the blue and green arrows in Figure 4-10a. In other words, a photovoltage enhancement of ~70 mV is possible by removing nonidealities from these MIS systems.

Figure 4-10a also shows that even if all nonidealities were eliminated ($n = 1$), the optimal thickness of 2 nm HfO_2 would generate a photovoltage that is still ~80 mV below the flat-band potential (i.e., V_{losses}=80 mV). Based on equation 4-29, the V_{losses} can theoretically be eliminated by using an insulator with a tunnel probability (T_t) less than 0.0001 (gray star in Figure 4-10a). This tunneling probability can be achieved with an HfO_2 layer of ~3 nm; however, as we previously established a thick HfO_2 insulator leads to additional photovoltage drops because the hole transport is impeded. This analysis suggests that HfO_2 may not be suitable to maximize photovoltage, and insulators with better selectivity toward hole transport compared to the electron transport are necessary to further improve the performance.

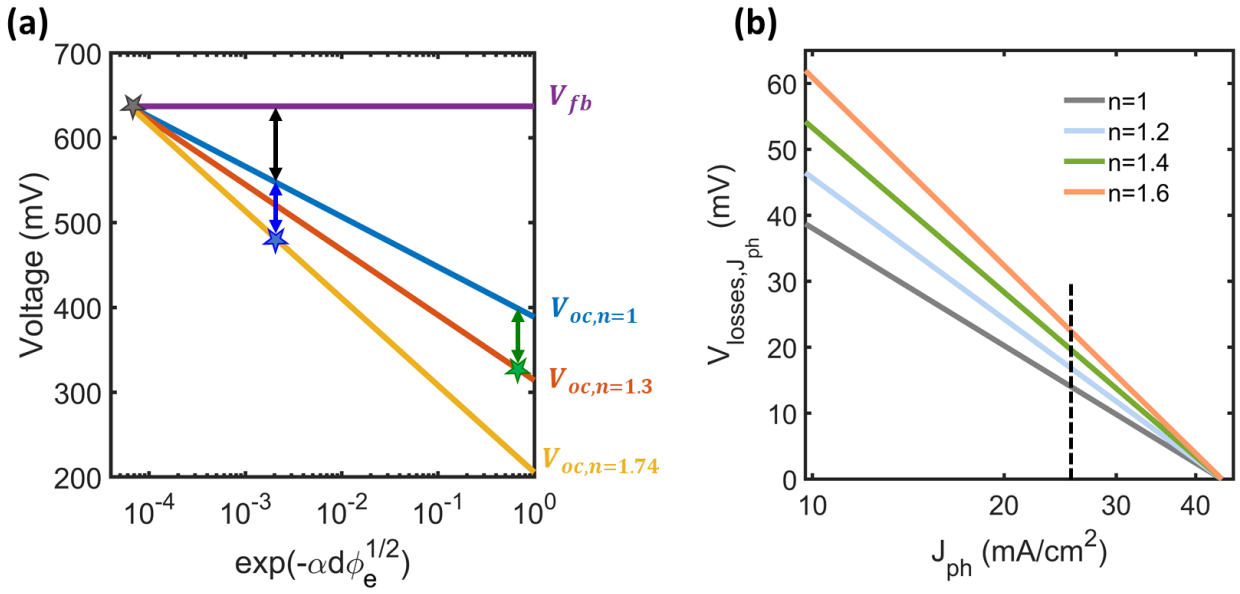

Figure 4-10. (a) Modeled (lines) and experimental (stars) photovoltages and flat-band potential as a function of the tunneling probability for the Ir/HfO_2/n-Si MIS samples. The model lines were obtained using equation 4-29 and the data from Figure 4-4. The blue star represents the experimental data point for the Ir/HfO_2/n-Si system with the optimal 2 nm HfO_2, and the green star represents the Ir/n-Si system without an insulator. The blue and green arrows correspond to the ~70 mV V_{losses} associated with nonidealities in the system as described in the text. The black arrow represents additional V_{losses} totaling 80 mV. The gray star represents a system that achieves the photovoltage upper limit of the flat-band potential, which can be obtained if the tunnel probability is less than 0.0001 (assuming no changes to J_{ph}). (b) Modeled V_{losses} as a function of photocurrent and ideality factor. The dashed line represents the photocurrent observed experimentally for Ir/HfO_2/n-Si photoelectrocatalysts.

Besides the dominant role of the insulator physical thickness and tunneling probabilities as well as system nonidealities, there are also losses associated with the photocurrent and light absorption in the semiconductor (J_{ph} in equation 4-29). The maximum photocurrent that can be obtained for Si under 1-sun illumination is ~44 mA/cm^2.[47] However, parasitic light absorption and reflection from the Ir catalyst layer (which was not optimized for the systems studied here) significantly lowers the photocurrent. The photocurrent for our samples was ~24 mA/cm^2, leading to photovoltage losses of 20-30 mV associated with the poor utilization of light (Figure 4-10b). The above discussion has assumed 1-sun illumination, but it is also worth noting that using concentrated light can result in higher photovoltages approaching the flat-band potential as well, although other considerations like temperature, resistance, and recombination pathways are additional complications to consider under high-injection of charge carriers.[34,48–50]

4.9 Conclusion

This work has allowed us to identify different parameters that play critical roles in the performance of these systems. Furthermore, through the combined experimental measurements and modeling we can identify the best approaches that can be employed to improve the performance of these systems. For example, our work on planar Ir/n-Si systems has shown that the introduction of an HfO_2 insulator and optimizing its thickness results in significantly increased photovoltage (in this case by ~160 mV). We also learned that these increases in photovoltage are not sufficient to approach the upper performance limits of the flat-band potential (in this case, the maximum measured photovoltage was ~150 mV lower than flat-band). We showed that these additional loses can be minimized by a combination of improving light absorption by the semiconductor (up to 30 mV under 1-sun illumination), removing nonidealities (up to 70 mV), and incorporating a different insulator with an improved carrier selectivity (up to

150 mV). Figure 4-11a illustrates the extent to which each of these factors can improve the photovoltage up to the flat-band potential. The above discussions and results of this work can help enable the overarching goal to develop a stable, efficient, and economical tandem system that is submerged in electrolyte to split water upon solar illumination. The next chapter addresses some of the key fabrication strategies to optimize the photovoltage.

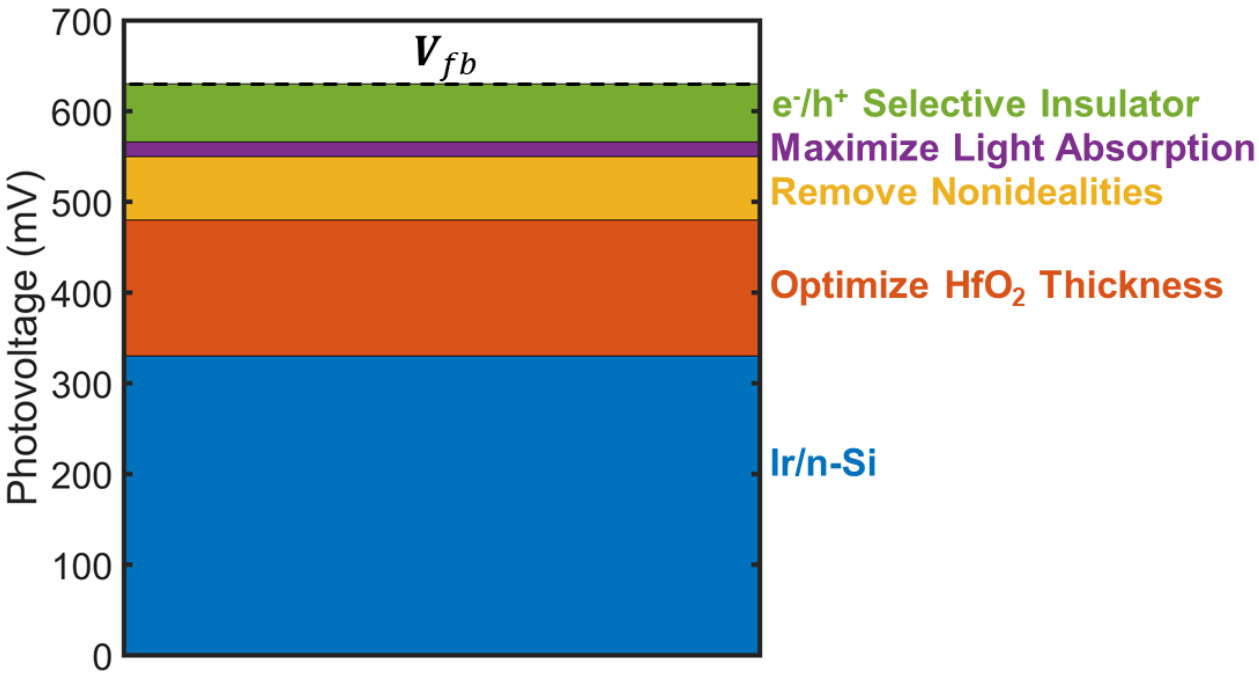

Figure 4-11. (a) Components that contribute to the photovoltage and the losses relative to the upper limit of the flat-band potential for the Ir/HfO_2/n-Si system. (b) Experimental photocurrent (relative to bare Si) for samples with Pt nanoparticles either deposited on the Si or embedded in the Si.

4.10 References

(1) Nellist, M. R.; Laskowski, F. A. L.; Lin, F.; Mills, T. J.; Boettcher, S. W. Semiconductor–Electrocatalyst Interfaces: Theory, Experiment, and Applications in Photoelectrochemical Water Splitting. *Acc. Chem. Res.* **2016**, *49* (4), 733–740. https://doi.org/10.1021/acs.accounts.6b00001.

(2) Chen, Z.; Dinh, H. N.; Miller, E. *Photoelectrochemical Water Splitting*; SpringerBriefs in Energy; Springer New York: New York, NY, 2013. https://doi.org/10.1007/978-1-4614-8298-7.

(3) F. Lichterman, M.; Hu, S.; H. Richter, M.; J. Crumlin, E.; Axnanda, S.; Favaro, M.; Drisdell, W.; Hussain, Z.; Mayer, T.; S. Brunschwig, B.; S. Lewis, N.; Liu, Z.; Lewerenz, H.-J. Direct Observation of the Energetics at a Semiconductor/Liquid Junction by Operando X-Ray Photoelectron Spectroscopy. *Energy Environ. Sci.* **2015**, *8* (8), 2409–2416. https://doi.org/10.1039/C5EE01014D.

(4) Wu, X.; Yang, E. S. Effective Metal Screening and Schottky-Barrier Formation in Metal-GaAs Structures. *IEEE Electron Device Lett.* **1990**, *11* (7), 315–317. https://doi.org/10.1109/55.56486.

(5) Rhoderick, E. H. Metal-Semiconductor Contacts. *IEE Proc. - Solid-State Electron Devices* **1982**, *129* (1), 1-. https://doi.org/10.1049/ip-i-1.1982.0001.

(6) Würfel, U.; Cuevas, A.; Würfel, P. Charge Carrier Separation in Solar Cells. *IEEE J. Photovolt.* **2015**, *5* (1), 461–469. https://doi.org/10.1109/JPHOTOV.2014.2363550.

(7) Walter, M. G.; Warren, E. L.; McKone, J. R.; Boettcher, S. W.; Mi, Q.; Santori, E. A.; Lewis, N. S. Solar Water Splitting Cells. *Chem. Rev.* **2010**, *110* (11), 6446–6473. https://doi.org/10.1021/cr1002326.

(8) Quinn, J.; Hemmerling, J.; Linic, S. Guidelines for Optimizing the Performance of Metal–Insulator–Semiconductor (MIS) Photoelectrocatalytic Systems by Tuning the Insulator Thickness. *ACS Energy Lett.* **2019**, *4* (11), 2632–2638. https://doi.org/10.1021/acsenergylett.9b01609.

(9) Esposito, D. V.; Levin, I.; Moffat, T. P.; Talin, A. A. H2 Evolution at Si-Based Metal–Insulator–Semiconductor Photoelectrodes Enhanced by Inversion Channel Charge Collection and H Spillover. *Nat. Mater.* **2013**, *12* (6), 562–568. https://doi.org/10.1038/nmat3626.

(10) Ji, L.; McDaniel, M. D.; Wang, S.; Posadas, A. B.; Li, X.; Huang, H.; Lee, J. C.; Demkov, A. A.; Bard, A. J.; Ekerdt, J. G.; Yu, E. T. A Silicon-Based Photocathode for Water Reduction with an Epitaxial $SrTiO_3$ Protection Layer and a Nanostructured Catalyst. *Nat. Nanotechnol.* **2015**, *10* (1), 84–90. https://doi.org/10.1038/nnano.2014.277.

(11) Handbook of Chemistry and Physics 100th Edition http://hbcponline.com/faces/contents/ContentsSearch.xhtml;jsessionid=B7D30DEC4C32CE3BC96D26E96D946820 (accessed 2019 -08 -25).

(12) McCrory, C. C. L.; Jung, S.; Peters, J. C.; Jaramillo, T. F. Benchmarking Heterogeneous Electrocatalysts for the Oxygen Evolution Reaction. *J. Am. Chem. Soc.* **2013**, *135* (45), 16977–16987. https://doi.org/10.1021/ja407115p.

(13) Jung, S.; L. McCrory, C. C.; M. Ferrer, I.; C. Peters, J.; F. Jaramillo, T. Benchmarking Nanoparticulate Metal Oxide Electrocatalysts for the Alkaline Water Oxidation Reaction. *J. Mater. Chem. A* **2016**, *4* (8), 3068–3076. https://doi.org/10.1039/C5TA07586F.

(14) Laskowski, F. A. L.; Oener, S. Z.; Nellist, M. R.; Gordon, A. M.; Bain, D. C.; Fehrs, J. L.; Boettcher, S. W. Nanoscale Semiconductor/Catalyst Interfaces in Photoelectrochemistry. *Nat. Mater.* **2020**, *19* (1), 69–76. https://doi.org/10.1038/s41563-019-0488-z.

(15) Li, S.; She, G.; Chen, C.; Zhang, S.; Mu, L.; Guo, X.; Shi, W. Enhancing the Photovoltage of Ni/n-Si Photoanode for Water Oxidation through a Rapid Thermal Process. *ACS Appl. Mater. Interfaces* **2018**, *10* (10), 8594–8598. https://doi.org/10.1021/acsami.7b16986.

(16) Coe, D. J.; Rhoderick, E. H. Silicide Formation in Ni-Si Schottky Barrier Diodes. *J. Phys. Appl. Phys.* **1976**, *9* (6), 965–972. https://doi.org/10.1088/0022-3727/9/6/009.

(17) The Physics and Chemistry of the Schottky Barrier Height. *Appl. Phys. Rev.* **2014**, *1* (1), 011304. https://doi.org/10.1063/1.4858400.

(18) Ohdomari, I.; Tu, K. N.; d'Heurle, F. M.; Kuan, T. S.; Petersson, S. Schottky-barrier Height of Iridium Silicide. *Appl. Phys. Lett.* **1978**, *33* (12), 1028–1030. https://doi.org/10.1063/1.90256.

(19) Wagner, L. F.; Young, R. W.; Sugerman, A. A Note on the Correlation between the Schottky-Diode Barrier Height and the Ideality Factor as Determined from I-V Measurements. *IEEE Electron Device Lett.* **1983**, *4* (9), 320–322. https://doi.org/10.1109/EDL.1983.25748.

(20) Card, H. C.; Rhoderick, E. H. Studies of Tunnel MOS Diodes I. Interface Effects in Silicon Schottky Diodes. *J. Phys. Appl. Phys.* **1971**, *4* (10), 1589. https://doi.org/10.1088/0022-3727/4/10/319.

(21) Quinn, J.; Hemmerling, J.; Linic, S. Maximizing Solar Water Splitting Performance by Nanoscopic Control of the Charge Carrier Fluxes across Semiconductor–Electrocatalyst Junctions. *ACS Catal.* **2018**, *8* (9), 8545–8552. https://doi.org/10.1021/acscatal.8b01929.

(22) Hemmerling, J.; Quinn, J.; Linic, S. Quantifying Losses and Assessing the Photovoltage Limits in Metal–Insulator–Semiconductor Water Splitting Systems. *Adv. Energy Mater.* **2020**, *10* (12), 1903354. https://doi.org/10.1002/aenm.201903354.

(23) Digdaya, I. A.; Trześniewski, B. J.; Adhyaksa, G. W. P.; Garnett, E. C.; Smith, W. A. General Considerations for Improving Photovoltage in Metal–Insulator–Semiconductor Photoanodes. *J. Phys. Chem. C* **2018**, *122* (10), 5462–5471. https://doi.org/10.1021/acs.jpcc.7b11747.

(24) Liu, X. X.; Sites, J. R. Solar-cell Collection Efficiency and Its Variation with Voltage. *J. Appl. Phys.* **1994**, *75* (1), 577–581. https://doi.org/10.1063/1.355842.

(25) Ng, K. K.; Card, H. C. Asymmetry in the SiO2 Tunneling Barriers to Electrons and Holes. *J. Appl. Phys.* **1980**, *51* (4), 2153–2157. https://doi.org/10.1063/1.327888.

(26) Scheuermann, A. G.; Lawrence, J. P.; Kemp, K. W.; Ito, T.; Walsh, A.; Chidsey, C. E. D.; Hurley, P. K.; McIntyre, P. C. Design Principles for Maximizing Photovoltage in Metal-

Oxide-Protected Water-Splitting Photoanodes. *Nat. Mater.* **2016**, *15* (1), 99–105. https://doi.org/10.1038/nmat4451.

(27) Quinn, J.; Hemmerling, J.; Linic, S. Maximizing Solar Water Splitting Performance by Nanoscopic Control of the Charge Carrier Fluxes across Semiconductor–Electrocatalyst Junctions. *ACS Catal.* **2018**, *8* (9), 8545–8552. https://doi.org/10.1021/acscatal.8b01929.

(28) Olsen, L. C. Model Calculations for Metal-Insulator-Semiconductor Solar Cells. *Solid-State Electron.* **1977**, *20* (9), 741–751. https://doi.org/10.1016/0038-1101(77)90002-8.

(29) Green, M. A. Limits on the Open-Circuit Voltage and Efficiency of Silicon Solar Cells Imposed by Intrinsic Auger Processes. *IEEE Trans. Electron Devices* **1984**, *31* (5), 671–678. https://doi.org/10.1109/T-ED.1984.21588.

(30) Shockley, W.; Queisser, H. J. Detailed Balance Limit of Efficiency of P-n Junction Solar Cells. *J. Appl. Phys.* **1961**, *32* (3), 510–519. https://doi.org/10.1063/1.1736034.

(31) Kowalczewski, P.; Andreani, L. C. Towards the Efficiency Limits of Silicon Solar Cells: How Thin Is Too Thin? *Sol. Energy Mater. Sol. Cells* **2015**, *143*, 260–268. https://doi.org/10.1016/j.solmat.2015.06.054.

(32) Card, H. C.; Rhoderick, E. H. Studies of Tunnel MOS Diodes I. Interface Effects in Silicon Schottky Diodes. *J. Phys. Appl. Phys.* **1971**, *4* (10), 1589–1601. https://doi.org/10.1088/0022-3727/4/10/319.

(33) Crowell, C. R.; Sze, S. M. Current Transport in Metal-Semiconductor Barriers. *Solid-State Electron.* **1966**, *9* (11), 1035–1048. https://doi.org/10.1016/0038-1101(66)90127-4.

(34) Hankin, A.; E. Bedoya-Lora, F.; C. Alexander, J.; Regoutz, A.; H. Kelsall, G. Flat Band Potential Determination: Avoiding the Pitfalls. *J. Mater. Chem. A* **2019**, *7* (45), 26162–26176. https://doi.org/10.1039/C9TA09569A.

(35) Handbook of Chemistry and Physics 100th Edition http://hbcponline.com/faces/contents/ContentsSearch.xhtml;jsessionid=B7D30DEC4C32CE3BC96D26E96D946820 (accessed 2019 -08 -25).

(36) Crowell, C. R.; Beguwala, M. Recombination Velocity Effects on Current Diffusion and Imref in Schottky Barriers. *Solid-State Electron.* **1971**, *14* (11), 1149–1157. https://doi.org/10.1016/0038-1101(71)90027-X.

(37) Holewinski, A.; Linic, S. Elementary Mechanisms in Electrocatalysis: Revisiting the ORR Tafel Slope. *J. Electrochem. Soc.* **2012**, *159* (11), H864. https://doi.org/10.1149/2.022211jes.

(38) Chand, S.; Kumar, J. Current Transport in Pd2Si/n-Si(100) Schottky Barrier Diodes at Low Temperatures. *Appl. Phys. A* **1996**, *63* (2), 171–178. https://doi.org/10.1007/BF01567646.

(39) Sah, C.; Noyce, R. N.; Shockley, W. Carrier Generation and Recombination in P-N Junctions and P-N Junction Characteristics. *Proc. IRE* **1957**, *45* (9), 1228–1243. https://doi.org/10.1109/JRPROC.1957.278528.

(40) Nussbaum, A. Generation-Recombination Characteristic Behavior of Silicon Diodes. *Phys. Status Solidi A* **1973**, *19* (2), 441–450. https://doi.org/10.1002/pssa.2210190207.

(41) Wittmer, M. Conduction Mechanism in PtSi/Si Schottky Diodes. *Phys. Rev. B* **1991**, *43* (5), 4385–4395. https://doi.org/10.1103/PhysRevB.43.4385.

(42) Recombination mechanisms and doping density in silicon: Journal of Applied Physics: Vol 54, No 7 https://aip.scitation.org/doi/abs/10.1063/1.332568 (accessed 2019 -08 -23).

(43) Werner, J. H.; Güttler, H. H. Barrier Inhomogeneities at Schottky Contacts. *J. Appl. Phys.* **1991**, *69* (3), 1522–1533. https://doi.org/10.1063/1.347243.

(44) Temperature dependence of characteristic parameters of the H-terminated Sn/p-Si(1 0 0) Schottky contacts - ScienceDirect https://www.sciencedirect.com/science/article/pii/S0169433203005646 (accessed 2019 -08 -23).

(45) Hiremath, R. K.; Rabinal, M. K.; Mulimani, B. G.; Khazi, I. M. Molecularly Controlled Metal−Semiconductor Junctions on Silicon Surface: A Dipole Effect. *Langmuir* **2008**, *24* (19), 11300–11306. https://doi.org/10.1021/la800882e.

(46) Bersch, E.; Rangan, S.; Bartynski, R. A.; Garfunkel, E.; Vescovo, E. Band Offsets of Ultrathin High-$\ensuremath{\kappa}$ Oxide Films with Si. *Phys. Rev. B* **2008**, *78* (8), 085114. https://doi.org/10.1103/PhysRevB.78.085114.

(47) Fan, R.; Mi, Z.; Shen, M. Silicon Based Photoelectrodes for Photoelectrochemical Water Splitting. *Opt. Express* **2019**, *27* (4), A51–A80. https://doi.org/10.1364/OE.27.000A51.

(48) Khan, M. A.; Al-Shankiti, I.; Ziani, A.; Wehbe, N.; Idriss, H. A Stable Integrated Photoelectrochemical Reactor for H2 Production from Water Attains a Solar-to-Hydrogen Efficiency of 18 % at 15 Suns and 13 % at 207 Suns. *Angew. Chem.* **2020**, *132* (35), 14912–14918. https://doi.org/10.1002/ange.202002240.

(49) Ziani, A.; Al-Shankiti, I.; Khan, M. A.; Idriss, H. Integrated Photo-Electrocatalytic (PEC) Systems for Water Splitting to Hydrogen and Oxygen under Concentrated Sunlight: Effect of Internal Parameters on Performance. *Energy Fuels* **2020**, *34* (10), 13179–13185. https://doi.org/10.1021/acs.energyfuels.0c02481.

(50) Gomes, W. P.; Cardon, F. Electron Energy Levels in Semiconductor Electrochemistry. *Prog. Surf. Sci.* **1982**, *12* (2), 155–215. https://doi.org/10.1016/0079-6816(82)90002-8.

Chapter 5

Strategies for Optimizing the Photovoltage of MIS photoelectrocatalysts

5.1 Introduction

New fundamental insights about MIS photoelectrocatalysts have been obtained from the thorough experimental and theoretical analyses in Chapters 3 and 4. So far, the primary strategy to optimize the photovoltage for the MIS systems has focused on tuning the insulator thickness which modulates the recombination flux of the charge carriers.[1–4] The work in Chapters 3 and 4, however, demonstrate that tuning the insulator thickness, while significantly improving the photovoltage, is not sufficient for Ir/HfO_2/n-Si systems to approach the photovoltage limits. Based on the theoretical analysis, the major obstacles preventing the systems from approaching their limits are (1) the presence of defect states at the interfaces and (2) the use of insulators that are not sufficiently selective for the desired charge carriers. Another opportunity for increasing the photovoltage is by increasing the flat-band potential (i.e., the upper photovoltage limit). This chapter provides design guidelines and insights on some of the key strategies to optimize the photovoltage of MIS photoelectrocatalysts.

5.2 Increasing Flat-band Potential

A higher flat-band potential means that a higher maximum photovoltage can be extracted from a system. As previously discussed, the flat-band potential for the ideal case is simply defined as the difference between the metal and the semiconductor Fermi levels or work functions:

$$V_{fb} = E_m - E_s \quad (5\text{-}1)$$

For n-type systems, the flat-band potential can be increased by using a higher work function metal and/or by using a semiconductor with a lower work function, while the opposite is true for p-type systems.

5.2.1 Varying Work Function of the Metal

For the case of p-type systems for the hydrogen evolution reaction (HER), we have demonstrated the increase in the flat-band potential by utilizing different metals with low work functions. One of the challenges is that metals with low work functions are generally not good HER catalysts, so bilayer metal systems have been employed.[5–8] Our group developed MIS systems with either Pt-Ti or Pt-Al as the metal bilayer component on HfO_2/p-Si.[7] In these systems, Pt is the top metal which serves as the HER catalyst, while Ti and Al are the underlayer metals which set the barrier height and flat-band potential. On the basis of the tabulated work function values, Al (work function of ~4.06–4.26 eV[9]) is expected to generate a higher flat-band potential with p-Si compared to that with Ti (work function of ~4.33 eV[10]).

The flat-band potential and the semiconductor doping density for the Al and Ti based systems with varied HfO_2 thickness were evaluated using the Mott-Schottky method in a ferri/ferrocyanide redox solution (details in Chapter 2). The barrier heights of the MIS systems are then measured using the following equation that was also described in Chapter 4:

$$\phi_{b,ideal} = V_{fb} + V_n = V_{fb} + \frac{kT}{q} ln \frac{N_C}{N_D} \quad (5\text{-}2)$$

The resulting barrier height data for each system is provided Figure 5-1. The barrier heights for the Al-containing samples (median 0.97eV) was ~100 mV larger than the barrier heights for the Ti-containing samples (median 0.86eV). Since all samples have the same semiconductor doping density, it is evident that the flat-band potential is also ~100 mV larger for the Al-based samples.

The barrier heights and the flat-band potentials are also not strongly dependent on the insulator thickness, in accordance with equations 5-1 and 5-2 which are not a function of the insulator.

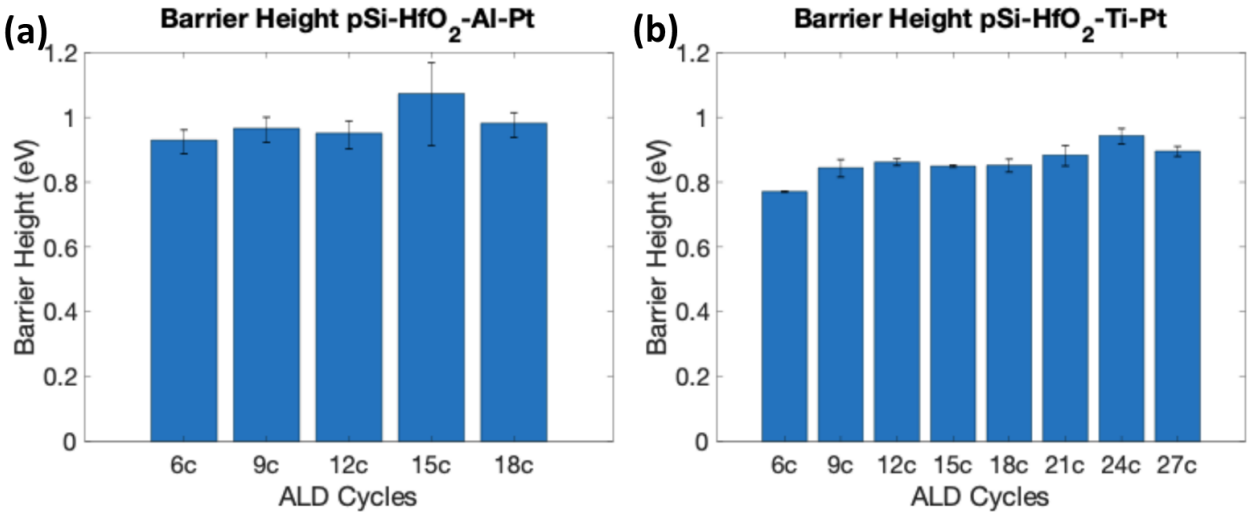

Figure 5-1: Measured barrier heights for the Al-based (a) and Ti-based (b) MIS systems as a function of the number of ALD cycles which govern the thickness of the HfO_2 insulator layer

The increased flat-band potential and barrier height have significant implications on the photovoltage as a function of HfO_2 thickness. Data in Figure 5-2 show the LSVs and generated open-circuit photovoltages for each of the systems. The Al-containing system, with the higher flat-band potential and barrier height, achieves a higher photovoltage (285 mV) compared to the Ti-containing sample (167 mV). This difference corresponds with the difference in the barrier height and matches the theoretical expectations from Chapter 4. The Al and Ti-based samples also exhibit different responses when varying the HfO_2 insulator layer. Both samples improve from adding an insulator, but the optimal insulator thickness is different (1.9 nm for the Al-based system compared to 2.6 nm for the Ti-based system). In other words, the systems with different barrier heights have inherently different levels of recombination, and the low-barrier system requires a thicker HfO_2 layer to sufficiently decrease the recombination. Ultimately both systems generate similar photovoltages of ~515 mV after optimizing the insulator thickness. These

trends were corroborated with a comprehensive finite-difference time-domain (FDTD) model that iteratively solves the two governing equations for the transfer of charge carriers in these systems, Poisson's and the continuity equations.[1,7,11,12] This numerical model also qualitatively agrees with the analytical modeling in Chapter 4.

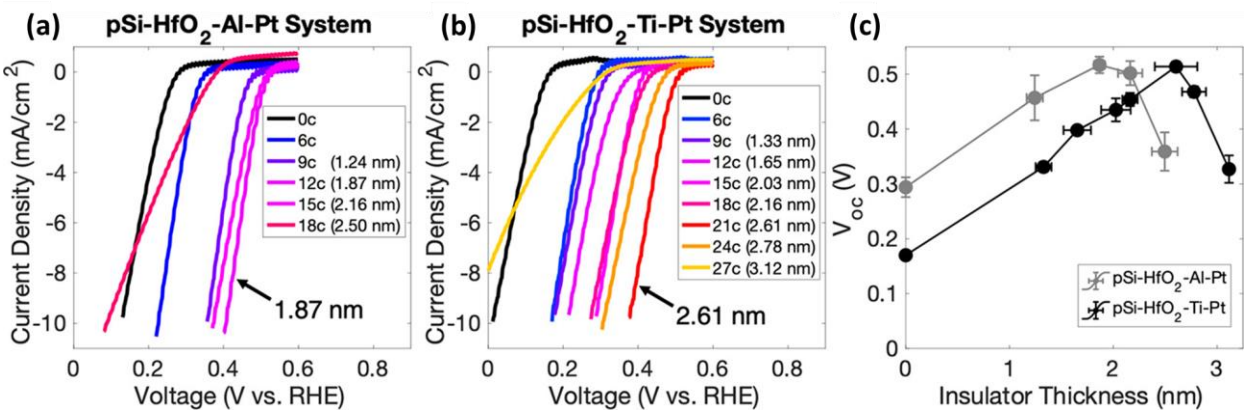

Figure 5-2: Electrochemical performance of the photocathodes in light-driven HER. (a,b) Linear sweep voltammograms of the pSi-HfO_2–Al–Pt and pSi-HfO_2–Ti–Pt electrodes at various insulator thicknesses. (a) The photovoltage of the pSi-HfO_2–Al–Pt samples improves with insulator thickness up to 1.9 nm and decreases thereafter. The photovoltage for the highest-performing insulator thickness is 517 mV. (b) The pSi-HfO_2–Ti–Pt samples show improving photovoltage up to 2.6 nm, after which it decreases. The photovoltage for the highest-performing insulator thickness is 514 mV. (c) V_{oc} for the pSi-HfO_2–Al–Pt and pSi-HfO_2–Ti–Pt samples plotted as a function of increasing insulator thickness.

5.2.2 Increasing Semiconductor Doping Density

For a given semiconductor, the Fermi level and work function can be modified by varying the doping density in the semiconductor. Mott-Schottky plots were once again used to evaluate the flat-band potential for Ir/HfO_2/n-Si systems with a different semiconductor doping densities (low-doped ~5 ohm-cm resistivity compared to high-doped ~0.5 ohm-cm resistivity). In Figure 5-3a, it is clear that the doping density significantly impacts the slope of the Mott-Schottky plots, as expected from the Mott-Schottky equation. The closeup region in Figure 5-3b

near the x-axis shows that the flat-band potential is increased by nearly 100 mV (shifted to the left) for the higher doping density.

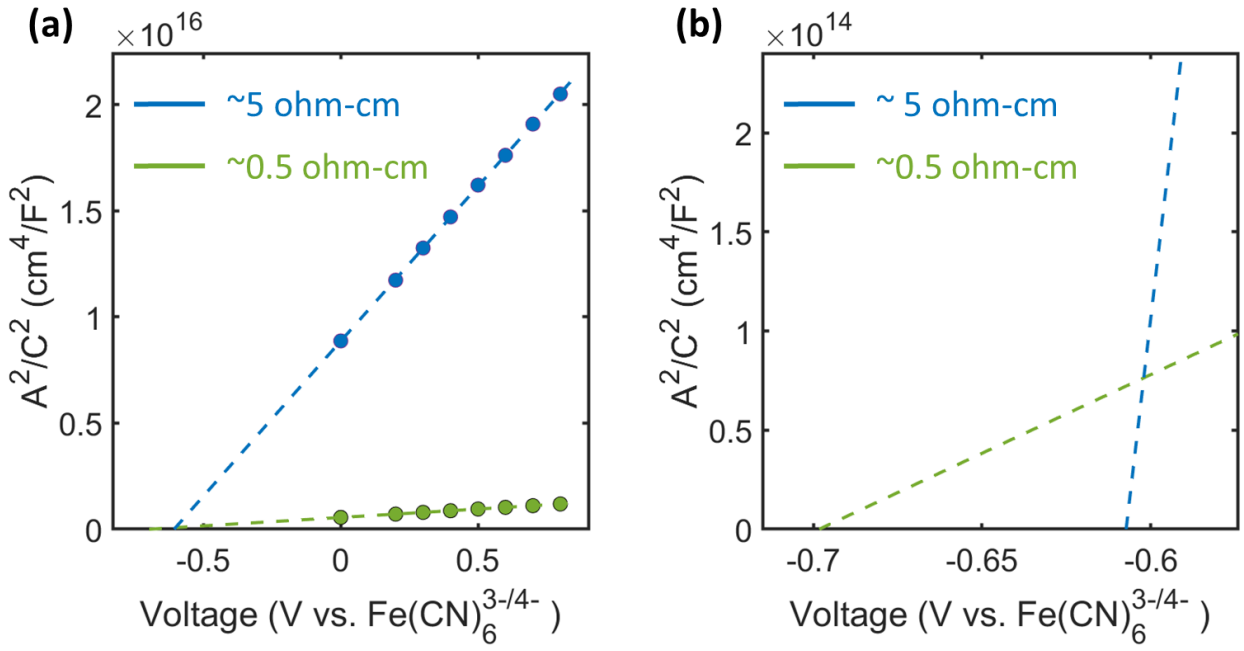

Figure 5-3: Mott-Schottky plots for Ir/19-cycle HfO_2/n-Si systems with a different semiconductor doping densities (~5 ohm-cm resistivity compared to ~0.5 ohm-cm resistivity). The right side is a closeup of the figure near the x-intercept which shows that the flat-band potential is increased by nearly 100 mV from increasing the semiconductor doping density.

It is important to note that large changes to the semiconductor doping density can also impact the minority diffusion length and the photo-limited current, and it can also impact the recombination current, introducing alternative recombination mechanisms like Auger recombination or thermionic field emission as the semiconductor behaves more like a metal from the higher doping.[13–17] Overall, there is a tradeoff between the increased flat-band potential and these other losses from the increased semiconductor doping density. The higher doped Si of ~0.5 ohm-cm explored herein significantly increases the flat-band potential, and yet is not too highly doped to result in other losses. Indeed, the highest photovoltages in the literature have been

obtained with similarly doped Si.[18,19] The remainder of this chapter uses the higher doped n-Si with resistivity of ~0.5 ohm-cm used in MIS architecture for the water oxidation reaction.

5.3 Characteristics and Performance of Systems with Higher Doped n-Si

Before identifying the approaches to optimize the photovoltage, the experimental performance of the MIS photoelectrocatalysts on higher doped Si must first be evaluated. Besides HfO_2, an additional insulator layer, Al_2O_3 is explored in this section. Al_2O_3 has been previously studied in MIS systems water oxidation to achieve high performance, but the tunneling properties and ideality factor are typically not evaluated.[2,4,19–23] 20 cycles for both HfO_2 and Al_2O_3 were used during the fabrication of the MIS systems which yields the optimal thickness of about 2 nm. Thus, the two studied systems are Ir/20cyc Al_2O_3/n-Si (higher doped) and Ir/20cyc HfO_2/n-Si (higher doped), and the only difference between these systems is the insulator layer component.

Data in Figure 5-4 shows the measured open-circuit photovoltages (V_{oc}), flat-band potential (V_{fb}) and voltage losses (i.e., $V_{losses} = V_{fb} - V_{oc}$) for the HfO_2-containing and Al_2O_3-containing MIS photoelectrocatalysts. Both systems have the same flat-band potential (~0.74 eV) which is expected from equation 5-1 because both systems include the same Ir metal and similar Si doping densities. The system with Al_2O_3 outperforms the HfO_2 system by about 75 mV. In other words, the Al_2O_3 system is closer by ~75 mV to achieving the upper photovoltage of the flat-band potential and therefore exhibits lower V_{losses}.

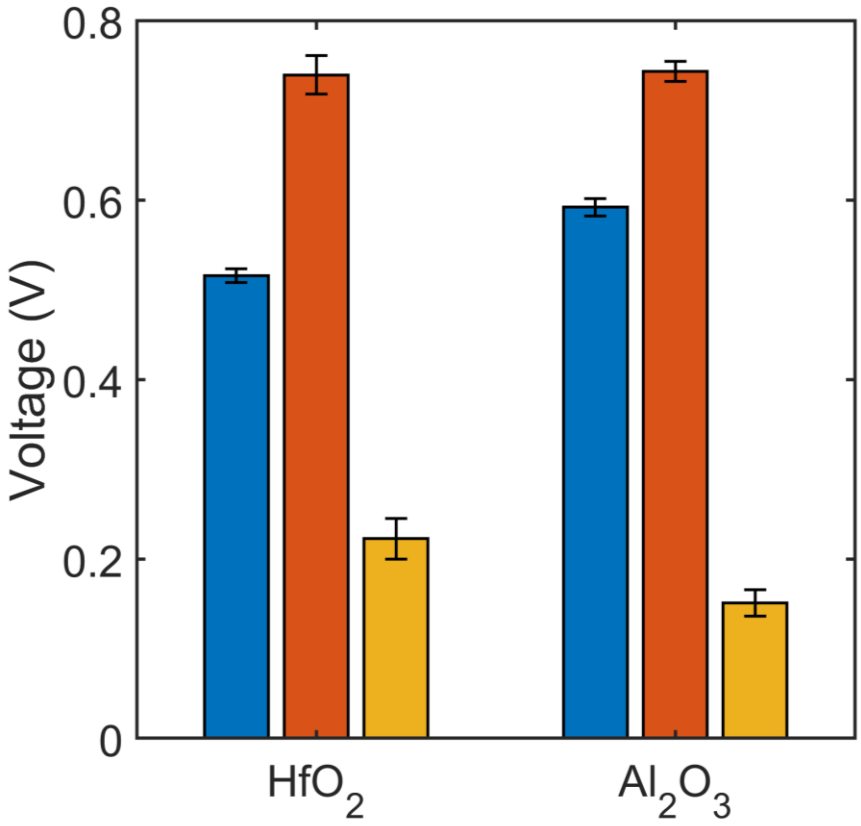

Figure 5-4: Experimental open-circuit photovoltage (blue), flat-band potential (orange), and V_{losses} (yellow) for the HfO_2-containing and Al2O3-containing MIS photoelectrocatalysts.

To evaluate if these voltage losses are related to the presence of nonidealities, the ideality factor and recombination current was also measured by varying the light intensity. The results are shown in Figure 5-5. Interestingly, the ideality factor is the same value of ~1.6 for both the HfO_2 and Al_2O_3 MIS samples (Figure 5-5a). On the other hand, the Al_2O_3 sample has significantly lower reverse saturation recombination current (Figure 5-5b). This suggests that Al_2O_3 is superior to HfO_2 in terms of minimizing recombination by being a better charge carrier selective insulator layer. Specifically, the tunnel probability is about an order of magnitude lower tunnerling probability term for Al_2O_3 compared to HfO_2 using the process described in Chapter 4. However, Al_2O_3 is not superior to HfO_2 in terms of minimizing the overall contributions from

nonidealities. Using the analysis from Chapter 4, it is determined that nonidealities result in up to 90 mV in losses for the HfO_2 sample and up to 55 mV in losses for the Al_2O_3 sample. Therefore, the photovoltage for Al_2O_3 and HfO_2 based MIS systems can still increase significantly if the nonidealities can be removed.

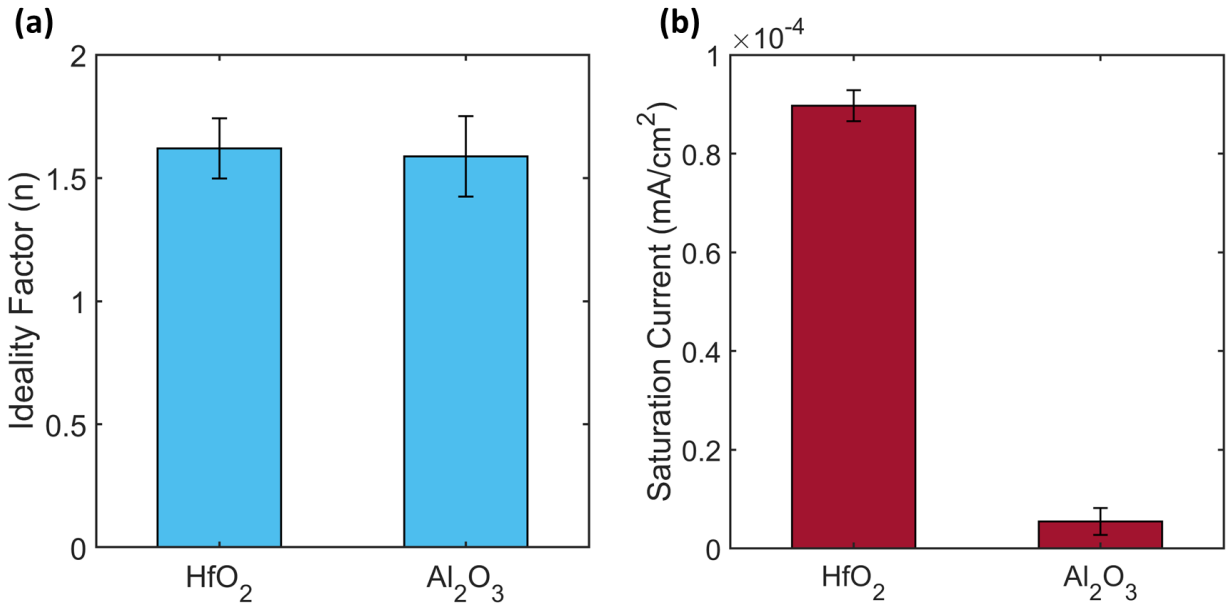

Figure 5-5: (a) Experimental ideality factors amd (b) reverse saturation recombination currents for HfO_2-containing and Al_2O_3-containing MIS photoelectrocatalysts with 20 cycles of the insulator layer.

5.4 Annealing to Remove Nonidealities

As discussed in Chapter 3, the nonidealities are probably associated with the presence of interfacial defects or surface states in the MIS systems, particularly at the insulator/semiconductor interface.[18,21,24] To passivate these defect states, the samples were rapid thermal annealed for 10 minutes under a forming gas (5% H_2 and 95% N_2) ambient environment at 300 to 500 degrees Celsius. The elevated temperatures can restructure the atoms at the insulator/semiconductor interface, and the hydrogen atoms from the gas ambient can diffuse through the insulator layer and interact with the insulator/semiconductor interface to passivate

the defect states.[18,25,26] The samples in this section were annealed after the insulator deposition, but before the metal deposition. This process is shown in Figure 5-6, and the fabrication steps are identical to non-annealed systems except for the addition of the annealing step.

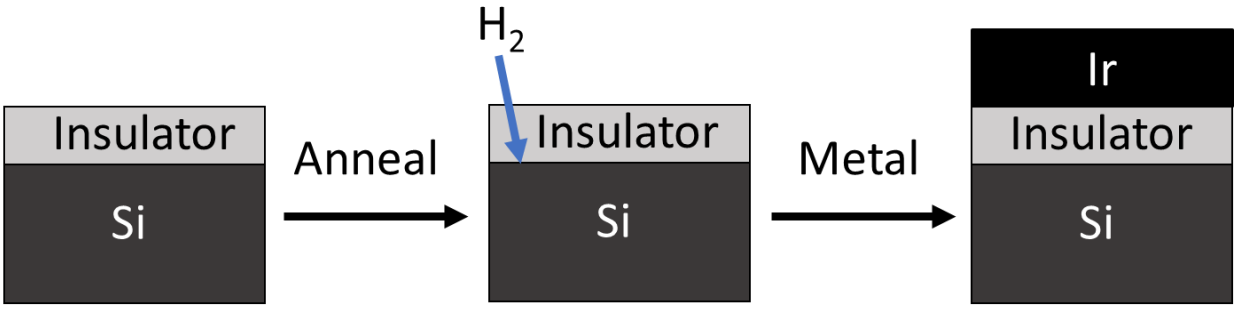

Figure 5-6: Steps in the fabrication process showing that the annealing step was performed after the insulator deposition, but before the metal deposition.

The ideality factors for both the HfO_2 and Al_2O_3 samples as a function of the annealing temperature are shown in Figure 5-7. The data shows that the ideality factor gets lower and lower (i.e., the systems become more ideal approaching n=1) as the annealing temperature increases. This indicates that the annealing process may passivate the defect states resulting in more ideal interfaces. Interestingly, the ideality factor falls below the value of 1 for the HfO_2 (n=0.93) and Al_2O_3 (n=0.71) samples after annealing at 500 degrees Celsius. Ideality factors below the ideal value of 1 have been observed under high injection conditions from Auger recombination in pn junction Si solar cells.[15] However, Auger recombination is not expected to be prevalent in the current systems under 1 sun-illumination and the relative low semiconductor doping density compared to pn junction Si solar cells. It is worth noting that the samples annealed at 500 degrees Celsius were also more resistive than the other samples, so it is also possible that the additional resistance interferes with the measurement for the ideality factor or that the systems have alternative recombination pathways that cannot be accurately captured by the simple diode

equation upon which this method is based. Overall, the annealing condition of 400 degrees Celsius results in ideality factors closest to the ideal value of 1 for both HfO_2 and Al_2O_3 MIS systems.

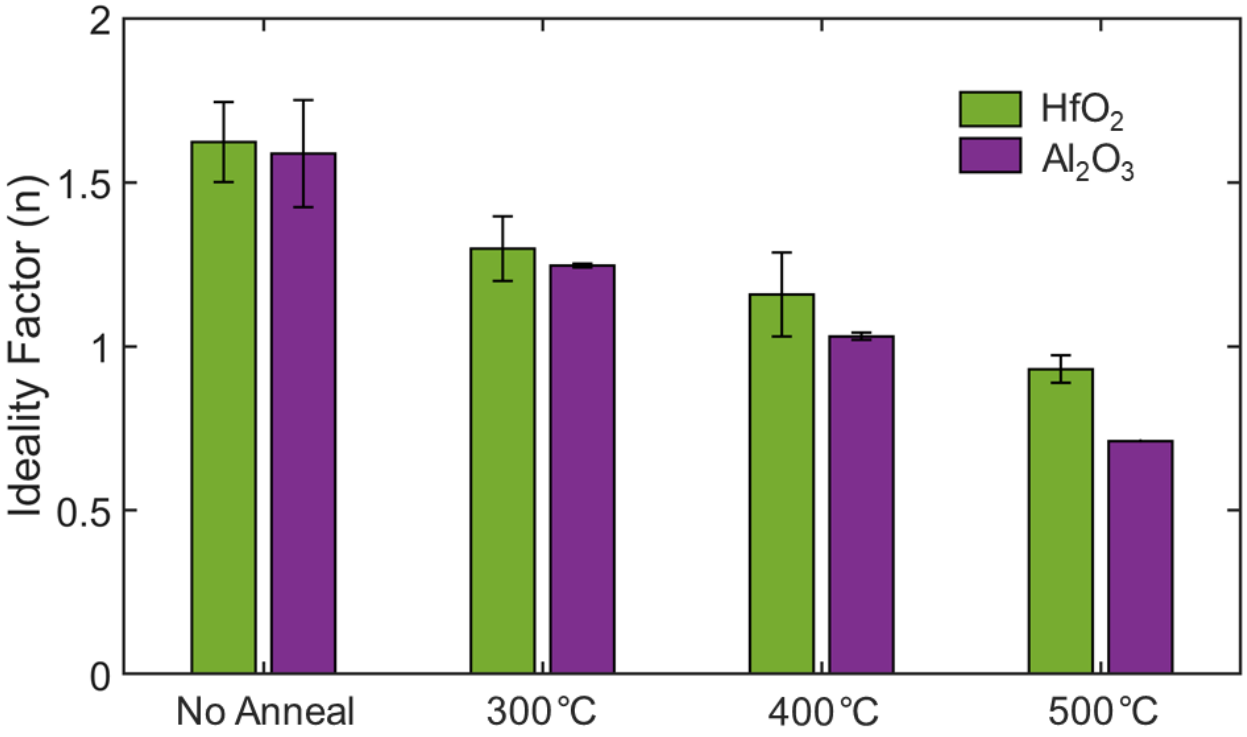

Figure 5-7: Experimental ideality factors for HfO_2-containing and Al_2O_3-containing MIS photoelectrocatalysts as a function of the annealing temperature. Samples were annealed in forming gas (5% H_2 and 95% N_2) for 10 minutes with rapid heating and cooling.

The question is if this removal of nonidealities results in an enhanced photovoltage as predicted in Chapter 4. Data in Figure 5-8 shows the photovoltage for each system as a function of the annealing temperature. For the HfO_2 systems, the optimal photovoltage is obtained from annealing at 400 degrees Celsius, which corresponds with the HfO_2 system that also is the most ideal. Specifically, the photovoltage increases from 516 mV for the non-annealed system up to 573 mV for 400°C annealed system. Of the theoretical 90 mV that that theoretically be improved by removing the nonidealities, the HfO_2 system experimentally improved by 57 mV.

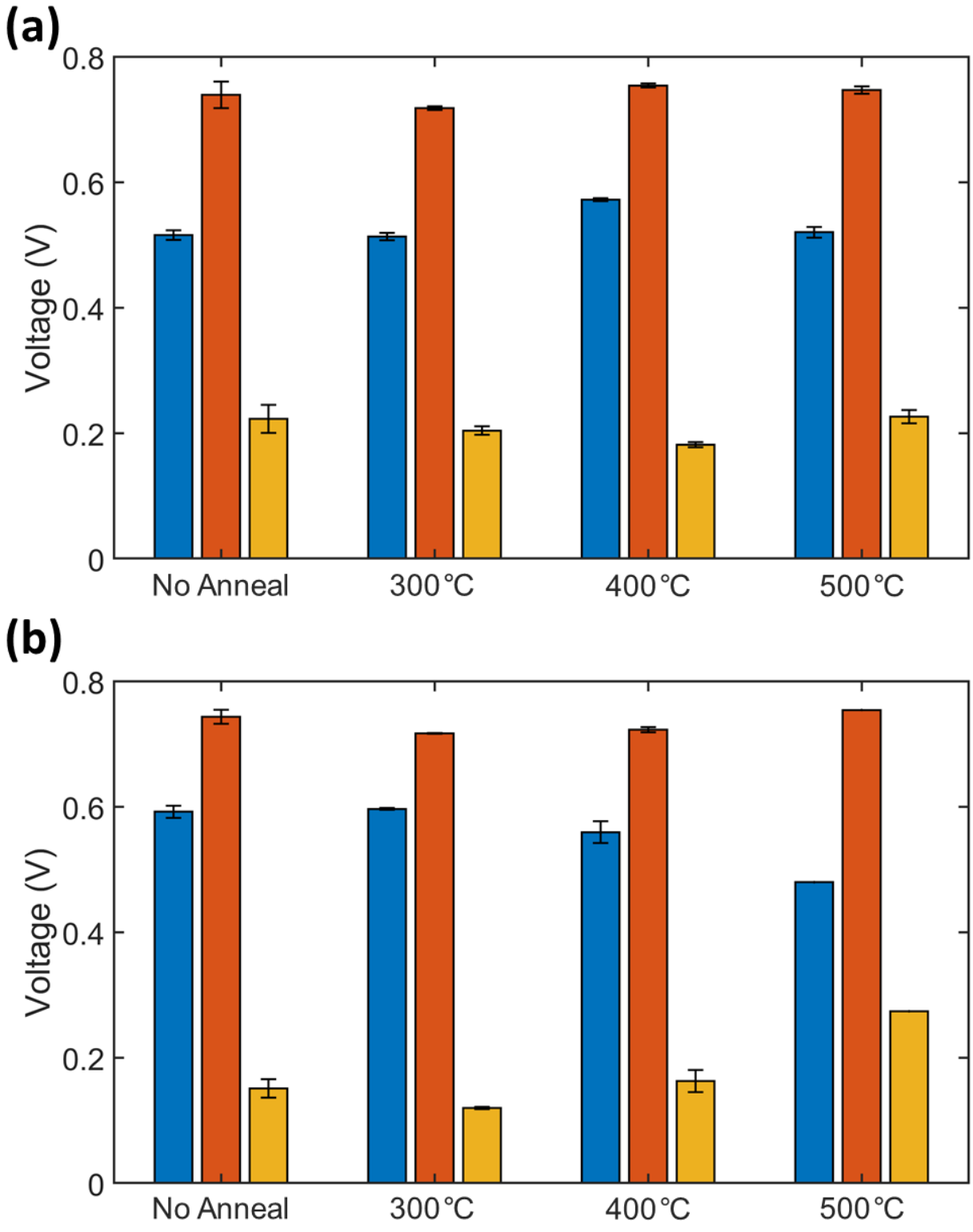

Figure 5-8: Experimental open-circuit photovoltage (blue), flat-band potential (orange), and V_{losses} (yellow) for the (a) HfO_2-containing and (b) Al2O3-containing MIS photoelectrocatalysts as a function of the annealing temperature.

In contrast, the Al_2O_3 system experiences no significant enhancement in the photovoltage from the annealing process. The highest performance of 597 mV is obtained after annealing at 200℃ which is not statistically significant over the 592 mV photovoltage for the non-annealed system (Figure 5-8b). Furthermore, the photovoltage drops to 560 mV for the 400℃ annealed system. This result is unexpected because the Al_2O_3 400℃ annealed system is very close to ideal with n=1.03. It is worth noting that the flat-band potentials are similar for all tested samples with slight variations associated with slight differences in the Si doping density between samples. Therefore, variations in the flat-band potential cannot explain any of the shifts in the photovoltage. Instead, the photovoltage losses associated with annealing, despite the idealized interfaces, is attributed to the tunneling probability of the Al_2O_3 (Figure 5-9). Specifically, the tunneling probability through the Al_2O_3 decreases by a factor of 25 after annealing at 400℃. In other words, 25 times more electrons will recombine by tunneling through the insulator. Even though the Al_2O_3 system benefits from the improved ideality factor, the severe losses from the tunneling probably result in a net loss in the photovoltage. In contrast, the tunneling probability term for the HfO_2 sample is only marginally impacted by annealing, and therefore, a photovoltage enhancement is observed due to the improved ideality factor. The reason why annealing could impact the tunneling probability is still being investigated, but the tunneling probability is dominated by the insulator thickness and the insulator conduction band offset. Therefore, tunneling probability losses are either associated with insulator thickness variation or due to changes in the insulator offsets as the amorphous insulator may become more crystalline during the annealing process.

It is also worth noting that annealing after the metal deposition (instead of just before metal deposition) as well as annealing in an oxygen ambient environment were also explored. Both approaches resulted in significant losses in performance. Annealing after the metal deposition lowers the flat-band potential, and it is likely that the metal reacts with the insulator during the annealing step which lowers the performance. Meanwhile, annealing in oxygen ambient typically results in very resistive samples. The insulator layer may grow and become more resistive as it oxidizes during the annealing step which lowers the performance.

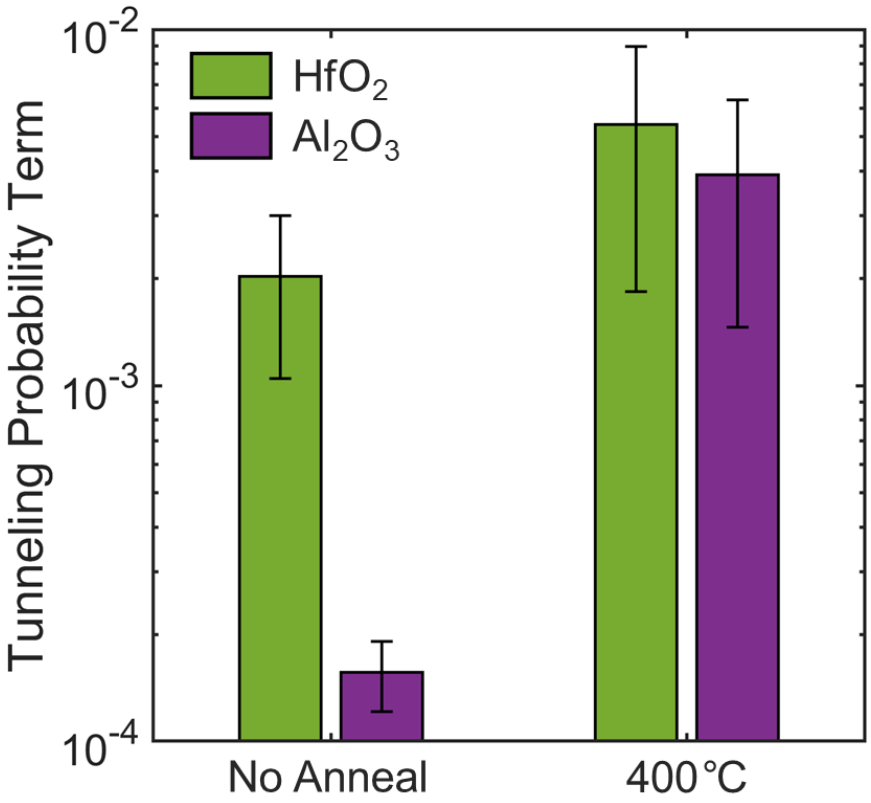

Figure 5-9: Experimental tunnel probability terms for for HfO_2-containing and Al_2O_3-containing MIS photoelectrocatalysts as a function of the annealing condition (non-annealed compared to annealed at 400 degrees Celsius).

5.5 Vary Insulator Composition to Improve Charge Carrier Selectivity

Chapter 4 also highlighted the importance of improving the charge carrier selectivity of the insulator layer in order to approach the upper photovoltage limits. The Al_2O_3 based system yielded a high photovoltage of 597 mV, but the voltage losses are still between 120 to 150 mV depending on the variation in the flat-band potential and the annealing temperature. The tunneling probability for Al_2O_3 based systems (~2 nm thick Al_2O_3) was about 1.6×10^{-4} for non-annealed samples and 2.6×10^{-4} for 300℃ annealed samples. However, to reach the upper photovoltage limit for these systems, an Al_2O_3 thickness of ~3 nm is required to sufficiently minimize the recombination rates. The challenge is that the resistance gets very large for insulators thicker than 2 nm because the holes have a difficult time to tunneling through the insulator. Therefore, the goal is to use an improved 3 nm thick insulator layer that (1) allows holes to easily tunnel through thus minimizing resistance losses and (2) prevent electrons from tunneling through thus minimize the recombination current. The strategy used herein is to vary the insulator composition by doping the Al_2O_3 layer with HfO_2 to investigate how the dopant atoms impact the charge transfer.

The fabricated samples use identical Si and Ir semiconductor and catalyst layers, and the only difference is the composition of the insulator layer. Mixtures of Al_2O_3 and HfO_2 were obtained by alternating the ALD precursor throughout the deposition. First, we started with insulators mixtures that resulted in a total of 20 cycles, so it could be directly compared with the previous samples with 20 cycles of Al_2O_3. For these initial samples the insulator consisted of 20% HfO_2 and 80% Al_2O_3 as the ALD cycle ratio of HfO_2:Al_2O_3 was 1:4. The order of the ALD cycles was also varied to see how the quality of the interfaces could change. Overall, the three general categories of insulator with a total number of 20 ALD cycles are (1) pure Al_2O_3, (2)

HfO_2:Al_2O_3 with a ratio 1:4 in which the Al_2O_3 was deposited first (denoted "20cyc Alloy Al-first"), and (3) HfO_2:Al_2O_3 with a ratio 1:4 in which the HfO_2 was deposited first (denoted "20cyc Alloy Hf-first"). An illustration of these insulators is provided in Figure 5-10.

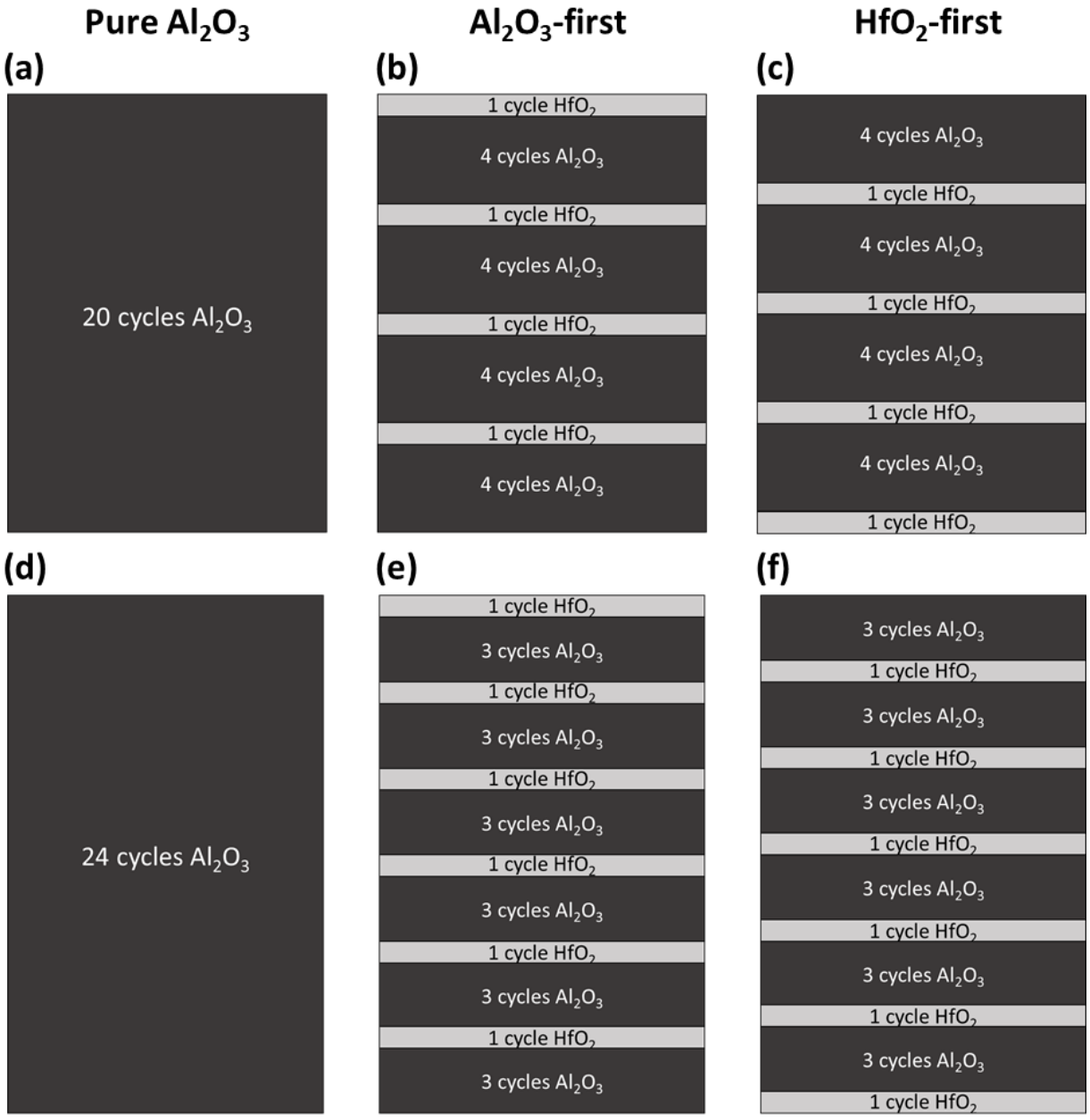

Figure 5-10: Illustration of the different insulator compositions that were investigated.

The data in Figure 5-11 shows the experimental photovoltage and flat-band potential for each of the 20 cycle insulator compositions. All samples have a similar flat-band potential which is expected because each sample has the Ir metal layer and similar Si doping density. The pure Al_2O_3 and the Al-first sample have similar photovoltage of about 590 mV while the Hf-first sample has slightly lower photovoltage of 563 mV.

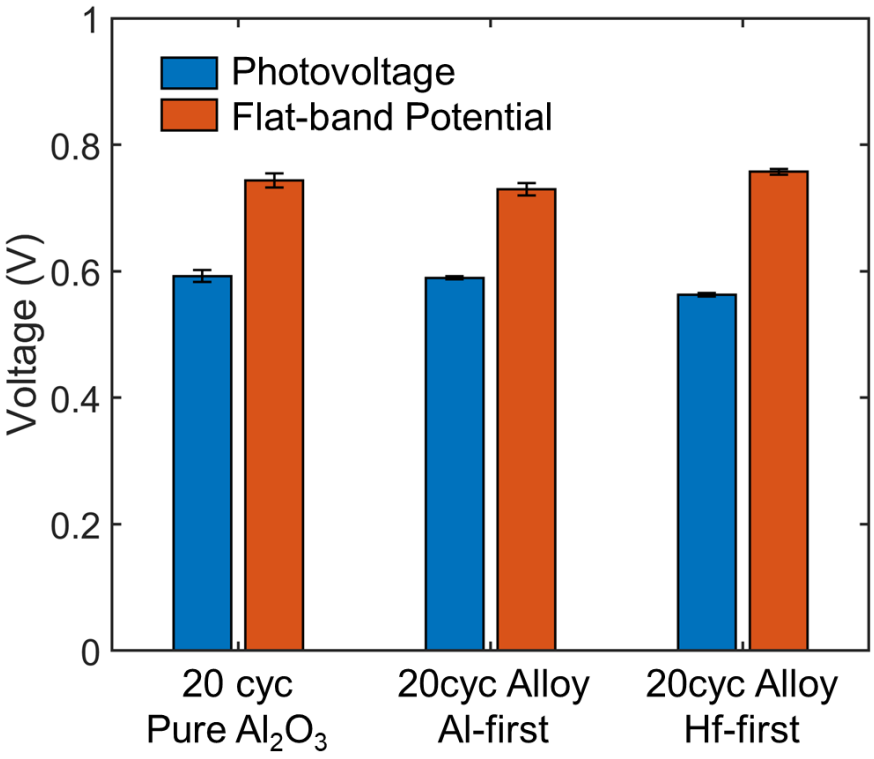

Figure 5-11: Experimental photovoltage and flat-band potential for each of the 20 cycle insulator compositions.

The data in Figure 5-12 shows the experimental ideality factor and reverse saturation recombination current for each of the 20 cycle insulator compositions. Again, the pure Al_2O_3 and the Al-first sample have similar performance in both metrics, while the Hf-first sample deviates significantly. Specifically, the Hf-first sample behaves more ideally (n=1.32) and the recombination current is lower by a factor of 2.5. Despite these promosing values, the Hf-first

sample still exhibits a lower photovoltage, ultimately because the tunneling probability is about an order of magnitude lower compared to the other samples. This lower tunneling probability is probably because the insulator layer is physically thinner as a result of poor nucleation of the HfO_2 cycle during the ALD process. Cross-sectional STEM imaging would be needed to confirm this hypothesis. It is less likely that the HfO_2 doping addition makes an intrinsic difference to the tunneling probability beside affecting the thickness, because the Al-first sample with the same 20% HfO_2 composition does not result in deviation in the tunneling probability. This analysis demonstrates that the order of the ALD cycling can have a significant impact on the overall performance.

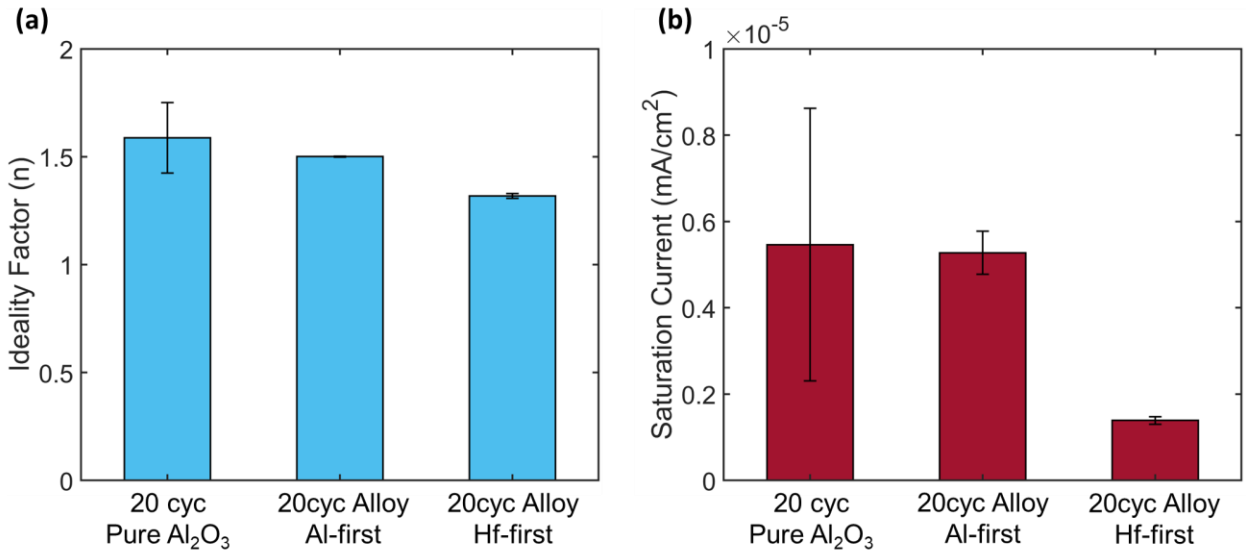

Figure 5-12: (a) Ideality factor (b) and reverse saturation recombination current for each of the 20 cycle insulator compositions.

The next step was to investigate if higher photovoltage can be obtained for thicker insulator layers, which would be possible only if the insulator is more carrier selective to allow holes to travel through without adding resistance losses. Instead of 20 total ALD cycles, now 24 total ALD cycles was used to make analogous samples to the previous ones. Also, instead of

20% HfO_2 to 80% Al_2O_3, the alloy ratio was 25% HfO_2 to 75% Al_2O_3 which is a 3:1 Al_2O_3:HfO_2 ratio (Figure 5-10d-f). The goal of using slightly higher HfO_2 doping concentration was to improve the conductivity, as thicker samples are more resistive. The compiled photovoltages for each sample are plotted in Figure 5-13. The pure Al_2O_3 with 24 cycles yields a very low photovoltage of about 180 mV, which is expected due to the significant resistance the system experiences as a result of the thicker insulator layer. Both the alloy samples exhibit higher photovoltages, with the Al-first yielding the highest photovoltage of ~320 mV. The alloy samples also experienced a lower series resistance, which is likely the reason for the higher photovoltages. This analysis is a proof of concept which demonstrates that doping or alloying the insulator layer with multiple components can improve the conductivity and performance. However, if the insulators were truly carrier selective, then the theoretical photovoltage for these thicker samples would be about 670 mV.

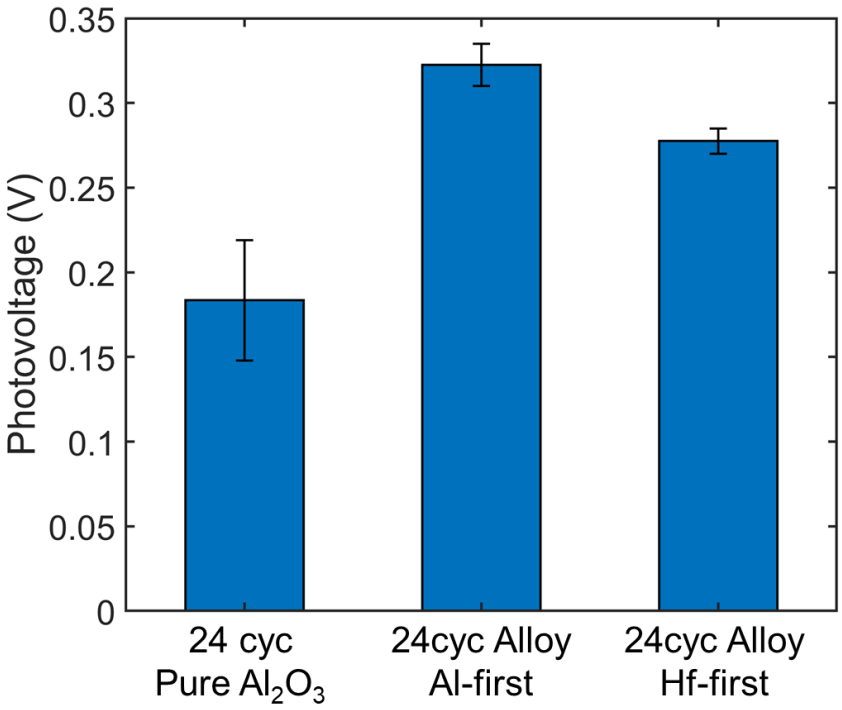

Figure 5-13: (a) Ideality factor (b) and reverse saturation recombination current for each of the 20 cycle insulator compositions.

5.6 Conclusions

This chapter focused on developing strategies to optimize the photovoltage of MIS photoelectrocatalysts. The flat-band potential was increased by varying the work function of the metal layer and by increasing the doping density of the semiconductor. Two different types of insulators were compared to identify which one results in higher performance and better tunneling probabilities. Both insulators still result in significant (>55 mV) losses from the presence of nonidealities and have an ideality factor of about 1.6. To improve the performance, the samples were annealed in forming gas at various temperatures to passivate the defect states in the interface. This resulted in significant improvement for HfO_2 as the defect states were passivated. The defect states were also passivated for the Al_2O_3 samples (as evidenced by a lower ideality factor closer to 1), but interestingly this did not improve the generated photovoltage. Annealing did not impact the flat-band potential, so the annealing step must either be altering the insulator tunneling probability or introducing an alternative recombination pathway. Finally, the composition and the order of the insulator layer was varied to form layered alloy insulator structures in an attempt to improve the charge carrier selectivity. This is not an exhaustive list of every possible method to improve the performance, and other possible strategies to improve the nonidealities and the charge carrier selectivity which will be discussed in Chapter 8.

5.7 References

(1) Quinn, J.; Hemmerling, J.; Linic, S. Maximizing Solar Water Splitting Performance by Nanoscopic Control of the Charge Carrier Fluxes across Semiconductor–Electrocatalyst Junctions. *ACS Catal.* **2018**, *8* (9), 8545–8552. https://doi.org/10.1021/acscatal.8b01929.

(2) Digdaya, I. A.; Trześniewski, B. J.; Adhyaksa, G. W. P.; Garnett, E. C.; Smith, W. A. General Considerations for Improving Photovoltage in Metal–Insulator–Semiconductor Photoanodes. *J. Phys. Chem. C* **2018**, *122* (10), 5462–5471. https://doi.org/10.1021/acs.jpcc.7b11747.

(3) G. Scheuermann, A.; D. Prange, J.; Gunji, M.; D. Chidsey, C. E.; C. McIntyre, P. Effects of Catalyst Material and Atomic Layer Deposited TiO 2 Oxide Thickness on the Water Oxidation Performance of Metal–Insulator–Silicon Anodes. *Energy Environ. Sci.* **2013**, *6* (8), 2487–2496. https://doi.org/10.1039/C3EE41178H.

(4) Park, M.-J.; Jung, J.-Y.; Shin, S.-M.; Song, J.-W.; Nam, Y.-H.; Kim, D.-H.; Lee, J.-H. Photoelectrochemical Oxygen Evolution Improved by a Thin Al2O3 Interlayer in a NiOx/n-Si Photoanode. *Thin Solid Films* **2016**, *599*, 54–58. https://doi.org/10.1016/j.tsf.2015.12.062.

(5) Esposito, D. V.; Levin, I.; Moffat, T. P.; Talin, A. A. H_2 Evolution at Si-Based Metal–Insulator–Semiconductor Photoelectrodes Enhanced by Inversion Channel Charge Collection and H Spillover. *Nat. Mater.* **2013**, *12* (6), 562–568. https://doi.org/10.1038/nmat3626.

(6) V. Esposito, D.; Lee, Y.; Yoon, H.; M. Haney, P.; Y. Labrador, N.; P. Moffat, T.; Alec Talin, A.; A. Szalai, V. Deconvoluting the Influences of 3D Structure on the Performance of Photoelectrodes for Solar-Driven Water Splitting. *Sustain. Energy Fuels* **2017**, *1* (1), 154–173. https://doi.org/10.1039/C6SE00073H.

(7) Quinn, J.; Hemmerling, J.; Linic, S. Guidelines for Optimizing the Performance of Metal–Insulator–Semiconductor (MIS) Photoelectrocatalytic Systems by Tuning the Insulator Thickness. *ACS Energy Lett.* **2019**, *4* (11), 2632–2638. https://doi.org/10.1021/acsenergylett.9b01609.

(8) Ji, L.; McDaniel, M. D.; Wang, S.; Posadas, A. B.; Li, X.; Huang, H.; Lee, J. C.; Demkov, A. A.; Bard, A. J.; Ekerdt, J. G.; Yu, E. T. A Silicon-Based Photocathode for Water Reduction with an Epitaxial $SrTiO_3$ Protection Layer and a Nanostructured Catalyst. *Nat. Nanotechnol.* **2015**, *10* (1), 84–90. https://doi.org/10.1038/nnano.2014.277.

(9) Eastment, R. M.; Mee, C. H. B. Work Function Measurements on (100), (110) and (111) Surfaces of Aluminium. *J. Phys. F Met. Phys.* **1973**, *3* (9), 1738–1745. https://doi.org/10.1088/0305-4608/3/9/016.

(10) Eastman, D. E. Photoelectric Work Functions of Transition, Rare-Earth, and Noble Metals. *Phys. Rev. B* **1970**, *2* (1), 1–2. https://doi.org/10.1103/PhysRevB.2.1.

(11) Mills, T. J.; Lin, F.; Boettcher, S. W. Theory and Simulations of Electrocatalyst-Coated Semiconductor Electrodes for Solar Water Splitting. *Phys. Rev. Lett.* **2014**, *112* (14), 148304. https://doi.org/10.1103/PhysRevLett.112.148304.

(12) Hemmerling, J. R.; Mathur, A.; Linic, S. Design Principles for Efficient and Stable Water Splitting Photoelectrocatalysts. *Acc. Chem. Res.* **2021**, *54* (8), 1992–2002. https://doi.org/10.1021/acs.accounts.1c00072.

(13) Zanuccoli, M.; Magnone, P.; Sangiorgi, E.; Fiegna, C. Analysis of the Impact of Geometrical and Technological Parameters on Recombination Losses in Interdigitated

Back-Contact Solar Cells. *Sol. Energy* **2015**, *116*, 37–44. https://doi.org/10.1016/j.solener.2015.03.042.

(14) Rhoderick, E. H. Metal-Semiconductor Contacts. *IEE Proc. - Solid-State Electron Devices* **1982**, *129* (1), 1-. https://doi.org/10.1049/ip-i-1.1982.0001.

(15) Cuevas, A. The Recombination Parameter J0. *Energy Procedia* **2014**, *55*, 53–62. https://doi.org/10.1016/j.egypro.2014.08.073.

(16) Dziewior, J.; Silber, D. Minority-carrier Diffusion Coefficients in Highly Doped Silicon. *Appl. Phys. Lett.* **1979**, *35* (2), 170–172. https://doi.org/10.1063/1.91024.

(17) Cai, Q.; Hong, W.; Jian, C.; Li, J.; Liu, W. Impact of Silicon Resistivity on the Performance of Silicon Photoanode for Efficient Water Oxidation Reaction. *ACS Catal.* **2017**, *7* (5), 3277–3283. https://doi.org/10.1021/acscatal.7b00507.

(18) Scheuermann, A. G.; Lawrence, J. P.; Meng, A. C.; Tang, K.; Hendricks, O. L.; Chidsey, C. E. D.; McIntyre, P. C. Titanium Oxide Crystallization and Interface Defect Passivation for High Performance Insulator-Protected Schottky Junction MIS Photoanodes. *ACS Appl. Mater. Interfaces* **2016**, *8* (23), 14596–14603. https://doi.org/10.1021/acsami.6b03688.

(19) Luo, Z.; Liu, B.; Li, H.; Chang, X.; Zhu, W.; Wang, T.; Gong, J. Multifunctional Nickel Film Protected N-Type Silicon Photoanode with High Photovoltage for Efficient and Stable Oxygen Evolution Reaction. *Small Methods 0* (0), 1900212. https://doi.org/10.1002/smtd.201900212.

(20) G. Scheuermann, A.; W. Kemp, K.; Tang, K.; Q. Lu, D.; F. Satterthwaite, P.; Ito, T.; D. Chidsey, C. E.; C. McIntyre, P. Conductance and Capacitance of Bilayer Protective Oxides for Silicon Water Splitting Anodes. *Energy Environ. Sci.* **2016**, *9* (2), 504–516. https://doi.org/10.1039/C5EE02484F.

(21) Digdaya, I. A.; Adhyaksa, G. W. P.; Trześniewski, B. J.; Garnett, E. C.; Smith, W. A. Interfacial Engineering of Metal-Insulator-Semiconductor Junctions for Efficient and Stable Photoelectrochemical Water Oxidation. *Nat. Commun.* **2017**, *8*, ncomms15968. https://doi.org/10.1038/ncomms15968.

(22) Zhao, C.; Guo, B.; Xie, G.; Li, C.; Xie, W.; Dai, Y.; Gong, J.; Gong, J. R. Metal Sputtering Buffer Layer for High Performance Si-Based Water Oxidation Photoanode. *ACS Appl. Energy Mater.* **2020**, *3* (9), 8216–8223. https://doi.org/10.1021/acsaem.0c00609.

(23) Wang, S.; Wang, T.; Liu, B.; Li, H.; Feng, S.; Gong, J. Spatial Decoupling of Light Absorption and Reaction Sites in N-Si Photocathodes for Solar Water Splitting. *Natl. Sci. Rev.* **2020**, No. nwaa293. https://doi.org/10.1093/nsr/nwaa293.

(24) Mikolasek, M.; Frohlich, K.; Husekova, K.; Racko, J.; Rehacek, V.; Chymo, F.; Tapajna, M.; Harmatha, L. Silicon Based MIS Photoanode for Water Oxidation: A Comparison of

RuO2 and Ni Schottky Contacts. *Appl. Surf. Sci.* **2018**, *461*, 48–53. https://doi.org/10.1016/j.apsusc.2018.04.234.

(25) Gougam, A. B.; Rajab, B.; Bin Afif, A. Investigation of C-Si Surface Passivation Using Thermal ALD Deposited HfO2 Films. *Mater. Sci. Semicond. Process.* **2019**, *95*, 42–47. https://doi.org/10.1016/j.mssp.2019.02.012.

(26) Cui, J.; Wan, Y.; Cui, Y.; Chen, Y.; Verlinden, P.; Cuevas, A. Highly Effective Electronic Passivation of Silicon Surfaces by Atomic Layer Deposited Hafnium Oxide. *Appl. Phys. Lett.* **2017**, *110* (2), 021602. https://doi.org/10.1063/1.4973988.

Chapter 6

Insights from Modeling Nanoparticle Metal/Semiconductor Systems

6.1 Introduction

The previous chapters have focused on uniform films of metals and insulators to enhance the stability and ensure the semiconductor avoids direct contact with the corrosive electrolyte. Recently, unexpected stability has been demonstrated for PEC systems consisting of electrodeposited Ni nanoparticles on Si in which the Si is directly exposed to an alkaline electrolyte. Hours of stability have been achieved because of anodic passivation of the Si, forming stable SiO_x.[1] In addition to providing stability, nanoparticle catalysts can be tuned to minimize parasitic light absorption[2–4] and enhance the rates of the desired chemical reactions.[5–9] Furthermore, nanoparticle catalyst/semiconductor systems may exhibit enhanced performance if operating in the "pinch-off" regime, where sufficiently small nanoparticles with a low potential barrier to recombination are surrounded by a region with a high potential barrier to recombination. The effective barrier height of the nanocontact is significantly larger than otherwise predicted for the nanoparticle itself, or when compared to systems with bulk films.[10–13]

A decade after being predicted, the pinch-off effect has been experimentally demonstrated for Ni nanoparticles on a Si substrate.[14,15] These works suggest that the pinch-off effect may be an inherent feature of sufficiently small nanoparticle catalysts on semiconductors, and this phenomenon has been of recent interest in the field of water splitting. Electrodepositing Ni nanoparticles on Si has been the most-reported strategy. Specifically, high photovoltages and good onset potentials have been obtained using activated Ni nanoparticles,[1,16,17] Fe-modified Ni

nanoparticles,[18] Ir-modified Ni nanoparticles,[19] and thermally oxidized Ni nanoparticles.[20] Besides Ni, electrodeposited Co and Fe nanoparticles may also benefit from the pinch-off effect.[17,21,22]

Despite claims that the pinch-off effect is the reason for enhanced photovoltage of water splitting systems, there has been minimal attempts to find quantitative agreement between experimental systems and the theoretical pinch-off effect.[15] Furthermore, there has been no theoretical guidance on the critical parameters that can be tuned to optimize the performance of pinched-off systems. In this chapter, we establish a comprehensive theoretical model to obtain a better understanding of the factors that influence the photovoltage in pinched-off photoelectrocatalysts. The interplay of semiconductor doping density, nanoparticle radius, and catalyst coverage are highlighted as important parameters to optimize performance. The results are important for fundamentally understanding and optimizing photovoltage of nanoparticle catalyst/semiconductor photoelectrocatalysts and opens the door for the rational design of future device architectures.

6.2 Analytical Model for Pinch-off Effect

The pinch-off effect is used to describe a system consisting of nanoparticles with a low barrier to recombination (ϕ_b^{np}) surrounded by a region with a large barrier to recombination (ϕ_b^0). The barrier to recombination is called the barrier height which is defined as the difference between the band edge of the semiconductor (E_{cb}) and the work function (or Fermi level, E_F) of the metal or electrolyte as illustrated in Figure 6-1. In Figure 6-1, the nanoparticle is assumed to be sufficiently large that the system can be treated as two independent and distinct regions with different barrier heights. An alternative illustration of these high and low barrier heights is shown in Figure 6-2a.

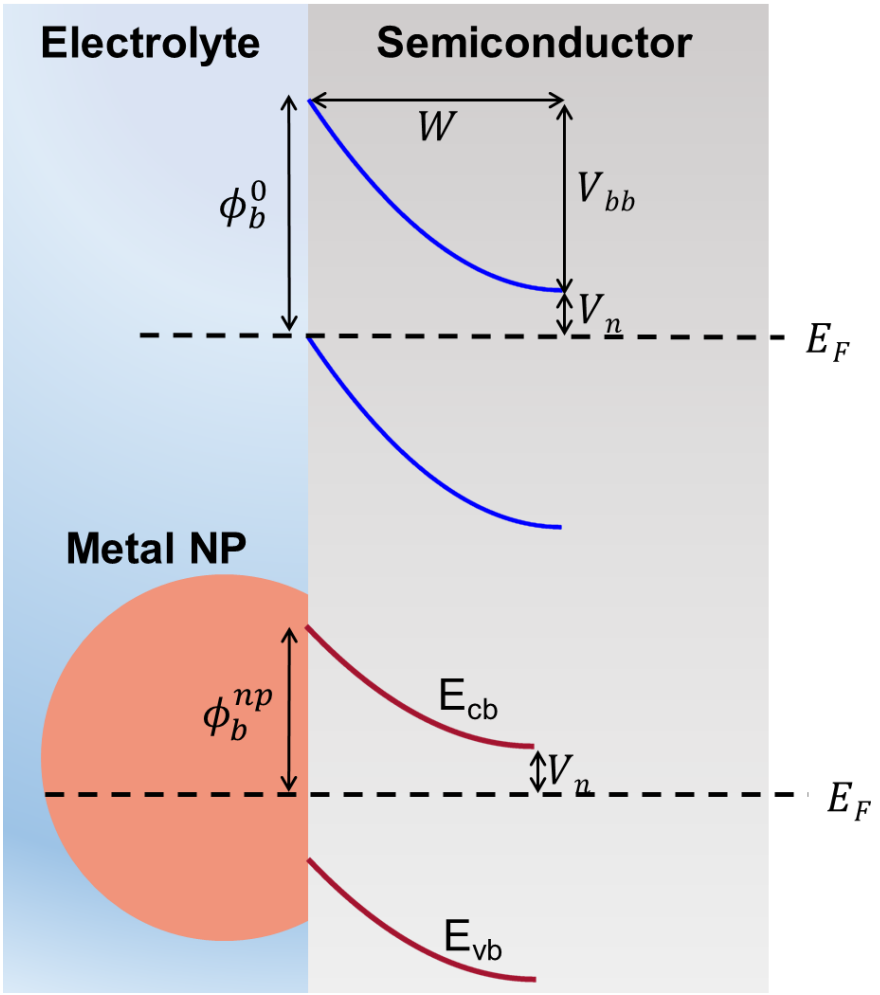

Figure 6-1: Illustration and energy band diagram for the types of systems studied in this chapter. The nanoparticle is assumed to be sufficiently large that the system can be treated as two independent and distinct regions with different barrier heights. The variables and key parameters are defined throughout the text.

If the nanoparticle is sufficiently small, then the high barrier and low barrier regions may interact and result in a new barrier height underneath the nanoparticle. This resulting barrier height is called the "effective barrier height" (ϕ_b^{eff}), and the height is this barrier is bounded by the high and low barrier regions (i.e., $\phi_b^{np} < \phi_b^{eff} < \phi_b^0$). An illustration of the effective barrier height is shown in Figure 6-2b. This is significant because an increase in the barrier height is well known to improve the photovoltage in metal-semiconductor systems by decreasing electron/hole (e^-/h^+) recombination (which is also described in Chapter 4).[23–27] Therefore,

systems with pinched-off nanoparticles are predicted to generate higher photovoltage than equivalent systems with larger nanoparticles or with planar catalysts.

The following condition must be met for a nanoparticle with radius (r) to be pinched-off:[10]

$$r < \frac{W\Delta}{2V_{bb}} \quad \text{6-1}$$

Where W is the width of the depletion region in the high barrier region (see Figure 6-1). Δ is the difference between the low barrier region (ϕ_b^{np}) and the high barrier region (ϕ_b^0):

$$\Delta = \phi_b^0 - \phi_b^{np} \quad \text{6-2}$$

And V_{bb} is the band bending in the semiconductor which is defined as

$$V_{bb} = \phi_b^0 - V_n - V_a \quad \text{6-3}$$

Where V_n is the offset between the semiconductor conduction band and Fermi level and V_a is the applied potential in the system (relative to the Fermi level of the majority carriers in the semiconductor). We used equation 6-1 to determine the upper bound for the nanoparticle radius in which the pinch-off effect is expected to occur, and only studied nanoparticles smaller than this upper bound.

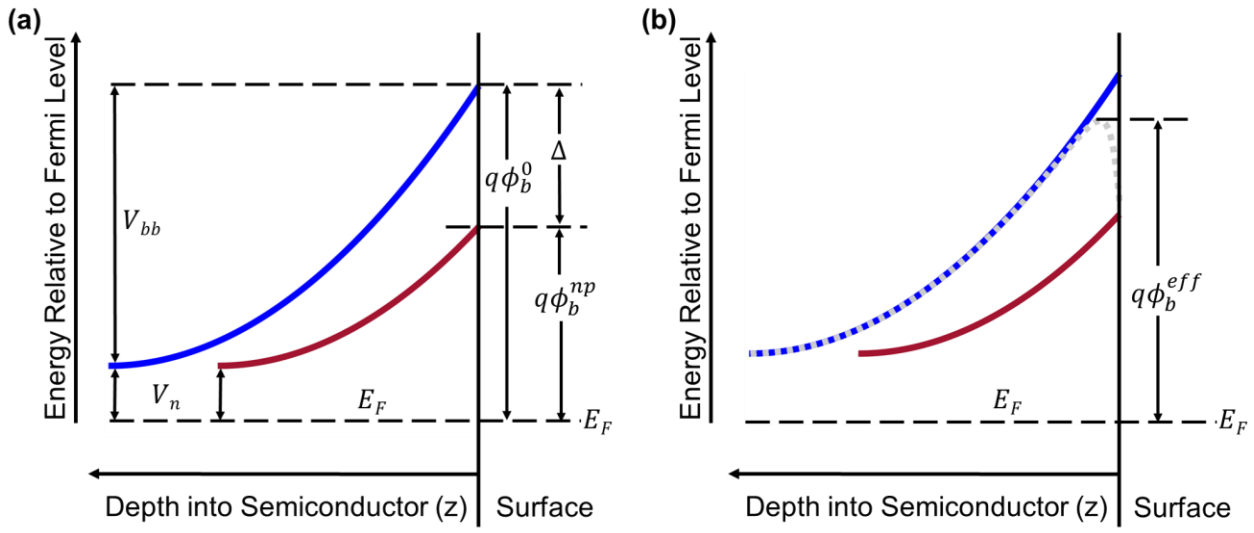

Figure 6-2: Energy band diagrams that illustrate the key parameters that are described throughout the text. (a) Illustration of the high barrier height and low barrier height and well as their difference (Δ). (b) If the nanoparticle is sufficiently small, the nanoparticle becomes pinched off which results in an effective barrier height (ϕ_b^{eff}) that is larger than the natural barrier height of the nanoparticle (ϕ_b^{np}).

To predict the performance of pinched-off systems, our model system consists of metal nanoparticles on a semiconductor and immersed in electrolyte, as shown in Figure 6-1. The model is general to a variety of electrochemical systems, but our focus is on the experimentally relevant system of Ni nanoparticle deposited on n-Si and immersed in water to perform the OER upon solar illumination. These types of Ni/Si systems have been of great interest for solar water splitting,[1,15,20,28–32] but the electronic properties and overall performance have not been quantitatively linked to the physical and chemical characteristics of the interface.

All charge transfer is assumed to take place through the Ni nanoparticles (i.e., there are no reactions or recombination at the semiconductor/electrolyte interface). This results in an upper limit estimate on the performance of pinched-off systems. The system is characterized by a low barrier height region under the Ni nanoparticles (ϕ_b^{np}) and a high barrier height region induced by the electrolyte (ϕ_b^0). The low barrier height is set at 0.6 eV which is the typical

barrier height for Ni on n-Si found experimentally.[15,30] The high barrier height is set to the upper limit which is governed by the onset of strong inversion in the semiconductor. Strong inversion occurs when the minority carriers outnumber the majority carrier doping density, and the corresponding barrier height (ϕ_b^{inv}) is expressed by:[14]

$$\phi_b^{inv} = \frac{2kT}{q} ln\left(\frac{N_d}{N_i}\right) + V_n \qquad 6\text{-}4$$

Here, N_i is the intrinsic carrier concentration in the semiconductor. According to this equation, a higher doping density leads to a higher maximum barrier height because more minority carriers need to accumulate before they outnumber the dopant ion concentration. This trend is illustrated in Figure 6-3. Because we are interested in modeling the upper photovoltage limit for pinched-off systems, we set ϕ_b^0 equal to ϕ_b^{inv} in the model. Now that the low barrier and high barrier regions have been defined, the key to modeling these systems is to predict the effective barrier height (ϕ_b^{eff}) that develops from the interaction of these regions.

An analytical expression for ϕ_b^{eff} has been previously derived for a circular nanoparticle contact on a semiconductor:[12,14,15]

$$\phi_b^{eff} = \phi_b^0 - \left(\frac{3q\Delta r^2 V_{bb} N_d}{4\varepsilon_s}\right)^{1/3} \qquad 6\text{-}5$$

V_n is the offset between the semiconductor conduction band and Fermi level and V_a is the applied potential relative to the electrolyte Fermi level. This equation demonstrates that the effective barrier height is a complicated function of different parameters, but one of the key trends is that ϕ_b^{eff} approaches the upper limit of ϕ_b^0 as the nanoparticle radius approaches 0. In this limit, the high barrier region dominates the barrier height of the nanocontact. This general trend is illustrated in Figure 6-3a.

The effective barrier height is important to model these systems because it significantly contributes to the reverse saturation current density ($J_{s,pinch}$) which is associated with e^-/h^+ recombination. An analytical expression for $J_{s,pinch}$ has been previously derived for a circular nanoparticle contact by assuming that the recombination current is dominated by thermionic emission throughout an effective area (S_{eff}) and over an effective barrier height (ϕ_b^{eff}):[12,14,15]

$$J_{s,pinch} = A^* T^2 f_c \frac{S_{eff}}{S} exp\left(-\frac{q\phi_b^{eff}}{kT}\right) \quad 6\text{-}6$$

Where

$$S_{eff} = \left(\frac{4\pi kT}{3q}\right)\left(\frac{3\Delta r^2}{4}\right)^{1/3}\left(\frac{\varepsilon_s}{qN_d V_{bb}}\right)^{2/3} \quad 6\text{-}7$$

Here, A^* is Richardson's constant, ε_s is the permittivity of the semiconductor f_c is the catalyst coverage defined as the ratio of the semiconductor surface covered by catalyst, S is the physical surface area of the nanoparticle in contact with the semiconductor ($S = \pi r^2$). From the above equation, in addition to the effective barrier height (ϕ_b^{eff}), the total effective area of the nanoparticles deposited on the semiconductor ($f_c \frac{S_{eff}}{S}$) is another major contribution to the reverse saturation recombination current ($J_{s,pinch}$). As plotted in Figure 6-3b, $\frac{S_{eff}}{S}$ (with a constant f_c of 15%) decreases as the nanoparticle radius increases. The implications of this trend are discussed in the next section. In short, the recombination current is directly proportional to the total effective area of the nanoparticles ($f_c \frac{S_{eff}}{S}$) because the charge carrier recombination is assumed to only occur from thermionic emission near the nanoparticle contacts.[14,15] While this assumption is not particularly valid for practical systems, we make this assumption because we are interested in modeling the upper performance limit for the pinch-off effect. Practical systems are therefore expected to perform worse than the models predict because practical systems will

have an additional recombination pathway in the regions between the nanoparticles (i.e., at the semiconductor/electrolyte interface). This additional recombination term could be added to the model in equation 6-6 which has been described in prior work.[14]

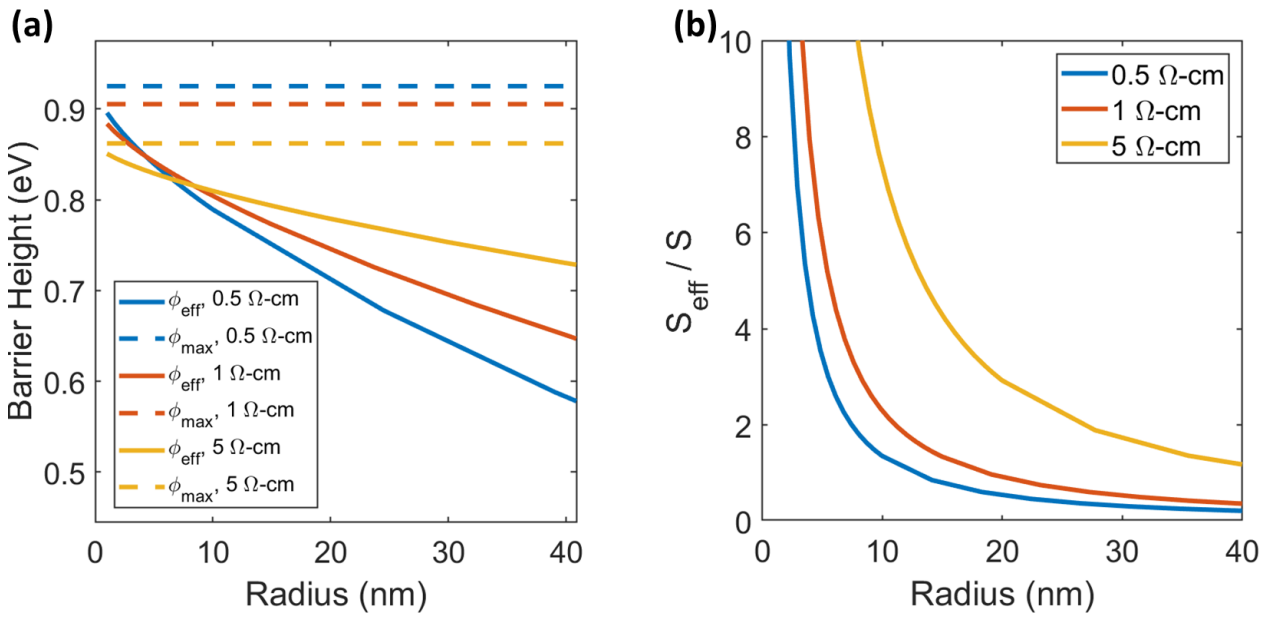

Figure 6-3: Modeled (a) barrier heights and (b) $\frac{S_{eff}}{S}$ for pinched-off systems as a function of nanoparticle radius and doping density. The catalyst coverage is 15%.

Now that the recombination pathway has been identified, we can define the current-voltage relationship for the overall photoelectrochemical system, which can be modeled using the illuminated diode equation:[14,15]

$$J_{pinch} = J_{ph} - J_{s,pinch}\left(exp\left(-\frac{qV_a}{nkT}\right) - 1\right) \qquad 6\text{-}8$$

Where J_{pinch} is the total current density through the system, J_{ph} is the photocurrent density generated from absorbing light, q is the elementary charge, n is the ideality factor (which is assumed to equal 1 in this work meaning that the systems behave like an ideal diode), k is the Boltzmann constant, and T is temperature. The first term after the equal sign (J_{ph}) is the hole

current that reaches the catalyst to perform OER while the second term is the electron current that reaches the metal and recombines with the holes.

Using the above equations, we can model the current-voltage characteristics for pinched-off systems. The primary performance metric we model is the photovoltage, which is the voltage generated upon illuminating the semiconductor. Specifically, we model the open-circuit photovoltage by setting J_{pinch} to zero (i.e., open-circuit condition). The voltage required to make J_{pinch} equal 0 is the value for the open-circuit photovoltage.

We note that the pinch-off effect is theoretically applicable for nanoparticles up to about 70 nm for the highest semiconductor doping density case, but the analytical model loses accuracy for larger nanoparticles. Therefore, our modeling focuses on small nanoparticles ($r < 40nm$) which is in the range where the pinch-off effect holds, and the analytical model is most accurate.

6.3 Modeling Light Absorption and Photo-limited Current

The final important parameter needed to model the current-voltage relationship of pinched-off nanoparticles on semiconductors is the photo-limited current (J_{ph} in equation 6-8). The photo-limited current is ultimately governed by what how much light is absorbed by the silicon. If 100% of the photons above the band gap of 1.1 eV are absorbed then, the upper limit for the photocurrent is about 44 mA/cm^2. However, Si experiences significant losses from reflection, and the nanoparticles on the surface will also parasitically absorb and reflect light.

The fractional reflection and nanoparticle absorption of the Ni/Si systems were calculated using the COMSOL Multiphysics finite-element based software and performed by Steven Chavez. The 'Wave Optics' module was used to calculate the radiative field resulting from a TE-polarized electromagnetic wave incident on a Ni hemisphere of diameter d resting on

a silicon substrate using the 'full-field/scattered-field' formulation (Figure 6-4). In this formulation, the model is first solved without the presence of the nanoparticle (the scatterer) to obtain the background electric field. This is achieved by setting the simulation up with two port conditions: the first defining the incident plane wave allowing for specular reflection and the second acting as an absorber of the transmitted plane wave. In the model, the plane wave is sent from Port 1 with a total power P (in W) and absorbed at Port 2. The calculated field is then used as an input for a second simulation that introduces the Ni hemisphere as the scatterer. In the model geometry, Perfectly Matched Layers (PMLs) are used to act as an absorber of the scattered field.

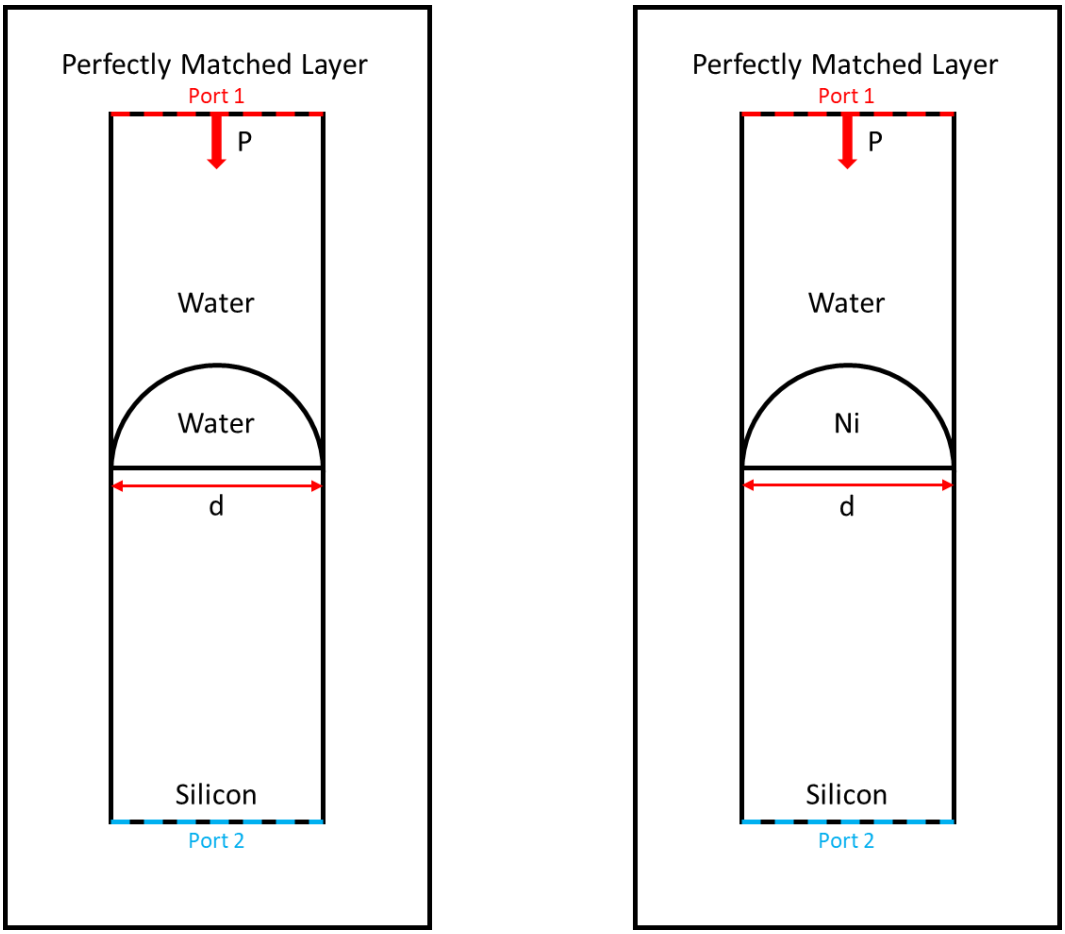

Figure 6-4: Schematic of the model geometry used in the COMSOL simulations. The background electromagnetic field is first calculated in the absence of the nanoparticle (Left) and then used as an input for the simulation of the scattered field (Right).

Dielectric data for Ni and Si (Figure 6-5) were obtained from COMSOL's optical materials database[33,34] and a region of water was defined around the particle by setting the real part of the dielectric function equal to 1.33.

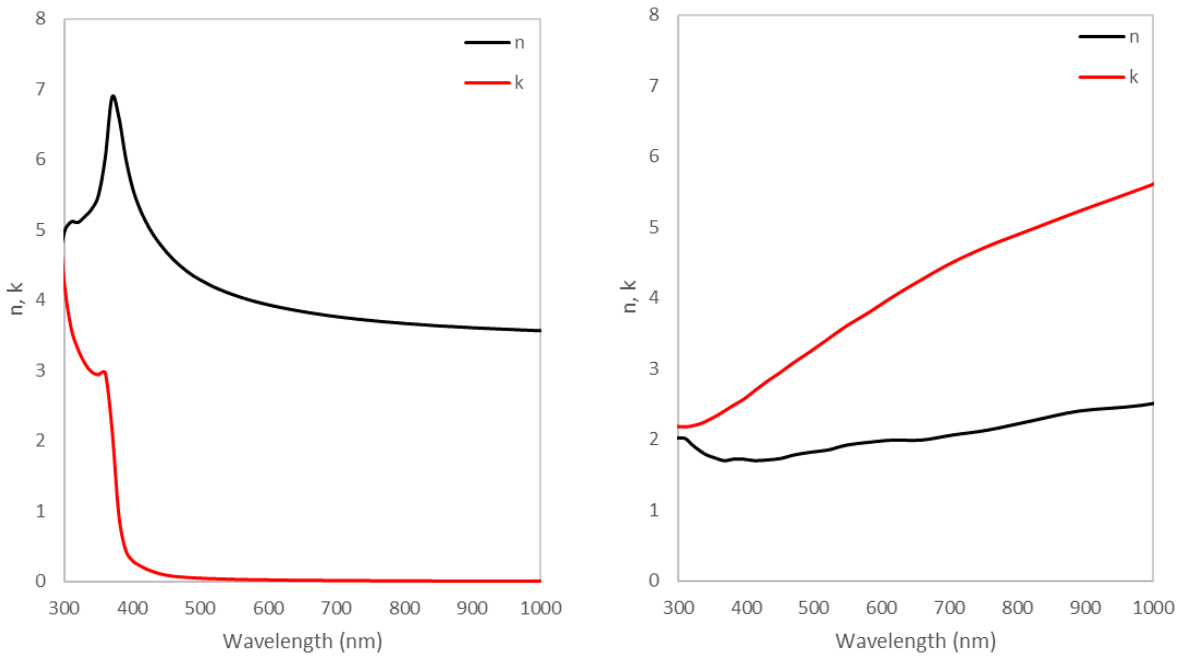

Figure 6-5: The refractive index (*n*) and extinction coefficient (*k*) used in the model for Si (Left) and Ni (Right).

This modeling allowed us to determine the total light transmission through an individual Ni nanoparticle as a function of the nanoparticle radius, and the data is shown in Figure 6-6. For regions without Ni nanoparticles, the light absorption in the Si was approximated using OPAL 2 from PV Lighthouse and using a Si thickness of 525 μm and a 0.6 nm SiO_2 native oxide layer, and water on top. This resulted in 75.7% of the possible photons being absorbed by the Si. Then a weighted average based on the coverage of the nanoparticles and the region without nanoparticles was used to determine overall fraction of light that the Si can absorb.

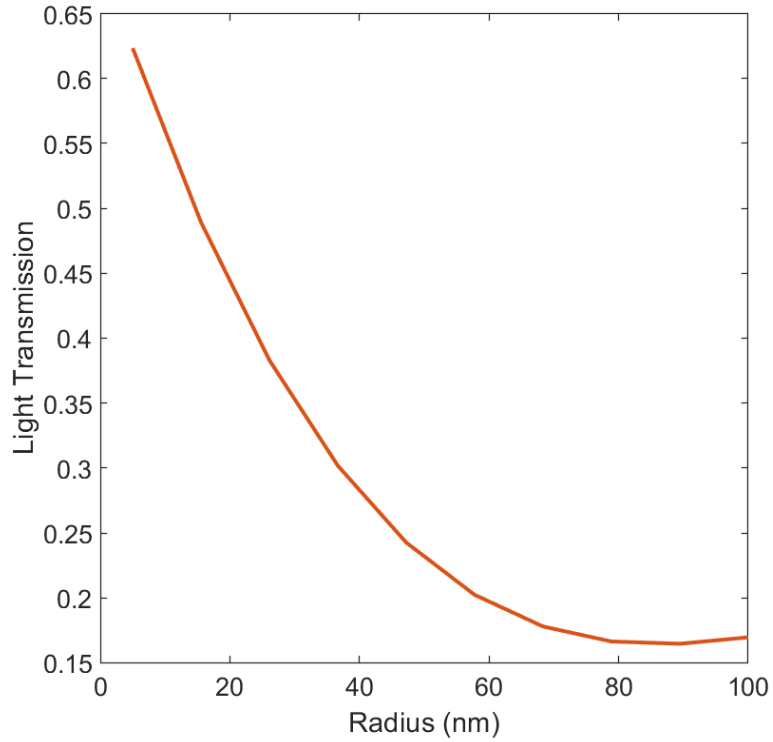

Figure 6-6: Modeled total light transmission through an individual Ni nanoparticle as a function of the nanoparticle radius.

6.4 Key Physical Parameters that Impact Performance

6.4.1 Radius Impact on Effective Barrier Height, Effective Area, and Light Absorption

We have plotted different variables as a function of nanoparticle radii ranging from 1-40 nm which demonstrates the importance of the nanoparticle radius on the photovoltage generated by the system. Figure 6-7 shows the modeled photovoltage as a function of nanoparticle radius and the semiconductor doping density for a catalyst coverage of 15%. The model predicts an optimal nanoparticle radius ranging from 3-10 nm depending on the Si doping density. This prediction of an optimal nanoparticle radius has not been previously reported, as previous works modeled radii > 35 nm.[15]

The volcano-type relationship can be understood be considering the two key contributions to the recombination: the effective barrier height and the effective area (see equation 6-6). As shown in Figure 6-3a, the effective barrier height (ϕ_b^{eff}) increases as the nanoparticle radius decreases. The higher barrier height exponentially lowers recombination rates which explains the right side of the volcano. The photovoltage loss on the left side of the volcano is associated with total effective area of the nanoparticles on the semiconductor ($f_c \frac{S_{eff}}{S}$). As shown in Figure 6-3b, the ratio of the effective area to the actual physical area significantly increases for small nanoparticles. This is because the physical area scales with radius squared ($S = \pi r^2$), while the effective area scales with radius to the 2/3 power (see equation 6-7). This increase in $f_c \frac{S_{eff}}{S}$ increases the recombination rates ($J_{s,pinch}$ in equation 6-6) which causes the decline in photovoltage for the smallest nanoparticles.

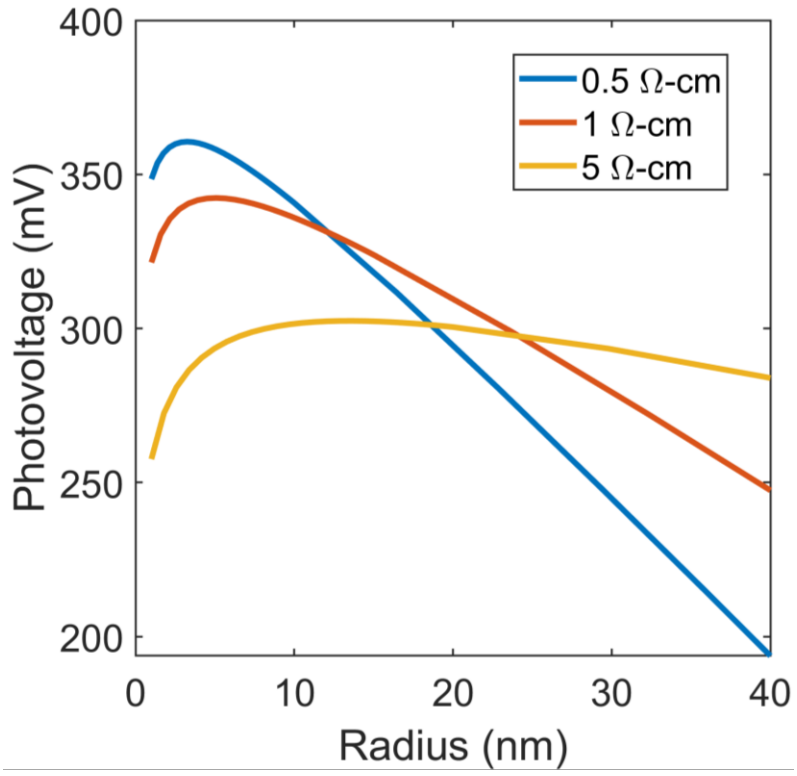

Figure 6-7: Modeled photovoltage as a function of nanoparticle radius and doping density. The catalyst coverage is 15% (i.e., f_c=0.15).

It is also worth noting that the nanoparticle radius impacts the photo-limited current density as shown in Figure 6-8. In general, the photo-limited current decreases as the nanoparticle radius increases because less light can transmit through a bigger nanoparticle. A similar argument is true for higher catalyst coverage because there are a higher number of nanoparticles that block the incident light. These photo-limited current losses are already factored into the photovoltage calculations in Figure 6-7, and only have a small impact on the generated photovoltage. However, the photo-limited current does have a large impact on the overall efficiency of the system as well as the maximum power that the system can generate. Overall, these results show that lower nanoparticle radius is generally beneficial in terms of photovoltage and photo-limited current density, but other factors must be considered as well to obtain the complete picture and further optimize these systems.

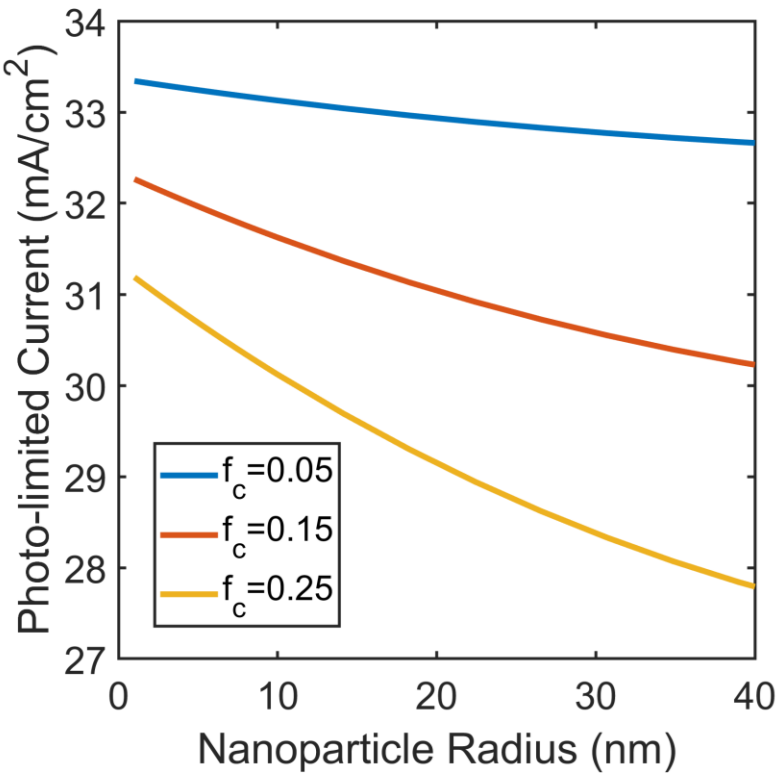

Figure 6-8: Modeled photo-limited current density as a function of nanoparticle radius and the catalyst coverage.

6.4.2 Semiconductor Doping Density

The importance of semiconductor doping density for optimizing the photovoltage is also evident from Figure 6-7b. The optimal nanoparticle radius depends on the doping density. Specifically, 3 nm particles are optimal for the 0.5 ohm-cm doping, while 10 nm particles are optimal for 5 ohm-cm doping. In general, the highest photovoltage is possible for the highest doping density (0.5 ohm-cm in this case) as long as thermionic emission remains the dominant recombination mechanism.[35] Higher doping density is beneficial because it allows for a higher maximum barrier height as shown in Figure 6-3a (ϕ_b^{inv} in equation 6-4). However, doping densities significantly higher than the 0.5 ohm-cm case can also impact the recombination current, introducing alternative recombination mechanisms like Auger recombination or thermionic field emission as the semiconductor behaves more like a metal from the higher doping.[35–38] Therefore, Si with a doping density higher than 0.5 ohm-cm was not modeled in this analysis.

Interestingly, the benefit from higher doping (0.5 ohm-cm) only applies for ultrasmall nanoparticles <10 nm radius because the photovoltage and the effective barrier height rapidly drop for larger nanoparticles. In contrast, the lower doping density of 5 ohm-cm results in a less dramatic losses in the photovoltage and effective barrier height as the nanoparticle radius gets larger (Figure 6-7 and Figure 6-3a). This means that the lower doped semiconductor can yield higher photovoltages for nanoparticles with radius greater than 25 nm (Figure 6-7). The critical importance of doping density on the pinch-off effect has not been previously identified in the literature, and these results can help guide the design and optimization of experimental systems. In many cases, fabricating uniformly dispersed <25 nm nanoparticles on Si is difficult. In these cases, the modeled results suggest that lower doped silicon (5 ohm-cm) should be used.

6.4.3 Catalyst Coverage

As seen in equation 6-6, the catalyst coverage (f_c) is also a key parameter that governs the reverse saturation recombination current in the system. The data in Figure 6-9a, is a plot of the catalyst coverage and the resulting photovoltage for the three different semiconductor doping densities. The selected nanoparticle radius used for each doping density was based on the radius that yielded the optimal photovoltage in Figure 6-7. The data shows that a decrease in the catalyst coverage (while keeping all other parameters constant except the photo-limited current which is also a function of catalyst coverage as seen in Figure 6-8) results in a higher photovoltage. This is because lower catalyst coverage decreases overall recombination rates as there is less surface area for the recombination pathways to occur (see equation 6-6). In general, the low catalyst coverage and recombination for nanoparticle-based systems is another inherent advantage compared to planar systems in which the catalyst coverage is equal to 1.

The data in Figure 6-9a show that the theoretical photovoltage of pinched-off systems can approach 500 mV if the catalyst coverage is below 0.001%. We note that such a low catalyst coverage would not be practical because of significant resistance losses, associated with charges traveling long distances between the nanoparticles. These resistance losses would significantly lower the performance. Furthermore, such a low catalyst coverage would also result in a low catalyst surface area for the reaction and therefore result in large kinetic overpotentials (this wouldn't impact the photovoltage, but instead impact the onset potential which is another important performance metric to consider for practical systems).

Despite the importance of the catalyst coverage, many reports in the literature do not report this value.[20,39] The reports that do report catalyst coverage generally result in greater than 15% catalyst coverage.[1,15] However, the results here demonstrate that lower catalyst coverages

are preferable as long as the system remains stable and can minimize resistance. The interplay between resistance and recombination due to metal contacts has been the subject of previous studies in the solar cell literature.[40–42]

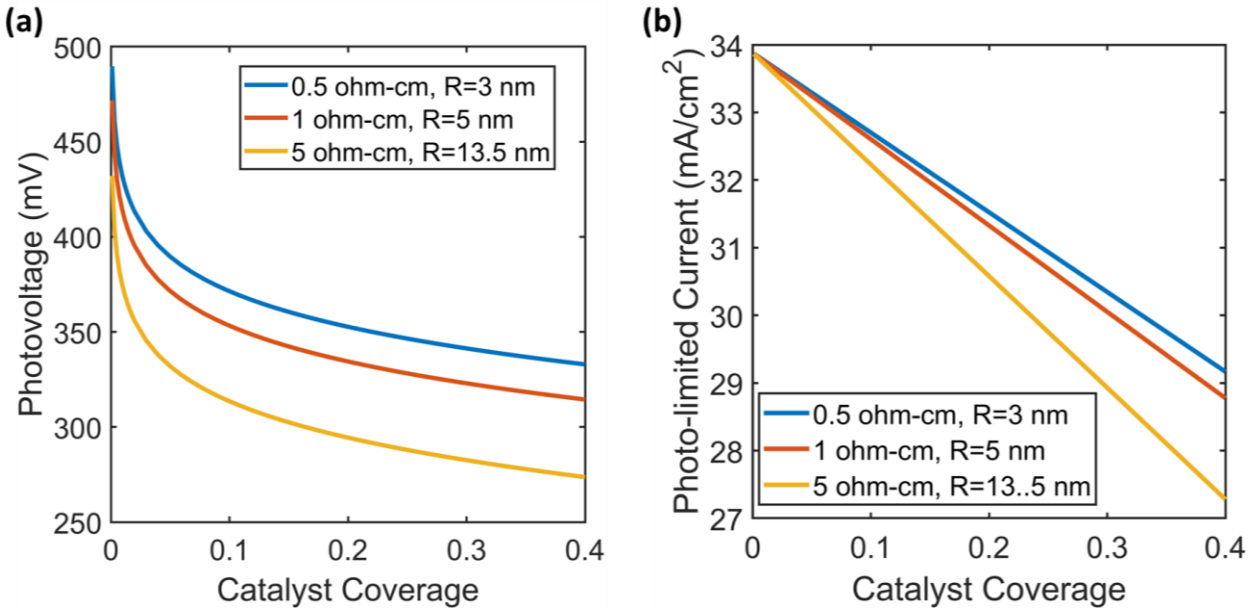

Figure 6-9: Modeled photo-limited current density as a function of nanoparticle radius and the catalyst coverage.

6.4.4 Comparison with Literature and Discussion

The analytical model describing the pinch-off effect has explored the impact of the key parameters including the nanoparticle radius, the semiconductor doping density, and the catalyst coverage. Each of these parameters can be experimentally modulated with relative ease. For an experimentally reasonable catalyst coverage of 15%, Si doping density of 1 ohm-cm, and nanoparticle radius of 30 nm, the theoretical photovoltage from the pinch-off effect is expected to be only 280 mV. Interestingly, most literature reports photovoltages exceeding 400 mV for Ni nanoparticles on Si, and several previous reports have achieved 500 mV of photovoltage.[15,39] Overall, the theoretical pinch-off effect is significantly underestimating the experimental

performance of comparable systems. We note that the analytical model was designed to output the upper limit of the pinch-off effect (i.e., ideal diode behavior, upper limit of the high barrier region equal to inversion, extended high barrier region, no alternative recombination mechanisms, etc.) and yet the model still yields low photovoltages. This suggests that the pinch-off effect as we know it cannot adequately explain the high performance seen experimentally. Additional explanations are required.

Previous work has suggested that a higher ideality factor could increase the photovoltage allowing it to match the experimental data.[15] However, any source of nonidealities resulting in the ideality being larger than 1 means that there is an alternative recombination mechanism that causes deviation from the ideal diode and ultimately causes worse performance.[24] Therefore, an ideality factor greater than 1 cannot be added to a model without influencing the barrier height or adding an alternative recombination mechanism (i.e., space-charge recombination, thermionic-field emission, etc.). We have added an ideality factor of greater than 1 to the model, and the nonidealities result in a lower barrier height in the high barrier and low barrier regions (see Chapter 4 for how the nonidealities lower the barrier height). Figure 6-10 plots the photovoltage as a function of the nanoparticle radius and the ideality factor for the high doping case (0.5 ohm-cm) and 15% catalyst coverage. The data shows that the photovoltage significantly decreases from adding nonidealities, ultimately because the barrier heights end up being decreased from the nonidealities.[24,43]

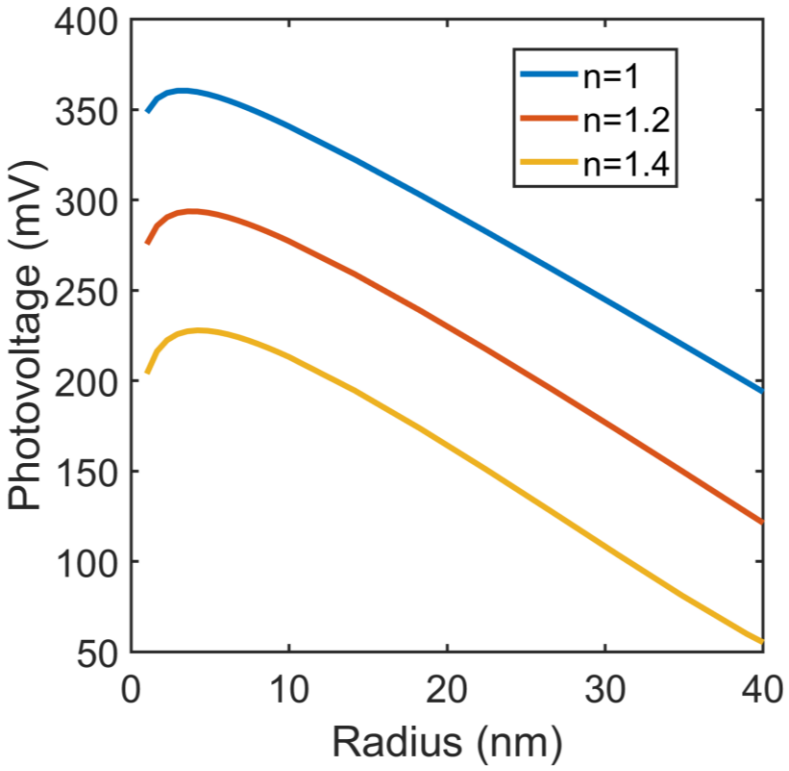

Figure 6-10: Modeled photovoltage as a function of nanoparticle radius and the ideality factor. The catalyst coverage is 15% and the Si doping density is 0.5 ohm-cm.

So far, the analytical model has used the onset of the inversion layer as the upper limit to the barrier height in the high barrier region.[14] This also corresponds to the maximum depletion width in the semiconductor space charge region. For Si with 0.5 ohm-cm resistivity, the inversion layer barrier height is about 0.925 eV. However, barrier heights exceeding the inversion layer barrier height have been reported in previous literature.[15] A barrier height beyond the inversion limit would result in an inversion layer within the first few nanometers of the Si surface. We have explored using higher barrier heights of 1 and 1.1 eV (with 1.1 eV being a fundamental upper limit for Si which is equivalent to the band gap[44]), and the results are plotted in Figure 6-11 for 0.5 ohm-cm resistivity and 15% catalyst coverage. The analytical model predicts that the photovoltage can exceed 500 mV if a barrier height of 1.1 eV is used for

nanoparticles with radius lower than 10 nm. However, the photovoltage for nanoparticles with >30 nm which is common for experimental systems[15,39] would still yield less than 400 mV of theoretical photovoltage, still much less than the experimental photovoltage. It is also worth noting that the above analytical model may not accurate when the barrier heights are high enough to induce inversion. The equations for the analytical model were derived when the semiconductor is in depletion,[12] and it is unclear how the system would change upon inversion in the semiconductor. Overall, the pinch-off effect cannot explain the high photovoltages from experiments, which suggests that there must be alternative contributions to experimental systems that are improving the performance.

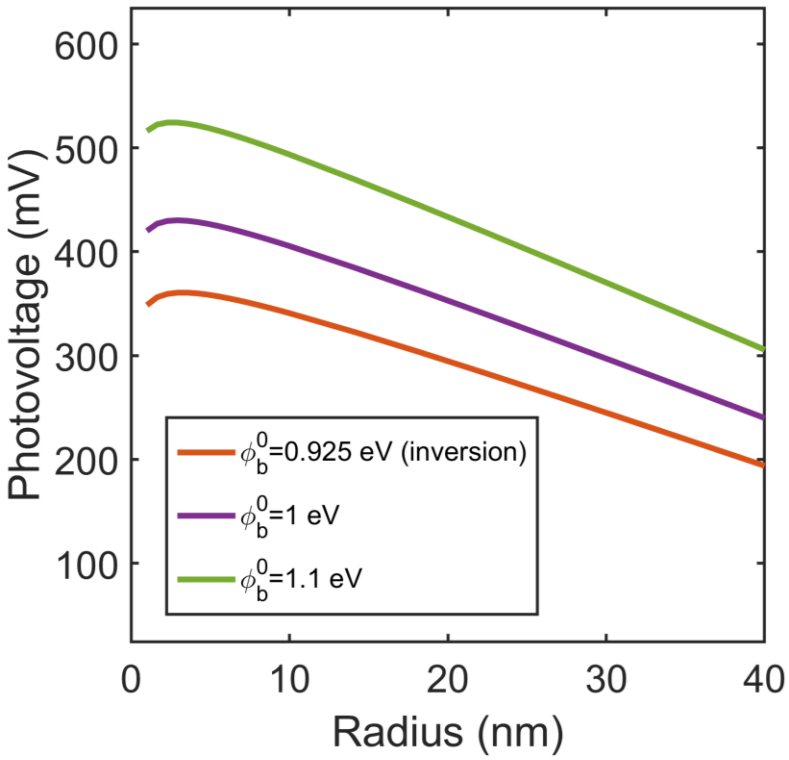

Figure 6-11: Modeled photovoltage as a function of nanoparticle radius and the barrier height of the high barrier region. The catalyst coverage is 15% and the Si doping density is 0.5 ohm-cm.

6.5 COMSOL Model for Pinch-off Effect

The analytical model for the pinch-off effect was derived with some assumptions that limit its overall accuracy.[14] Therefore, to confirm the general trends from the analytical model, a more rigorous finite element model was created using COMSOL Multiphysics using the Semiconductor Module.[45] In short, the model is based on a cylindrical Si semiconductor with axial symmetry about the center (red dashed line in Figure 6-12). A low-barrier nanoparticle is placed on the Si and surrounded by a high-barrier shell to induce the pinch-off effect (Figure 6-12). The barrier heights, nanoparticle radius, and Si doping density are the same as with the analytical model. The high barrier region is treated like an insulator, so that no charge can pass through the high barrier region (similar to the analytical model where no charge passes directly from the semiconductor to the electrolyte). Charge only travels through the low barrier nanoparticle, and through the ohmic back contact in the model. We note that the model is designed with inputs to be directly comparable to the analytical model, but the COMSOL model should be more accurate by avoiding the assumptions built into the analytical model.

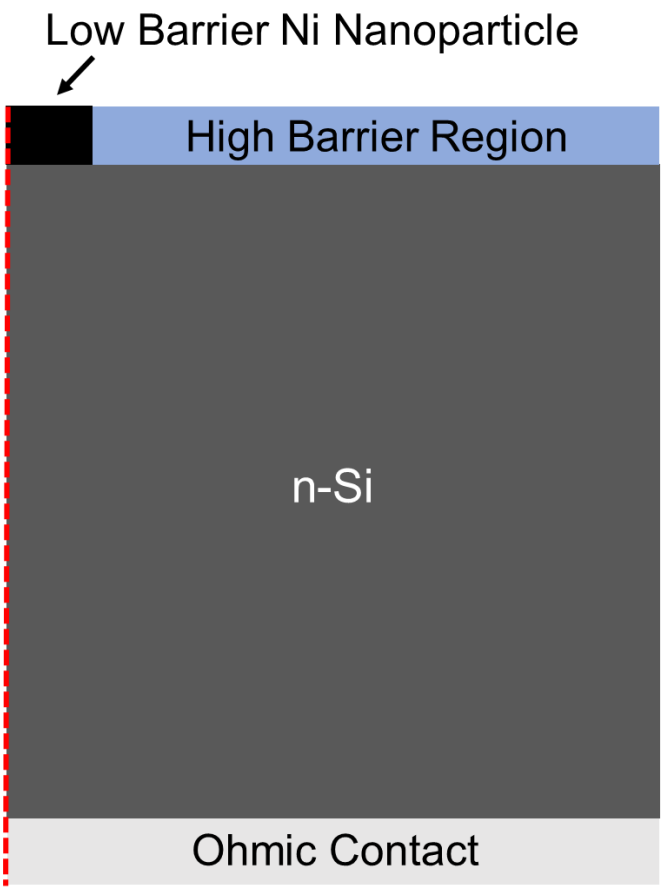

Figure 6-12: Schematic of the model geometry used for COMSOL simulations. The Si has dimensions of 1x1 μm, which is big enough to fit the entire space charge region, but small enough to minimize resistance losses. The radius of the nanoparticle is varied, and the size of the high barrier region covers the entire surface of the Si that is not already covered by the nanoparticle. The red dashed line marks the axis in which the system is rotated with axial symmetry.

The effective barrier height of the system is evaluated by investigating the conduction band edges relative to the Fermi level in equilibrium (Figure 6-13a). A plot of the effective barrier height as a function of the nanoparticle radius is shown in Figure 6-13b. For a nanoparticle with radius of 70 nm, there is no pinch-off effect observed because this is right at the cutoff for the pinch-off effect based on equation 6-1. Meanwhile the highest barrier height is obtained for the lowest nanoparticle radius of 5 nm.

For comparison, the effective barrier heights obtained from the analytical model are also plotted in Figure 6-13b. The results are similar for radii lower than 20 nm, but the gap gets wider for larger nanoparticles. For nanoparticles greater than 40 nm in radius, the analytical model predicts effective barrier heights that are even lower than the barrier height of the nanoparticle (0.6 eV, dashed gray line in Figure 6-13b). Such low barrier heights should be physically impossible, which is why the above analytical modeling has focused on small nanoparticle radii. The error in the analytical model is because of the approximation of the nanoparticle as a point dipole which is necessary to generate simple analytical solutions.[12] The nanoparticle can be more accurately approximated as a dipole layer.[11] Indeed, the effective barrier heights using a dipole layer agrees very well with the COMSOL model (Figure 6-13b).

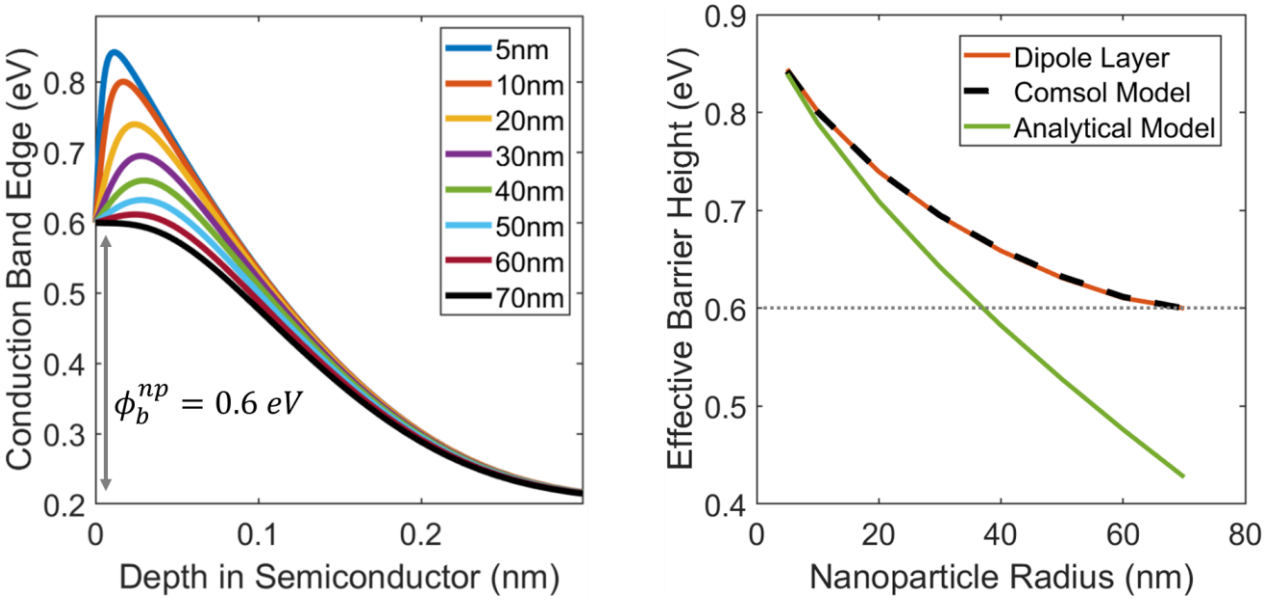

Figure 6-13: (a) Pinched-off system modeled conduction band edges (relative to the Fermi level) into the depth of the Si which is evaluated at zero bias in equilibrium for different nanoparticle radii. The peak of the conduction band edge is used to determine the effective barrier height. (b) Compiled effective barrier heights as a function of nanoparticle particle radius as evaluated using different models and methods. For both (a) and (b), the Si resistivity was 0.5 ohm-cm (i.e., the high doping case).

The photovoltages are extracted from the model by obtaining current-voltage plots in the dark. Assuming these systems (like most solar cells) obey the diode equation, then the only difference between a dark and illuminated current voltage plot is a constant equal to the photo-limited current.[46,47] Therefore, the photovoltage can be extracted using the dark current-voltage plot combined with the photo-limited currents discussed in sections 1536.3 and 6.4.1 To confirm the accuracy of this method, charge carrier generation to simulate sunlight was also employed to produce an illuminated current-voltage plot and extract the photovoltage. The photovoltage from both methods are within 1%, which confirms that these systems are accurately captured by the diode equation.

Figure 6-14 shows the compiled data for the effective barrier heights and the generated photovoltage as a function of nanoparticle radius and Si doping density. The figure compiles the data from both the analytical model (lines) and the COMSOL model (circles). Data in Figure 6-14a shows that the effective barrier height for both models agree well for the lower doping cases of Si with 1 and 5 ohm-cm. The error is only a problem for the high doped case for nanoparticles larger than 10 nm. Data in Figure 6-14b shows that COMSOL model predicts a lower photovoltage than the analytical model. Overall, the photovoltages from the COMSOL model are about 10-50 mV lower. Regardless, both models follow the same general trend in which higher photovoltages are generally obtained for smaller nanoparticles.

The exact reason for the discrepancy in the models could be due to a variety of reasons. Whereas the analytical model is highly idealized, the COMSOL model is more realistic. The COMSOL model includes some alternative recombination mechanisms such as space charge recombination and shunt resistance which may lower the photovoltage relative to the analytical model. Meanwhile, we can rule out the contribution from the effective barrier heights in Figure

6-14a because they cannot explain the difference between the models. We can also rule out the impact of series resistance since it is negligible for the systems studied in COMSOL. But it could possible that the effective area of the nanoparticles could contribute to the discrepancy since the analytical model can have error for the smallest nanoparticles when $\frac{S_{eff}}{S}$ is very large (see Figure 6-3b). Overall, the COMSOL modeling confirms the general trends from the analytical model, and the conclusion still stands that experimental systems significantly outperform the theoretical photovoltages expected from the pinch-off effect.

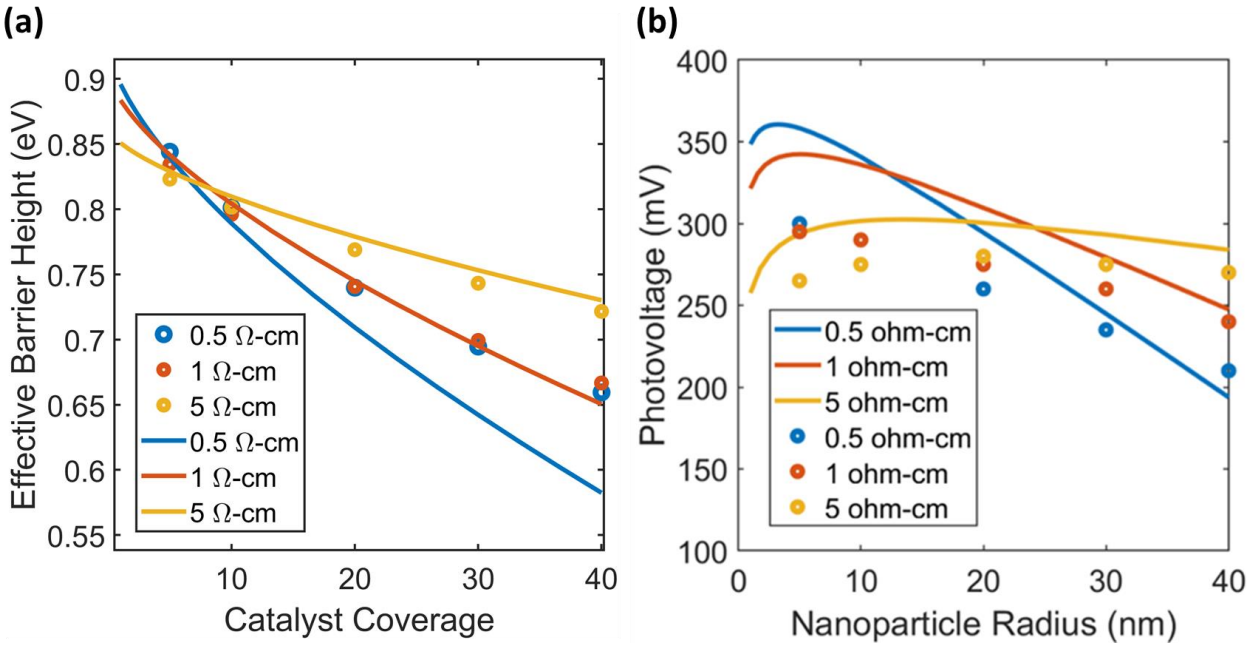

Figure 6-14: Compiled data for the effective barrier heights (a) and the generated photovoltage (b) as a function of nanoparticle radius and Si doping density. The circle data points are from the COMSOL model and the lines are from the analytical model.

6.6 Conclusions

The pinch-off effect has been widely used to explain large photovoltages of metal nanoparticle/semiconductor systems. However, a close analysis of how the important parameters contribute to the photovoltage has not been rigorously performed. Using analytical and COMSOL

modeling, we have demonstrated the importance of tuning the catalyst coverage, the nanoparticle radius, and the semiconductor doping density to optimize the performance. However, the modeled photovoltages are typically far less than 400 mV, while experimental photovoltages of 500 mV have been obtained with comparable systems with the same Ni nanoparticles on Si semiconductor.[15,39] Overall, the pinch-off effect cannot explain the high photovoltages from experiments, which suggests that there must be alternative contributions to experimental systems that are improving the performance. The next chapter takes a closer look at the experimental systems to establish plausible explanations for why experimental systems perform well with such high photovoltages. To conclude, this chapter aimed to clarify assumptions often made about pinched-off nanoparticle systems and shed light on interactions that may have been previously overlooked. Knowledge of these additional interactions may help optimize future nanoparticle devices and more clearly explain observed phenomena.

6.7 References

(1) Oh, K.; Mériadec, C.; Lassalle-Kaiser, B.; Dorcet, V.; Fabre, B.; Ababou-Girard, S.; Joanny, L.; Gouttefangeas, F.; Loget, G. Elucidating the Performance and Unexpected Stability of Partially Coated Water-Splitting Silicon Photoanodes. *Energy Environ. Sci.* **2018**, *11* (9), 2590–2599. https://doi.org/10.1039/C8EE00980E.

(2) Hernley, P. A.; Chavez, S. A.; Quinn, J. P.; Linic, S. Engineering the Optical and Catalytic Properties of Co-Catalyst/Semiconductor Photocatalysts. *ACS Photonics* **2017**, *4* (4), 979–985. https://doi.org/10.1021/acsphotonics.7b00047.

(3) Hong, W.; Cai, Q.; Ban, R.; He, X.; Jian, C.; Li, J.; Li, J.; Liu, W. High-Performance Silicon Photoanode Enhanced by Gold Nanoparticles for Efficient Water Oxidation. *ACS Appl. Mater. Interfaces* **2018**, *10* (7), 6262–6268. https://doi.org/10.1021/acsami.7b16749.

(4) Hernley, P. A.; Linic, S. Modeling the Impact of Metallic Plasmonic Resonators on the Solar Conversion Efficiencies of Semiconductor Photoelectrodes: When Does Introducing Buried Plasmonic Nanostructures Make Sense? *J. Phys. Chem. C* **2018**, *122* (42), 24279–24286. https://doi.org/10.1021/acs.jpcc.8b07214.

(5) Xie, S.; Zhang, Q.; Liu, G.; Wang, Y. Photocatalytic and Photoelectrocatalytic Reduction of CO 2 Using Heterogeneous Catalysts with Controlled Nanostructures. *Chem. Commun.* **2016**, *52* (1), 35–59. https://doi.org/10.1039/C5CC07613G.

(6) Zhao, G.; Huang, X.; Wang, X.; Wang, X. Progress in Catalyst Exploration for Heterogeneous CO2 Reduction and Utilization: A Critical Review. *J. Mater. Chem. A* **2017**, *5* (41), 21625–21649. https://doi.org/10.1039/C7TA07290B.

(7) Thalluri, S. M.; Bai, L.; Lv, C.; Huang, Z.; Hu, X.; Liu, L. Strategies for Semiconductor/Electrocatalyst Coupling toward Solar-Driven Water Splitting. *Adv. Sci.* **2020**, *7* (6), 1902102. https://doi.org/10.1002/advs.201902102.

(8) Laursen, S.; Linic, S. Geometric and Electronic Characteristics of Active Sites on TiO2-Supported Au Nano-Catalysts: Insights from First Principles. *Phys. Chem. Chem. Phys.* **2009**, *11* (46), 11006–11012. https://doi.org/10.1039/B912641D.

(9) Laursen, S.; Linic, S. Oxidation Catalysis by Oxide-Supported Au Nanostructures: The Role of Supports and the Effect of External Conditions. *Phys. Rev. Lett.* **2006**, *97* (2), 026101. https://doi.org/10.1103/PhysRevLett.97.026101.

(10) Sullivan, J. P.; Tung, R. T.; Pinto, M. R.; Graham, W. R. Electron Transport of Inhomogeneous Schottky Barriers: A Numerical Study. *J. Appl. Phys.* **1991**, *70* (12), 7403–7424. https://doi.org/10.1063/1.349737.

(11) Tung, R. T. Electron Transport of Inhomogeneous Schottky Barriers. *Appl. Phys. Lett.* **1991**, *58* (24), 2821–2823. https://doi.org/10.1063/1.104747.

(12) Tung, R. T. Electron Transport at Metal-Semiconductor Interfaces: General Theory. *Phys. Rev. B* **1992**, *45* (23), 13509–13523. https://doi.org/10.1103/PhysRevB.45.13509.

(13) Loget, G. Water Oxidation with Inhomogeneous Metal-Silicon Interfaces. *Curr. Opin. Colloid Interface Sci.* **2019**, *39*, 40–50. https://doi.org/10.1016/j.cocis.2019.01.001.

(14) Rossi, R. C.; Lewis, N. S. Investigation of the Size-Scaling Behavior of Spatially Nonuniform Barrier Height Contacts to Semiconductor Surfaces Using Ordered Nanometer-Scale Nickel Arrays on Silicon Electrodes. *J. Phys. Chem. B* **2001**, *105* (49), 12303–12318. https://doi.org/10.1021/jp011861c.

(15) Laskowski, F. A. L.; Oener, S. Z.; Nellist, M. R.; Gordon, A. M.; Bain, D. C.; Fehrs, J. L.; Boettcher, S. W. Nanoscale Semiconductor/Catalyst Interfaces in Photoelectrochemistry. *Nat. Mater.* **2020**, *19* (1), 69–76. https://doi.org/10.1038/s41563-019-0488-z.

(16) Tilley, S. D.; Cornuz, M.; Sivula, K.; Grätzel, M. Light-Induced Water Splitting with Hematite: Improved Nanostructure and Iridium Oxide Catalysis. *Angew. Chem. Int. Ed.* **2010**, *49* (36), 6405–6408. https://doi.org/10.1002/anie.201003110.

(17) Oh, K.; Dorcet, V.; Fabre, B.; Loget, G. Dissociating Water at N-Si Photoanodes Partially Covered with Fe Catalysts. *Adv. Energy Mater.* **2020**, *10* (3), 1902963. https://doi.org/10.1002/aenm.201902963.

(18) Cai, Q.; Hong, W.; Jian, C.; Liu, W. Ultrafast Hot Ion-Exchange Triggered Electrocatalyst Modification and Interface Engineering on Silicon Photoanodes. *Nano Energy* **2020**, *70*, 104485. https://doi.org/10.1016/j.nanoen.2020.104485.

(19) Zhang, P.; Wang, W.; Wang, H.; Li, Y.; Cui, C. Tuning Hole Accumulation of Metal Oxides Promotes the Oxygen Evolution Rate. *ACS Catal.* **2020**, *10* (18), 10427–10435. https://doi.org/10.1021/acscatal.0c02882.

(20) Lee, S. A.; Lee, T. H.; Kim, C.; Lee, M. G.; Choi, M.-J.; Park, H.; Choi, S.; Oh, J.; Jang, H. W. Tailored NiOx/Ni Cocatalysts on Silicon for Highly Efficient Water Splitting Photoanodes via Pulsed Electrodeposition. *ACS Catal.* **2018**, *8* (8), 7261–7269. https://doi.org/10.1021/acscatal.8b01999.

(21) Hill, J. C.; Landers, A. T.; Switzer, J. A. An Electrodeposited Inhomogeneous Metal-Insulator-Semiconductor Junction for Efficient Photoelectrochemical Water Oxidation. *Nat. Mater.* **2015**, *14* (11), 1150–1155. https://doi.org/10.1038/nmat4408.

(22) Lee, S. A.; Lee, T. H.; Kim, C.; Choi, M.-J.; Park, H.; Choi, S.; Lee, J.; Oh, J.; Kim, S. Y.; Jang, H. W. Amorphous Cobalt Oxide Nanowalls as Catalyst and Protection Layers on N-Type Silicon for Efficient Photoelectrochemical Water Oxidation. *ACS Catal.* **2020**, *10* (1), 420–429. https://doi.org/10.1021/acscatal.9b03899.

(23) Digdaya, I. A.; Trześniewski, B. J.; Adhyaksa, G. W. P.; Garnett, E. C.; Smith, W. A. General Considerations for Improving Photovoltage in Metal–Insulator–Semiconductor Photoanodes. *J. Phys. Chem. C* **2018**, *122* (10), 5462–5471. https://doi.org/10.1021/acs.jpcc.7b11747.

(24) Hemmerling, J.; Quinn, J.; Linic, S. Quantifying Losses and Assessing the Photovoltage Limits in Metal–Insulator–Semiconductor Water Splitting Systems. *Adv. Energy Mater.* **2020**, *10* (12), 1903354. https://doi.org/10.1002/aenm.201903354.

(25) Quinn, J. P.; Hemmerling, J.; Linic, S. Guidelines for Optimizing the Performance of Metal-Insulator-Semiconductor (MIS) Photoelectrocatalytic Systems by Tuning the Insulator Thickness. *ACS Energy Lett.* **2019**. https://doi.org/10.1021/acsenergylett.9b01609.

(26) Quinn, J.; Hemmerling, J.; Linic, S. Maximizing Solar Water Splitting Performance by Nanoscopic Control of the Charge Carrier Fluxes across Semiconductor–Electrocatalyst Junctions. *ACS Catal.* **2018**, *8* (9), 8545–8552. https://doi.org/10.1021/acscatal.8b01929.

(27) Zhang, Z.; Yates, J. T. Band Bending in Semiconductors: Chemical and Physical Consequences at Surfaces and Interfaces. *Chem. Rev.* **2012**, *112* (10), 5520–5551. https://doi.org/10.1021/cr3000626.

(28) Kenney, M. J.; Gong, M.; Li, Y.; Wu, J. Z.; Feng, J.; Lanza, M.; Dai, H. High-Performance Silicon Photoanodes Passivated with Ultrathin Nickel Films for Water Oxidation. *Science* **2013**, *342* (6160), 836–840. https://doi.org/10.1126/science.1241327.

(29) L. Laskowski, F. A.; R. Nellist, M.; Venkatkarthick, R.; W. Boettcher, S. Junction Behavior of N-Si Photoanodes Protected by Thin Ni Elucidated from Dual Working Electrode Photoelectrochemistry. *Energy Environ. Sci.* **2017**, *10* (2), 570–579. https://doi.org/10.1039/C6EE03505A.

(30) Li, S.; She, G.; Chen, C.; Zhang, S.; Mu, L.; Guo, X.; Shi, W. Enhancing the Photovoltage of Ni/n-Si Photoanode for Water Oxidation through a Rapid Thermal Process. *ACS Appl. Mater. Interfaces* **2018**, *10* (10), 8594–8598. https://doi.org/10.1021/acsami.7b16986.

(31) Liu, D.; Jiang, T.; Liu, D.; Zhang, W.; Qin, H.; Yan, S.; Zou, Z. Silicon Photoanode Modified with Work-Function-Tuned Ni@FeyNi1−y(OH)2 Core-Shell Particles for Water Oxidation. *ChemSusChem* **2020**, *13* (22), 6037–6044. https://doi.org/10.1002/cssc.202002049.

(32) Cai, Q.; Hong, W.; Jian, C.; Liu, W. A High-Performance Silicon Photoanode Enabled by Oxygen Vacancy Modulation on NiOOH Electrocatalyst for Water Oxidation. *Nanoscale* **2020**, *12* (14), 7550–7556. https://doi.org/10.1039/D0NR00921K.

(33) Green, M. A.; Keevers, M. J. Optical Properties of Intrinsic Silicon at 300 K. *Prog. Photovolt. Res. Appl.* **1995**, *3* (3), 189–192. https://doi.org/10.1002/pip.4670030303.

(34) Johnson, P. B.; Christy, R. W. Optical Constants of Transition Metals: Ti, V, Cr, Mn, Fe, Co, Ni, and Pd. *Phys. Rev. B* **1974**, *9* (12), 5056–5070. https://doi.org/10.1103/PhysRevB.9.5056.

(35) Rhoderick, E. H. Metal-Semiconductor Contacts. *IEE Proc. - Solid-State Electron Devices* **1982**, *129* (1), 1-. https://doi.org/10.1049/ip-i-1.1982.0001.

(36) Zanuccoli, M.; Magnone, P.; Sangiorgi, E.; Fiegna, C. Analysis of the Impact of Geometrical and Technological Parameters on Recombination Losses in Interdigitated Back-Contact Solar Cells. *Sol. Energy* **2015**, *116*, 37–44. https://doi.org/10.1016/j.solener.2015.03.042.

(37) Cuevas, A. The Recombination Parameter J0. *Energy Procedia* **2014**, *55*, 53–62. https://doi.org/10.1016/j.egypro.2014.08.073.

(38) Cai, Q.; Hong, W.; Jian, C.; Li, J.; Liu, W. Impact of Silicon Resistivity on the Performance of Silicon Photoanode for Efficient Water Oxidation Reaction. *ACS Catal.* **2017**, *7* (5), 3277–3283. https://doi.org/10.1021/acscatal.7b00507.

(39) Loget, G.; Fabre, B.; Fryars, S.; Mériadec, C.; Ababou-Girard, S. Dispersed Ni Nanoparticles Stabilize Silicon Photoanodes for Efficient and Inexpensive Sunlight-Assisted Water Oxidation. *ACS Energy Lett.* **2017**, *2* (3), 569–573. https://doi.org/10.1021/acsenergylett.7b00034.

(40) Meier, D. L.; Schroder, D. K. Contact Resistance: Its Measurement and Relative Importance to Power Loss in a Solar Cell. *IEEE Trans. Electron Devices* **1984**, *31* (5), 647–653. https://doi.org/10.1109/T-ED.1984.21584.

(41) Meier, D. L.; Chandrasekaran, V.; Gupta, A.; Yelundur, V.; Rohatgi, A. Silver Contact Grid: Inferred Contact Resistivity and Cost Minimization in 19% Silicon Solar Cells. *IEEE J. Photovolt.* **2013**, *3* (1), 199–205. https://doi.org/10.1109/JPHOTOV.2012.2217939.

(42) Gessert, T. A.; Coutts, T. J. Grid Metallization and Antireflection Coating Optimization for Concentrator and One-sun Photovoltaic Solar Cells. *J. Vac. Sci. Technol. A* **1992**, *10* (4), 2013–2024. https://doi.org/10.1116/1.578018.

(43) Wagner, L. F.; Young, R. W.; Sugerman, A. A Note on the Correlation between the Schottky-Diode Barrier Height and the Ideality Factor as Determined from I-V Measurements. *IEEE Electron Device Lett.* **1983**, *4* (9), 320–322. https://doi.org/10.1109/EDL.1983.25748.

(44) Walter, M. G.; Warren, E. L.; McKone, J. R.; Boettcher, S. W.; Mi, Q.; Santori, E. A.; Lewis, N. S. Solar Water Splitting Cells. *Chem. Rev.* **2010**, *110* (11), 6446–6473. https://doi.org/10.1021/cr1002326.

(45) Semiconductor Software - Modeling the Physics of Semiconductor Devices https://www.comsol.com/semiconductor-module (accessed 2021 -07 -15).

(46) Lindholm, F. A.; Fossum, J. G.; Burgess, E. L. Application of the Superposition Principle to Solar-Cell Analysis. *IEEE Trans. Electron Devices* **1979**, *26* (3), 165–171. https://doi.org/10.1109/T-ED.1979.19400.

(47) Böer, K. W. *Introduction to Space Charge Effects in Semiconductors*; Springer Series in Solid-State Sciences; Springer-Verlag: Berlin Heidelberg, 2010. https://doi.org/10.1007/978-3-642-02236-4.

Chapter 7

Atomistic Characterization and Properties of Nanoscale Metal/Semiconductor Interfaces on Water Splitting Photoelectrocatalysts

7.1 Introduction

The previous chapter developed models to obtain new insights and design principles for photoelectrocatalysts consisting of metal electrocatalyst nanoparticles dispersed on a semiconductor. The benefits of nanoparticle electrocatalysts is that they serve to enhance the rates of the desired chemical reactions,[1–5] improve the system stability,[6] and increase light absorption in the semicoductor.[7–11] Furthermore, the performance of these nanoparticle electrocatalyst/semiconductor (np-EC/SC) photoelectrocatalysts is to a large degree governed by the interface between the semiconductor and the electrocatalyst. These interfaces govern the transfer of photo-excited electrons and holes from the semiconductor to the electrocatalyst and therefore govern the generated photovoltage which is one of the critical figures of merit for solar water splitting performance.[12,13]

Despite the importance of the np-EC/SC interface, its physical and chemical properties are poorly understood and difficult to characterize. The challenge is that the interface is complex on atomic and nanoscales, often dynamic under reaction conditions, and inaccessible to direct experimental probes. For example, under the conditions of photoelectrocatalytic water oxidation reaction, there is a strong thermodynamic driving force to oxidize the interface at the regions that are accessible to the reacting electrolyte.[14] This driving force can lead to changes to the interface relative to the as-prepared material. The atomistic changes to the interface may affect the work

function, oxidation state, and catalytic function of the catalyst and semiconductor.[15,16] These changes can have a profound effect on the performance as described recently in the studies of individual electrocatalysts nanoparticles on Si semiconductor.[17]

In this contribution we shed light on the complexities associated with the evolution of the semiconductor/nanoparticle-electrocatalyst interface under photoelectrochemical water oxidation conditions. We do this by focusing on systems that contain planar silicon semiconductor in contact with nickel electrocatalysts. These types of Ni/Si systems have been of great interest for solar water splitting,[6,17–23] but the electronic properties and overall performance have not been quantitatively linked to the physical and chemical characteristics of the interface. Herein, we demonstrate the critical importance of the EC/SC interface by comparing the interfacial properties and the performance of planar Ni/Si systems and nanoparticle Ni/Si systems. We observe that under reaction conditions adventitious Ni oxide and Si oxide layers evolve at the interface between the Si and Ni nanoparticles. More importantly, we show that these atomistic changes to the interface need to be built into any physical model that can even qualitatively capture the behavior of these systems. Specifically, we show that the interfacial oxide layers play a critical role in (1) minimizing the electron/hole recombination by influencing the charge carrier fluxes, (2) increasing the barrier height of the EC/SC junction, and (3) improving the stability of the system. The findings show that to capture and optimize the behavior of multifunctional EC/SC systems, the atomistic structure of the interface under reaction conditions needs to be characterized. These results offer new insights and design principles to optimize the flux of charge carriers through EC/SC interfaces which are ubiquitous in photoelectrocatalysis.

7.2 Fabrication and Characterization

7.2.1 Fabrication of Ni Nanoparticles on Si

We fabricated and analyzed three experimental systems: (1) 5 nm of planar Ni film electrocatalyst evaporated on HF-etched Si (pf-Ni/Si), (2) 5 nm of planar Ni film evaporated on Si with a native silicon oxide layer (pf-Ni/SiO_2/Si), and (3) nanoparticle Ni electrodeposited on HF-etched Si (np-Ni/Si). The fabrication of planar systems was described in Chapter 2, while the nanoparticle Ni samples were fabricated using electrodeposition similar to previous reports.[17,24] In short, a three electrode setup (Ag/AgCl reference electrode and Pt wire counter electrode) was used with a Ni electrodeposition solution consisting of 0.01 M $NiCl_2$ and 0.1 M H_3BO_3. Before electrodeposition, the Si was HF-etched and then stored in water until it was time for fabrication. The electrodeposition of Ni nanoparticles occurred chronoamperometry for 5 seconds in which the potential was held at -2.3 V vs Ag/AgCl. The fabrication and experimental testing of the np-Ni/Si samples were performed by Aarti Mathur.

7.2.2 Electrochemical CVs and Photovoltage

Each sample was electrochemically tested and the cyclic voltammograms after 30 cycles of activation are provided in Figure 7-1 with the full CVs shown in a-c and a closeup of the photovoltage in d-f. The data in Figure 7-1a,d show that planar Ni electrocatalyst deposited on pristine planar Si (pf-Ni/Si), exhibits poor performance, generating only ~65 mV photovoltage under solar illumination. On the other hand, planar Ni electrocatalysts deposited on oxidized Si (pf-Ni/SiO_2/Si) yielded a higher photovoltage of 230 mV. The data also show that Ni nanoparticles Ni electrodeposited on Si (np-Ni/Si) generated a photovoltage of ~480 mV, which is comparable with previous literature results.[17,24]

The photo-limited current density for pf-Ni/SiO_2/n-Si (20.5 mA/cm^2) and np-Ni/n-Si (21 mA/cm^2) are very similar, meaning that the light transmission through the Ni overlayer is comparable despite the different architecture. While the Ni nanoparticles cover only about 21% of the Si surface, only a small fraction of the light can transmit through the relatively thick (> 40 nm) nanoparticles. Meanwhile the thin planar Ni (~5 nm) enables a larger fraction of the light to transmit through the layer. We also note that the photo-limited current of pf-Ni/n-Si does not plateau but instead continues to increase with increasing voltage. This phenomenon is due to the significant dark current that the system generates (in addition to the light current) because the barrier height is so poor and allows for a significant shunt current. After subtracting the dark current, the measured photo-limited current density is 20 mA/cm^2, in good agreement with the other samples.

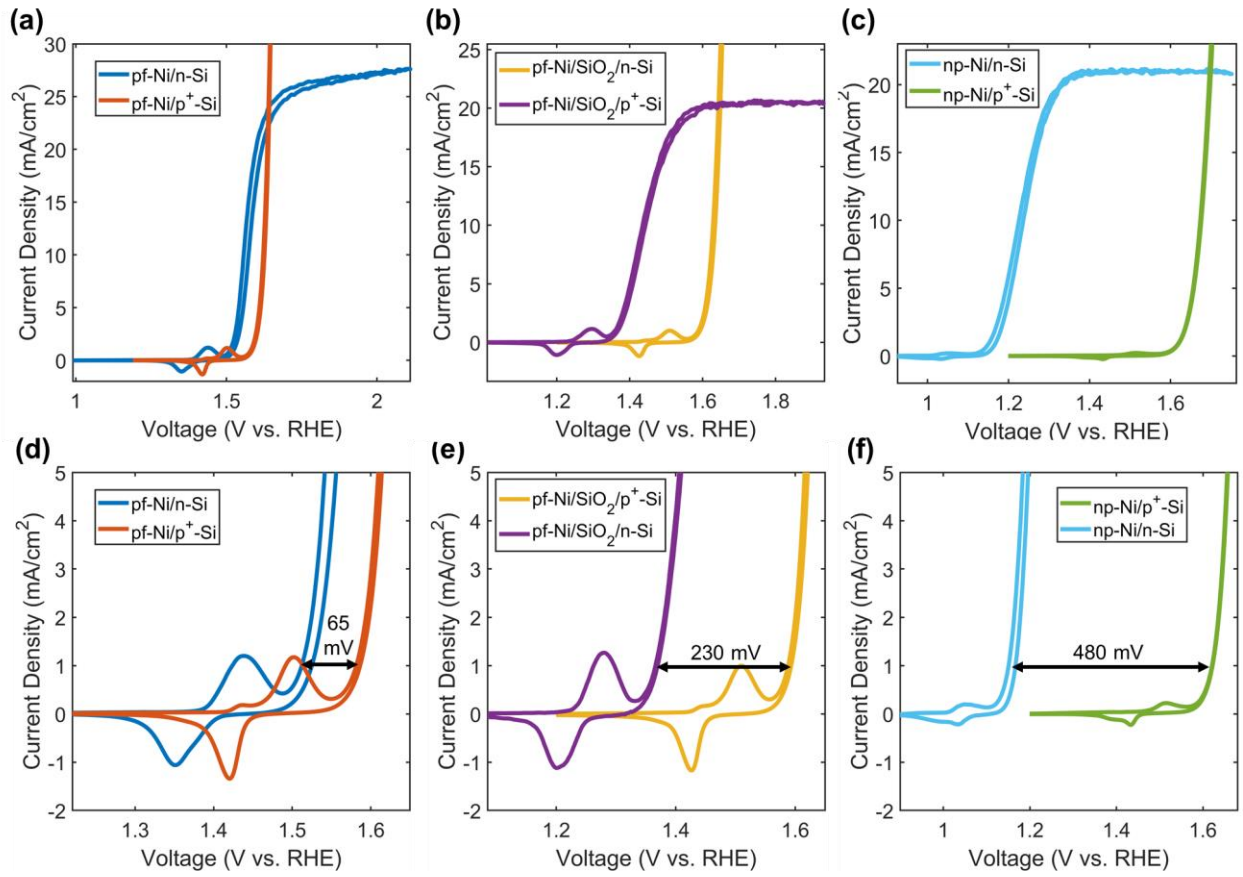

Figure 7-1: Cyclic Voltammetry plots after 30 cycles of activation for (a,d) pf-Ni /Si, (b,e) pf-Ni/SiO_2/Si, and (c,f) np-Ni/Si samples. Both illuminated n-Si and dark electrocatalytic p^+-Si are tested for each system architecture. These types of plots are used to evaluate the generated photovoltage, the onset potential and the kinetic overpotential for each system. It is noted that p^+-Si samples are valid controls for evaluating the photovoltage because the corresponding p^+-Si and n-Si samples each have similar number of Ni active sites as observed by the comparable sizes of the Ni oxidation and reduction peaks.

7.2.3 SEM Characterization

Figure 7-2 shows the scanning electron micrograph (SEM) top-down views of the np-Ni/n-Si and np-Ni/p^+-Si systems after the electrochemical cycling. For the electrodeposited Ni nanoparticles on both n-Si and p^+-Si, the average nanoparticle radius was 37.5 nm and 43.8 nm respectively and the nanoparticle size distributions (Figure 7-2c) are similar, confirming that the p^+-Si samples are valid electrocatalytic controls for evaluating the photovoltage. The top-down SEM images also reveal that around 22% of the Si surface is covered by the Ni nanoparticles.

Unlike the nanoparticle systems, the SEM images for the planar samples show minimal features indicating that the catalyst is planar and covering 100% of the Si surface (Figure 7-2d).

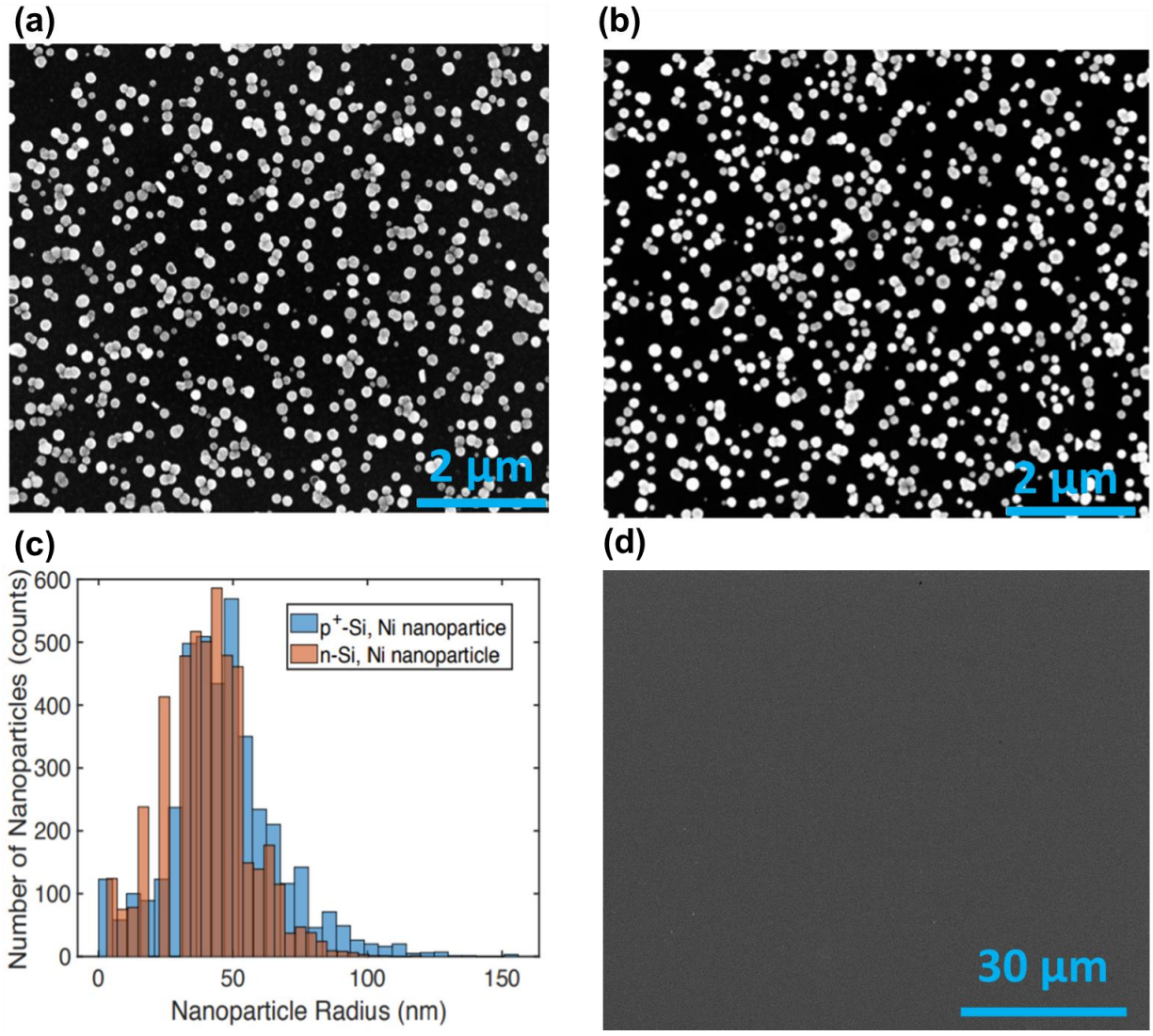

Figure 7-2: High magnification SEM characterization of (a) np-Ni/n-Si with 30% catalyst coverage, (b) np-Ni/p^+-Si with 21% catalyst coverage. (c) Size distribution of the nanoparticles which yields an average of 40 nm for np-Ni/n-Si and 56 nm for np-Ni/p^+-Si. (d) Lower magnification SEM characterization for np-Ni/n-Si showing minimal defects and 100% catalyst coverage.

7.2.4 Evolution of the Performance Over Time

We also monitored the performance of these systems over extended potential cycling. The data in Figure 7-1a show that under illumination the onset potential of each sample slightly

improves as the number of voltage sweeps increases during testing. The onset potential is governed by two factors: (1) the system's generated photovoltage and (2) the electrocatalyst overpotential. These two contributions can be deconvoluted by comparing the n-Si and p^+-Si data in Figure 7-3a,b. For all planar and nanoparticle Ni samples, the p^+-Si electrocatalytic overpotential improves at the same rate as the onset potentials for the n-Si samples, meaning that the generated photovoltage for each system is not changing as the function of voltage cycling (Figure 7-3c). As discussed in the supplement, the systems experience an increase in catalytic activity as more Ni is oxidized and incorporated with Fe ions from the electrolyte during each voltage sweep.[25] This leads to the observed increase in the onset potential, which is not accompanied with the increase in the system's generated photovoltage. These trends also continue for longer term cycling and stability testing (see supplement for details).

Figure 7-3 show that under illumination the onset potential of each sample slightly improves as the number of voltage sweeps increases during testing. The onset potential is governed by two factors: (1) the system's generated photovoltage and (2) the electrocatalyst overpotential. These two contributions can be deconvoluted by comparing the n-Si and p^+-Si data in Figure 7-3a,b. For all planar and nanoparticle Ni samples, the data shows that the p^+-Si electrocatalytic overpotential improves at the same rate as the onset potentials for the n-Si samples. Specifically, both the planar and nanoparticle systems experience an increase in catalytic activity as more Ni is oxidized and incorporated with Fe ions from the electrolyte during each voltage sweep.[25–29] This leads to the observed increase in the onset potential. Meanwhile, the data in Figure 7-3c show that the generated photovoltage for each system is not significantly changing as the function of voltage cycling (Figure 7-3c). Therefore, the overall

improvement of the onset potential over extended cycling is attributed to an increase in the catalytic activity rather than any change in the generated photovoltage.

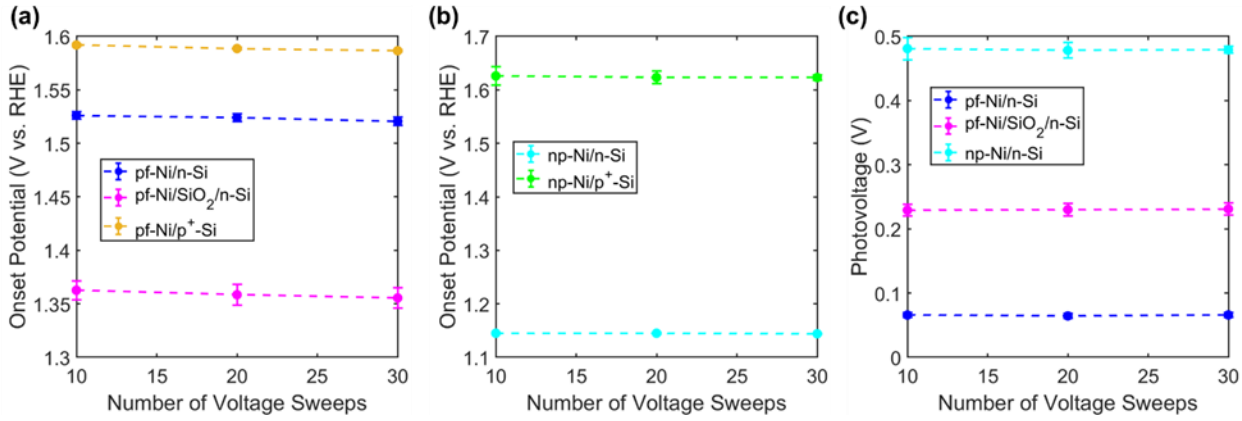

Figure 7-3: (a) Evolution of the onset potentials as a function of increasing voltage sweeps for 1-sun illuminated nickel systems and dark catalyst control samples for (a) pf-Ni/Si and pf-Ni/SiO_2/Si and (b) np-Ni/Si. (c) Photovoltage as a function of voltage sweeps for pf-Ni/Si, pf-Ni/SiO_2/Si, and np-Ni/Si systems, defined as the difference in onset potentials between illuminated systems and respective dark electrocatalytic controls.

7.2.5 STEM Characterization of the Interfaces

To understand the significant differences in the measured photovoltage for each system in Figure 7-1, we characterized the Ni/Si interface using scanning transmission electron microscopy (STEM) cross-sectional imaging. The STEM image of a representative nanoparticle in Figure 7-4 shows that the radius of the contact area at the Ni nanoparticle/Si interface is significantly smaller than the nanoparticle radius. On average, the actual contact area of the interface is a factor of ~2 times smaller than the amount of Si surface that appears to be covered based on the SEM images in Figure 7-2. We note that the nanoparticle radius is an important consideration for light absorption and transmission, but the contact radius is critically important for the charge transfer and recombination at the nanoparticle/semiconductor interface. By combining the SEM top-down view with the STEM cross-sectional view, we measure that the actual catalyst contact area is approximately 10% of the Si surface

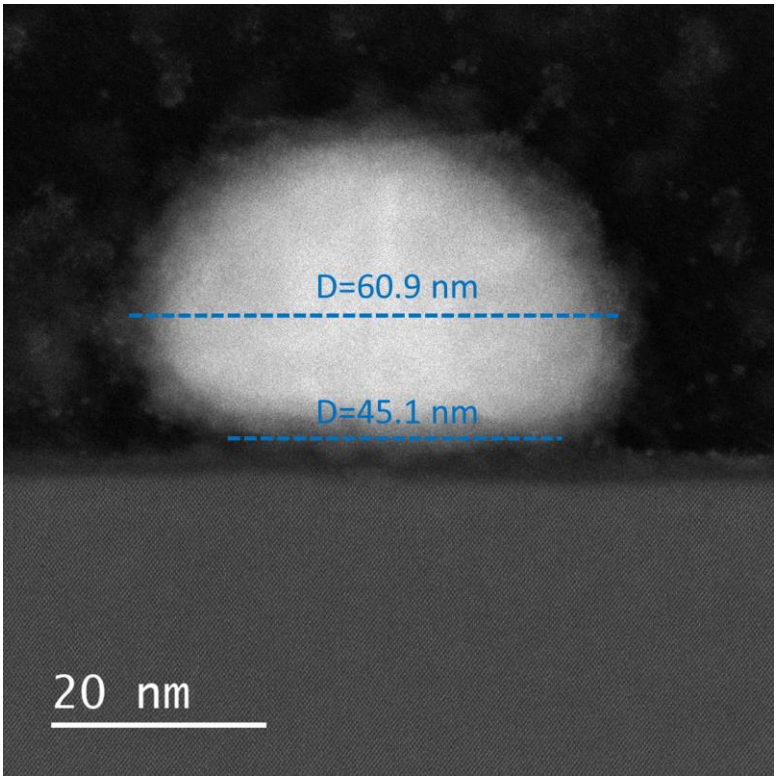

Figure 7-4: Cross-sectional STEM image of nanoparticle system demonstrating the difference in the actual contact radius compared to the nanoparticle radius.

We also performed elemental mapping of the interfaces for each photoelectrocatalyst system. Figure 7-5a,b shows the cross-sectional STEM images for the planar Ni samples after OER experimental testing. The data show that in these systems, the Ni atoms at the surface of the Ni electrocatalyst that are directly exposed to the electrolyte are oxidized. The electrolyte does not penetrate through the Ni film, so the underlying Ni/Si interface remains buried and unaffected by the electrolyte. The pf-Ni/Si system exhibits a direct Ni/Si contact without an interfacial layer while pf-Ni/SiO_2/n-Si exhibits a 1.6 nm thick SiO_2 interfacial layer.

The data in Figure 7-5c show that as-deposited Ni nanoparticles on Si are in metallic state with undetectable NiO_x. On the other hand, after OER testing, a thin NiO_x shell surrounds the Ni nanoparticles, forming a core-shell Ni/ NiO_x structure. The NiO_x shell is formed in-situ as a

result of the interaction between the system and the electrolyte under the oxidizing conditions of OER. The cross-sectional images also show that the interface between the Ni and the Si is fully oxidized, with layers of SiO_2 and NiO_x forming during OER. This result contrasts with previous reports which generally assume that the interface is a direct Ni/Si contact.[17] Comparing the images in Figure 7-5c,d shows that the as-deposited and post-testing samples exhibit the same SiO_2 thickness (~2.3 nm) throughout the system. This indicates that the SiO_2 layer is formed before Ni electrodeposition when the Si is exposed to air or the electrodeposition electrolyte and also demonstrates that the SiO_2 is stable (i.e., not growing or being etched) throughout the timescale of the experiments (30 voltage sweeps). Meanwhile, the NiO_x layer at the interface grows from 0 nm to approximately 2.4 nm throughout the experiments, which is comparable to the thickness of the NiO_x shell surrounding the nanoparticles.

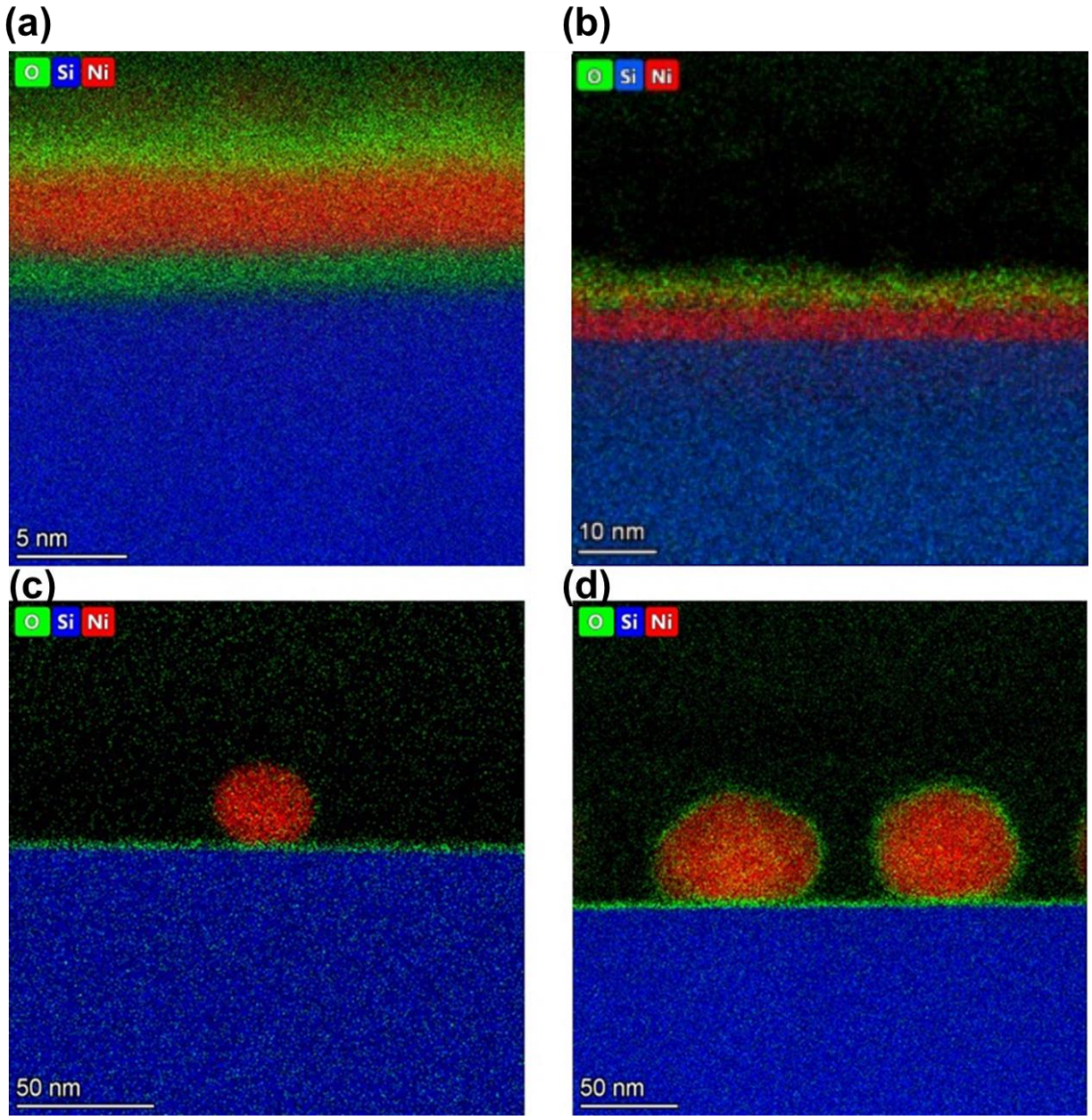

Figure 7-5: EDS analysis of the STEM cross sections for (a) Tested pf-Ni/SiO_2/n-Si (b) tested pf-Ni/n-Si (c) as-deposited np-Ni/n-Si, (d) Tested np-Ni/n-Si.

The question is to what extent these atomistic changes impact the performance of the Ni/Si photoelectrocatalysts in OER. The changes that can play a significant role in generating a photovoltage are: (i) the formation of the interfacial NiO_x and SiO_2 layers can lead to the change in the barrier height, (ii) the formation of the thin SiO_2 insulator layers can lead to the change in

the flux of energetic electrons and holes across the metal/semiconductor interface, (iii) the precise geometry of the interfacial contact area will also modulate the transfer of charge carriers across the interface.

It is important to quantify how these atomistic geometric changes impact the performance of the Ni/Si photoelectrocatalysts in OER. The atomistic changes that can play a significant role in affecting a photovoltage are:

(i) The formation of the interfacial NiO_x layers can lead to the change in the static barrier height between EC and SC. For metal-EC/SC contacts, the equilibration between the SC and EC Fermi levels results in an electric potential barrier height that promotes a selective transfer of one charge carrier (in this case, holes) while impeding the transport of the opposite charge carrier.[30] This potential barrier (also known as the barrier height), governs the e^-/h^+ recombination rates and is dependent on the properties of the metal/semiconductor interface. A smaller barrier leads to higher recombination rates and photovoltage losses.

(ii) The formation of the interfacial SiO_2 layers can also impact the magnitude of the barrier height since the direct Si/Ni contacts can lead to formation of Ni silicide or the undesired Fermi level pinning due to the creation of direct Ni-Si chemical bonds.

(iii) The formation of the thin SiO_2 insulator layers can also lead to the change in the flux of energetic electrons and holes across the metal/semiconductor interface since these charge carriers need to tunnel through the insulator to reach the electrocatalyst. This also can affect the recombination rates and impact the photovoltage.[12,31–34]

(iv) The geometry of the interfacial contact area will also modulate the transfer of charge carriers across the interface, i.e., the rate of the collection of charge carriers by the EC is affected by the interfacial contact EC/SC area.[35]

7.2.6 Experimental and Modeled Barrier Heights at the Metal/Semiconductor Interface

To test whether the barrier height is different for the oxidized interface in contact with Ni compared to the non-oxidized Si/Ni interface, we performed the Mott-Schottky analysis and light intensity variation experiments as detailed in Chapter 2. The pf-Ni/n-Si sample does not have enough space charge capacitance to perform the Mott-Schottky analysis, and so the light intensity experiments were used to determine the barrier height instead (which is possible because there is no insulator layer). The compiled ideality factors and ideal barrier heights from these experiments are provided in Figure 7-6. The resulting barrier height for pf-Ni/n-Si (i.e., Si in direct contact with Ni) is 0.59 eV which is consistent with previously reported values.[17,21] Such a low barrier height is typically attributed to Fermi level pinning or to the formation of a nickel silicide at the interface.[36,37] Meanwhile, the ideal barrier height of the planar Ni/SiO_2/Si was measured to be 0.67 eV. The results demonstrate that the SiO_2 interfacial layer significantly improves the Mott-Schottky barrier height, probably by physically preventing the formation of Ni silicide at the interface.[36,37]

It is worth noting that the ideality factor for the pf-Ni/n-Si is close to 1 which is relatively common for Schottky contacts,[36–38] while the pf-Ni/SiO_2/Si systems have an ideality factor of ~1.7. Therefore, the native oxide layer results in nonidealities which are comparable to the nonidealities previously discussed in Chapters 3 through 5. Following previous discussions, these nonidealities result in actual barrier heights that are lower than the ideal barrier height which is evaluated by the Mott-Schottky equation. However, the enhanced tunneling probability

from the SiO_2 more than compensates for the lower barrier height to yield a higher photovoltage (Figure 7-1).

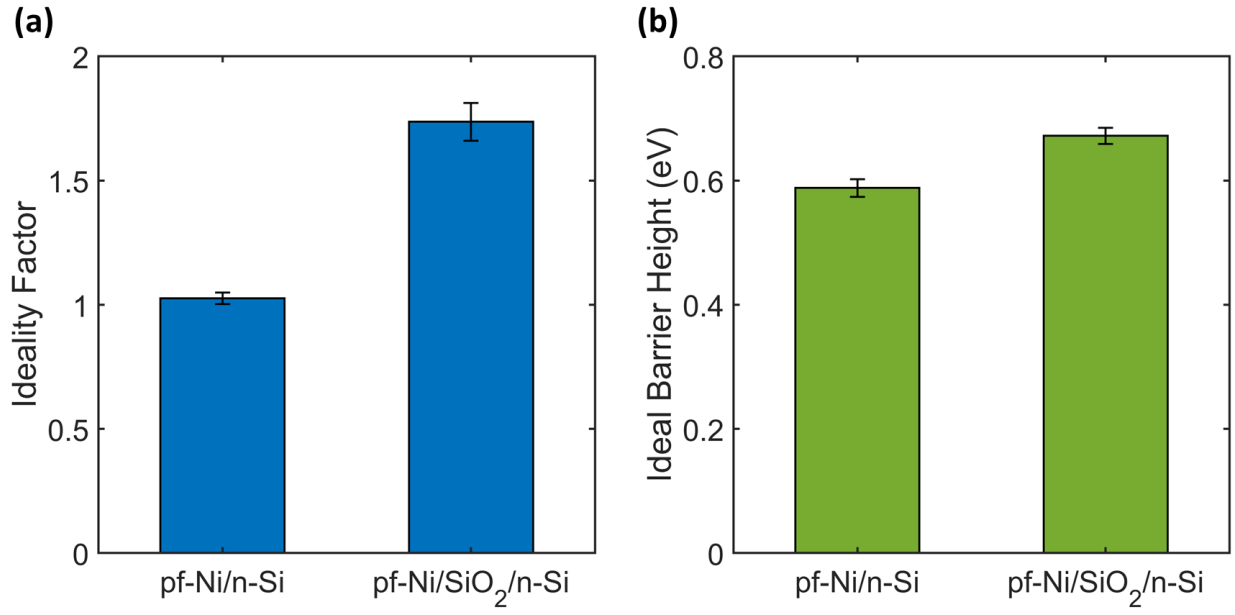

Figure 7-6: (a) Ideality factors and (b) ideal barrier heights measured from combined Mott-Schottky analysis and light intensity experiments for pf-Ni/n-Si and pf-Ni/ SiO_2/n-Si.

Due to the heterogeneous nature of the np-EC/SC systems (i.e., a fraction of Si is covered by Ni and the rest with the electrolyte), the barrier height cannot be directly evaluated with Mott-Schottky analysis. The nanoparticle systems are expected to have a similar barrier height to the pf-Ni/SiO_2/n-Si system because both contain similar SiO_2 interfacial layers. As demonstrated above, the nanoparticle systems, however, also have a thin interfacial NiO_x layer, so we explored how the additional oxidation of interfacial Ni atoms under the OER conditions could enhance the barrier height. We synthesized planar Si/SiO_2/NiO_x/Ni systems by oxidizing the Ni layers in the planar Si/SiO_2/Ni sample and depositing an additional 20 nm thick Ni layer on the NiO_x. While this system is not identical to the system that contained Ni nanoparticles, the Mott-Schottky analysis showed that the barrier height was not enhanced further by the NiO_x layer. A control

sample of 20-Ni/SiO_2/n-Si without the NiO_x interfacial layer was also fabricated. The CVs in Figure 7-7a in a ferri/ferrocyanide electrolyte shows that the sample with NiO_x is highly resistive. In contrast, our experimental nanoparticle systems are not resistive, which suggests the that the NiO_x is not significantly impacting the performance. Figure 7-7b shows the flat-band potentials for each system. The presence of interfacial NiO_x results in a slightly lower flat-band potential, meaning that the effective work function of the NiO_x/Ni contact is lower than the pure Ni contact. This analysis suggests interfacial NiO_x has a negligible or detrimental effect on the barrier height of the system. Indeed, such a thin NiO_x layer (~2 nm) underneath a >20 nm Ni np overlayer is expected to have a negligible impact on the effective work function and barrier height of the junction because the thick overlayer tends to dominate the junction characteristics, especially when there is considerable interdiffusion between the layers.[39]

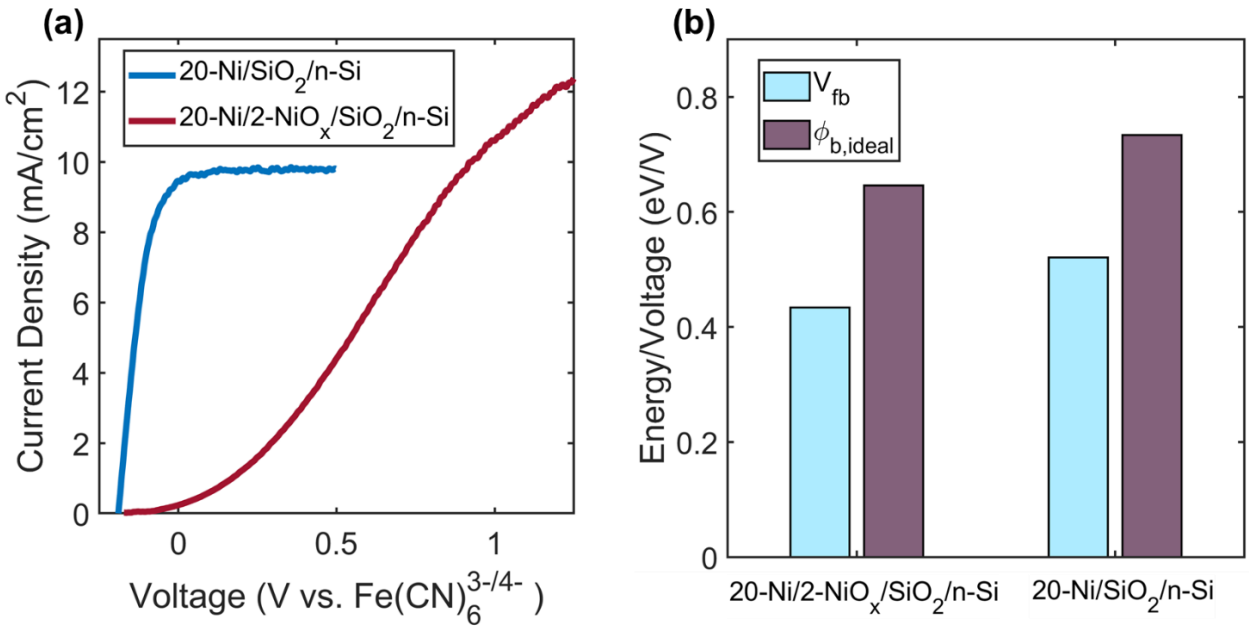

Figure 7-7: (a) CVs in 350/50 mM ferri/ferrocyanide and 1 M KCl electrolyte under approximately 1-sun illumination. The curves are corrected for solution resistance and the dark current was subtracted. (b) Measured flat-band potentials and ideal barrier heights for 20-Ni/2-NiO_x /SiO_2/n-Si and 20-Ni/SiO_2/n-Si.

We also note that previous literature has attributed the high photovoltages of nanoparticle systems to the so-called, pinch-off effect.[35,40] Specifically, it has been proposed that the evolution of a high work function NiO_x (>5 eV[15,41–43]) shell surrounding the nanoparticle increases the effective barrier height.[17,18,23,44,45] To investigate this possibility, we modeled the nanoparticle systems with COMSOL finite-element simulations similar to the methods discussed in the previous chapter. The primary difference from the modeling in the previous chapter is that the high barrier region is now modeled as a thin shell surrounding the nanoparticle rather than as an extended region (Figure 6-12). The dimensions of the contact area and shell thickness are based on the cross-sectional STEM analysis, and the contact barrier heights are varied based on experimental and literature values. We note that the model is designed to capture the upper-bound on the pinch-off effect by (1) removing all other sources of recombination besides recombination under the nanoparticle contact, (2) using the upper limit for the barrier height of the oxide shell, and (3) minimizing resistance losses.

Ni Nanoparticles with radius of 20 nm and 40 nm with a barrier height of 0.6 eV (matching the experiment results) were each surrounded by a 10 nm thick NiO_x shell with a work function of 5.15 eV. This work function yields band bending equal to the band gap of Si which is the upper limit, and this was selected to predict the upper limit to the pinch-off effect that could be induced by a high work function shell.

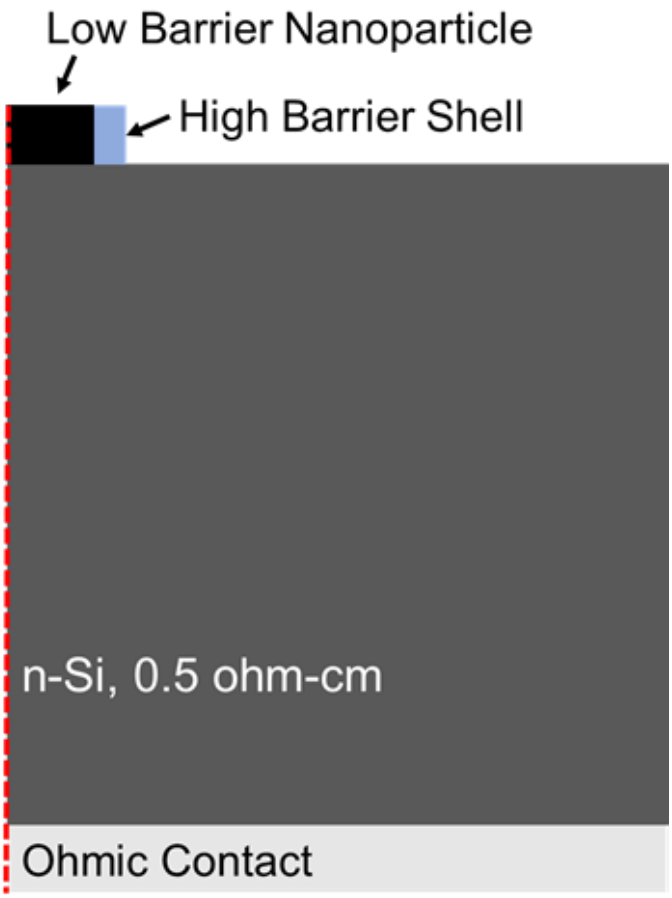

Figure 7-8: Schematic of the model geometry used for COMSOL simulations. The overall dimensions of the Si is 1x1 μm, which is big enough to fit the entire space charge region, but small enough to minimize resistance losses. The radius of the nanoparticle is 20 or 40 nm with a barrier height of 0.6 eV and each nanoparticle is surrounded by a 10 nm thick NiO_x shell with a work function of 5.15 eV. The resistivity of the Si is 0.5 ohm-cm which is comparable to the experimental Si used in this study. In some models, the shell is reduced to zero to determine how the shell impacts the band bending and effective barrier height. The red dashed line marks the axis in which the system is rotated with axial symmetry.

The data in Figure 7-9 conduction band edges plotted into the depth of the Si semiconductor for each nanoparticle size. For the case of 40 nm radius, the effective barrier height is the same for a nanoparticle with a high work function shell and a nanoparticle without the shell (i.e., the effective barrier height remains at the non-pinched-off value of 0.6 eV). The introduction of the shell only widens the barrier, but the recombination current is governed by the height of the barrier, not the width. For the case of the 20 nm radius, the effective barrier

height slightly increases by a few mV after adding a high work function shell compared to a nanoparticle without the shell. However, this increase is quite negligible and only increases the systems generated photovoltage by a few mV, not nearly enough to explain the high performance observed experimentally. These results corroborate the results from Chapter 6 in that the pinch-off effect is expected to have a negligible impact on the effective barrier height and the photovoltage generated by these systems.

Furthermore, we observed no photovoltage enhancement in Figure 7-3c despite the extensive oxidation of the Ni nanoparticles, confirming that the NiO_x does not significantly impact the photovoltage. We can therefore assume that the barrier height in the nanoparticle systems is similar to the barrier height in the planar $Si/SiO_2/Ni$ systems (~0.67 eV).

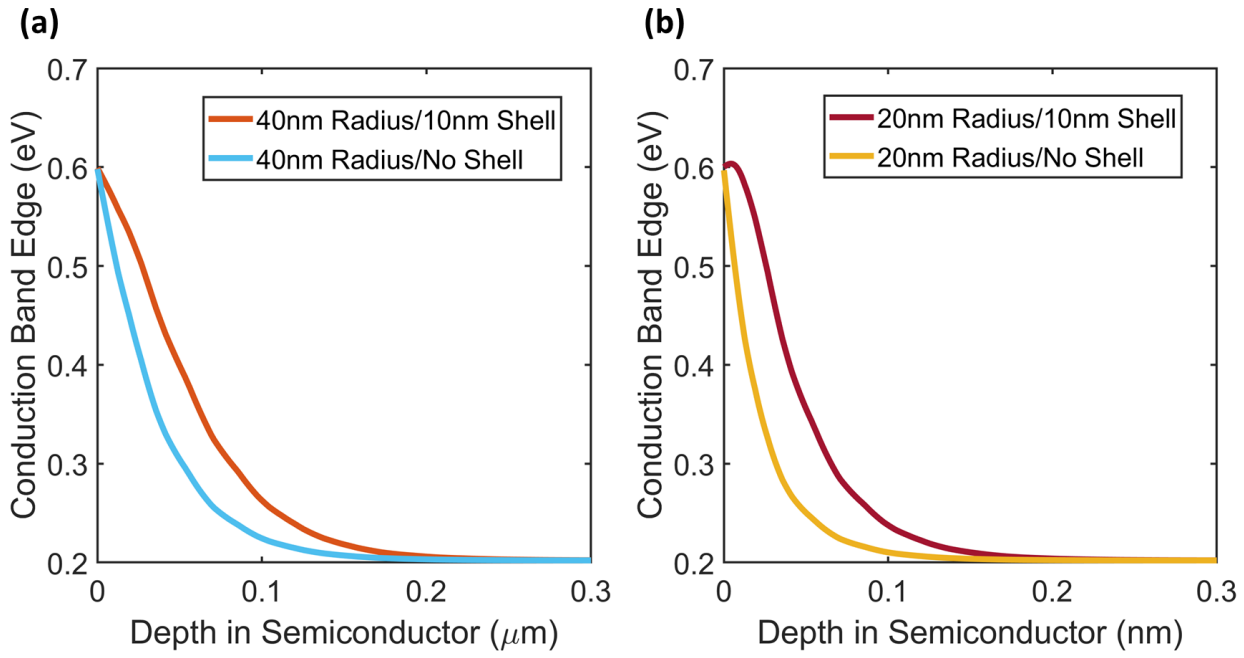

Figure 7-9: Conduction band edges plotted into the depth of the Si semiconductor for Ni nanoparticles with (a) 40 nm radius and (b) 20 nm radius with and without a high work function shell.

To summarize, the compiled results show that: (1) the EC/SC contact area is significantly lower than the area covered by the nanoparticles, and only a relatively small fraction of the Si

surface (~10 percent) is in the direct contact with the electrocatalysts and (2) in the case where the electrolyte can reach the interface, there is a degree of oxidation of the interfacial Ni and Si atoms. The presence of the oxides increases the barrier height from 0.59 eV for the pf-Ni/n-Si to 0.67 eV for pf-Ni/SiO_2/n-Si. Furthermore, the presence of the SiO_2 insulator at the interface will impact the flow of energetic charge carriers, which need to tunnel from the semiconductor to the electrocatalyst through the interface.[12,34]

7.3 Interfacial Insights from Modeling

We have developed analytical models to describe how these changes to the nanoparticle system impact the overall OER performance. The model is based on the illuminated diode equation, in which the relationship between the photovoltage (V_{ph}) and the net current (J_{net}) through an EC/SC interface is given by the expression:[31]

$$|V_{ph}| \approx \frac{nkT}{q}\left[ln\frac{J_{ph}-J_{net}}{J_s}\right] \quad 7\text{-}1$$

Where n is the ideality factor, k is the Boltzmann constant, T is temperature, J_{ph} is the photo-limited current density, and J_s is the dark saturation current which is related to the rate at which electrons can migrate to the metal electrocatalyst and recombine with holes. J_s is a critical parameter governing e^-/h^+ recombination rates and the generated photovoltage. For the initial case of a planar metal/semiconductor interface, J_s can be evaluated using the following expression:[36]

$$J_s = A^*T^2 exp\left(-\frac{q\phi_b}{kT}\right) \quad 7\text{-}2$$

Here, A^* is Richardson's constant, and ϕ_b is the barrier height which is defined as the difference between the silicon conduction band and the effective work function of the metal at the interface (see Figure 7-10a).

The pf-Ni/n-Si system with direct Ni/Si contact can be modeled using equations 7-1 and 7-2. In general, the current-voltage curves are modeled by (1) using the experimentally evaluated barrier height, ideality factor, and photo-limited current density, (2) plugging equation 2 into equation 1, and (3) incorporating the electrocatalytic current which is modeled using the Butler-Volmer equation.

Modeling planar systems with interfacial insulator layers or Ni nanoparticle systems introduce a few physical changes that need to be introduced in the model. These physical changes affect the reverse saturation recombination current. These changes include an increase in the barrier height from 0.59 to 0.67 eV due to the presence of the SiO_2 at the interface, the lower Si/Ni contact area, and the fact that the formation of the Si insulator limits the flow of charge carriers which now must tunnel through the insulator. The reverse saturation recombination current can be generalized to account for these modifications:

$$J_s = f_c A^* T^2 exp\left(-\frac{q\phi_b}{kT}\right) exp\left(-\propto d\sqrt{\phi_e}\right)$$

Here, f_c is the fraction of the semiconductor surface in direct contact with the catalyst ($f_c = 1$ for planar films, $f_c < 1$ for nanoparticles). The second exponential term ($T_t = exp\left(-\propto d\sqrt{\phi_e}\right)$) is the probability that an electron will tunnel through the insulator where $\propto$ is a constant approximately equal to 1,[46] d is the insulator thickness, and ϕ_e is the offset between the insulator conduction band and semiconductor conduction band (see Figure 7-10a for illustrations of these variables). For bulk SiO_2, ϕ_e exceeds 3 eV, but the actual offset is significantly lower for nanoscale SiO_2.[47,48] Using previously described methodology,[31] we calculate an insulator offset of 0.14 eV and a tunneling probability of 0.002 for pf-Ni/SiO_2/n-Si with 1.6 nm thick SiO_2. We incorporate this tunneling probability and other experimental parameters to obtain an excellent model fit to the experimental data for pf-Ni/SiO_2/n-Si (Figure 7-10b). Assuming the same

insulator offset for the np-Ni/Si system with 2.3 nm thick SiO_2, we calculate the tunneling probability to be ~1×10^{-4}. This means that the SiO_2 layer in np-Ni/n-Si decreases recombination rates by preventing 99.99% of the electrons from tunneling through the insulator. These results are comparable to previous tunneling probabilities obtained for ~2 nm thick SiO_2.[46,48,49]

Using the experimental catalyst contact area, barrier height, ideality factor, and tunneling probability, we have modeled the I-V curves for np-Ni/Si (see supplement for details). There is uncertainty in the modeling based on the standard deviations of the measured experimental parameters (particularly the SiO_2 thickness), and the upper and lower bounds for the model are shown in Figure 7-10c. The experimental I-V curves in Figure 7-10c are within the bounds of the model. Therefore, the model captures the critical physical features that contribute to the enhanced performance of these complex nanoparticle systems. Such a good fit to the experimental data would not be possible without accounting for the interfacial SiO_2 layer. Indeed, alternative contributions like the pinch-off effect are expected to be negligible, and the COMSOL simulations without an insulator layer underpredicts the photovoltage by hundreds of mV. These modeling efforts therefore emphasize the critical role of the SiO_2, the barrier height and the interfacial geometry in these systems.

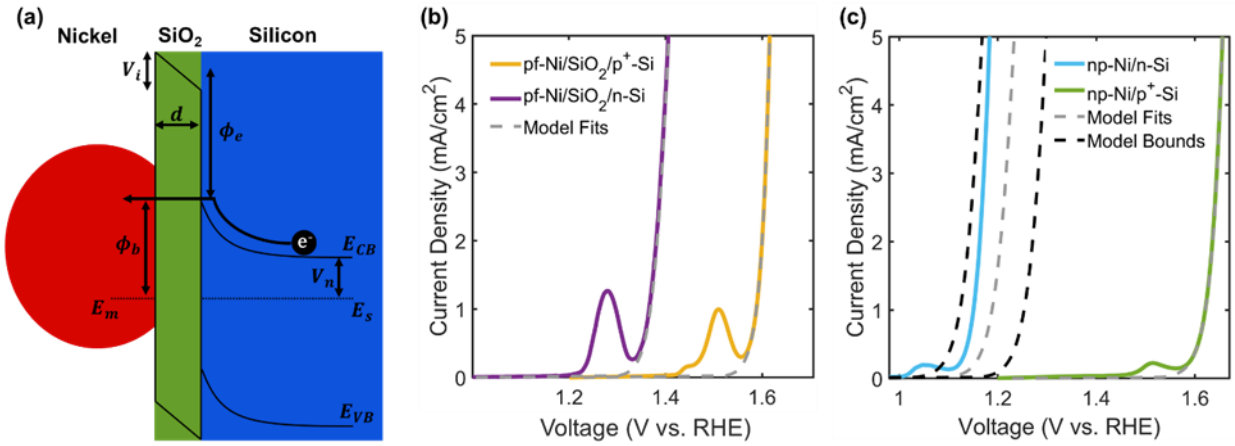

Figure 7-10: (a) Energy band diagram of a nanoparticle-based system that illustrates the key parameters. (b,c) Experimental current-voltage forward sweeps overlaid with the corresponding modeled fits for (b) pf-Ni/SiO_2/Si and (c) np-Ni/Si.

7.4 Conclusions

Investigating the true nature of the interface between nanoscale catalysts and semiconductor light absorbers is of high interest to rigorously understand the performance of water splitting devices. We experimentally compared the performance of planar nickel and nickel nanoparticle electrocatalysts deposited on Si to determine how both systems evolve over time and highlight the importance of the interfaces. Average photovoltages of ~480 mV were recorded for nanoparticle systems, compared to 230 mV for planar Ni/SiO_2/Si, and only 65 mV for planar Ni/Si. STEM and EDS analysis identified the presence of a static 2.3 nm silicon oxide at the semiconductor/catalyst interface for nanoparticles before and after testing under OER conditions while an NiO_x shell surrounds the nanoparticle including at the interface.

Detailed computational modeling confirms that the presence of an advantageous silicon oxide insulator layer serves to enhance the barrier height and provide hole selectivity to dramatically improve the photovoltage for nanoparticle systems. STEM and EDS analysis of samples before and after testing showed the growth of a nickel oxide shell that gradually

increased the catalytically active area but did not significantly impact the barrier height or the system's generated photovoltage. Instead, our modeling efforts demonstrate that the combination of low catalyst/semiconductor contact area and the SiO_2 layer are the major contributors towards the high performing nanoparticle photoelectrocatalysts. These insights can be used to design novel photoelectrocatalysts with improved interfaces and highly stable nanoscale catalyst geometry.

7.5 References

(1) Xie, S.; Zhang, Q.; Liu, G.; Wang, Y. Photocatalytic and Photoelectrocatalytic Reduction of CO 2 Using Heterogeneous Catalysts with Controlled Nanostructures. *Chem. Commun.* **2016**, *52* (1), 35–59. https://doi.org/10.1039/C5CC07613G.

(2) Zhao, G.; Huang, X.; Wang, X.; Wang, X. Progress in Catalyst Exploration for Heterogeneous CO2 Reduction and Utilization: A Critical Review. *J. Mater. Chem. A* **2017**, *5* (41), 21625–21649. https://doi.org/10.1039/C7TA07290B.

(3) Thalluri, S. M.; Bai, L.; Lv, C.; Huang, Z.; Hu, X.; Liu, L. Strategies for Semiconductor/Electrocatalyst Coupling toward Solar-Driven Water Splitting. *Adv. Sci.* **2020**, *7* (6), 1902102. https://doi.org/10.1002/advs.201902102.

(4) Laursen, S.; Linic, S. Geometric and Electronic Characteristics of Active Sites on TiO2-Supported Au Nano-Catalysts: Insights from First Principles. *Phys. Chem. Chem. Phys.* **2009**, *11* (46), 11006–11012. https://doi.org/10.1039/B912641D.

(5) Laursen, S.; Linic, S. Oxidation Catalysis by Oxide-Supported Au Nanostructures: The Role of Supports and the Effect of External Conditions. *Phys. Rev. Lett.* **2006**, *97* (2), 026101. https://doi.org/10.1103/PhysRevLett.97.026101.

(6) Oh, K.; Mériadec, C.; Lassalle-Kaiser, B.; Dorcet, V.; Fabre, B.; Ababou-Girard, S.; Joanny, L.; Gouttefangeas, F.; Loget, G. Elucidating the Performance and Unexpected Stability of Partially Coated Water-Splitting Silicon Photoanodes. *Energy Environ. Sci.* **2018**, *11* (9), 2590–2599. https://doi.org/10.1039/C8EE00980E.

(7) Hernley, P. A.; Chavez, S. A.; Quinn, J. P.; Linic, S. Engineering the Optical and Catalytic Properties of Co-Catalyst/Semiconductor Photocatalysts. *ACS Photonics* **2017**, *4* (4), 979–985. https://doi.org/10.1021/acsphotonics.7b00047.

(8) Hong, W.; Cai, Q.; Ban, R.; He, X.; Jian, C.; Li, J.; Li, J.; Liu, W. High-Performance Silicon Photoanode Enhanced by Gold Nanoparticles for Efficient Water Oxidation. *ACS Appl. Mater. Interfaces* **2018**, *10* (7), 6262–6268. https://doi.org/10.1021/acsami.7b16749.

(9) Hernley, P. A.; Linic, S. Modeling the Impact of Metallic Plasmonic Resonators on the Solar Conversion Efficiencies of Semiconductor Photoelectrodes: When Does Introducing Buried Plasmonic Nanostructures Make Sense? *J. Phys. Chem. C* **2018**, *122* (42), 24279–24286. https://doi.org/10.1021/acs.jpcc.8b07214.

(10) Ingram, D. B.; Linic, S. Water Splitting on Composite Plasmonic-Metal/Semiconductor Photoelectrodes: Evidence for Selective Plasmon-Induced Formation of Charge Carriers near the Semiconductor Surface. *J. Am. Chem. Soc.* **2011**, *133* (14), 5202–5205. https://doi.org/10.1021/ja200086g.

(11) Chavez, S.; Govind Rao, V.; Linic, S. Unearthing the Factors Governing Site Specific Rates of Electronic Excitations in Multicomponent Plasmonic Systems and Catalysts. *Faraday Discuss.* **2019**, *214* (0), 441–453. https://doi.org/10.1039/C8FD00143J.

(12) Hemmerling, J. R.; Mathur, A.; Linic, S. Design Principles for Efficient and Stable Water Splitting Photoelectrocatalysts. *Acc. Chem. Res.* **2021**, *54* (8), 1992–2002. https://doi.org/10.1021/acs.accounts.1c00072.

(13) Scheuermann, A. G.; Chidsey, C. E. D.; McIntyre, P. C. Understanding Photovoltage in Insulator-Protected Water Oxidation Half-Cells. *J. Electrochem. Soc.* **2016**, *163* (3), H192–H200. https://doi.org/10.1149/2.0601603jes.

(14) Chen, S.; Wang, L.-W. Thermodynamic Oxidation and Reduction Potentials of Photocatalytic Semiconductors in Aqueous Solution. *Chem. Mater.* **2012**, *24* (18), 3659–3666. https://doi.org/10.1021/cm302533s.

(15) Greiner, M. T.; Helander, M. G.; Wang, Z.-B.; Tang, W.-M.; Lu, Z.-H. Effects of Processing Conditions on the Work Function and Energy-Level Alignment of NiO Thin Films. *J. Phys. Chem. C* **2010**, *114* (46), 19777–19781. https://doi.org/10.1021/jp108281m.

(16) Sivanantham, A.; Ganesan, P.; Vinu, A.; Shanmugam, S. Surface Activation and Reconstruction of Non-Oxide-Based Catalysts Through in Situ Electrochemical Tuning for Oxygen Evolution Reactions in Alkaline Media. *ACS Catal.* **2020**, *10* (1), 463–493. https://doi.org/10.1021/acscatal.9b04216.

(17) Laskowski, F. A. L.; Oener, S. Z.; Nellist, M. R.; Gordon, A. M.; Bain, D. C.; Fehrs, J. L.; Boettcher, S. W. Nanoscale Semiconductor/Catalyst Interfaces in Photoelectrochemistry. *Nat. Mater.* **2019**, 1–8. https://doi.org/10.1038/s41563-019-0488-z.

(18) Lee, S. A.; Lee, T. H.; Kim, C.; Lee, M. G.; Choi, M.-J.; Park, H.; Choi, S.; Oh, J.; Jang, H. W. Tailored NiOx/Ni Cocatalysts on Silicon for Highly Efficient Water Splitting Photoanodes via Pulsed Electrodeposition. *ACS Catal.* **2018**, *8* (8), 7261–7269. https://doi.org/10.1021/acscatal.8b01999.

(19) Kenney, M. J.; Gong, M.; Li, Y.; Wu, J. Z.; Feng, J.; Lanza, M.; Dai, H. High-Performance Silicon Photoanodes Passivated with Ultrathin Nickel Films for Water Oxidation. *Science* **2013**, *342* (6160), 836–840. https://doi.org/10.1126/science.1241327.

(20) L. Laskowski, F. A.; R. Nellist, M.; Venkatkarthick, R.; W. Boettcher, S. Junction Behavior of N-Si Photoanodes Protected by Thin Ni Elucidated from Dual Working Electrode Photoelectrochemistry. *Energy Environ. Sci.* **2017**, *10* (2), 570–579. https://doi.org/10.1039/C6EE03505A.

(21) Li, S.; She, G.; Chen, C.; Zhang, S.; Mu, L.; Guo, X.; Shi, W. Enhancing the Photovoltage of Ni/n-Si Photoanode for Water Oxidation through a Rapid Thermal Process. *ACS Appl. Mater. Interfaces* **2018**, *10* (10), 8594–8598. https://doi.org/10.1021/acsami.7b16986.

(22) Liu, D.; Jiang, T.; Liu, D.; Zhang, W.; Qin, H.; Yan, S.; Zou, Z. Silicon Photoanode Modified with Work-Function-Tuned Ni@FeyNi1−y(OH)2 Core-Shell Particles for Water Oxidation. *ChemSusChem* **2020**, *13* (22), 6037–6044. https://doi.org/10.1002/cssc.202002049.

(23) Cai, Q.; Hong, W.; Jian, C.; Liu, W. A High-Performance Silicon Photoanode Enabled by Oxygen Vacancy Modulation on NiOOH Electrocatalyst for Water Oxidation. *Nanoscale* **2020**, *12* (14), 7550–7556. https://doi.org/10.1039/D0NR00921K.

(24) Loget, G.; Fabre, B.; Fryars, S.; Mériadec, C.; Ababou-Girard, S. Dispersed Ni Nanoparticles Stabilize Silicon Photoanodes for Efficient and Inexpensive Sunlight-Assisted Water Oxidation. *ACS Energy Lett.* **2017**, *2* (3), 569–573. https://doi.org/10.1021/acsenergylett.7b00034.

(25) Anantharaj, S.; Kundu, S.; Noda, S. "The Fe Effect": A Review Unveiling the Critical Roles of Fe in Enhancing OER Activity of Ni and Co Based Catalysts. *Nano Energy* **2021**, *80*, 105514. https://doi.org/10.1016/j.nanoen.2020.105514.

(26) Trotochaud, L.; Young, S. L.; Ranney, J. K.; Boettcher, S. W. Nickel–Iron Oxyhydroxide Oxygen-Evolution Electrocatalysts: The Role of Intentional and Incidental Iron Incorporation. *J. Am. Chem. Soc.* **2014**, *136* (18), 6744–6753. https://doi.org/10.1021/ja502379c.

(27) Corrigan, D. A. The Catalysis of the Oxygen Evolution Reaction by Iron Impurities in Thin Film Nickel Oxide Electrodes. *J. Electrochem. Soc.* **1987**, *134* (2), 377. https://doi.org/10.1149/1.2100463.

(28) Stevens, M. B.; Enman, L. J.; Batchellor, A. S.; Cosby, M. R.; Vise, A. E.; Trang, C. D. M.; Boettcher, S. W. Measurement Techniques for the Study of Thin Film Heterogeneous Water Oxidation Electrocatalysts. *Chem. Mater.* **2017**, *29* (1), 120–140. https://doi.org/10.1021/acs.chemmater.6b02796.

(29) Chung, D. Y.; Lopes, P. P.; Farinazzo Bergamo Dias Martins, P.; He, H.; Kawaguchi, T.; Zapol, P.; You, H.; Tripkovic, D.; Strmcnik, D.; Zhu, Y.; Seifert, S.; Lee, S.; Stamenkovic, V. R.; Markovic, N. M. Dynamic Stability of Active Sites in Hydr(Oxy)Oxides for the Oxygen Evolution Reaction. *Nat. Energy* **2020**, *5* (3), 222–230. https://doi.org/10.1038/s41560-020-0576-y.

(30) Zhang, Z.; Yates, J. T. Band Bending in Semiconductors: Chemical and Physical Consequences at Surfaces and Interfaces. *Chem. Rev.* **2012**, *112* (10), 5520–5551. https://doi.org/10.1021/cr3000626.

(31) Hemmerling, J.; Quinn, J.; Linic, S. Quantifying Losses and Assessing the Photovoltage Limits in Metal–Insulator–Semiconductor Water Splitting Systems. *Adv. Energy Mater.* **2020**, *10* (12), 1903354. https://doi.org/10.1002/aenm.201903354.

(32) Quinn, J.; Hemmerling, J.; Linic, S. Maximizing Solar Water Splitting Performance by Nanoscopic Control of the Charge Carrier Fluxes across Semiconductor–Electrocatalyst Junctions. *ACS Catal.* **2018**, *8* (9), 8545–8552. https://doi.org/10.1021/acscatal.8b01929.

(33) Quinn, J.; Hemmerling, J.; Linic, S. Guidelines for Optimizing the Performance of Metal–Insulator–Semiconductor (MIS) Photoelectrocatalytic Systems by Tuning the Insulator Thickness. *ACS Energy Lett.* **2019**, *4* (11), 2632–2638. https://doi.org/10.1021/acsenergylett.9b01609.

(34) Digdaya, I. A.; Trześniewski, B. J.; Adhyaksa, G. W. P.; Garnett, E. C.; Smith, W. A. General Considerations for Improving Photovoltage in Metal–Insulator–Semiconductor Photoanodes. *J. Phys. Chem. C* **2018**, *122* (10), 5462–5471. https://doi.org/10.1021/acs.jpcc.7b11747.

(35) Rossi, R. C.; Lewis, N. S. Investigation of the Size-Scaling Behavior of Spatially Nonuniform Barrier Height Contacts to Semiconductor Surfaces Using Ordered Nanometer-Scale Nickel Arrays on Silicon Electrodes. *J. Phys. Chem. B* **2001**, *105* (49), 12303–12318. https://doi.org/10.1021/jp011861c.

(36) Rhoderick, E. H. Metal-Semiconductor Contacts. *IEE Proc. - Solid-State Electron Devices* **1982**, *129* (1), 1-. https://doi.org/10.1049/ip-i-1.1982.0001.

(37) Tung, R. T. (董梓則). The Physics and Chemistry of the Schottky Barrier Height. *Appl. Phys. Rev.* **2014**, *1* (1), 011304. https://doi.org/10.1063/1.4858400.

(38) Coe, D. J.; Rhoderick, E. H. Silicide Formation in Ni-Si Schottky Barrier Diodes. *J. Phys. Appl. Phys.* **1976**, *9* (6), 965–972. https://doi.org/10.1088/0022-3727/9/6/009.

(39) Lu, C.-H.; Wong, G. M. T.; Birringer, R.; Dauskardt, R.; Deal, M. D.; Clemens, B. M.; Nishi, Y. Bilayer Metal Gate Electrodes with Tunable Work Function: Mechanism and Proposed Model. *J. Appl. Phys.* **2010**, *107* (6), 063710. https://doi.org/10.1063/1.3326237.

(40) Tung, R. T. Electron Transport at Metal-Semiconductor Interfaces: General Theory. *Phys. Rev. B* **1992**, *45* (23), 13509–13523. https://doi.org/10.1103/PhysRevB.45.13509.

(41) Javad Eslamibidgoli, M.; Groß, A.; Eikerling, M. Surface Configuration and Wettability of Nickel(Oxy)Hydroxides: A First-Principles Investigation. *Phys. Chem. Chem. Phys.* **2017**, *19* (34), 22659–22669. https://doi.org/10.1039/C7CP03396F.

(42) Ratcliff, E. L.; Meyer, J.; Steirer, K. X.; Garcia, A.; Berry, J. J.; Ginley, D. S.; Olson, D. C.; Kahn, A.; Armstrong, N. R. Evidence for Near-Surface NiOOH Species in Solution-Processed NiOx Selective Interlayer Materials: Impact on Energetics and the Performance of Polymer Bulk Heterojunction Photovoltaics. *Chem. Mater.* **2011**, *23* (22), 4988–5000. https://doi.org/10.1021/cm202296p.

(43) Wang, X.; Liu, X.; Tong, C.-J.; Yuan, X.; Dong, W.; Lin, T.; Liu, L.-M.; Huang, F. An Electron Injection Promoted Highly Efficient Electrocatalyst of FeNi 3 @GR@Fe-NiOOH for Oxygen Evolution and Rechargeable Metal–Air Batteries. *J. Mater. Chem. A* **2016**, *4* (20), 7762–7771. https://doi.org/10.1039/C6TA01541G.

(44) Xu, G.; Xu, Z.; Shi, Z.; Pei, L.; Yan, S.; Gu, Z.; Zou, Z. Silicon Photoanodes Partially Covered by Ni@Ni(OH)2 Core–Shell Particles for Photoelectrochemical Water Oxidation. *ChemSusChem* **2017**, *10* (14), 2897–2903. https://doi.org/10.1002/cssc.201700825.

(45) Yeh, Y.-H.; Chuang, C.-H.; Yu, T.-Y.; Liu, M.-C.; Cheng, Y.-J. Junction Energetics Engineering Using Ni/NiOx Core-Shell Nanoparticle Coating for Efficient Photoelectrochemical Water Splitting. *Int. J. Hydrog. Energy* **2019**, *44* (31), 16594–16602. https://doi.org/10.1016/j.ijhydene.2019.04.167.

(46) Card, H. C.; Rhoderick, E. H. Studies of Tunnel MOS Diodes I. Interface Effects in Silicon Schottky Diodes. *J. Phys. Appl. Phys.* **1971**, *4* (10), 1589–1601. https://doi.org/10.1088/0022-3727/4/10/319.

(47) Robertson, J. Band Offsets of Wide-Band-Gap Oxides and Implications for Future Electronic Devices. *J. Vac. Sci. Technol. B Microelectron. Nanometer Struct. Process. Meas. Phenom.* **2000**, *18* (3), 1785–1791. https://doi.org/10.1116/1.591472.

(48) Olsen, L. C. Model Calculations for Metal-Insulator-Semiconductor Solar Cells. *Solid-State Electron.* **1977**, *20* (9), 741–751. https://doi.org/10.1016/0038-1101(77)90002-8.

(49) Card, H. C. Potential Barriers to Electron Tunnelling in Ultra-Thin Films of SiO2. *Solid State Commun.* **1974**, *14* (10), 1011–1014. https://doi.org/10.1016/0038-1098(74)90414-1.

Chapter 8

Conclusions and Future Prospects

8.1 Summary of Results and Key Strategies

As described in previous chapters, there has been considerable interest in developing MIS photoelectrocatalysts throughout the past decade. The initial interest in the introduction of insulators was primarily driven by the desire to enhance the stability of various semiconductors under corrosive water splitting conditions. In Chapters 3-5, we have described the recent work aimed at shedding light on the connections between the introduction of an insulator and the performance of MIS systems. This work has allowed us to identify different parameters that play critical roles in the performance of these systems. Furthermore, through experimental measurements and modeling we have identified the best approaches that can be employed to improve the performance of these systems.

For example, the work in Chapters 3 and 4 on planar Ir/n-Si systems have shown that the introduction of an HfO_2 insulator and optimizing its thickness results in significantly increased photovoltage (in this case by ~160 mV). We also learned that these increases in photovoltage are not sufficient to approach the upper performance limits of the flat-band potential (in this case, the maximum measured photovoltage was ~150 mV lower than the flat-band potential). We showed that these additional loses can be minimized by a combination of improving light absorption by the semiconductor (up to 30 mV under 1-sun illumination), removing nonidealities (up to 70 mV), and incorporating a different insulator with an improved carrier selectivity (up to 150 mV).

Chapter 5 introduced several methods to increase the flat-band potential so that higher performance limits can be theoretically reached. Leveraging the insights from the modeling, we also introduced several strategies such as annealing and varying the insulator composition to overcome some of the losses and approach the upper photovoltage limits.

Chapters 6 and 7 transition from traditional MIS systems to nanoparticle electrocatalysts deposited on Si. For these systems, and virtually all photoelectrocatalysts, the atomistic interfacial properties are critical for understanding and predicting the performance. The high efficiency of these nanoparticle-based systems has been previously associated with the so-called "pinch-off" effect. However, the results in Chapters 6 and 7 demonstrate that an adventitious SiO_2 insulator layer at the nanoparticle Ni/Si interface may be the primary explanation for the good performance of these systems. This means that even these systems behave comparably with traditional MIS systems as even an unintentional interfacial insulator layer can significantly improve the performance for nanoparticle-based systems. Overall, this combined work highlights the importance of the interfaces in driving charge transport and offers design guidelines that are broadly applicable to a variety of photoelectrocatalysts.

8.2 Additional Methods and Considerations to Enhance Performance and Practicality of Water Splitting Photoelectrocatalysts

It is critical to understand how to engineer MIS systems that can approach the upper performance limits. This dissertation has focused on the generated photovoltage as the key performance metric, but additional performance metrics of importance include the maximum power (which is directly related to the overall solar-to-hydrogen efficiency of the system) and the onset potential which both have different implications when it comes to optimization.[1–3] For example, the photocurrent or total light absorption does not have a large impact on the

photovoltage because of how is scales with the natural log, but the maximum power scales linearly with current (i.e., P=IV). Meanwhile the onset potential includes the contribution from photovoltage, but also considers the catalytic overpotential. So even if a photoelectrocatalyst has an excellent photovoltage, the onset potential will not be good unless the kinetics are also fast.

This dissertation has not yet discussed key strategies to increase light absorption in the semiconductor, which again is particularly important when considering the overall power and efficiency. To maximize light absorption in the semiconductor, there are several useful strategies such as texturing the surface, introducing an antireflection coating, and incorporating plasmonic metal nanoparticles.[4–13] For example, our group demonstrated that by embedding nanoparticle electrocatalysts in a semiconductor as opposed to dispersing them on the semiconductor's surface, the light reflection and parasitic light absorption by the metal are minimized.[14] In this particular example, 150 nm diameter Pt nanoparticles were embedded into p-type Si and the system was analyzed for photoelectrochemical HER activity. The embedded nanoparticle system increases the light-limited photocurrent by ~24% compared to the non-embedded system and by ~15% compared to bare Si. Furthermore, this strategy of embedding nanoparticles can introduce unique catalytic active sites. A fundamental understanding of the catalysis and measuring rates is another important focus in the literature.[15–17] Indeed, improving the catalysis is important to enhancing the onset potential. Many new electrocatalysts have achieved highly efficient and stable water electrolysis,[18–25] but in most cases, these electrocatalysts are not integrated with semiconductors for solar water splitting.[26,27] Significant improvements could be possible with more cross-fertilization of ideas between these sub-fields.

In addition to the management of light reflections and absorption, significant efforts need to focus on identifying the physical sources of nonidealities. In general, an insulator introduces

additional interfaces which are often sources of defect states that can result in significant charge build-up and a voltage drop in the insulator. The presence of these interfacial defect states will appear as an ideality factor greater than 1 in these systems. This dissertation (Chapter 5) has focused on annealing techniques to remove the defect states.[28–33] Another strategy to improve interfacial quality is through chemical medication of the Si surface.[34–37] In addition to interfacial defects, nonidealities can result from image force lowering, barrier height inhomogeneity, recombination in the semiconductor depletion region, and field emission.[28] While these nonidealities may be negligible for some MIS systems, including the ones discussed above, removing these sources of nonidealities would require alternative approaches for different systems.

The results in Chapter 4 show that systems incorporating an insulator with improved e^-/h^+ selectivity can generate photovoltages that approach the upper limits. To this end, novel insulators with better e^- or h^+ selectivity, depending on the desired half-reaction, should be explored. Indeed, this strategy has been implemented in high-efficiency photovoltaics, and the charge carrier selectivity may be improved by introducing dopant ions to the insulator or by utilizing alternative transition metal oxides such as MoO_x or V_2O_x.[38–43] We note that even with a perfectly selective insulator, the photovoltage may remain slightly below the flat-band potential as other recombination mechanisms (e.g., radiative recombination, Shockley-Read-Hall Recombination, or recombination at the back contact) may become dominant and limit the performance.[28]

Despite the importance of the flat-band potential, only a few studies have explored methods to increase it. As discussed in Chapter 5, one method to achieve a higher flat-band potential is to increase the doping density of semiconductors, although one must be aware that

the doping density can also influence the photocurrent and the minority carrier diffusion length.[28] Furthermore, if the doping density becomes too large, this can introduce alternative recombination pathways from field emission and Auger recombination.[44] As also discussed in Chapter 5, the flat-band potential can also be increased by incorporating metals or metal oxides with high (for n-Si) and low (for p-Si) work functions. The methods are based on the simplified form of the flat-band potential in which the insulator does not impact the result. However, if an insulator has fixed charges at the surface or charges within the bulk, then this can also impact the flat-band potential (see equation 4-6). It may be possible to manipulate these charges to improve the flat-band potential and increase the overall performance.

Overall Si has been widely studied for water splitting using a variety of architectures including MIS, nanoparticle/Si junction (both studied in this dissertation), p-n junctions, and heterojunctions.[45,46] A comprehensive comparison of the prospects for these general architectures could help guide the field. The key aspects to consider would be performance metrics of photovoltage, onset potential, maximum power, and stability while also considering the expenses. In terms of expenses, nearly every water splitting study with Si uses monocrystalline silicon[45] but expenses can be significantly lower using polycrystalline Si. Therefore, it would be insightful to explore which of the architectures are most suitable for overcoming the challenges of polycrystalline Si such as lower diffusion lengths, grain boundaries, and impurities.[47] In terms of stability, the perhaps the longest stability has been demonstrated using ALD heterojunctions with months of stability.[48,49]

So far, this dissertation has only discussed work on specifically protecting and improving the Si semiconductor. Moving forward, significant effort should be dedicated to implementation of MIS concepts to wider band gap semiconductors. Some groups have studied the performance

of MIS architecture for Ni/TiO_2/$BiVO_4$[50] and graded MoS_x/c-TiO_2/$GaInP_2$[51] MIS systems; however, the important fundamental concepts of photovoltage, flat-band potential, and barrier height were not analyzed. p-type Cu_2O (band gap ~2.1 eV) is a suitable option for coupling with n-Si in a tandem configuration. Good performance has been achieved by forming pn heterojunctions for solar cell and water splitting applications,[52–56] but MIS junctions with Cu_2O have not yet been demonstrated. If high performance can be obtained with pn junctions, then in principle high performance can also be obtained with MIS junctions where the work function and barrier height are relatively easy to tune using the metal layer. It is important to note that the equations and theory used throughout this dissertation apply for systems with high carrier mobility in the bulk of the semiconductor. But many wide band gap semiconductors have poor carrier mobilities, and so additional recombination mechanisms may need to be considered to obtain a complete picture of the MIS system performance.

8.3 Tandem Systems for Overall Photoelectrochemical Water Splitting

More research should also focus on incorporating Si into practical tandem water splitting systems. So far, the STH efficiency of Si coupled to other wide band gap semiconductors in a tandem configuration is below 5%, and the semiconductors are electrically connected with wires.[57–62] A more integrated design consists of Si in direct contact with a wide band gap semiconductor. Attempts at fabricating fully-integrated tandem structures utilizing Si have not generated enough voltage to split water[63–65] until very recently.[45,66] Instead, higher efficiencies have been reported using wired designs or Si solar cells.[67–69] Besides Si, STH efficiencies exceeding 10% have been obtained using wired III/V semiconductors, although these tend to be expensive and unstable.[70–74] In addition to the costs and the generated photovoltage, important considerations for integrated tandem systems are the design of the interfaces between the

semiconductors and the light absorption and photocurrent matching between the semiconductors. Since Si is the bottom absorber in the tandem configuration, photons will enter the Si through the backside, and the high-energy photons will be preferentially absorbed by the wide-band gap semiconductor.[75] Thus, the photocurrent through Si in the tandem configuration will be significantly lower compared to 1-sun illumination used in experiments. Based on the results of Chapter 4, the lower photocurrent will only modestly decrease the photovoltage, but this has important implications for the total generated power and for current matching with the wide band gap semiconductor.[76]

Additional factors that need further study and performance improvements to improve the economic viability of overall water splitting with tandem structures include stability and degradation pathways, the impact of using concentrated sunlight, integration of membranes to separate products, integration with state-of-the-art catalysts, and overall reactor design. The above discussions and results of this dissertation aim to help achieve the overarching goal in the solar water splitting community to develop stable, efficient, and economical tandem photoelectrocatalysts to produce abundant hydrogen for sustainable energy storage and generation.

8.4 References

(1) Stevens, M. B.; Enman, L. J.; Batchellor, A. S.; Cosby, M. R.; Vise, A. E.; Trang, C. D. M.; Boettcher, S. W. Measurement Techniques for the Study of Thin Film Heterogeneous Water Oxidation Electrocatalysts. *Chem. Mater.* **2017**, *29* (1), 120–140. https://doi.org/10.1021/acs.chemmater.6b02796.

(2) Chen, Z.; Dinh, H. N.; Miller, E. *Photoelectrochemical Water Splitting*; SpringerBriefs in Energy; Springer New York: New York, NY, 2013. https://doi.org/10.1007/978-1-4614-8298-7.

(3) Chen, Z.; Jaramillo, T. F.; Deutsch, T. G.; Kleiman-Shwarsctein, A.; Forman, A. J.; Gaillard, N.; Garland, R.; Takanabe, K.; Heske, C.; Sunkara, M.; McFarland, E. W.; Domen, K.; Miller, E. L.; Turner, J. A.; Dinh, H. N. Accelerating Materials Development

for Photoelectrochemical Hydrogen Production: Standards for Methods, Definitions, and Reporting Protocols. *J. Mater. Res.* **2010**, *25* (1), 3–16. https://doi.org/10.1557/JMR.2010.0020.

(4) Ji, L.; Hsu, H.-Y.; Li, X.; Huang, K.; Zhang, Y.; Lee, J. C.; Bard, A. J.; Yu, E. T. Localized Dielectric Breakdown and Antireflection Coating in Metal–Oxide–Semiconductor Photoelectrodes. *Nat. Mater.* **2017**, *16* (1), 127–131. https://doi.org/10.1038/nmat4801.

(5) V. Esposito, D.; Lee, Y.; Yoon, H.; M. Haney, P.; Y. Labrador, N.; P. Moffat, T.; Alec Talin, A.; A. Szalai, V. Deconvoluting the Influences of 3D Structure on the Performance of Photoelectrodes for Solar-Driven Water Splitting. *Sustain. Energy Fuels* **2017**, *1* (1), 154–173. https://doi.org/10.1039/C6SE00073H.

(6) Yul Lim, S.; Ha, K.; Ha, H.; Youn Lee, S.; Seok Jang, M.; Choi, M.; Dong Chung, T. Three-Dimensionally Patterned Ag–Pt Alloy Catalyst on Planar Si Photocathodes for Photoelectrochemical H 2 Evolution. *Phys. Chem. Chem. Phys.* **2019**, *21* (8), 4184–4192. https://doi.org/10.1039/C8CP07304J.

(7) Chen, C.-J.; Veeramani, V.; Wu, Y.-H.; Jena, A.; Yin, L.-C.; Chang, H.; Hu, S.-F.; Liu, R.-S. Phosphorous-Doped Molybdenum Disulfide Anchored on Silicon as an Efficient Catalyst for Photoelectrochemical Hydrogen Generation. *Appl. Catal. B Environ.* **2020**, *263*, 118259. https://doi.org/10.1016/j.apcatb.2019.118259.

(8) Hong, W.; Cai, Q.; Ban, R.; He, X.; Jian, C.; Li, J.; Li, J.; Liu, W. High-Performance Silicon Photoanode Enhanced by Gold Nanoparticles for Efficient Water Oxidation. *ACS Appl. Mater. Interfaces* **2018**, *10* (7), 6262–6268. https://doi.org/10.1021/acsami.7b16749.

(9) Hernley, P. A.; Linic, S. Modeling the Impact of Metallic Plasmonic Resonators on the Solar Conversion Efficiencies of Semiconductor Photoelectrodes: When Does Introducing Buried Plasmonic Nanostructures Make Sense? *J. Phys. Chem. C* **2018**, *122* (42), 24279–24286. https://doi.org/10.1021/acs.jpcc.8b07214.

(10) Ingram, D. B.; Linic, S. Water Splitting on Composite Plasmonic-Metal/Semiconductor Photoelectrodes: Evidence for Selective Plasmon-Induced Formation of Charge Carriers near the Semiconductor Surface. *J. Am. Chem. Soc.* **2011**, *133* (14), 5202–5205. https://doi.org/10.1021/ja200086g.

(11) Chavez, S.; Govind Rao, V.; Linic, S. Unearthing the Factors Governing Site Specific Rates of Electronic Excitations in Multicomponent Plasmonic Systems and Catalysts. *Faraday Discuss.* **2019**, *214* (0), 441–453. https://doi.org/10.1039/C8FD00143J.

(12) Linic, S.; Aslam, U.; Boerigter, C.; Morabito, M. Photochemical Transformations on Plasmonic Metal Nanoparticles. *Nat. Mater.* **2015**, *14* (6), 567–576. https://doi.org/10.1038/nmat4281.

(13) Linic, S.; Chavez, S.; Elias, R. Flow and Extraction of Energy and Charge Carriers in Hybrid Plasmonic Nanostructures. *Nat. Mater.* **2021**, 1–9. https://doi.org/10.1038/s41563-020-00858-4.

(14) Hernley, P. A.; Chavez, S. A.; Quinn, J. P.; Linic, S. Engineering the Optical and Catalytic Properties of Co-Catalyst/Semiconductor Photocatalysts. *ACS Photonics* **2017**, *4* (4), 979–985. https://doi.org/10.1021/acsphotonics.7b00047.

(15) Dix, S. T.; Lu, S.; Linic, S. Critical Practices in Rigorously Assessing the Inherent Activity of Nanoparticle Electrocatalysts. *ACS Catal.* **2020**, *10* (18), 10735–10741. https://doi.org/10.1021/acscatal.0c03028.

(16) Cleve, T. V.; Moniri, S.; Belok, G.; More, K. L.; Linic, S. Nanoscale Engineering of Efficient Oxygen Reduction Electrocatalysts by Tailoring the Local Chemical Environment of Pt Surface Sites. *ACS Catal.* **2017**, *7* (1), 17–24. https://doi.org/10.1021/acscatal.6b01565.

(17) Dix, S. T.; Linic, S. In-Operando Surface-Sensitive Probing of Electrochemical Reactions on Nanoparticle Electrocatalysts: Spectroscopic Characterization of Reaction Intermediates and Elementary Steps of Oxygen Reduction Reaction on Pt. *J. Catal.* **2021**, *396*, 32–39. https://doi.org/10.1016/j.jcat.2021.02.009.

(18) Jung, S.; L. McCrory, C. C.; M. Ferrer, I.; C. Peters, J.; F. Jaramillo, T. Benchmarking Nanoparticulate Metal Oxide Electrocatalysts for the Alkaline Water Oxidation Reaction. *J. Mater. Chem. A* **2016**, *4* (8), 3068–3076. https://doi.org/10.1039/C5TA07586F.

(19) McCrory, C. C. L.; Jung, S.; Peters, J. C.; Jaramillo, T. F. Benchmarking Heterogeneous Electrocatalysts for the Oxygen Evolution Reaction. *J. Am. Chem. Soc.* **2013**, *135* (45), 16977–16987. https://doi.org/10.1021/ja407115p.

(20) Masa, J.; Andronescu, C.; Schuhmann, W. Electrocatalysis as the Nexus for Sustainable Renewable Energy: The Gordian Knot of Activity, Stability, and Selectivity. *Angew. Chem. Int. Ed.* **2020**, *59* (36), 15298–15312. https://doi.org/10.1002/anie.202007672.

(21) Li, Y.; Dong, Z.; Jiao, L. Multifunctional Transition Metal-Based Phosphides in Energy-Related Electrocatalysis. *Adv. Energy Mater.* **2020**, *10* (11), 1902104. https://doi.org/10.1002/aenm.201902104.

(22) Liu, J.; Liu, H.; Chen, H.; Du, X.; Zhang, B.; Hong, Z.; Sun, S.; Wang, W. Progress and Challenges Toward the Rational Design of Oxygen Electrocatalysts Based on a Descriptor Approach. *Adv. Sci.* **2020**, *7* (1), 1901614. https://doi.org/10.1002/advs.201901614.

(23) Song, J.; Wei, C.; Huang, Z.-F.; Liu, C.; Zeng, L.; Wang, X.; J. Xu, Z. A Review on Fundamentals for Designing Oxygen Evolution Electrocatalysts. *Chem. Soc. Rev.* **2020**, *49* (7), 2196–2214. https://doi.org/10.1039/C9CS00607A.

(24) Zhu, K.; Shi, F.; Zhu, X.; Yang, W. The Roles of Oxygen Vacancies in Electrocatalytic Oxygen Evolution Reaction. *Nano Energy* **2020**, *73*, 104761. https://doi.org/10.1016/j.nanoen.2020.104761.

(25) Zhao, T.; Wang, Y.; Karuturi, S.; Catchpole, K.; Zhang, Q.; Zhao, C. Design and Operando/in Situ Characterization of Precious-Metal-Free Electrocatalysts for Alkaline Water Splitting. *Carbon Energy* **2020**, *2* (4), 582–613. https://doi.org/10.1002/cey2.79.

(26) Gao, R.; Yan, D. Recent Development of Ni/Fe-Based Micro/Nanostructures toward Photo/Electrochemical Water Oxidation. *Adv. Energy Mater. 0* (0), 1900954. https://doi.org/10.1002/aenm.201900954.

(27) Ye, S.; Ding, C.; Liu, M.; Wang, A.; Huang, Q.; Li, C. Water Oxidation Catalysts for Artificial Photosynthesis. *Adv. Mater.* **2019**, *31* (50), 1902069. https://doi.org/10.1002/adma.201902069.

(28) Hemmerling, J.; Quinn, J.; Linic, S. Quantifying Losses and Assessing the Photovoltage Limits in Metal–Insulator–Semiconductor Water Splitting Systems. *Adv. Energy Mater.* **2020**, *10* (12), 1903354. https://doi.org/10.1002/aenm.201903354.

(29) Scheuermann, A. G.; Lawrence, J. P.; Meng, A. C.; Tang, K.; Hendricks, O. L.; Chidsey, C. E. D.; McIntyre, P. C. Titanium Oxide Crystallization and Interface Defect Passivation for High Performance Insulator-Protected Schottky Junction MIS Photoanodes. *ACS Appl. Mater. Interfaces* **2016**, *8* (23), 14596–14603. https://doi.org/10.1021/acsami.6b03688.

(30) Chuang, C.-H.; Lai, Y.-Y.; Hou, C.-H.; Cheng, Y.-J. Annealed Polycrystalline TiO2 Interlayer of the N-Si/TiO2/Ni Photoanode for Efficient Photoelectrochemical Water Splitting. *ACS Appl. Energy Mater.* **2020**, *3* (4), 3902–3908. https://doi.org/10.1021/acsaem.0c00319.

(31) Hemmerling, J. R.; Mathur, A.; Linic, S. Design Principles for Efficient and Stable Water Splitting Photoelectrocatalysts. *Acc. Chem. Res.* **2021**, *54* (8), 1992–2002. https://doi.org/10.1021/acs.accounts.1c00072.

(32) Li, S.; She, G.; Chen, C.; Zhang, S.; Mu, L.; Guo, X.; Shi, W. Enhancing the Photovoltage of Ni/n-Si Photoanode for Water Oxidation through a Rapid Thermal Process. *ACS Appl. Mater. Interfaces* **2018**, *10* (10), 8594–8598. https://doi.org/10.1021/acsami.7b16986.

(33) Tung, C.-W.; Kuo, T.-R.; Hsu, C.-S.; Chuang, Y.; Chen, H.-C.; Chang, C.-K.; Chien, C.-Y.; Lu, Y.-J.; Chan, T.-S.; Lee, J.-F.; Li, J.-Y.; Chen, H. M. Light-Induced Activation of Adaptive Junction for Efficient Solar-Driven Oxygen Evolution: In Situ Unraveling the Interfacial Metal–Silicon Junction. *Adv. Energy Mater.* **2019**, *9* (31), 1901308. https://doi.org/10.1002/aenm.201901308.

(34) Boucher, D. G.; Kearney, K.; Ertekin, E.; Rose, M. J. Tuning P-Si(111) Photovoltage via Molecule|Semiconductor Electronic Coupling. *J. Am. Chem. Soc.* **2021**, *143* (6), 2567–2580. https://doi.org/10.1021/jacs.0c12075.

(35) Seo, J.; Kim, H. J.; Pekarek, R. T.; Rose, M. J. Hybrid Organic/Inorganic Band-Edge Modulation of p-Si(111) Photoelectrodes: Effects of R, Metal Oxide, and Pt on H2 Generation. *J. Am. Chem. Soc.* **2015**, *137* (9), 3173–3176. https://doi.org/10.1021/ja5126287.

(36) Brown, E. S.; Hlynchuk, S.; Maldonado, S. Chemically Modified Si(111) Surfaces Simultaneously Demonstrating Hydrophilicity, Resistance against Oxidation, and Low Trap State Densities. *Surf. Sci.* **2016**, *645*, 49–55. https://doi.org/10.1016/j.susc.2015.10.056.

(37) O'Leary, L. E.; Strandwitz, N. C.; Roske, C. W.; Pyo, S.; Brunschwig, B. S.; Lewis, N. S. Use of Mixed CH3–/HC(O)CH2CH2–Si(111) Functionality to Control Interfacial Chemical and Electronic Properties During the Atomic-Layer Deposition of Ultrathin Oxides on Si(111). *J. Phys. Chem. Lett.* **2015**, *6* (4), 722–726. https://doi.org/10.1021/jz502542a.

(38) Gao, P.; Yang, Z.; He, J.; Yu, J.; Liu, P.; Zhu, J.; Ge, Z.; Ye, J. Dopant-Free and Carrier-Selective Heterocontacts for Silicon Solar Cells: Recent Advances and Perspectives. *Adv. Sci.* **2018**, *5* (3), 1700547. https://doi.org/10.1002/advs.201700547.

(39) Bowden, S.; Ghosh, K.; Honsberg, C. Non PN Junction Solar Cells Using Carrier Selective Contacts. In *Physics, Simulation, and Photonic Engineering of Photovoltaic Devices II*; International Society for Optics and Photonics, 2013; Vol. 8620, p 86200T. https://doi.org/10.1117/12.2004259.

(40) Yang, Z.; Gao, P.; Sheng, J.; Tong, H.; Quan, C.; Yang, X.; Chee, K. W. A.; Yan, B.; Zeng, Y.; Ye, J. Principles of Dopant-Free Electron-Selective Contacts Based on Tunnel Oxide/Low Work-Function Metal Stacks and Their Applications in Heterojunction Solar Cells. *Nano Energy* **2018**, *46*, 133–140. https://doi.org/10.1016/j.nanoen.2018.01.043.

(41) Bullock, J.; Hettick, M.; Geissbühler, J.; Ong, A. J.; Allen, T.; Sutter-Fella, C. M.; Chen, T.; Ota, H.; Schaler, E. W.; De Wolf, S.; Ballif, C.; Cuevas, A.; Javey, A. Efficient Silicon Solar Cells with Dopant-Free Asymmetric Heterocontacts. *Nat. Energy* **2016**, *1* (3), 1–7. https://doi.org/10.1038/nenergy.2015.31.

(42) Meyer, J.; Hamwi, S.; Kröger, M.; Kowalsky, W.; Riedl, T.; Kahn, A. Transition Metal Oxides for Organic Electronics: Energetics, Device Physics and Applications. *Adv. Mater.* **2012**, *24* (40), 5408–5427. https://doi.org/10.1002/adma.201201630.

(43) Hussain, S. Q.; Mallem, K.; Khan, M. A.; Khokhar, M. Q.; Lee, Y.; Park, J.; Lee, K. S.; Kim, Y.; Cho, E. C.; Cho, Y. H.; Yi, J. Versatile Hole Carrier Selective MoOx Contact for High Efficiency Silicon Heterojunction Solar Cells: A Review. *Trans. Electr. Electron. Mater.* **2019**, *20* (1), 1–6. https://doi.org/10.1007/s42341-018-00089-0.

(44) Rhoderick, E. H. Metal-Semiconductor Contacts. *IEE Proc. - Solid-State Electron Devices* **1982**, *129* (1), 1-. https://doi.org/10.1049/ip-i-1.1982.0001.

(45) Luo, Z.; Wang, T.; Gong, J. Single-Crystal Silicon-Based Electrodes for Unbiased Solar Water Splitting: Current Status and Prospects. *Chem. Soc. Rev.* **2019**, *48* (7), 2158–2181. https://doi.org/10.1039/C8CS00638E.

(46) Fan, R.; Mi, Z.; Shen, M. Silicon Based Photoelectrodes for Photoelectrochemical Water Splitting. *Opt. Express* **2019**, *27* (4), A51–A80. https://doi.org/10.1364/OE.27.000A51.

(47) Narayanan, S.; Wenham, S. R.; Green, M. A. 17.8-Percent Efficiency Polycrystalline Silicon Solar Cells. *IEEE Trans. Electron Devices* **1990**, *37* (2), 382–384. https://doi.org/10.1109/16.46370.

(48) Zhou, X.; Liu, R.; Sun, K.; Friedrich, D.; T. McDowell, M.; Yang, F.; T. Omelchenko, S.; H. Saadi, F.; C. Nielander, A.; Yalamanchili, S.; M. Papadantonakis, K.; S. Brunschwig, B.; S. Lewis, N. Interface Engineering of the Photoelectrochemical Performance of Ni-Oxide-Coated n-Si Photoanodes by Atomic-Layer Deposition of Ultrathin Films of Cobalt Oxide. *Energy Environ. Sci.* **2015**, *8* (9), 2644–2649. https://doi.org/10.1039/C5EE01687H.

(49) Zhou, X.; Liu, R.; Sun, K.; M. Papadantonakis, K.; S. Brunschwig, B.; S. Lewis, N. 570 MV Photovoltage, Stabilized n-Si/CoO x Heterojunction Photoanodes Fabricated Using Atomic Layer Deposition. *Energy Environ. Sci.* **2016**, *9* (3), 892–897. https://doi.org/10.1039/C5EE03655K.

(50) McDowell, M. T.; Lichterman, M. F.; Spurgeon, J. M.; Hu, S.; Sharp, I. D.; Brunschwig, B. S.; Lewis, N. S. Improved Stability of Polycrystalline Bismuth Vanadate Photoanodes by Use of Dual-Layer Thin TiO2/Ni Coatings. *J. Phys. Chem. C* **2014**, *118* (34), 19618–19624. https://doi.org/10.1021/jp506133y.

(51) Gu, J.; Aguiar, J. A.; Ferrere, S.; Steirer, K. X.; Yan, Y.; Xiao, C.; Young, J. L.; Al-Jassim, M.; Neale, N. R.; Turner, J. A. A Graded Catalytic–Protective Layer for an Efficient and Stable Water-Splitting Photocathode. *Nat. Energy* **2017**, *2* (2), 1–8. https://doi.org/10.1038/nenergy.2016.192.

(52) Cendula, P.; Mayer, M. T.; Luo, J.; Grätzel, M. Elucidation of Photovoltage Origin and Charge Transport in Cu2O Heterojunctions for Solar Energy Conversion. *Sustain. Energy Fuels* **2019**, *3* (10), 2633–2641. https://doi.org/10.1039/C9SE00385A.

(53) Paracchino, A.; Mathews, N.; Hisatomi, T.; Stefik, M.; David Tilley, S.; Grätzel, M. Ultrathin Films on Copper(i) Oxide Water Splitting Photocathodes: A Study on Performance and Stability. *Energy Environ. Sci.* **2012**, *5* (9), 8673–8681. https://doi.org/10.1039/C2EE22063F.

(54) Son, M.-K.; Steier, L.; Schreier, M.; T. Mayer, M.; Luo, J.; Grätzel, M. A Copper Nickel Mixed Oxide Hole Selective Layer for Au-Free Transparent Cuprous Oxide Photocathodes. *Energy Environ. Sci.* **2017**, *10* (4), 912–918. https://doi.org/10.1039/C6EE03613A.

(55) Pan, L.; Kim, J. H.; Mayer, M. T.; Son, M.-K.; Ummadisingu, A.; Lee, J. S.; Hagfeldt, A.; Luo, J.; Grätzel, M. Boosting the Performance of Cu 2 O Photocathodes for Unassisted Solar Water Splitting Devices. *Nat. Catal.* **2018**, *1* (6), 412–420. https://doi.org/10.1038/s41929-018-0077-6.

(56) Toe, C. Y.; Scott, J.; Amal, R.; Ng, Y. H. Recent Advances in Suppressing the Photocorrosion of Cuprous Oxide for Photocatalytic and Photoelectrochemical Energy Conversion. *J. Photochem. Photobiol. C Photochem. Rev.* **2019**, *40*, 191–211. https://doi.org/10.1016/j.jphotochemrev.2018.10.001.

(57) Vijselaar, W.; Westerik, P.; Veerbeek, J.; Tiggelaar, R. M.; Berenschot, E.; Tas, N. R.; Gardeniers, H.; Huskens, J. Spatial Decoupling of Light Absorption and Catalytic Activity of Ni–Mo-Loaded High-Aspect-Ratio Silicon Microwire Photocathodes. *Nat. Energy* **2018**, *3* (3), 185–192. https://doi.org/10.1038/s41560-017-0068-x.

(58) Feng, S.; Wang, T.; Liu, B.; Hu, C.; Li, L.; Zhao, Z.-J.; Gong, J. Enriched Surface Oxygen Vacancies of Photoanodes by Photoetching with Enhanced Charge Separation. *Angew. Chem. Int. Ed.* **2020**, *59* (5), 2044–2048. https://doi.org/10.1002/anie.201913295.

(59) Jang, J.-W.; Du, C.; Ye, Y.; Lin, Y.; Yao, X.; Thorne, J.; Liu, E.; McMahon, G.; Zhu, J.; Javey, A.; Guo, J.; Wang, D. Enabling Unassisted Solar Water Splitting by Iron Oxide and Silicon. *Nat. Commun.* **2015**, *6* (1), 1–5. https://doi.org/10.1038/ncomms8447.

(60) Liu, B.; Feng, S.; Yang, L.; Li, C.; Luo, Z.; Wang, T.; Gong, J. Bifacial Passivation of n - Silicon Metal–Insulator–Semiconductor Photoelectrodes for Efficient Oxygen and Hydrogen Evolution Reactions. *Energy Environ. Sci.* **2020**, *13* (1), 221–228. https://doi.org/10.1039/C9EE02766A.

(61) Xu, P.; Feng, J.; Fang, T.; Zhao, X.; Li, Z.; Zou, Z. Photoelectrochemical Cell for Unassisted Overall Solar Water Splitting Using a BiVO 4 Photoanode and Si Nanoarray Photocathode. *RSC Adv.* **2016**, *6* (12), 9905–9910. https://doi.org/10.1039/C5RA20115B.

(62) Abdi, F. F.; Han, L.; Smets, A. H. M.; Zeman, M.; Dam, B.; van de Krol, R. Efficient Solar Water Splitting by Enhanced Charge Separation in a Bismuth Vanadate-Silicon Tandem Photoelectrode. *Nat. Commun.* **2013**, *4* (1), 2195. https://doi.org/10.1038/ncomms3195.

(63) Kunturu, P. P.; Zachariadis, C.; Witczak, L.; Nguyen, M. D.; Rijnders, G.; Huskens, J. Tandem Si Micropillar Array Photocathodes with Conformal Copper Oxide and a Protection Layer by Pulsed Laser Deposition. *ACS Appl. Mater. Interfaces* **2019**, *11* (44), 41402–41414. https://doi.org/10.1021/acsami.9b14408.

(64) Vijselaar, W.; Kunturu, P. P.; Moehl, T.; Tilley, S. D.; Huskens, J. Tandem Cuprous Oxide/Silicon Microwire Hydrogen-Evolving Photocathode with Photovoltage Exceeding 1.3 V. *ACS Energy Lett.* **2019**, *4* (9), 2287–2294. https://doi.org/10.1021/acsenergylett.9b01402.

(65) R. Shaner, M.; T. Fountaine, K.; Ardo, S.; H. Coridan, R.; A. Atwater, H.; S. Lewis, N. Photoelectrochemistry of Core–Shell Tandem Junction n–p + -Si/n-WO 3 Microwire Array Photoelectrodes. *Energy Environ. Sci.* **2014**, *7* (2), 779–790. https://doi.org/10.1039/C3EE43048K.

(66) Vanka, S.; Zhou, B.; Awni, R. A.; Song, Z.; Chowdhury, F. A.; Liu, X.; Hajibabaei, H.; Shi, W.; Xiao, Y.; Navid, I. A.; Pandey, A.; Chen, R.; Botton, G. A.; Hamann, T. W.; Wang, D.; Yan, Y.; Mi, Z. InGaN/Si Double-Junction Photocathode for Unassisted Solar Water Splitting. *ACS Energy Lett.* **2020**, *5* (12), 3741–3751. https://doi.org/10.1021/acsenergylett.0c01583.

(67) Eftekharinia, B.; Pezeshki, H.; Dabirian, A. Unassisted Water Splitting Using Standard Silicon Solar Cells Stabilized with Copper and Bifunctional NiFe Electrocatalysts. *ACS Appl. Mater. Interfaces* **2020**, *12* (15), 17424–17435. https://doi.org/10.1021/acsami.9b22622.

(68) Fu, H.-C.; Varadhan, P.; Lin, C.-H.; He, J.-H. Spontaneous Solar Water Splitting with Decoupling of Light Absorption and Electrocatalysis Using Silicon Back-Buried Junction. *Nat. Commun.* **2020**, *11* (1), 3930. https://doi.org/10.1038/s41467-020-17660-0.

(69) Lee, M.; Ding, X.; Banerjee, S.; Krause, F.; Smirnov, V.; Astakhov, O.; Merdzhanova, T.; Klingebiel, B.; Kirchartz, T.; Finger, F.; Rau, U.; Haas, S. Bifunctional CoFeVOx Catalyst for Solar Water Splitting by Using Multijunction and Heterojunction Silicon Solar Cells. *Adv. Mater. Technol.* **2020**, *5* (12), 2000592. https://doi.org/10.1002/admt.202000592.

(70) Cheng, W.-H.; Richter, M. H.; May, M. M.; Ohlmann, J.; Lackner, D.; Dimroth, F.; Hannappel, T.; Atwater, H. A.; Lewerenz, H.-J. Monolithic Photoelectrochemical Device for Direct Water Splitting with 19% Efficiency. *ACS Energy Lett.* **2018**, *3* (8), 1795–1800. https://doi.org/10.1021/acsenergylett.8b00920.

(71) Verlage, E.; Hu, S.; Liu, R.; R. Jones, R. J.; Sun, K.; Xiang, C.; S. Lewis, N.; A. Atwater, H. A Monolithically Integrated, Intrinsically Safe, 10% Efficient, Solar-Driven Water-Splitting System Based on Active, Stable Earth-Abundant Electrocatalysts in Conjunction with Tandem III–V Light Absorbers Protected by Amorphous TiO 2 Films. *Energy Environ. Sci.* **2015**, *8* (11), 3166–3172. https://doi.org/10.1039/C5EE01786F.

(72) May, M. M.; Lewerenz, H.-J.; Lackner, D.; Dimroth, F.; Hannappel, T. Efficient Direct Solar-to-Hydrogen Conversion by in Situ Interface Transformation of a Tandem Structure. *Nat. Commun.* **2015**, *6* (1), 1–7. https://doi.org/10.1038/ncomms9286.

(73) Ben-Naim, M.; Britto, R. J.; Aldridge, C. W.; Mow, R.; Steiner, M. A.; Nielander, A. C.; King, L. A.; Friedman, D. J.; Deutsch, T. G.; Young, J. L.; Jaramillo, T. F. Addressing the Stability Gap in Photoelectrochemistry: Molybdenum Disulfide Protective Catalysts for Tandem III–V Unassisted Solar Water Splitting. *ACS Energy Lett.* **2020**, *5* (8), 2631–2640. https://doi.org/10.1021/acsenergylett.0c01132.

(74) Moon, C.; Seger, B.; Vesborg, P. C. K.; Hansen, O.; Chorkendorff, I. Wireless Photoelectrochemical Water Splitting Using Triple-Junction Solar Cell Protected by TiO2. *Cell Rep. Phys. Sci.* **2020**, *1* (12), 100261. https://doi.org/10.1016/j.xcrp.2020.100261.

(75) Bae, D.; Pedersen, T.; Seger, B.; Malizia, M.; Kuznetsov, A.; Hansen, O.; Chorkendorff, I.; K. Vesborg, P. C. Back-Illuminated Si Photocathode: A Combined Experimental and Theoretical Study for Photocatalytic Hydrogen Evolution. *Energy Environ. Sci.* **2015**, *8* (2), 650–660. https://doi.org/10.1039/C4EE03723E.

(76) Walter, M. G.; Warren, E. L.; McKone, J. R.; Boettcher, S. W.; Mi, Q.; Santori, E. A.; Lewis, N. S. Solar Water Splitting Cells. *Chem. Rev.* **2010**, *110* (11), 6446–6473. https://doi.org/10.1021/cr1002326.